MONASH University

Interfacial Flows in Drying Blood Droplets and Paper-Based Diagnostics

A thesis submitted for the degree of
Doctor of Philosophy

by

Michael J. Hertaeg

Supervised by Prof. Gil Garnier and Assoc Prof. Rico Tabor

Department of Chemical Engineering

Faculty of Engineering

August 2020

"From my earliest recollection I have had an irresistible liking for mechanics and the physical laws on which mechanics as a science is based..., my attention drawn to various mechanical phenomena for the explanation of which I discovered that a knowledge of mathematics was essential."

Osborne Reynolds

Copyright Notice

Contents

Abstract

Recently, there has been great advances in the field of low-cost diagnostics. Two promising platforms that have emerged are paper and drying droplets. Both utilise passive interfacial flows generated by capillary pressure and therefore do not require any external actuators to function. In this thesis, the fundamental mechanisms behind flow in these two styles of diagnostics and the effect of biological components, such as cells and proteins are investigated. These new concepts are validated by developing novel blood diagnostic techniques for the analysis of forward and reverse blood groups, SARS-CoV-2 antibodies and haematocrit.

In paper-based diagnostics, reagents and samples to analyse are typically liquids which are introduced by droplet deposition, where droplets are deposited onto the device with a pipette or similar device. Also, the stain size and shape left by droplets of a biological analyte are convenient measures of its properties. In chapter 3, the stain growth of a droplet of red blood cell suspension deposited on paper previously wetted with an antibody solution is analysed. The stain size can be used to identify the presence or absence of agglutination less than 10 seconds after deposition. This phenomenon can be used to quickly and cheaply determine forward blood groups or the presence of antigens on the red blood cell membrane. This is currently the fastest blood tying test which can be easily automated and scaled up. Reverse group diagnostics (the analysis of antibodies in plasma) and the detection of SARS-CoV-2 (COVID-19) antibodies are also demonstrated with this technique. However, the error rate is higher than is demonstrated with the forward group tests. The technique presented in Chapter 4 overcomes sensitivity and reproducibility issues in reverse testing by premixing and incubating reactants before depositing a single droplet on the paper. This produces very different results and leads to ring deposits that are analysed with image processing to identify results.

Before droplet wicking diagnostics such as these can be efficiently designed and optimised, the mechanisms leading to stain formation from a sessile droplet on a paper surface must be clearly understood. In this system, the droplet will remain above the surface of the paper for a short time and then completely absorb. Before absorption, the wet area is generally saturated with fluid. However, after absorption, any further increase in wet area must be balanced by a decrease in local volume fraction. This causes most of the stain to be unsaturated after this point. The process of wicking in

paper is well studied in saturated infinite reservoir systems. However, finite reservoir systems including radially wicking droplets, are not well understood. In this thesis, three fundamental aspects of a droplet wicking radially into paper were investigated; their analysis forms the main content of Chapters 5, 6 and 7. In Chapter 5, the final stain size reached by a fluid was explored by measuring the stain area produced by a range of model fluids. Surface tension and viscosity did not significantly affect results. However, protein content due to adsorption of some blood components during wicking was extremely important. This was correlated with contact angle experiments, where protein content caused an increase to the solid-liquid interfacial tension. In Chapter 6, the cause of the first-to-second stage transition observed in stain growth kinetics was investigated and the dynamics for simple fluids was modelled from first principles. The stain growth transition was modelled using continuum mechanics and incorporating the effects of both the removal of the droplet reservoir a finite time after initiation and a porosimetry hysteresis. In Chapter 7, the effects of cells and proteins on this process was studied. The dominant effect of biological components was the increase in the severity of porosimetry hysteresis. This was due to contact angle effects from protein/cell adsorption which caused additional pinning forces. A numerical model to predict stain dynamics in the first stage was also developed and correlated to experimental results.

The dried deposit left by dried blood droplets on glass was analysed in Chapter 8 and compared with simple colloid systems. Dried deposits showed a strong relationship with RBC concentration implying a possible haematocrit diagnostic technique. RBC and protein solutions generally dry in ring-like profiles, where much of the non-volatile components have accumulated at the droplet's edge. Previous research on simple particles have shown a suppression of ring structures at high initial concentration. However, RBC solutions show more defined ring structures with increasing concentration. This was caused by a difference in drying dynamics between the two systems. In red blood cell suspensions, the drying front halted before it reaches the centre of the droplet. Further evaporation caused the central fluid region to invert and form the concave surface seen in dried profiles. In simple particle suspensions this front continues until the centre of the droplet is reached. The causes of the halt in front progression and its influence on dried profiles and crack patterns are analysed.

In Chapter 9 the effect of contact angle on pattern formation in drying droplets was investigated. A numerical model was developed that showed good agreement with experimental results produced with a polystyrene particle suspension. The success of the

model identified the importance of the relative strength of surface tension and viscosity effects. The relationship between contact angle and this ratio was determined and a dimensionless number that can predict the onset of ring profile formation was proposed.

This thesis provides a new insight into the fundamental mechanisms of interfacial flows of multicomponent biological fluids in evaporating droplets and porous media. It provides a unique assessment of complex biological processes analysed from a colloids and fluid mechanics perspective, addressing critical gaps in knowledge that enables the effective optimisation of low-cost diagnostic devices. Modelling techniques are introduced to streamline the design and optimisation of diagnostic devices. The objective of this thesis is to replace trial and error experimentation approaches with informed design and computational fluid dynamics simulations.

Thesis including published works declaration

I hereby declare that this thesis contains no material which has been accepted for the award of any other degree or diploma at any university or equivalent institution and that, to the best of my knowledge and belief, this thesis contains no material previously published or written by another person, except where due reference is made in the text of the thesis.

This thesis includes 3 original papers published in peer reviewed journals and 2 submitted publications. The core theme of the thesis is interfacial flow in low-cost diagnostics. The ideas, development and writing up of all the papers in the thesis were the principal responsibility of myself, the student, working within the Department of Chemical Engineering under the supervision of Prof. Gil Garnier.

The inclusion of co-authors reflects the fact that the work came from active collaboration between researchers and acknowledges input into team-based research.

In the case of 3 chapters my contribution to the work involved the following:

Thesis Chapter	Publication Title	Status	Nature and % of student contribution	Co-author name(s) Nature and % of Co-author's contribution	Co-authors, Monash student
5	Effect of protein adsorption on the radial wicking of blood droplets in paper	Published	Key ideas, experimental work, analysis of results, writing up, 75%	Rico Tabor (10%), Gil Garnier (15%) supervision and input into manuscript.	No
6	Dynamics of stain growth from sessile droplets on paper	Published	Key ideas, writing code, experimental work, analysis of results, writing up, 65%	Rico Tabor (10%), Gil Garnier (15%) supervision and input into manuscript. Joseph Berry (10%) advice on simulations and input into manuscript.	No
7	Radial wicking of biological fluids in paper	Published	Key ideas, writing code, experimental work, analysis of results, writing up, 70%	Rico Tabor (10%), Gil Garnier (15%) supervision and input into manuscript. Joseph Berry (5%) advice on simulations and input into manuscript.	No

I have renumbered sections of submitted or published papers in order to generate a consistent presentation within the thesis.

Student name: Michael Hertaeg

Student signature: Date:

I hereby certify that the above declaration correctly reflects the nature and extent of the student's and co-authors' contributions to this work. In instances where I am not the responsible author I have consulted with the responsible author to agree on the respective contributions of the authors.

Main supervisor name: Gil Garnier

Main supervisor signature: Date:

Acknowledgements

First, I would like to express my sincere gratitude to my supervisors Gil Garnier and Rico Tabor for selecting me for this position and their constant support and guidance.

I also thank my external collaborators Alex Routh and Joseph Berry for their input, which allowed me to expand the project to encompass a scope far beyond what was originally intended.

I acknowledge the contributions of all members of the Blood group at BioPria: Heather McLiesh, Clare Manderson, Whui-Lyn Then, Janine Lodewyke, Julie Courgibet, Marek Bialkower, Rodrigo Curvello and Diana Alves, who contributed directly or indirectly to the success of this project through comments at group meetings or casual conversations.

I also acknowledge the support of the staff and students at BioPria during my time there including: Shaun Ang, Janette Anthony, Melanie Barajas, Warren Batchelor, Christine Browne, Mostafa Dehghani, Uthpala Garusinghe, Thilina Gunawardhana, Laila Hossain, Maoqi Lin, Maisha Maliha, Llyza Mendoza, Humayun Nadeem, Mahdi Naseri, Aysu Onur, Ragesh Prathapan, Vikram Raguwanshi, Kirubanandan Shanmugam, Scot Sharman and Joanne Tanner

I would also like to thank my parents for always encouraging and supporting me.

Finally, I also gratefully acknowledge Haemokinesis, ARC Linkage Grant (LP160100544), the Australian Government Research Training Program, the Faculty of Engineering and Monash University for providing me the living allowance/tuition fee scholarships, research funding and travel grants which have made my research possible. I also would like to thank the Monash eResearch Centre and eSolutions-Research Support Services for the use of the MonARCH HPC Cluster.

List of Figures

List of Tables

Chapter 1

Introduction

Despite significant advances in medical technology in recent years, a significant portion of the world's population does not have access to even basic medical care. There were an estimated 8.6 million deaths in 2016 in low to middle income countries as a direct cause of a lack of access to sufficient medical care [1]. While there are several factors that contribute to this unfortunate statistic, the cost of medical devices is undoubtedly one of them. Due to this, there is increasing interest in the field of low-cost diagnostic devices that can be operated quickly and with minimal training.

Microfluidic 'lab on chip' techniques are used to produce many diagnostic devices that are significantly smaller, cheaper and more portable than their laboratory-based counterparts. However, traditional microfluidic systems generally require pumps or other external electrical devices, and are not recyclable/biodegradable. Paper-based microfluidic devices take advantage of passive flows that are produced spontaneously in porous materials upon contact with a wetting fluid and therefore, generally do not require any additional equipment. Paper is also cheap, light weight, bio-compatible, wettable, easily modified by cutting or folding and simply disposed of by incineration. These properties make paper a versatile platform for many devices that are currently in use. The most common example of this style of device is the One Step hCG Urine Test for at home pregnancy screening [2].

Although many innovative products have been designed and manufactured, the design process has typically been performed using a trial and error approach. This is because many aspects of wicking phenomena in paper are not fully understood. This is particularly true for biological fluids, where the high cell/biomolecule content leads to anomalous rheological and interfacial behaviours. Before the efficient design and

optimisation of paper-based diagnostics can be performed, the effect of the properties of complex fluids must be characterised and explained from a fundamental perspective.

In addition to paper, pattern formation in drying systems has also been utilised for low cost diagnostics [3]. Here, the patterns left after droplets of biological fluids have evaporated on impermeable surfaces are representative of several important medical conditions; including anaemia, thalisemia and carcinoma. These patterns are a result of evaporation induced capillary flows that cause the redistribution of constituents. Although this process has received significant attention in recent years, the fundamental mechanisms that lead to pattern formation, especially in complex biological systems, remain poorly understood. Before this technique can be used to engineer robust diagnostics the controlling mechanisms behind this process must be studied.

In this thesis, the fundamental mechanisms behind the capillary induced transport of biological fluids in paper and drying sessile droplets are investigated and linked with novel diagnostic applications. In the process, the concept of the Lucas-Washburn equation and the coffee ring phenomena are revisited and the ability of paper to produce medical grade diagnostics is analysed. In chapter 3, the radial wicking of a droplet of blood is used to engineer a rapid and low-cost blood diagnostic technique for blood grouping. Also, the developed technique is successfully applied to detect SARS-CoV-2 (COVID-19) antibodies in patient plasma. In chapters 5, 6 and 7, the radial wicking of a droplet of blood and model fluids on paper is systematically analysed from a fundamental colloidal and fluid mechanics perspective. The universality of sessile droplet wicking in porous media is questioned from a fundamental and broad industrial perspective. Chapters 8 and 9 investigate the fundamental mechanism behind pattern formation in drying droplets and the variation between the behaviour of simple and complex fluids. Each published or submitted chapter includes a preface section that provides a brief outline of the chapter in the context of the thesis.

1.1 References

[1] Margaret E. Kruk, Anna D. Gage, Naima T. Joseph, Goodarz Danaei, Sebastián García-Saisó, and Joshua A. Salomon. Mortality due to low-quality health systems in the universal health coverage era: a systematic analysis of amenable deaths in 137 countries. *The Lancet*, 392(10160):2203–2212, 2018.

[2] Katarzyna M. Koczula and Andrea Gallotta. Lateral flow assays. *Essays in Bio-*

chemistry, 60(1):111–120, 2016.

[3] D. Brutin, B. Sobac, B. Loquet, and J. Sampol. Pattern formation in drying drops of blood. *Journal of Fluid Mechanics*, 667:85–95, 2011.

Chapter 2

Literature Review

2.1 Overview

This review focuses on the use of capillary induced transport to produce low-cost analytical devices. Blood is briefly introduced from a physical science perspective and the relevant areas of ABO blood typing are discussed. However, the details of this extensive field and many of the biological processes are not included as they are not directly relevant to the vision of of this thesis. The wicking of wetting fluids in paper-like materials is analysed in detail. This includes the fundamental mechanisms derived from micro-scale surface forces, and existing modelling techniques to predict larger scale behaviour. Techniques to control fluid flow in these systems and some of the resulting analytical devices are also reviewed. This is combined with a review of the fundamental processes affecting the evaporation of a droplet of colloidal suspension on an impermeable surface. Coffee ring formation and the effect of biological fluids are emphasised. Recent advances in the understanding of this process are discussed including: modes of evaporation, evaporation profile, internal flow, particle aggregation and predictive modelling.

2.2 Blood

2.2.1 Components

In our bodies, blood serves three main functions: transport, maintain bulk equilibrium and facilitate the body's immune responses [1]. To fulfil these functions among many more requires the composition of blood to contain a multitude of cells, proteins, lipids and electrolytes/ions. Red blood cells (RBCs) are the largest and most abundant cell

found in blood, making up approximately 45% of blood by volume [2]. They contain haemoglobin which allows them to transport both oxygen and carbon dioxide [3]. It is the haemoglobin in RBCs that gives them their colour. Healthy RBCs are typically biconcave disks approximately 8µm in diameter [4]. This shape maximises surface area as well as minimises the bending energy of the cell [5]. RBC membranes are also very flexible making the cells highly deformable. This is required as they are routinely required to pass through constrictions smaller than their cross section in small blood vessels [6]. Other blood cells such as platelets and leukocytes (white cells) constitute a significantly smaller fraction of blood. Platelets are small discoid cells with a diameter of approximately 3 µm. They have several key functions in many processes including thrombosis (clotting), haemostasis, vessel constriction/repair and inflammation [7, 8]. There are 5 types of leukocytes in blood and all play a role in immune defence [1]. The sizes of each type vary. However, all are typically larger than the average RBC at 6-10 µm [1, 9].

Blood cells are suspended by electrostatic repulsion in a solution called plasma. Plasma is composed mostly of water (90% by mass), proteins (6% by mass) and electrolytes (1% by mass) [10]. There are many types of protein in plasma, although the reported average concentration of each protein in a typical blood sample varies greatly [1, 11, 12]. It is generally accepted that the most abundant blood protein is albumin (approx 38.7g/L) [13] followed by globulins (approx 25g/L) and then fibrinogen (approx 3g/L) [10]. Blood proteins are responsible for a wide variety of functions, including transport, immune responses and thrombosis [4].

2.2.2 Rheology

Bulk Rheology

Blood is a shear thinning, viscoelastic and thixotropic fluid [14]. This means the effective viscosity of blood changes as a function of shear rate and time, and blood has solid-like elastic properties. Due to this, quantifying the exact rheological properties of blood is an ongoing challenge and currently, there is no universally accepted model that can describe flow behaviour in all circumstances. However, there are many models that can be applied with great accuracy to specific systems and limited conditions [15–18]. The complex non-Newtonian properties of blood are largely caused by the concentration, shape and deformability of RBCs [1, 19, 20]. RBCs also tend to form rouleaux aggregates in low shear flows, which causes time dependant behaviour [21]. Blood rheology is therefore highly dependent on haematocrit or the concentration of RBCs,

which can vary significantly between individuals [20, 22]. Plasma also exhibits weak viscoelasticity [23]. Despite complex non-Newtonian properties, it is not necessary in all cases to include the non-Newtonian properties of blood for accurate modelling [24]. Due to this, and for simplicity, much of the analysis presented in this thesis assumes a constant viscosity for both plasma and blood.

Surface Rheology

Many of the components in blood are tensioactive and readily adsorb onto many surfaces and air interfaces [25]. This produces complex interfacial behaviour with a significant dynamic component that is a function of concentration, flow conditions and geometry [26, 27]. This is probably the reason why the reported value of blood surface tension varies so significantly in literature, with some quoting a value close to water 69.8 mN/m [28], 73 mN/m [29] and some as low as 57mN/m [30]. The surface tension of blood is also temperature dependant [30], which is also often not considered in measurements.

2.2.3 Blood Groups

Blood groups were first identified in 1901 by Lansteiner with blood from himself and 5 co-workers that was presented in a classic 1.5 page communication [31, 32]. He identified three distinct blood groups (A, B and O) based on agglutination properties. The AB group was discovered soon after and was included in the ABO system. This was an important discovery as blood group compatibility is essential for safe blood transfusions [33]. Transfusion is a common treatment of major haemorrhages, cancer and complications during childbirth. Before the procedure, blood grouping is performed to ensure compatibility between the donor's blood and the patient's immune system [34].

The RBC membrane is a complex structure with many components that perform specific functions [35]. Several of these components, usually proteins and sugars are identified as antigens as they readily react with antibodies created by the immune system. It is the presence of specific antigens in an individual's RBC membrane that identifies the forward blood groups, while the presence of specific antibodies in an individual's plasma determines the reverse blood groups. Generally, both forward and reverse testing must take place before transfusion to ensure compatibility. The structure and function of the red cell membrane and the related immune responses have been studied in detail for many years [36, 37]; however, only blood grouping antigens and antibodies will be considered in this review. Currently the International Society of Blood Transfusion

recognises 339 blood group antigens, divided amongst 33 blood group systems [33]. Despite the large amount of blood group systems, the ABO system remains the most clinically relevant. This is because there is a high likelihood of a serious immune reaction if ABO groups are matched incorrectly. The D blood group is also commonly clinically important and is represented by the positive or negative sign in the standard representation of blood groups. For example A+ RBC's will have both A and D antigens expressed on their membranes.

There are many techniques used to perform both forward and reverse blood typing diagnostics. However, most of these methods function on the detection of an antibody-antigen reaction upon combination of incompatible samples (eg A RBCs with B plasma). This results in the antibody binding to the antigen sites on a red cell. If the antibody is a common pentamer Immunoglobulin M (IgM) antibody (used for ABO typing) it is able to bridge the cell-cell electrostatic repulsion force due to surface charge and cause RBCs to bond together. This forms large agglutinates which can be detected by a change in optical appearance and rheological behaviour [33, 38–42].

2.3 Wicking in Paper

The wicking or spontaneous imbibition of wetting fluids into porous media is of importance to many industries including manufacturing [43], agriculture [44], textiles [45], printing and recently biodiagnostics [46]. Paper is a porous material composed of a non-woven matrix of fibres and has been used extensively for communication, filtration and hygiene applications for many years [47]. The fibrous matrix of a typical paper sheet includes many empty pores that can be readily filled with an imbibing liquid. The volume fraction of empty pores to fibres in paper is referred to as porosity and impacts wicking characteristics significantly. The most common source of paper fibres is cellulose from wood pulp, the relative concentration and aspect ratio of these can be tuned to produce a wide variety of papers (copy, towel, filter, etc). Additives including fillers, wet strength and sizing agents are also commonly added to tailor properties [47]. In this section, the fundamental mechanisms leading to wicking in paper and the current modelling approaches are reviewed.

2.3.1 Capillarity and the Lucas-Washburn Equation

The surface tension or surface energy of an interface is defined as the increase in internal energy if the surface is reversibly expanded by a unit amount at constant temperature. It has the units of Joules per meter squared and is a component of the system's total potential energy [48]. As all systems tend to minimise their potential energy, this produces a force that scales with the length of an interface. Surface tension is commonly expressed by the unit Newtons per meter, which is dimensionally consistent with the energy definition. The force developed due to a minimisation of surface energy, is responsible for many commonplace phenomena, including the spherical shape of small droplets and the ability of small insects to walk on water [49].

Due to this effect, a curved interface will only be in equilibrium with its surroundings if there is a higher pressure on the concave side. The pressure difference required to stabilise an interface is referred to as Laplace pressure, and is calculated using equation 2.1.

$$\Delta P = \frac{\gamma}{\frac{1}{R_1} + \frac{1}{R_2}} \tag{2.1}$$

Where γ is the surface tension of the interface, R_1 and R_2 are the two principal radii of curvature and ΔP is the pressure differential over the interface. In most cases examined in this thesis, the concave side of the interface is open to atmosphere and is therefore, at atmospheric pressure. This means the gauge pressure on the convex side is equal to $-\Delta P$. The value ΔP is often referred to as the capillary pressure.

When a small volume of liquid intersects a solid surface, an apparent equilibrium condition is quickly reached that corresponds to the minimum surface energy configuration [50]. This state is not a true equilibrium, due to thermodynamic complexities that are discussed below. However, much analysis assumes equilibrium conditions. Bond number quantifies the dominance of gravity over surface tension and is given by $Bo = \frac{\Delta \rho g L^2}{\gamma}$. Where $\Delta\rho$ is the difference in density between the two phases, g is the gravitational acceleration and γ is the surface tension of the interface. At low Bond numbers, where the effect of surface tension dominates gravity, the drop forms a spherical cap shape defined by a contact angle and radius. The contact angle is defined as the internal angle between the surface and a tangent to the drop at the intersection of the three phases: solid, liquid and vapour. This intersection is referred to as the contact line (Figure 2.1). The Young equation (equation 2.2) gives a simple description of the contact angle (θ) using a horizontal force balance or a minimisation of excess free energy and the three

relevant surface tensions: liquid-vapour (γ_{lv}), solid-liquid (γ_{sl}), and solid-vapour (γ_{sv}) [51, 52]. This historic equation relates the relative magnitudes of the three relevant surface tensions: solid-liquid, liquid-vapour and solid-vapour (Figure 2.1) to the contact angle. The contact angle is typically independent of droplet size in meso-scale droplets and is widely used as a convenient measure of surface properties [53, 54].

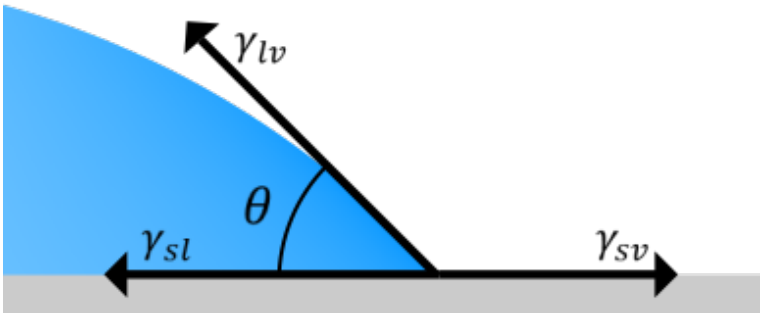

Figure 2.1: Schematic representation of the triple line.

$$\gamma_{sv} = \gamma_{sl} + \gamma_{lv} cos\theta \tag{2.2}$$

Although useful, the Young equation gives an incomplete picture of contact angle. This is because of several assumptions made in its derivation that will be discussed briefly. A perfectly smooth and chemically homogeneous surface is assumed. Surface roughness influences contact angle by making hydrophobic surfaces more hydrophobic, and hydrophilic surfaces more hydrophilic [55]. Another assumption made is the absence of contact angle hysteresis which is caused by surface roughness and chemical heterogeneities. Contact angle hysteresis is defined by a difference of advancing and receding contact angle, where the measured contact angle is higher at an advancing edge than a receding one. This is most easily observed by looking at the shape of a droplet sliding down an incline as seen in Figure 2.2. This phenomenon occurs because the free energy of the system varies as a function of contact line position. In the perfect system defined in the derivation of the Young equation, there is a single minimum in free energy corresponding to the droplet's equilibrium position. However, in a real heterogeneous system, there are several, creating many discrete stable configurations that correspond to local minima in free energy. This produces pinning forces that act to keep the droplet in a stable configuration. The resulting effect on contact angle can be demonstrated by including the pinning force in the Young equation on the right-hand side of equation 2.2. For an advancing interface this force is positive, and negative for a receding [55]. The maximum magnitude of the pinning force determines the hysteresis severity and

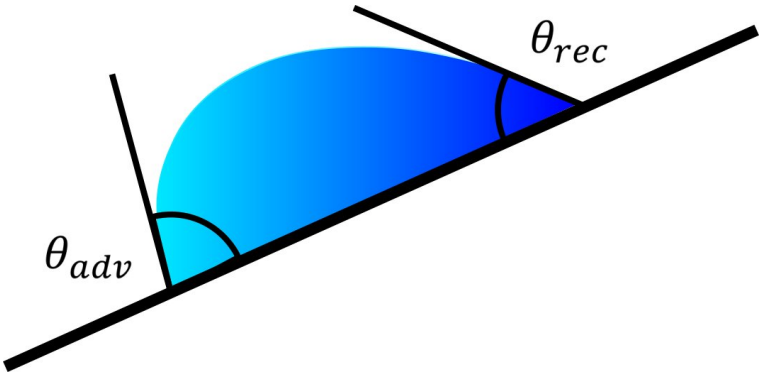

Figure 2.2: Advancing and receding contact angle on a sliding drop.

increases with physical and chemical heterogeneity.

The assumption of equilibrium made in the derivation of the Young equation is also not valid in many cases. This assumption is obviously violated by absorbent materials; however, droplets are also thermodynamically unstable in most conditions due to Kelvin effects (dependence of saturation conditions on curvature) [48]. Thermodynamic analysis also shows that a microscopic adsorbed layer of liquid is always present on the apparent solid-vapour interface that intersects the macroscopic droplet at the contact line. This intersection leads to an extreme curvature at the contact line, implying a negative capillary pressure, which cannot be in equilibrium with the macroscopic droplet. This apparent paradox is resolved with the addition of surface forces or disjoining pressures, that are responsible for the anomalous microstructure in the vicinity of the contact line [52]. This microstructure/precursor film influences the macroscopic behaviour of the droplet and is required to understand many droplet spreading phenomena, as well as contact angle hysteresis on smooth homogeneous surfaces [50]. This combination of complex phenomena is often overlooked in contact angle investigations and is the source of much misinterpretation.

The concepts of Laplace pressure and contact angle where first combined in 1918 by Lucas [56] and later in 1921 by Washburn [57], to derive the well-known Lucas-Washburn equation. This equation predicts the spontaneous imbibition of wetting fluids into a large variety of porous materials. Lucas and Washburn modelled these materials as a collection of individual capillary tubes. For such systems wetting fluids create curved menisci and therefore capillary pressures are determined by contact angle and geometry. Figure 2.3 demonstrates the effect of contact angle on the curvature of the meniscus. The Lucas-Washburn equation is derived by assuming the capillary pressure is balanced

by the viscous effects due to the motion of fluid within the capillary tube and ignoring other effects such as inertia. Equation 2.3 gives the pressure differential by applying the Young-Laplace equation (equation 2.1) to a circular cross section. Equation 2.4 is the well-known Poiseuille equation, expressing the volumetric flow rate as a function of pressure and radius for laminar flow in circular cross sections. Combining these two equations and integrating, yields the Lucas-Washburn equation (equation 2.5).

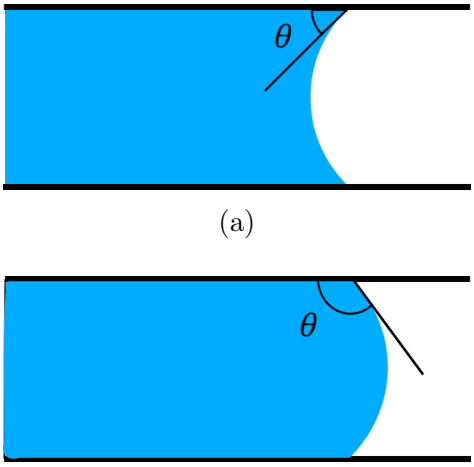

(a)

(b)

Figure 2.3: Meniscus geometry in capillary tube, (a) wetting and (b) non-wetting.

$$P_c = \frac{2\gamma cos\theta}{r} \tag{2.3}$$

$$\frac{dV}{dt} = \frac{\pi P_c}{8\mu l} r^4 \tag{2.4}$$

$$l = \sqrt{t\frac{r\gamma cos(\theta)}{2\mu}} \tag{2.5}$$

Where P_c is the capillary pressure, r is the radius of the capillary, V is the volume of fluid inside the capillary tube, μ is the viscosity of the fluid, t is time and l is the length of the section of tube that is occupied by fluid. As the effect of r is in most cases indistinguishable from other constants, they are commonly grouped together into a single empirical unknown term that is a function of fluid and material properties. This equation predicts the position of a wetting front will be proportional to the square root of time. This was observed in a huge variety of porous systems [57–59]. However, it does not apply in many cases [60] as real porous systems are significantly more complex than is considered in the derivation. There is a great range of literature concerning alterations to the Lucas-Washburn model to account for the dominance of a plethora

of ignored effects which are discussed in Section 2.3.3.

2.3.2 Wicking at the Pore Scale

Lucas-Washburn style models typically rely on empirical constants that are difficult to determine theoretically. This is primarily due to a disregard for pore scale mechanisms. An example where these are important is a penetrating fluid encountering a network discontinuity, such as an intersection with another pore. This behaviour has been studied in simplified experiments on model 2D porous networks [61, 62]. In these controlled systems, the pores only intersect at right angles allowing simple observations. In this case, four characteristic imbibition events where found (Figure 2.4). First; piston, where the wetting fluid flows through a single channel as in a simple capillary. Second; snap off, where the wetting fluid meets an open channel. In this situation the fluid can only spread further through a surface wetting mechanism, leading to a thin film that spreads around the outside of the channel. When the film encircles the circumference of the channel, spontaneous filling occurs due to a strong Laplace pressure. Third; imbibition 1, this describes the mechanism of filling a junction when three channels contain the wetting fluid. Fourth; imbibition 2, which occurs when there are two filled channels in a four-way junction.

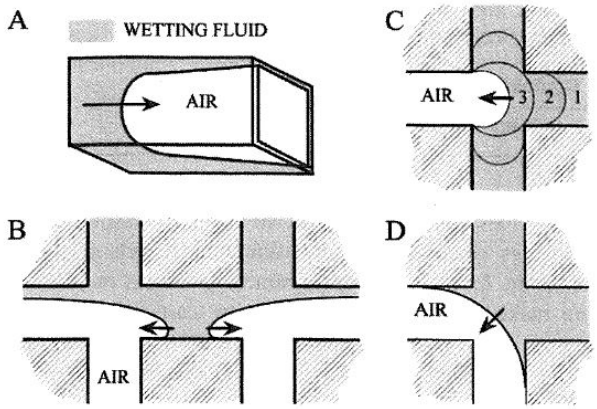

Figure 2.4: Diagrams of identified 2D imbibition events. A) piston, B) snap off, C) imbibition 1, D) imbibition 2. Reproduced from [62] with permission from De Gruyter.

By observing the relative timing of each event, the relative driving pressure of each event could be identified [61]. This is similar to the derivation of equation 2.3 where the Young-Laplace equation (equation 2.1) is applied to find the driving pressure for a cylindrical capillary undergoing piston imbibition. In the situation where there are two interfaces within a small distance, the local absolute pressure in the wetting fluid is

determined by the capillary pressure of the interface with the highest driving pressure (ΔP_{max}), which corresponds to a low absolute pressure (P_{abs}) in the region near the interface ($P_{abs} = P_{atm} - \Delta P_{max}$). This low pressure produces a force on the weaker interface, causing the fluid to preferentially move towards the interface with the greatest driving pressure ΔP_{max}. The weaker event occurs only when the distance between the two interfaces is such that the local absolute pressure rises to a value that enables the weaker event to occur ($P_{abs} = P_{atm} - \Delta P_{min}$). This sequence of preferential imbibition events is very similar to capillary fingering, a well-known phenomenon in porous media [63, 64]. Although these 2D experiments of imbibition events are much simpler than physical 3D porous networks, analysis shows that small variations in pore morphology can cause changes in wicking behaviour that are not included in Lucas-Washburn style models. This is demonstrated by the faster wicking of fluids in paper in the machine direction [65, 66] where there is a slight fibre alignment.

Detailed experimental imaging of paper during transport has revealed that bulk flow due through filled pores as in piston-like motion is quite rare [67]. This is because the complex fibrous matrix of paper has too many discontinuities for large menisci to form. Instead, the primary mechanism of wicking is by thin film growth and wicking though open crevasses created at fibre intersections, or surface roughness on individual fibres. Full saturation does occur a distance behind the front, which is caused by a spontaneous snap off mechanism once films have spread enough to self-intersect. This process is depicted in Figure 2.5.

A consequence of the dominance of film flow in paper is that there is a small transition region between the saturated and dry regions. In this region the fluid is contained in the very small inter/intrafibre crevasses due to the higher driving pressures to enter these sections. This is shown in the cryogenic SEM image in Figure 2.6 showing three distinct zones based on the level of saturation. This observation was also made with magnetic resonance imaging, where the presence of a precursor front of low saturation was identified [68].

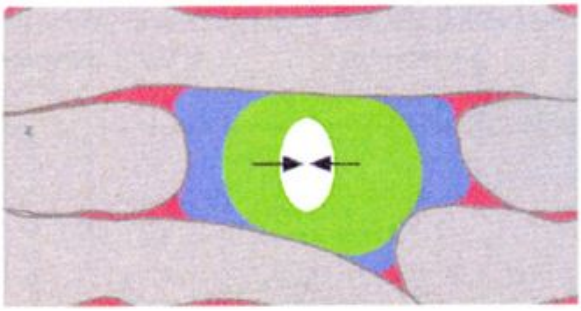

Figure 2.5: Diagram of the mechanism of pore filling. Red area indicates the region of strongest capillary pressure, where fluid initially enters. When pressure rises the blue and then green areas will be filled. The continuous boundary of green area would likely cause a rapid snap off event. Reproduced from [67].

2.3.3 Modelling Techniques

Due to the wide application of wicking in paper-like materials, there has been a great amount of research on developing mathematical models to describe the phenomena in a variety of systems [69]. These can be broadly grouped into three classes: capillary, continuum and pore scale [70].

Capillary Models

Capillary models, such as the Lucas-Washburn equation, simplify the system to bundles of capillaries. These were the first type of wicking models and are still the most widely used due to their simplicity. In the derivation of the classic Lucas-Washburn equation, the effects of inertia and gravity are ignored. This is because the Reynolds and Bond numbers of wicking systems are generally low enough to ignore these effects. Reynolds number is a numerical representation of the dominance of inertia over viscous forces given by $Re = \frac{\rho U L}{\mu}$. Where ρ and μ are the density and viscosity of the fluid respectively and U and L are the characteristic velocity and length respectively.

In wicking systems, the velocity of the fluid is high at very early times, causing a high Reynolds number. Even though this occurs very briefly, inertial effects are important in some systems as late stage predictions will be offset by the error in the early stages [71–74].

For large systems with a vertical inclination, gravity cannot be ignored. However, it is not always clear when it should be included. Although the Bond number gives the approximate ratio of surface tension to gravity forces the derivation assumes iden-

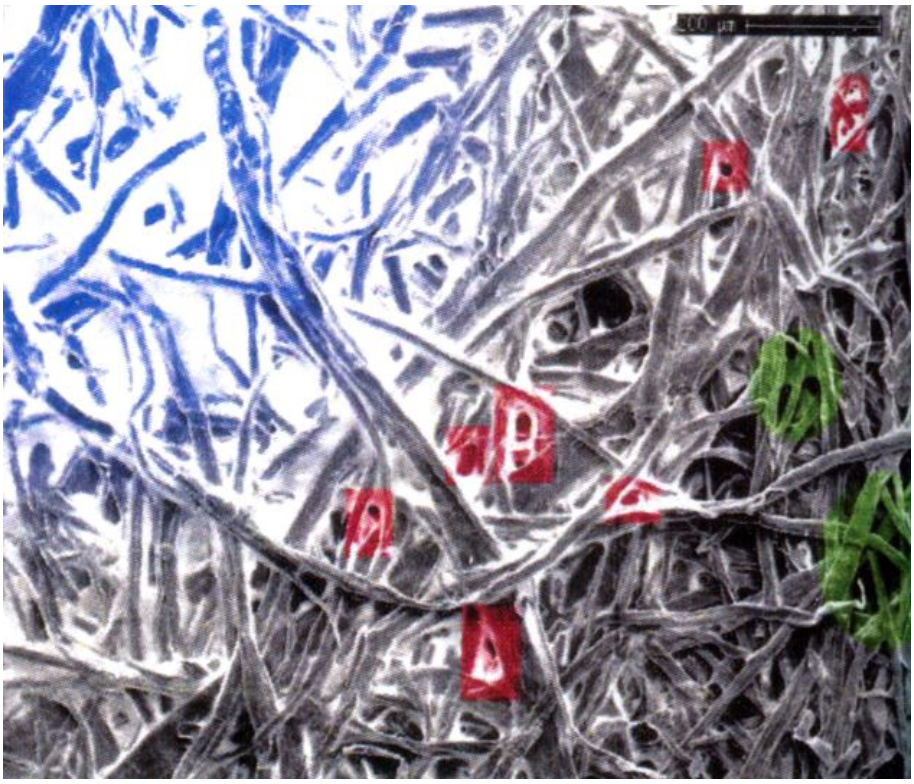

Figure 2.6: Low magnification image of a wicking front, shows the saturated zone (highlighted in blue) and partially saturated (red). Green shading indicates large empty pores in front of the front. Reproduced from [67].

tical length scales of the two effects. While this is appropriate for many systems, for wicking it is generally not applicable. The appropriate characteristic length to define surface tension in this system, is generally the pore diameter. However, the characteristic length for gravitational forces is the vertical height of the sample, which is typically several orders of magnitude large than the pore diameter. To account for this, Li et al. [60] introduced the dimensionless parameter 'CGR' defined as the ratio of capillary pressure and gravitational head. This formalism can be used to predict whether gravitational effects are dominant in wicking systems. The Lucas-Washburn equation can be generalised to include the effects of inertia and gravity to derive equation 2.6 [57, 75–77].

$$-\rho\frac{d(h\dot{h})}{dt} = \frac{2\gamma cos\theta}{r} + \frac{8\mu h}{r^2}\dot{h} + \rho g h \tag{2.6}$$

In most wicking models the contact angle is regarded as a constant. However, when fluid velocity becomes very high, usually at the very early times, a static contact angle assumption is not valid. Many researchers have investigated the dynamic contact angle

[78–80] and observations broadly follow the relation of Cox [81], where the contact angle is a function of front velocity.

$$\theta_d = (\theta_e^3 + 9B\frac{\mu}{\gamma}\frac{dl}{dt})^{\frac{1}{3}} \tag{2.7}$$

Where B is a characteristic of the system, generally regarded as a constant equal to 14 [82], θ_d is the dynamic contact angle and θ_e is the equilibrium contact angle. This dynamic contact angle can be used in wicking models [71]; however, as velocity decreases, the dynamic contact angle tends to quickly approach the equilibrium value.

There are many more examples of capillary models that have been derived for specific systems. These include: intra-fibre pores [83], non-uniform interconnected pores [84], fibre absorbency [85], changing pore size [86] and hydrophobic wax boundaries [87]. Despite these developments, most Lucas-Washburn based models are still heavily reliant on some empirical fitting. This is because the constant r used in the derivation can not be easily predicted from material geometry. A value based off the average pore size calculated from microscope images overestimates wicking rate by an order of magnitude [67].

Continuum Models

Continuum models generally utilise Darcy's law to relate pressure gradient to average velocity (equation 2.8). This has the key advantage over capillary models that it can be easily applied to more complex 2D or 3D geometry. In a simple wicking system this expression can be used to derive equation 2.9, which leads to an electrical circuit analogy as it is similar to Ohm's law. This technique is commonly used to describe flow in a wide range of paper-based analytical devices [88–90].

$$v = -\frac{k}{\mu}\nabla P \tag{2.8}$$

$$\dot{Q} = -\frac{kWH}{\mu L}\Delta P \tag{2.9}$$

Where v is the average fluid velocity, k is the permeability of the material, P is pressure, W is the width of the paper channel, H is the height of the paper channel and $\dot{Q}$ is the volumetric flow rate.

Darcy's law was used to derive simple expressions for flow in a range of specific ge-

ometries, [91, 92]. Elizalde et al. [93] derived a general equation for the flow of liquid wicking through arbitrary cross sections.

In more complex semi-saturated systems, Darcy's law can be combined with volume conservation to give Richards' equation [94] (equation 2.10). By assuming that pressure is solely a function of volume fraction the equation can be expressed in a diffusion form (equation 2.11).

$$\frac{\partial \phi}{\partial t} = \nabla \cdot \left(\frac{K(\phi)}{\mu} \nabla P \right) \tag{2.10}$$

$$\frac{\partial \phi}{\partial t} = \nabla \cdot \left(\frac{D(\phi)}{\mu} \nabla \phi \right), \tag{2.11}$$

$$D(\phi) = K(\phi) \frac{\partial P(\phi)}{\partial \phi}. \tag{2.12}$$

Where ϕ is the local volume fraction, $K(\phi)$ is the permeability as a function of ϕ. The solution of Richards' equation requires further expressions for permeability and pressure (equation 2.12) that are dependent on material properties [95]. Perez-Cruz et al. [96] used relations based on Brooks-Coorey models for flow through soils to express pressure and permeability as functions of local volume fraction [95]. This predicts the shape of wicking fronts around irregular geometries in paper (Figure 2.7). As the Brooks-Coorey model is empirical, this method requires some fitting to produce meaningful results. A non-empirical method for determining pressure and permeability functions has been employed by implementing a Full Morphology - Stokes method [70]. This gives the required constitutive equations based on measurements of pore scale geometry [97, 98].

Full-Morphology (FM) is an image analysis technique that gives the level of saturation at specified capillary pressures for porous materials [99, 100]. The technique relies on virtually fitting spheres of constant diameter into the void space in a representative volume of the material. The spheres can intersect each other but not the porous material. At each sphere size, corresponding to a capillary pressure, the total volume occupied by spheres in the virtual network is calculated. Therefore, by performing this operation at several different sphere diameters, the volume fraction at different capillary pressures can be probed. The effect of contact angle on the accuracy of this technique was investigated [101]. It was found that for low contact angles the geometric differences are negligible, and therefore the difference could be included by multiplying

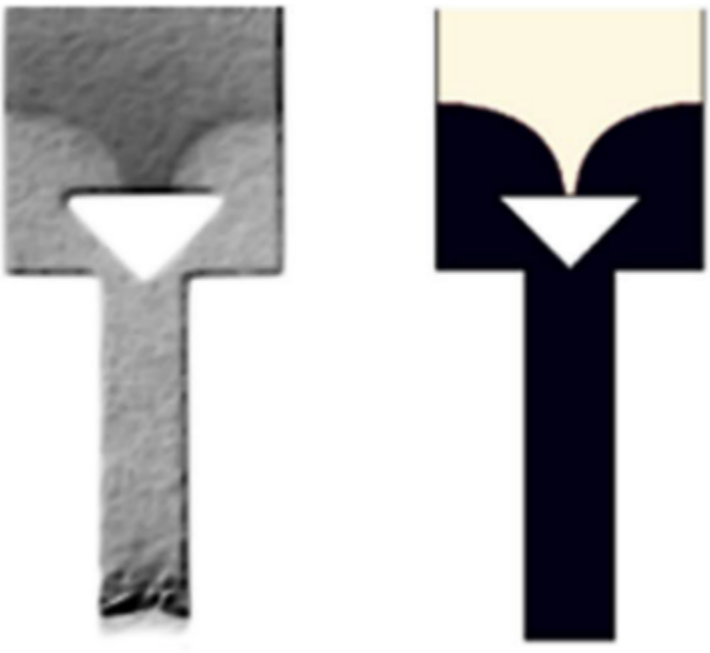

Figure 2.7: Wicking model based on Richards' equation. Left panel is the experimental image, right panel is the simulation result. Reproduced from [96] with permission from Springer.

the calculated pressure by the factor of $cos\theta$ implied by equation 2.3.

The other required expression to solve Richards' equation is material permeability. This can also be calculated from material geometry by performing a Stokes flow simulation, on the geometry calculated using FM methods. These two methods combined give the FM-Stokes method [70]. There are also other techniques for determining these constitutive equations, including other image-based methods [102], mercury intrusion [103] or centrifuge methods [104].

The Brinkman equation gives another continuum method for predicting flow in porous media [105]. This equation combines the Stokes equation for low Reynolds number flow and Darcy's law to give equation 2.13. Where v is the average velocity and a is a constant that is representative of the system. This equation is second order with velocity, allowing no slip and other more complex boundary condition to be implemented. This is demonstrated in Figure 2.8. Brinkman models are particularly appropriate in highly porous materials and have been applied to analyse paper-like materials in several ways [106–109].

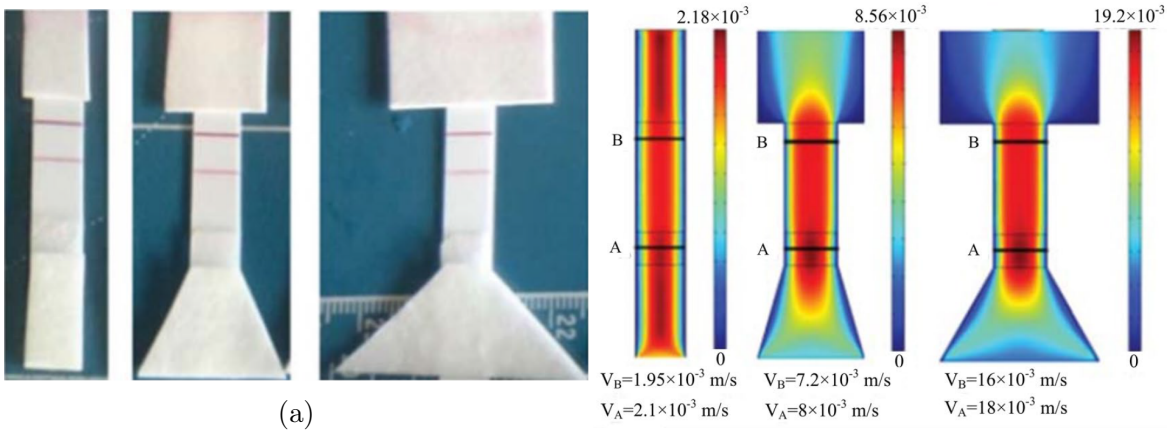

Figure 2.8: Predicting flow in paper channels using Brinkman's equation. (a) Image of paper strips. (b) Model predictions showing the implementation of a no-slip boundary condition. Reproduced from [106] with permission from Royal Society of Chemistry.

$$\mu\nabla^2 v - \nabla P - \mu a^2 v = 0 \tag{2.13}$$

Pore Scale Models

Pore scale models are used to investigate flow at a resolution smaller than the pore size in the material. As paper is often very thin, the total thickness is not significantly larger than the pore diameter, indicating that continuum scale modelling may not be appropriate. In papers where there is a large variation in pore diameter, wicking fronts are generally rough, these require pore scale resolution to predict accurately [70]. Pore scale models require pore geometry to be either measured or generated. This can be done with a variety of techniques including micro CT [110, 111], mercury porosimetry [112] and statistical methods [113]. Two specific pore scale methods will be briefly discussed here, pore network (PN) and interface tracking methods. However, there are other pore scale methods that have been applied to wicking systems such as the Lattice Boltzmann method [114, 115].

Pore network models represent the porous material as an interconnected network of pores and throats. The distribution and geometry of these pores and throats is generated based on a probability density function that is estimated from measurements of the investigated porous media. Pore network modelling requires a description of flow dynamics in each individual pore and throat system. This can be derived in many

systems as simple functions of geometry and wetting properties. The large-scale behaviour of the system is modelled by allowing the penetration of each individual pore and throat system once an adjacent pore has been filled. This technique was used to describe wicking processes in many porous materials including paper [116–119].

Traditional computational fluid dynamics techniques can also be used in wicking systems. Here, transport equations are solved over a representative mesh, which allows a high-resolution flow field to be calculated. However, a common difficulty in these types of simulations is interface tracking. This is because the exact position and shape of the front is generally very important in these systems. There are many techniques that perform this function [120] including the volume of fluid (VOF) method. VOF is a common technique used for modelling multiphase flows and has been successfully applied to paper [121, 122]. Briefly, this technique involves solving transport equations over the entire domain; however, specifying the properties in each cell by a scalar variable, usually called colour or volume fraction. If a cell is entirely occupied by a single phase the value will be either 0 or 1 depending on the phase. In a cell occupied by an interface the volume fraction will be between these values. Volume fraction is calculated at each time step using a simple convective equation that ensures the interface moves at the same velocity as the surrounding fluid. In wicking systems, the curvature of the interface and the pressure field are strongly linked, therefore an additional governing equation is required.

2.3.4 Finite Reservoirs

Much of the previous research on wicking only considered infinite reservoirs. For these systems there is commonly a very sharp wicking front where there is a clear distinction between wet and dry regions. If the fluid reservoir of the system was consumed or removed during wicking, fluid motion generally continues. However, it is now controlled by a redistribution mechanism rather than simply flowing from a reservoir [123]. Redistribution occurs as small pores have a greater capillary pressure (ΔP) than large ones (equation 2.3). At the time that the fluid reservoir is consumed/removed, the fluid is contained in only small pores near the wicking front and both large and small well inside the wet region [67] (Figure 2.6). This means the absolute pressure on the outside of the stain ($P_{abs} = P_{atm} - \Delta P$) is lower than at the centre, producing outward flow which empties the larger pores [124]. This causes the local concentration or saturation value to decrease with time in the central region. Many models such as Lucas-Washburn and Darcy's law assume full saturation and are therefore not suitable for the study of

wicking from non-infinite reservoirs.

The most common non-infinite reservoir wicking system is the absorption of a droplet into a porous material such as paper. This is a common process in paper-based diagnostics as droplet deposition is often the easiest method of introducing reagents and carrier fluids. In this system, the fluid wicks radially into the paper until at some point, the droplet is consumed. Wicking before the consumption of the drop is referred to as stage 1, and after is referred to as stage 2. These two stages are displayed in Figure 2.9. The first analysis of this process was published in 1955 and gives an empirical relationship that allows the determination of the volume of raindrops based on the size of stains left on paper [125]. Gilespie [126] was the first to record the dynamics of this process in paper and identified the two-stage behaviour in stain growth kinetics. An analytical model for second stage behaviour based on Darcy's law was developed, although excessive fitting parameters has prevented its broad use. Gilespie's model was improved on by several researchers [124, 127, 128], all these models can be broadly expressed with a simple power law with time (equation 2.14).

(a) (b)

Figure 2.9: Two stages of stain growth, (a) first and (b) second.

$$A \propto t^m \tag{2.14}$$

Where A is stain area and m is an empirical constant. Experimental results show good correlation with this power law. However, the value m varies in each stage. In literature the values for m in the first stage are in the range 0.10-0.33, and 0.39-0.50 in the second stage [124, 127, 129, 130].

Marmur [131] developed a model of a radial capillary to investigate Lucas-Washburn kinetics on a radial system. The modelled system was two parallel plates separated by a small distance. Liquid is introduced through a small hole in one of the plates. This yields equation 2.15.

$$\frac{A}{A_o}(\ln\frac{A}{A_o} - 1) = -1 + (\frac{2\pi d\gamma\cos\theta}{3A_o\mu})t \tag{2.15}$$

Where A_o is the area of the inlet, d is the separation of the two plates. Although it is not clear what value to use for A_0 and d in the comparison with a real system, this model was observed to be consistent with radial spreading of fluids from infinite reservoirs. These experiments were accomplished by supplying fluid at a single specified location via a capillary tube [124]. This radial capillary model was also consistent with wicking from droplets in the first stage, indicating that the capillary pressure and gravitational head from the droplet geometry does not affect behaviour [124]. Also, the behaviour of the stains after the capillary tube was removed was consistent with that of second stage droplet wicking [124]. These results show that the low value of m (equation 2.14) in the second stage of droplet wicking is caused solely by the fact that the amount of fluid is limited, and the spreading mechanism is dominated by fluid redistribution.

2.3.5 Biological Fluids

The wicking of biological fluids through porous materials has received only brief attention in literature and has focused almost entirely on blood pattern analysis for forensics. This is a method of reconstructing crime scenes by analysing the distribution, size and shape of blood deposits [132]. Blood pattern analysis is in most cases performed on hard, smooth surfaces. However, there are several publications relating to blood stains on paper/fabric. These documents analyse the appearance of blood stains between different modes of application [133], droplet velocity [134] and surface inclination (Figure 2.10) [135]. Li et al. [136] present a technique to predict the volume of a blood droplet by the size of the resulting stain. In this work they compare stain size at different haematocrit values and qualitatively analyse the stain growth dynamics.

(a) (b)

Figure 2.10: Blood stain from 31 µL drops of pig's blood on fabric inclined at a) 45° and b) 15° to the vertical. Reproduced from [135] with permission from Elsevier.

Although useful, previous research on blood spreading through paper and textiles has been largely focused on specific forensic applications. Due to this, the effect blood components such as cells and proteins have on wicking systems and the relevant fundamental mechanisms are poorly understood.

2.4 Paper-Based Diagnostics

Paper-based diagnostics or paper-based analytical devices (PADs) take advantage of passive flows that are induced due to capillary effects in porous media. These flows negate the need for the external pumping systems that are often required in traditional microfluidic devices [137–140]. Paper also has the advantage of being low-cost, light weight, biocompatible, easily manipulated by folding, cutting or stacking and can be simply disposed of by composting or incineration [46]. Due to their advantages, there are many examples of paper-based diagnostics in use and it remains an active research topic. A few recent reviews provide technical progress and biomedical perspectives [46, 141–144]. Here, the main styles of devices and the techniques implemented to control fluid flow will be discussed. Due to the advantages of paper as a substrate,

there are also examples of paper being used as a platform for traditional microfluidic techniques. This is where a hydrophobic paper or coating is used and fluid paths are cut out of the paper [145, 146]. In this situation, although paper is used, capillary forces are not dominant, meaning an external pump is still required. For this reason, they are considered to be traditional microfluidic systems for the purposes of this review. There are also several examples where wicking in threads is used to produce microfluidic devices which are not considered [147, 148]. Most PADs utilise reagents which are combined with the investigated sample and transported to one or many detection zones by capillary action. Results are typically identified visually by the user's eye based on colour changes or the distance of transport. Paper-based systems can be broadly classified by flow dimensions (Figure 2.11).

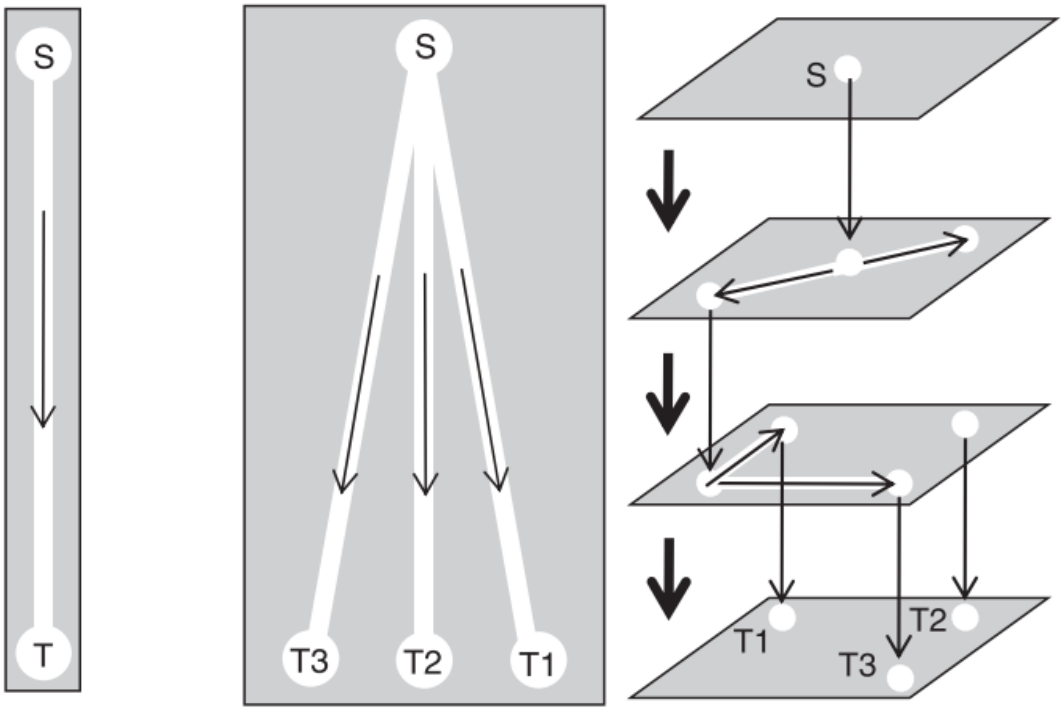

Figure 2.11: Representation of 3 classes of PADs, a) 1D, b) 2D and c) 3D. Reproduced from [141] with permission from De Gruyter.

2.4.1 1D

One dimensional (1D) PADs are the simplest to construct and were used as early as the 1940's. These consist of strips of constant width used as a medium to facilitate the transport of constituents and reactants. Early techniques were used to create chro-

matography [149, 150], electrophoresis and dipstick devices [151]. Since then, significant advances have led to linear paper-based lateral flow devices being used for a wide variety of diagnostics. These include fibrinogen levels in plasma [152] and RNA/DNA measurement [153, 154]. The most commonplace example of a 1D paper-based device is the One Step hCG Urine Test for at home pregnancy screening [155]. These systems typically rely on capillary action to combine the reactants and produce a colour change that is detected by eye. Linear systems have the advantage of simplicity and are cheap to manufacture. Although they are the least versatile in regard to controlling flow, properly designed, 1D paper diagnostics are very effective. Lateral flow diagnostics and dipsticks are the best known commercial systems.

2.4.2 2D

Additional functionality can be facilitated with 2D devices, where fluid is not confined to a single dimension, but takes full advantage of the paper surface in 2 dimensions (2D). This allows the addition of several reactants simultaneously as well as more complex control of flow [156, 157]. 2D PADs can be fabricated in several ways each utilising different methods to control flow [158]. The easiest of which is by varying geometry. This method is shown in Figure 2.12a where the distance and width of 'input legs' are varied to control the timing of the delivery of reagents [88, 159]. Models to predict the behaviour of fluid inside paper of complex geometry are discussed in section 2.3.3. However, the general rule for these systems is that a contracting channel width increases the velocity at the front and vice versa for expanding sections. This behaviour can be explained by considering an electrical circuit analogy for viscous resistance, pressure and volumetric flow [88].

Cutting paper to a specific geometry is a simple and effective method for the small-scale production of microfluidic devices. However, it is often more efficient to pattern paper to create hydrophobic/hydrophilic channels to control flow. This can be used to create similar devices as cut paper. However, due to the contact with a hydrophobic barrier, wicking can be slightly hindered [87]. These hydrophobic barriers can be produced with photolithography [160], wax patterning [161], plasma treatment [162], wet etching [163] and several other methods [158].

Many control elements have been implemented in 2D systems for producing time delays such as shunts [90], dissolvable barriers [164], dissolvable bridges [165] (Figure 2.12b) and several others [69, 143, 166]. It is not always clear if these devices belong in 2D

or 3D system categories as they are commonly applied to both systems. Currently, the only commercial 2D paper diagnostic system is the GLIF blood typing paper test that directly prints the sample's blood group [167].

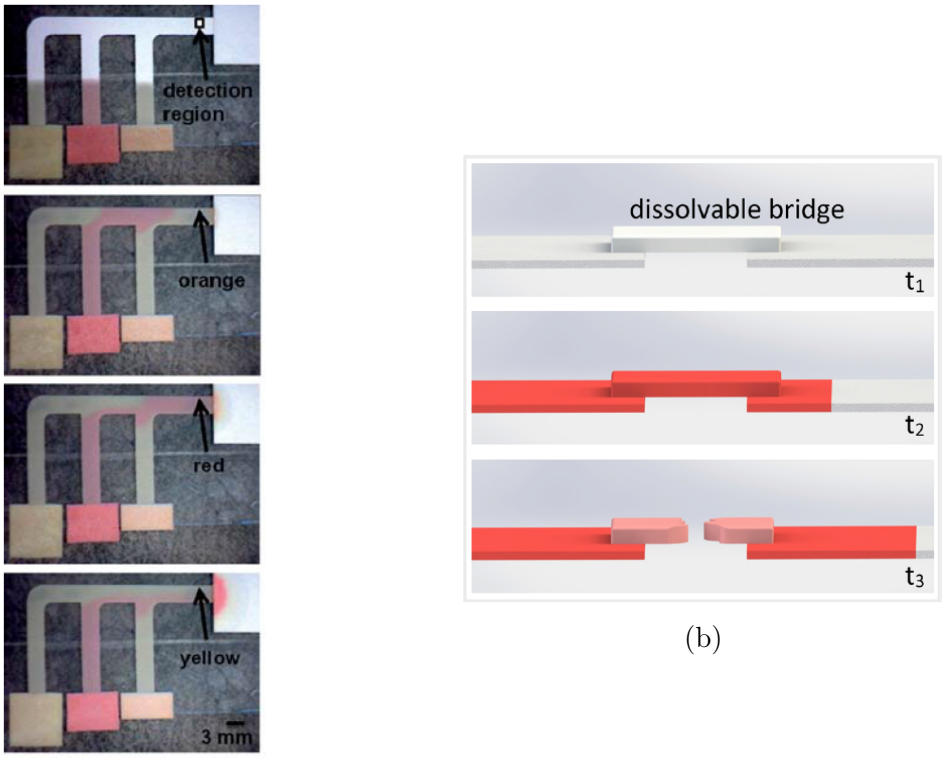

(a) (b)

Figure 2.12: Techniques to control the timing of transport in PADs, a) varying path lengths. Reproduced from [159] with permission from Royal Society of Chemistry, b) dissolvable bridge. Reproduced from [165] with permission from American Chemical Society.

2.4.3 3D

Utilising 3 dimensions (3D) allows reagents to be delivered to many reaction sites, allowing complex multi-functional devices to be designed. However, this comes at the cost of simplicity of use and manufacture. 3D PADs were first demonstrated by Martinez et al. [168] (Figure 2.13) with layers of paper and tape allowing several fluids to flow under and over each other. The tape produces an impermeable barrier that does not allow transport between layers. At sections where transport is desired, a hole is cut in the tape layer and a small amount of cellulose powder is added to bridge the air gap. Figure 2.13b shows a 9 layered device constructed using this technique capable of

selectively delivering reactants to 1024 detection zones. Similar devices can be manufactured using an origami method where the paper can be folded and unfolded along specified lines to quickly and accurately assemble a wide variety of devices [169–171]. 3D flows in single paper sheets are also possible by controlling the penetration of wax layers to create discrete channels [172–174].

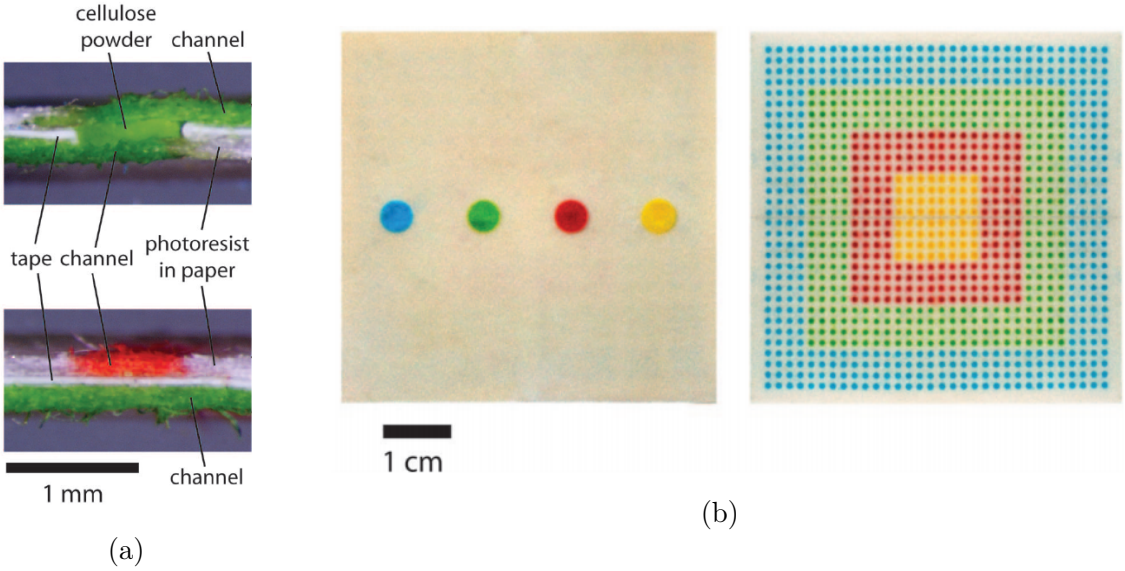

Figure 2.13: Multilayered 3D PADs. a) Tape barriers and cellulose powder channels between layers. b) Top and bottom surfaces of 9 layered device used to distribute 4 reagents to 1024 detection zones. Reproduced from [168] with permission from the National Academy of Sciences of the United States of America.

Layered and single sheet 3D designs have been utilised to produce a wide variety of versatile diagnostic devices. These are discussed in detail in the recent review articles [46, 141–144]. Here, three interesting techniques to control flow in these devices will be discussed briefly.

A significant advantage of PADs is their ease of use; however, a user is not generally able to customise a device to suit their needs without further equipment. User programmable devices have been made with 3D layered channels that can be customised by pressing particular locations on the device [175]. This can be useful as a user can designate the flow of reagents towards any number of detection zones. These devices are created by cutting holes in the non-permeable layer used to divide layers in multilayer PADs. This creates large air gaps that will not transport fluid. If force is applied to these regions the surrounding layers will irreversibly deform, filling the air gaps. This

creates a single use push button that allows flow between layers at the pressed location.

Although simple in operation, PADs often lack the accuracy and reproducibility of traditional methods, this is partially because the introduction of reagents or carrier fluids is by droplet deposition or elusion bath. These techniques are variable and can create reproducibility issues, especially when several tests are to be performed simultaneously. These issues are negated by using 3D slip layers. These are movable layers that allow the simultaneous and reproducible delivery of reagents to many detection zones. This can be utilised to efficiently test many samples [176], and the simplification of test methodologies to single step processes [177].

Li et al. [178] combined a 3D PAD with a hollow needle to create a one-touch device for the simultaneous investigation of blood cholesterol and glucose levels. By pressing on the needle, the device collects a blood sample and delivers it straight to a paper surface for separation and analysis. The combination of sample collection and the analysis of two components in a single device demonstrates the versatility of 3D PADs.

While very impressive and celebrated by many publications, there are no 3D PADs in commercial use. This is because their complexity of fabrication and the lack of reproducibility are currently not compatible with the economics and safety regulations of biomedical point of care devices.

2.4.4 Paper-Based Blood Typing

There are several examples of paper-based blood typing techniques. Most of these involve depositing a drop of blood onto paper that has been treated with antibodies. When a RBC antigen comes into contact with a specific antibody, a strong binding occurs. If the antibody is an IgM pentamer (used for ABO typing [33]) the antibody is large enough to bridge the cell-cell electrostatic repulsion forces from surface charge and facilitate the agglutination of RBCs [179–181]. Upon flushing with saline, individual RBCs wash away, and agglutinated cells remain in place. This is caused by the significant resistance to transport in agglutinated samples. There are many examples of this style of test with the primary difference being the method of saline flushing. If an elusion bath is used, negative results are identified by smearing in the eluded direction [180, 182–185]. A spot test is also used where the saline is deposited directly on to the stain on the paper [181, 186–189]. Here, a positive or negative result is determined by the presence of a defined red spot after washing. Li et al. [188] developed a technique

like the spot method where paper regions are selectively treated to spell the letters A, B and O. After washing, the results of the test are displayed in writing onto the paper surface. Khan et al. [179] developed a strip method where the wicked length of a blood droplet along antibody-soaked paper was utilised. If a specific antibody-antigen reaction had occurred, the final wicked length would be less. This is primarily caused by an increase in the effective viscosity of the suspension in agglutinated samples and a chromatography-like separation. Figure 2.14 gives a representation of each of the main types of paper-based blood typing diagnostics.

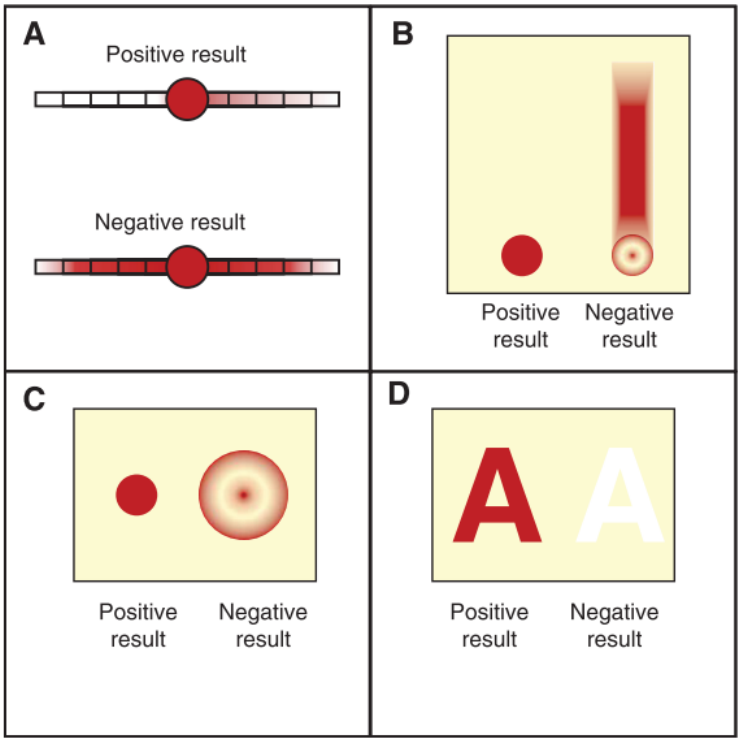

Figure 2.14: Representation of 4 styles of paper-based blood typing diagnostics. Reproduced from [141] with permission from De Gruyter.

2.5 Evaporating Droplets and the Coffee Ring

The evaporation of a sessile drop containing non-volatile components is a ubiquitous phenomenon that is present in everyday life and many manufacturing processes. Due to internal flows and the associated redistribution of constituents, the final dried profile is generally non-uniform. A variety of profile patterns are possible [190] and the most

commonly observed is a ring deposition. This is referred to as a coffee ring or coffee stain. In dilute suspensions this phenomenon produces a distinct ring where almost all the non-volatile component is transported to the edge. Deegan et al. [191] first analysed these ring deposits and found they were caused by an outward capillary flow that is required to maintain a spherical cap shape under non-uniform evaporation conditions. Since this famous publication, there has been a significant amount of research on predicting and controlling pattern formation in evaporating droplets. This is evidenced by the quantity of recent review articles and books devoted primarily to the topic [55, 192–201].

2.5.1 Modes of Evaporation

When a droplet smaller than the system's capillary length is in contact with a solid surface, the droplet assumes a spherical cap shape defined by any two variables out of contact radius, contact angle, height and volume. This is referred to as a two-parameter spherical cap. This quasi-equilibrium state is reached very quickly and can be considered instantaneous in the time scale of evaporation in most systems [50]. Evaporation causes a volume change in the droplet, and therefore causes either contact angle or contact radius to decrease [202]. Constant contact angle is more often observed in pure liquids over smooth, hydrophobic surfaces [203] and results in a non-linear evaporation rate [204]. Complexities such as adsorbed components and physical/chemical surface heterogeneities [205] cause additional pinning forces that must be overcome for triple line motion to take place and increase the likelihood of constant contact radius evaporation. Due to this, constant contact radius drying modes are common in colloidal systems [206]. A combination of the two modes is also possible, this is referred to as a mixed mode when the two occur simultaneously [207] and stick-slip when the two occur intermittently [208, 209].

2.5.2 Evaporation profile

Stagnant Air

The evaporation profile of a drop in stagnant air is a diffusion limited process as the time scale of equilibration of the saturated layer is orders of magnitude smaller than the time scale of evaporation [210, 211]. For diffusion dominated evaporation, the Laplace equation can be used. By solving this equation over a saturated droplet geometry and fitting to experimental data, expressions for evaporation profiles in general systems have been derived [202, 211, 212]. These predictions are generally similar to the historic equation proposed by Deegan et al. [213] (equation 2.16) where the evaporation rate

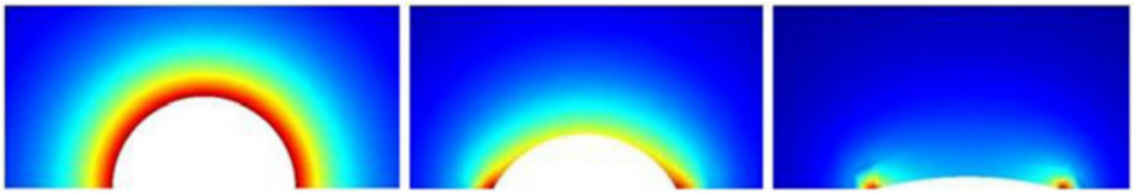

Figure 2.15: Numerical solution of the Laplace equation for several droplets of varying contact angle. Colour distribution represents mass flux. This demonstrates the uniform evaporation rate at higher contact angles and non-uniform and lower. Reproduced from [206] with permission from the Institute of Physics.

diverges at the droplet's edge. Although surpassed in accuracy by modern predictions [200], this equation is commonly incorporated in models for its simplicity [214, 215].

$$\dot{E}(r) \propto (1-r)^{-\lambda} \tag{2.16}$$

$$\lambda = \frac{\pi - 2\theta}{2\pi - 2\theta} \tag{2.17}$$

Where $\dot{E}(r)$ is the evaporation rate as a function of radius (r) and λ is a constant defined by a further function of contact angle (θ). The key aspects of this equation are the diverging flux at the edge and a uniform flux at a contact angle of $\frac{\pi}{2}$. This is shown in Figure 2.15, where the results from a numerical solution of the Laplace equation on droplets varying in contact angle are displayed [206]. The rationale behind an edge enhanced evaporation profile is there is a lower chance of a particle re colliding with the fluid at the edge.

Flowing Air

Unsurprisingly, the evaporation around a droplet in flowing air is enhanced significantly [216]. This is because external flows transport vapour away from the droplet's surface faster than would be possible by diffusion alone. The Peclet number ($Pe = LU/D$) provides a convenient method of determining the relative importance of diffusion and convection in a particular system. Where L is a characteristic length scale for the system (usually the droplet diameter), U is the flow velocity and D is the diffusivity. For large Peclet numbers the gradient of vapour pressure does not vary over the droplet's surface [206], causing a uniform evaporation rate over the whole drop. Routh [206] uses simple scaling arguments to show that the critical Peclet number required to achieve a non-uniform evaporation profile in small droplets is so low that it would be very difficult to achieve in a laboratory environment without very controlled conditions. Therefore, contrary to the assumption of many previous researchers, most films are likely to exhibit

uniform evaporation profiles.

2.5.3 Internal Flow

The two primary causes of internal flow in pinned droplets are capillary and Marangoni effects [198]. Capillary effects are imposed by surface tension where the droplet's surface deviates from a spherical cap. In both uniform and edge enhanced evaporation profiles, a slight curvature is developed at the droplet's edge causing an outward flow [213, 214] (Figure 2.16a). This flow carries non-volatile components, which leads to the commonly observed coffee ring deposit [191]. Similarly, when centrally enhanced evaporation is present, the same mechanism causes inward flow. Depending on the system, this can cause a uniform or central deposit to be formed [213, 217].

Marangoni effects are caused by surface tension gradients, which induce surface flows from regions of low surface tension towards regions of high surface tension. In droplets, this is usually caused by temperature gradients from evaporative cooling [218]. The temperature field inside an evaporating droplet is a complex function of the thermal properties, velocity field, evaporation profile and geometry. These were resolved numerically and analytically to determine the resulting flow field in several studies by Hu and Larson [218–220]. However, Marangoni flow can be demonstrated simply with a sessile droplet on a substrate at room temperature. Upon evaporation, the surface of the drop cools, generating a temperature gradient and therefore the transfer of heat energy from the substrate. In this example, the substrate is assumed to be an infinite heat source at room temperature. As the edge of the drop is close to the substrate the temperature there is higher, and conversely the centre of the drop is cooler because there is a longer thermal path to the heat source. Most fluids increase in surface temperature upon cooling, which results in a high surface tension at the centre of the drop and a low surface tension at the edge, producing recirculating flows (Figure 2.16b). These flows can influence deposition patterns and either create a uniform or central bump deposit [218]. Surface tension gradients and therefore Marangoni flows can also be caused by non-uniformly adsorbed constituents on the liquid-vapour interface [221, 222].

Many techniques have been proposed to control Marangoni flows in evaporating droplets to control pattern formation. These include heating and cooling the substrate [223], changing contact angle [219], using surfactants [221] and drying in an ethanol vapour environment [224].

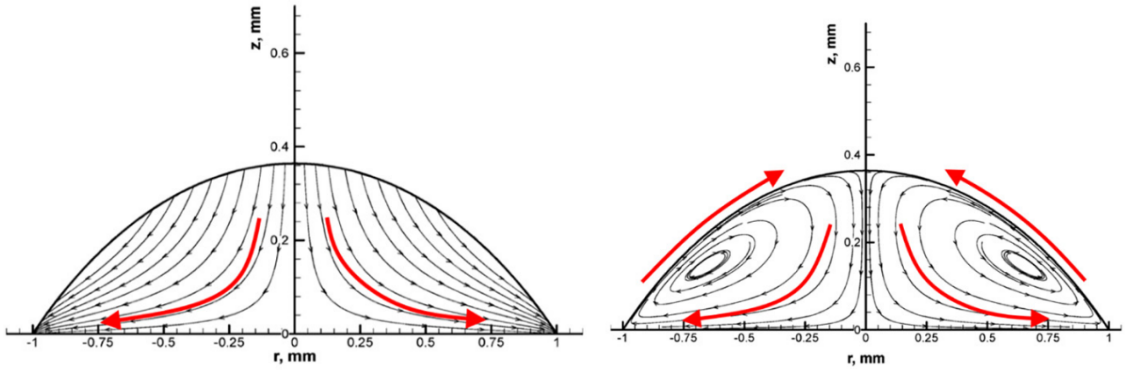

(a) (b)

Figure 2.16: Common flow mechanisms in evaporating droplets, a) capillary b) Marangoni. Reproduced from [198] with permission from Elsevier.

2.5.4 Particle Aggregation

In drying systems containing a non-volatile component, it is common for horizontal drying fronts to form [225, 226]. These fronts form when the local concentration of the suspension increases past a critical value that causes the effective viscosity to diverge. At this point a close-packed or consolidated structure [226, 227] forms in the drier region. This structure typically forms near the edge of a deposit first due to the higher rate of evaporation there. Although this region is in most cases rigid, there remains a volatile component in the inter-particle space which continues to evaporate. This evaporation causes menisci to form at the liquid-vapor interface, producing a negative capillary pressure that transports fluid into the formed consolidated region. As only the liquid component can penetrate, any particles transported by this flow deposit at the front. At some distance away from the moving consolidated front, viscous losses surpass the maximum capillary pressure. This is defined by meniscus geometry and surface tension. At this location evaporation is faster than flow from the fluid region therefore causing significant drying [226]. This causes a secondary front to form a short distance behind the consolidated front called the *cracking front* as there are typically cracks in this region.

In droplet systems a close-packed region forms very quickly at the edge of the drop and then propagates inward [228]. This means that at most stages during drying, two clearly delineated regions exist; a liquid and a consolidated. This consolidated region forms for two reasons: The increase in concentration caused by evaporation is more significant where the film is thin [206], and the evaporation-driven capillary flow bringing non-

volatile components to the edge, which increases the concentration [191, 213]. Once the consolidated region forms, an outward flow is induced due to the inter-particle menisci discussed in reference to horizontal drying fronts [225]. This shows that although insightful, analysis based on pure fluids such as those by Hu and Larson [218–220] are limited. This is because particle aggregation and the resulting inter-particle menisci, impact flow behaviour significantly. Yunker et al. [229] demonstrated that the coffee ring effect can be entirely suppressed with only slightly elliptical particles, demonstrating that particle interaction and packing affects final deposits significantly. Due to this, the models intended to predict the final deposit profile are generally heavily influenced by particle aggregation and the progression of the consolidated front.

2.5.5 Predictive Modelling

Many studies use the lubrication theory to predict the height profile in evaporating droplets as a function of radius and time. Equation 2.18 is derived assuming no Marangoni forces or vapour recoil. It also assumes that pressure is solely a function of local curvature, no shear at the free surface, no slip at the substrate and that the lubrication theory is valid as the drop is thin [230]. Here, it is presented in the form derived by Fischer [214].

$$\frac{\partial h}{\partial t} = -\frac{1}{3Ca}\frac{1}{r}\frac{\partial}{\partial r}\left[h^3 r \frac{\partial}{\partial r}\left(\frac{\partial h}{\partial r^2} + \frac{1}{r}\frac{\partial h}{\partial r}\right)\right] - EJ \tag{2.18}$$

Where Ca is the capillary number ($Ca = \frac{\mu U}{\gamma}$), J is a function giving the evaporation profile as a function of drop radius, h is the height of the droplets and E is the evaporation number which is a property of the system. This equation in slightly different forms was used in several studies [29, 215, 231–234] to predict final height profiles as it is a simple 1D equation for a single unknown and allows the evaporation rate and profile to be altered simply. Also, this equation allows the simple tracking of the drop interface, which is not straightforward in more complex methods [235]. This equation is typically combined with a mass balance equation to define the local concentration and viscosity of the suspension [215]. The small thickness of thin films means diffusion dominates in the vertical direction, leading to a 1D mass balance equation. Radial diffusion of the non-volatile component was considered by Tarasavich and co-workers [29].

This style of analysis also typically includes a threshold concentration above which the fluid solidifies [29, 215, 232], therefore providing a criterion with which to track

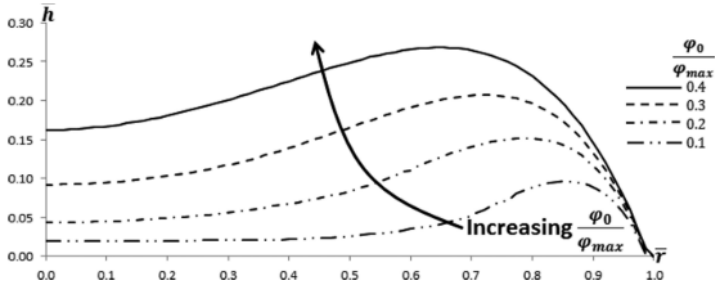

Figure 2.17: Predicted dried profiles varying initial volume fraction. Reproduced from [215] with permission from AIChE.

the consolidated front. There is disagreement on the flow conditions around and inside the consolidated region. Tarasavich and co-workers [29] assume there is no flow into the consolidated region, although they acknowledge the presence of evaporation there. Eales and co-workers [215] use a mass balance at the consolidated front to determine the flow rate into the consolidated region. They use a scaling factor to represent a decrease in evaporation rate because of the presence of the non-volatile component. Routh and Russel [225] assume that the consolidated region is evaporating at the same rate as in the liquid region and equate the flow into the consolidated region to the evaporation occurring there. Despite this discrepancy, all conditions produced coffee ring shapes, and the general trends of decreasing likelihood of coffee ring formation with increased initial volume fraction, increased diffusion and decreased evaporation from the consolidated region [215]. Theoretical results depicting the relationship between final profile and initial volume fraction are shown in Figure 2.17.

Hu and Larson [218] developed a unique method of predicting final shape of dried deposits. Here, particles are tracked in a derived flow field including the effects of Brownian diffusion. Once a particle collides with the substrate, it is assumed to remain there. The simulation ends when the drop has evaporated entirely and the particle density on the substrate as a function of radius is measured. This is found to match experimental results for dried deposits of octane and water (Figure 2.18).

Another notable modelling success was accomplished by Shur et al. [236] where the deposit left in a stick-slip regime droplet was predicted numerically. This was accomplished using simple geometric calculations and specifying two critical height/radius ratios that correspond to the value that causes the contact line to depin and pin. Results in Figure 2.19 are found by recording the locations where the contact line was pinned in simulations as this is general accepted as a requirement for particle deposi-

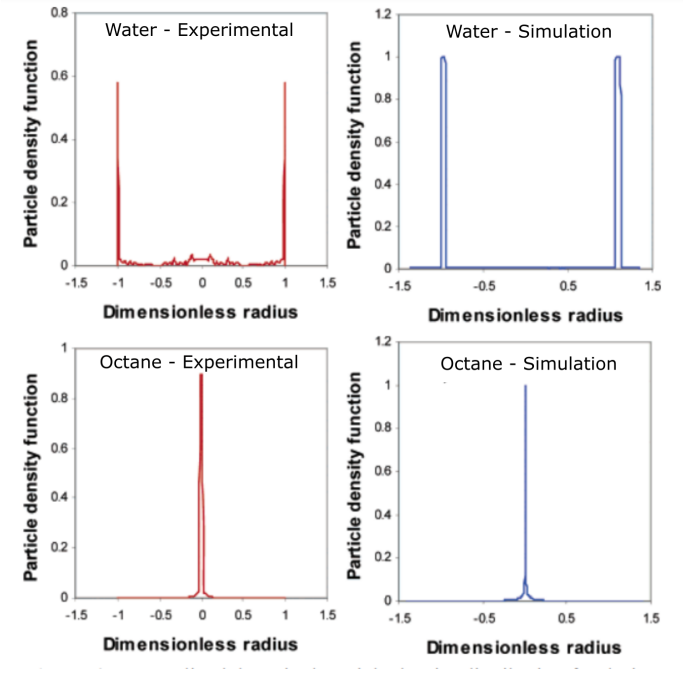

Figure 2.18: Numerical predictions of pattern formation based on Brownian diffusive model in octane and water based particle suspensions. Reproduced from [218] with permission from the American Chemical Society.

tion [206]. This technique has limitations; it cannot predict the height or thickness of the deposits. However, it demonstrates a level of predictive power that is impressive considering the flow field inside the droplet is not resolved.

2.5.6 Other Features

In combination with the redistribution of constituents while in the fluid phase, the final appearance of a dried deposit is severely influenced by secondary effects that occur in the later stages of drying [228]. These include cracking, wrinkling and buckling that all occur because of solid-like interactions during drying. Wrinkling and buckling are primarily caused by compressive stress and cracking is produced by tensile stress. These phenomena and their influence on dried patterns have received a lot of attention from researchers recently and are only briefly discussed here; for more information see reviews [194, 201].

Buckling and wrinkling are common in evaporating droplets where a skin layer is present [194]. Skin layers (also called crust and envelope layers) are created due to an accumulation of particles at the droplet's surface when the evaporation rate surpasses vertical

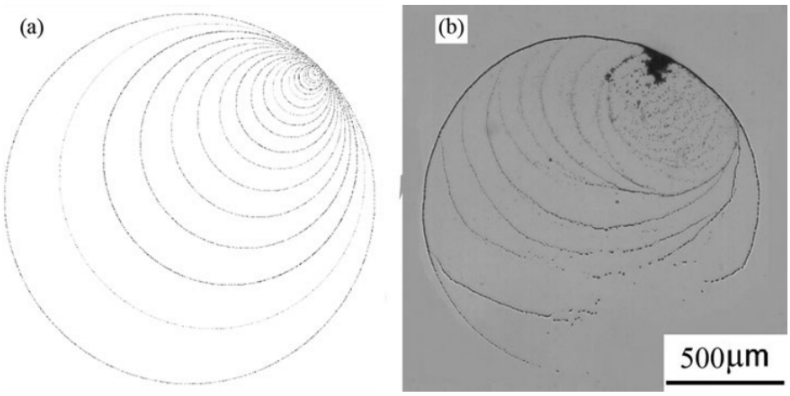

Figure 2.19: Predictions of pattern formation from stick-slip regime droplets. Reproduced from [236] with permission from Taylor & Francis.

diffusion, which leads to particles being collected by the moving interface [55, 206, 237–239]. The relationship between diffusion and evaporation rate is defined by Peclet number $Pe = H\dot{E}/D$. Where H is the vertical height of the fluid film, $\dot{E}$ is the evaporation rate and D is the diffusivity of particles. When $Pe >> 1$ a skin layer is likely to be formed and vice versa for when $Pe << 1$. The formed skin is elastic due to elastocapillarity effects [240]. Further evaporation after skin formation causes compressive stress, which leads to sudden buckling and wrinkling instabilities. These are responsible for a variety of complex morphologies [201]. The mechanical properties of the skin as well as the contact angle and drying conditions can be tuned to determine final profiles [241–243]. When skin layers have a high rigidity, a cavity or vacuole is formed inside the skin layer, which produces dried deposits that are hollow [244, 245].

Another common feature of drying suspensions is the formation of cracks. This phenomenon is not specific to droplet systems [206, 246, 247]. The general mechanism of crack formation in drying systems is by tensile stress caused by the evaporation induced shrinkage of a gelled suspension. This tensile stress is produced from a capillary pressure due to inter-particle menisci at the liquid-vapour interface [248]. As evaporation proceeds, the menisci recede, causing capillary pressure to increase in strength. This causes a force of increasing magnitude pulling the particles together. In simple systems, this causes a decrease in volume, but in the case of a thin film, the horizontal direction is constrained due to adherence to the substrate. This creates tensile stresses in the horizontal plane [249, 250]. The only way this stress can be relieved is through the formation of cracks [251]. This explanation is also used to describe why cracks are only present above a critical thickness and a minimum adhesion for a given material

[252]. Predictive modelling of cracks balance elastic energy recovery with the increase in surface energy corresponding to the creation of the crack face [206, 251]. This is a standard method used in determining fracture of elastic materials, although non-ideal properties such as particle deformability, viscoelasticity and non-uniform water content complicate these calculations for drying particle systems [201, 253–255].

2.5.7 Coffee Rings in Paper

Coffee stains are also observed in paper [256, 257], where non-volatile components in stains are transported outwards during drying. This leads to an accumulation at the edge after drying, which causes stains to have a dark edge on their boundary. This process has not been studied in detail and therefore the governing mechanisms are not well understood. However, stains in paper have pinned boundaries and experience edge enhanced evaporation similar to droplet systems. Due to this, the process is likely similar to ring formation in droplet systems, although chromatography effects must also be included. Coffee stains are only observed when the chromatographic mobility of the non-volatile component in paper is high [257].

2.5.8 Drying Droplets of Biological Fluids

An important application of the patterns left by evaporating droplets is the analysis of biological fluids for medical diagnostic purposes. This is an emerging field and much of the previous research has focused on plasma and blood, see reviews [10, 258]. The potential of this technique to be used for disease diagnostics has been theorised for several years [259], and has been found to be representative of many conditions including carcinoma [260], anaemia, hyperlipemia [2], thalassemia, jaundice [261] and many more [262].

Much of the previous research in this field has focused on the quantification of crack patterns; however, other methods have been investigated. Yakhno et al. [262] monitored the acoustic mechanical impedance as a function of time by drying the drop on the surface of a quartz resonator to identify key differences between blood from patients with various conditions.

Numerical modelling of both protein solutions [233] and whole blood [29] has been performed using similar models as previous studies relating to deposit patterns in simple suspensions. These produced realistic profiles but no detailed comparison with

experimental measurements have been performed.

Historically, research on drying blood droplets has primarily occurred in the field of forensics where blood pattern analysis is used to reconstruct crime scenes [132, 263]. However, this research has been heavily application driven and little attention is payed to the fundamental mechanisms that lead to the observed patterns.

Drying Plasma and Protein Solutions

The drying of a drop of plasma has been studied in isolation and shows distinct differences from dried droplets of whole blood and simple particle suspensions. Although a ring-like deposit is generally observed in these systems [10], the presence of proteins, salts and other macromolecules causes significant deviations from typical models for evaporating colloidal suspensions. Devineau et al. [264] demonstrated that pattern formation could be reliably used to discriminate single point mutation in human haemoglobin which is responsible for sickle cell anaemia For protein rich solutions, the mechanism of solidification is a gelation/crystallisation rather than particle aggregation. Many studies used albumin in an electrolyte solution as a model for plasma/serum as they produce very similar patterns [265].

Dried drops of plasma and protein solutions are generally characterised by 2 regions. An outer or periphery region and a central region [266], which are identified by different crack patterns. Although the influence of salt and protein concentration is not fully understood a strong relationship with pattern formation has been identified [267–272]. This is because of several complex competing mechanisms. Chen et al. [269] argued that the dependence on salt content is due to a decrease in Debye length, decreasing the effect of surface charge between individual protein molecules. They also debated that high salt concentrations cause the early formation of large salt crystals, which prevent the formation of large-scale protein structures. Buzoverya et al. [271] discussed the effect of varying protein concentration in regard to different levels of interaction between molecules, therefore effecting the timing and strength of gelation.

Tarasevich and Ayupova [265] demonstrated theoretically that the high diffusivity of salt results in a uniform distribution over the whole droplet. However, the comparatively low diffusivity of protein molecules means these accumulate preferentially on the outer edge of the drop. This leads to a relatively high concentration of proteins in the outer region and a high concentration of salt in the inner region. This difference could

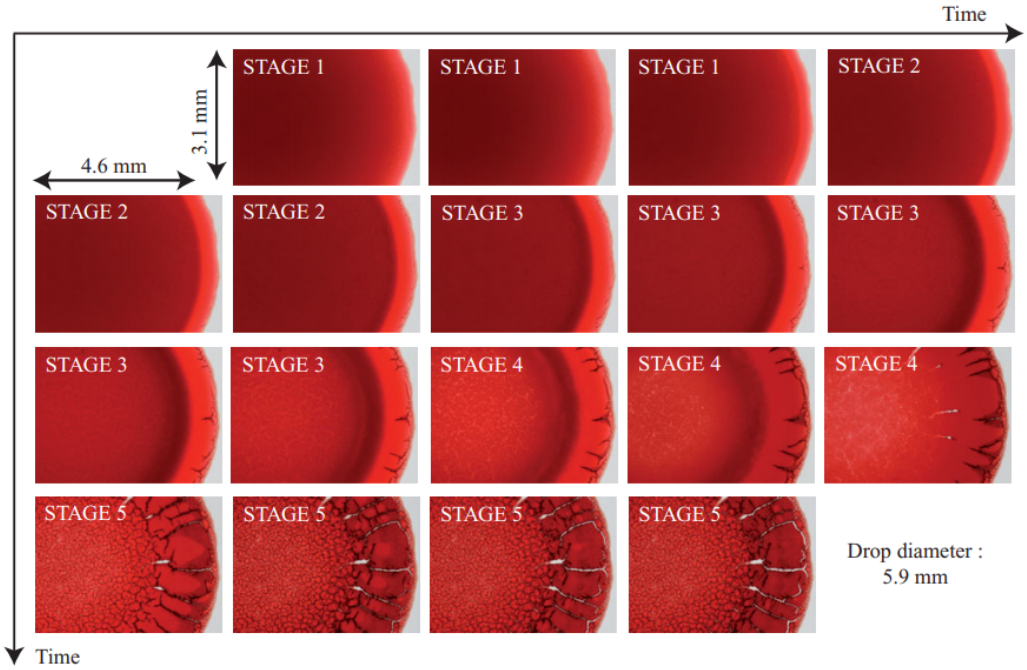

Figure 2.20: Stages involved in a drying droplet of blood. Reproduced from [2] with permission from Cambridge University Press.

be responsible for the observed differences in the peripheral and central zones.

Drying Whole Blood

Brutin et al. [2] monitored the appearance and weight of a drying drop of blood. 5 key stages were observed, which are shown in Figure 2.20. A simpler 3 stage description was later presented by Sobac et al. [28]. First, according to defined coffee ring mechanisms [191], a radial flow is developed. This causes the accumulation of non-volatile components at the droplet edge. Second, the local concentration in the outer region rises above a critical value and gels. This gelled 'foot' splits the droplet into two regions and the 'compaction front' that separates these two regions, propagates inwards, similar to what is observed in simple colloid systems. In this stage, the first cracks form in the gelled region and the height in the centre decreases linearly. The compaction front steadily decreases in speed and the end of this stage is marked by the rapid and homogeneous gelling of the remaining fluid area [28]. The final stage begins after complete gelation has occurred, when the rate of evaporation has decreased significantly. Evaporation after this point leads to further shrinkage and cracking. The final appearance of blood drops shows two clear regions [2]: an outer 'corona' characterised by regularly spaced radial cracks and an inner region with more disordered cracks. These two regions can

be identified in the later panels of Figure 2.20.

Until the late stages, the evaporative flux of blood is identical to pure water and plasma [2]. This shows that the early stage mechanism of RBC redistribution in drying droplets of blood is similar to water and plasma. Brutin et al. used the low capillary number of the blood system to propose that the induced flow is due to Marangoni convection not capillary transport. However, the source of the surface tension gradients required to produce Marangoni stresses are not mentioned. Marangoni flows in drying droplets generally cause a recirculating flow (Figure 2.16b) not the outward flow that is observed in blood drop systems [198]. Also, another study by Hu and Larson confirmed that there are no Marangoni flows in pure water droplets [218]. Therefore, if droplets of water and blood exhibit similar drying mechanisms in the early stages, Marangoni flow is unlikely to contribute.

Evaporation of blood droplets deviates from water measurements in the later stages because the gelation in the outer region slows evaporation significantly [28]. Sobac et al. [28] also fit weight measurements to a simple diffusive model and found a good fit when the evaporative area was decreased at a rate that matched the recorded shrinkage of the fluid region. This implies that negligible evaporation is occurring in the outer region once gelation has happened. The appearance of cracks in this region, before the remainder of the drop gels, also indicates a hindered evaporation as it implies the maximum capillary pressure has been exceeded [226].

There is a strong relationship between the final appearance of dried blood deposits and the relative humidity (RH) [273]. This relationship is shown in Figure 2.21 and is caused by changes in contact angle, spreading extent and evaporation rate. All of which are functions of RH in both blood and simple colloid systems [273, 274]. Evaporation from a droplet of blood follows standard diffusive models for droplet geometry [218, 273] until a point roughly 65% of the total drying time. At this point, the mass flux rapidly decreases, indicating a shift to a gelled/porous material [2].

The effect of drying rate on the spacing and orientation of cracks in whole blood deposits was investigated by Zeid et al. [275]. It was found that a high drying rate produces more radial cracks and a low rate results in more disordered cracks. Further detailed studies on blood [28, 250] identify that the cracking behaviour is caused by the expected build-up of stress due to the competition between tensile force as the gel

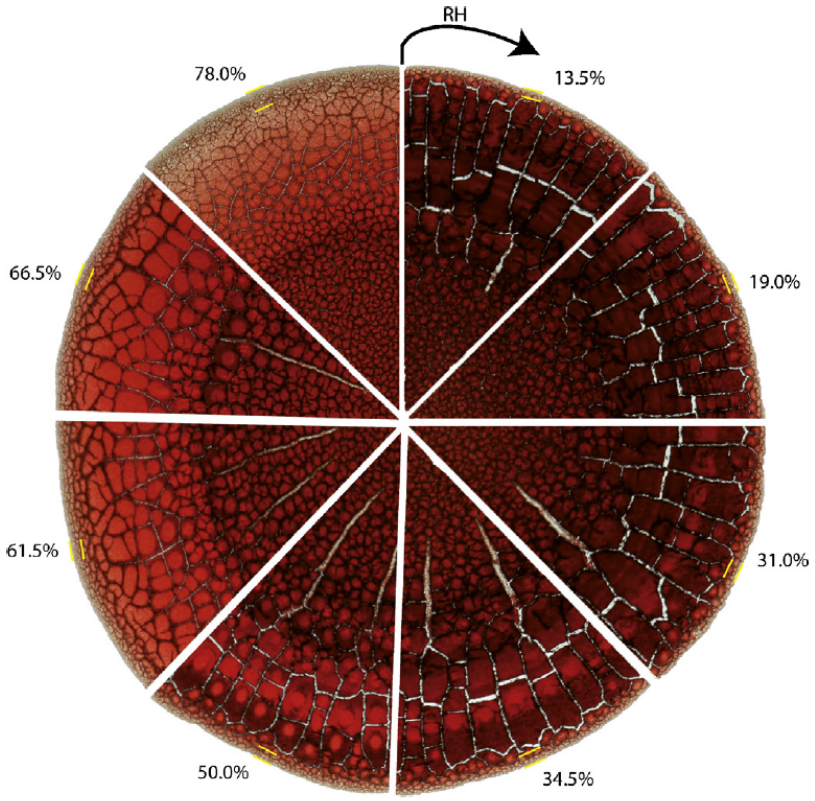

Figure 2.21: Effect of humidity on pattern formation in dried blood droplets. Reproduced from [273] with permission from Elsevier.

shrinks and adhesion to the substrate. However, once initial cracks form, delamination becomes a secondary mechanism to release stress. This causes the edges of individual plaques to detach from the substrate, creating concave surfaces. Further cracking can occur depending on the size and composition of the now individual plaques. This process of gradual delamination and further cracking has been studied for specific systems and is responsible for some very unique drying morphologies in other colloid systems [276]. This phenomenon also explains the intriguing near circular darker sections that form in the centre of blood plaques [28]. These dark sections are the regions in which there is still adhesion between the gel and the substrate, the lighter sections are where the material has delaminated.

2.6 Summary

The minimisation of surface energy leads to many spontaneous macro-scale phenomena including the wicking of wetting fluids in porous materials and evaporation induced

flows in drying droplets. Although interesting from a fundamental perspective, these flows can also be readily utilised to develop a multitude of low-cost diagnostic devices ranging in complexity. Capillary flow in paper is caused by a negative Laplace pressure, developed due to the curved menisci inside the material pores. This flow is regulated by the geometry of the paper and the characteristics of the porous network. There are many numerical approaches to predict this behaviour and they can be broadly grouped into three categories. The first is capillary, where the system is modelled as a collection of ideal capillary tubes. This technique is the simplest and oldest; however, it is not suited to complex and more realistic systems. The second, continuum, is where properties such as velocity and pressure are averaged over length scales much larger than the pores in the material. This approach leads to computationally efficient predictions, although they rely heavily on the determination of other constitutive equations for accuracy. The last, pore scale, is where the micro-scale fluid behaviour is included, typically at the cost of computational complexity.

There is surprisingly little literature characterising the flow of complex fluids in paper and porous media. Much of the wicking analysis of paper devices has been performed assuming Newtonian properties of liquids and omitted adsorption phenomena, despite the complex interfacial and rheological properties of biological fluids being so broadly quantified and published. Although there has been development in this field for forensic applications, the empirical nature of this research makes its application to fundamental studies difficult.

Passive flows in evaporating droplets can also be used for medical applications. Here, the redistribution of constituents that occurs can produce many different patterns that are indicative of a variety of conditions. There is extensive literature on the drying of droplets of simple particle suspensions, typically focusing on the well-known coffee ring effect. This is the most common pattern that is observed and is caused by an outward capillary flow that transports constituents to the edge of the droplet. This outward flow develops due to both the higher evaporation rate at the edge of the droplet and the effect of surface tension enforcing a spherical cap geometry. The coffee ring effect is usually regarded as a manufacturing defect; therefore, much of the literature is concerned with its mitigation or suppression.

As cracking patterns are the most identifiable feature of a dried deposit of biological fluids, the majority of the previous research on blood deposits have focused on this

topic. Cracks in drying films result from the release of internal stresses that are developed due to the shrinking film's adhesion to the substrate. However, whether they can be used for reliable diagnostics remains an unanswered question.

2.7 Gaps in Knowledge

This review highlights the many advances in the development of low-cost diagnostics based on a fundamental understanding of the principles of capillary induced flow in both paper and evaporating droplets. The review has also identified several significant gaps in the literature for each topic.

Radial Wicking in Paper

Although wicking from infinite reservoirs has been well quantified in paper, wicking from finite reservoirs such as sessile droplets remains poorly understood. A key characteristic of these systems is the effective removal of the reservoir a finite time after wicking has initiated, which causes a stage transition in wicking dynamics. Previous research has identified that wicking continues after the removal of this interface due to the redistribution of fluid from large to small pores. However, several key aspects of the process are still not understood. These include:

- What determines the final stain size?
- What is the mechanism behind first to second stage transition?
- How does the wicking process differ between biological and simple fluids?

Evaporating Droplets

Pattern formation in evaporating droplets on impermeable surfaces has been analysed extensively for simple systems such as particles in suspension. However, there is little theoretical modelling that is compared with experimental results. Also, the effect of the contact angle formed by the suspension with the surface has not been investigated rigorously. Deposits left by dried droplets of blood have been characterised in previous studies. However, there is limited linkage of the fundamental mechanisms with existing drying literature. These gaps are summarised in the following two research questions:

- What is the effect of the contact angle of the suspension with the surface?
- What are the dominant mechanisms leading to the deposit profile of biological fluids in evaporating droplets?

2.8 Research Objectives

The objectives of this thesis are twofold. First, to investigate the fundamental mechanism of capillary induced blood flows over two platforms: paper and solid surfaces. Second, to apply this understanding to develop and engineer novel diagnostics. The specific aims which form the experimental chapters of this thesis are:

1. To quantify the mechanism(s) determining equilibrium stain size of a droplet on paper.

2. To analyse and mathematically model the first-to-second stage mechanism and its relationship to the rate of stain growth from a droplet on paper.

3. To measure the cause of porosimetry hysteresis in paper-based wicking systems and identify its relationship with the anomalous wicking behaviour of biological fluids

4. To develop a high throughput, paper-based blood typing technique

5. To develop a fluid mechanics model to describe the effect of contact angle on the onset of ring formation (coffee ring) in drying droplets.

6. To identify the governing parameters leading to the anomalous deposit morphology of a dried droplet of blood

2.9 Thesis Outline

This thesis consists of 7 experimental chapters of which 3 are published and 2 are submitted in peer reviewed journals. All published papers are reformatted for consistent presentation and the original publications are given in Appendix A. A summary of each chapter in this thesis is outlined below.

- Chapter 1 - Introduction
  This chapter introduces microfluidics as a technique to create low-cost and portable diagnostic devices. The importance of spontaneous flows induced by interfacial phenomena and their applications in both paper and evaporating drop-based diagnostics are introduced.

- Chapter 2 - Literature Review
  The previous literature on both wicking in paper and evaporating droplets is

reviewed. The fundamental mechanisms and various modelling techniques for both systems are discussed, as well as several techniques for controlling the flow of fluid. Existing blood diagnostic devices and the techniques that are utilised in each are also noted.

- Chapter 3 - High Throughput Blood Typing
  There are many examples of paper-based blood typing diagnostics in literature. These diagnostics are useful in low-cost point of care applications. However, none are suitable for large-scale high throughput applications such as hospitals and blood banks, where thousands of tests are performed every day. This is because previous paper-based systems are single use tests that are generally not scalable. In this chapter, a simple, automatable and paper-based method for forward blood group testing is presented. The test can be performed in under 10 seconds, which is significantly faster than all other blood typing techniques. Reverse group diagnostics and the detection of COVID-19 antibodies are also demonstrated with this technique.

  The main content of this chapter was submitted to *ACS Sensors*.

- Chapter 4 - Paper-Based Reverse Blood Typing
  Reverse typing is required for the safe matching of donor and patient blood and involves determining the antibodies that are present in the donor's plasma. Reverse testing is demonstrated with the high throughput test introduced in Chapter 3. However, the error rate makes it not appropriate for most blood typing applications. Here, another paper-based reverse typing method is introduced using premixed and incubated reagent cells combined with the donor plasma. This methodology showed a higher sensitivity but requires more time to complete. Commercial paper towel and a custom made handsheet paper were tested and both can discriminate test results and demonstrate a significant difference between slow and fast velocity flows in paper-based agglutination diagnostics.

- Chapter 5 - Equilibrium Stain Size
  In this chapter, the governing parameters leading to the equilibrium stain size of droplets on paper is studied. This was achieved by measuring the stain size of many fluids varying in viscosity, surface tension and protein content and comparing those to blood and plasma. Liquid physical properties, such as surface tension

and viscosity, do not affect the final stain size significantly. However, there is a strong dependence on protein concentration. The predominant effect of protein in blood on blood stains was identified with contact angle measurements on model cellulose surfaces. Upon adsorption, blood proteins increase the solid-liquid interfacial energy, increasing the contact angle and therefore reducing the driving force behind further stain growth.

The main content of this chapter is published as
Michael J Hertaeg, Rico F. Tabor, Gil Garnier. Effect of protein adsorption on the radial wicking of blood droplets in paper: *Journal of Colloid and Interface Science*, 528:116–123, 2018

- Chapter 6 - Transient stain growth
  The aim of this chapter is to investigate the transient behaviour of a droplet of a model fluid wicking radially into paper. This is characterised by two distinct stages; before the droplet has been absorbed and after. The stain area in these two stages is represented by a power law with time. However, the power decreases significantly after the stage transition. Here, a numerical model is presented capable of predicting both of these stages and the transition. The dominant cause of the stage transition was the effective removal of the droplet reservoir, as well as a significant porosimetry hysteresis that is introduced in the second stage.

  The main content of this chapter is published as
  Michael J Hertaeg, Rico F. Tabor, Joseph D. Berry, Gil Garnier. Dynamics of stain growth from sessile droplets on paper: *Journal of Colloid and Interface Science*, 528:116–123, 2018

- Chapter 7 - Wicking of Biological Fluids
  The stain growth behaviour of biological fluids is significantly different to the simple fluids discussed in Chapter 6. This chapter identifies the dominant cause of the anomalous wicking behaviour to be an increased hysteresis severity in these systems. This was caused by contact angle effects brought about by protein adsorption onto paper fibres. By including these effects, a predictive model of the radial wicking of a droplet of biological fluids was developed.

  The main content of this chapter is published as
  Michael J. Hertaeg, Rico F. Tabor, Joseph D. Berry, Gil Garnier. Radial Wicking of Biological Fluids in Paper: *Langmuir*, 36:8209-8217,

2020

- Chapter 8 - Pattern Formation in Blood Drops
  This chapter investigates the dominant mechanisms leading to ring formation in drying blood droplets. This is undertaken to better understand the diagnostic potential of this process. Optical profilometry measurements are performed on red blood cell suspensions varying in concentration and protein content. The contact angle of the suspension with the surface is also varied. A ring is formed in almost all circumstances and demonstrates significant differences in behaviour when compared to simple colloidal suspensions. In drying droplet systems, a consolidated region forms at the outer edge producing a compaction front that propagates towards the centre. The discrepancy between blood and simple colloids is identified to be caused by the consolidated front which slows down and halts after a short drying time for blood. However, for simple colloids, this front continues until the centre is reached. This is because in drying droplets of simple colloidal suspensions, a consolidated region forms at the edge at very early times and then propagates inwards until the centre is reached. For blood, this front halts a short time after drying has begun. Possible causes of front slow-down in blood are investigated including: increased viscous losses in the consolidated region due to particle deformation, decrease in maximum capillary pressure due to gelled proteins accumulating at the solid-liquid interface and poroelasticity due to gelation in the central region.

- Chapter 9 - Predictive Modelling of Coffee Rings
  Although there has been significant research into drying droplets, the fundamental mechanisms that lead to pattern formation are not well understood. Before pattern formation in drying blood droplets can be comprehensively modelled, simpler colloidal systems must be studied further. In this chapter, a numerical model is presented for predicting ring formation as a function of contact angle and initial volume fraction. Results are in broad agreement with experiments using polystyrene particles.

  The main content of this chapter was submitted to *Physical Review Letters*.

- Chapter 10 - Conclusion
  The final chapter summarises the contributions of this thesis and provides perspective on the place of this research in the fields of paper-based diagnostics and evaporating droplets on impermeable surfaces.

2.10 References

[1] Mark Thiriet. *The Biology and Mechanics of Blood Flows*. Springer, 2008.

[2] D. Brutin, B. Sobac, B. Loquet, and J. Sampol. Pattern formation in drying drops of blood. *Journal of Fluid Mechanics*, 667:85–95, 2011.

[3] Atul Mehta and Victor Hoffbrand. *Haematology at a Glance*. John Wiley & Sons, 2009.

[4] James H Jandl. *Blood: textbook of hematology*. Little Brown, 1996.

[5] Peter B Canham. The minimum energy of bending as a possible explanation of the biconcave shape of the human red blood cell. *Journal of Theoretical Biology*, 26(1), 1970.

[6] Jens G. Danielczok, Emmanuel Terriac, Laura Hertz, Polina Petkova-Kirova, Franziska Lautenschläger, Matthias W. Laschke, and Lars Kaestner. Red blood cell passage of small capillaries is associated with transient Ca2+-mediated adaptations. *Frontiers in Physiology*, 8:979, 2017.

[7] James N. George. Platelets. *Lancet*, 355(9214):1531–1539, 2000.

[8] Paul Harrison. Platelet function analysis. *Blood Reviews*, 19(2):111–123, 2005.

[9] L Dean. Blood Groups and Red Cell Antigens. *The ABO blood group*, page Chapter 5, 2005.

[10] Ruoyang Chen, Liyuan Zhang, Duyang Zang, and Wei Shen. Blood drop patterns: Formation and applications. *Advances in colloid and interface science*, 231:1–14, 2016.

[11] Basem N Azab, Vijaya R Bhatt, Steven Vonfrolio, Rana Bachir, Vladimir Rubinshteyn, Homam Alkaied, Ayman Habeshy, Jignesh Patel, Antonio I Picon, and Scott W Bloom. Value of the pretreatment albumin to globulin ratio in predicting long-term mortality in breast cancer patients. *The American Journal of Surgery*, 206(5):764–770, 2013.

[12] Masaki Otagiri and Victor Tuan Giam Chuang. *Albumin in Medicine: Pathological and Clinical Applications*. Springer, 2016.

[13] David J. Greenblatt. Reduced Serum Albumin Concentration in the Elderly: A Report from the Boston Collaborative Drug Surveillance Program. *Journal of the American Geriatrics Society*, 27(1):20–22, 1979.

[14] Oguz K Baskurt and Herbert J Meiselman. Blood rheology and hemodynamics. In *Seminars in thrombosis and hemostasis*, pages 548–4662. 2003.

[15] Fuat Yilmaz and Mehmet Yaşar Gundogdu. A critical review on blood flow in large arteries; relevance to blood rheology, viscosity models, and physiologic conditions. *Korea Australia Rheology Journal*, 20(4):197–211, 2008.

[16] Y. I. Cho and K. R. Kensey. Effects of the non-Newtonian viscosity of blood on flows in a diseased arterial vessel. Part 1: Steady flows. *Biorheology*, 28(3-4):241–262, 1991.

[17] Mohan Anand and Kumbakonam R Rajagopal. A mathematical model to describe the change in the constitutive character of blood due to platelet activation. *Comptes Rendus Mecanique*, 330(8):557–562, 2002.

[18] K R Rajagopal and A R Srinivasa. A thermodynamic frame work for rate type fluid models. *Journal of Non-Newtonian Fluid Mechanics*, 88(3):207–227, 2000.

[19] Holger. Schmid-Schönbein, ROE. Wells, and Jerry. Goldstone. Influence of deformability of human red cells upon blood viscosity. *Circulation research*, 25(2):131–143, 1969.

[20] A L Copley and G Stainsby. *Flow Properties of Blood*. Pergamon Press, 1960.

[21] H. Bäumler, B. Neu, E. Donath, and H. Kiesewetter. Basic phenomena of red blood cell rouleaux formation. *Biorheology*, 36(5-6):439–442, 1999.

[22] Yildirim Çinar, A Mete Şenyol, and Kamber Duman. Blood viscosity and blood pressure: role of temperature and hyperglycemia. *American journal of hypertension*, 14(5):433–438, 2001.

[23] M Brust, C Schaefer, R Doerr, L Pan, M Garcia, P E Arratia, and C Wagner. Rheology of human blood plasma: Viscoelastic versus Newtonian behavior. *Physical Review Letters*, 110(7):78305, 2013.

[24] H Steffan, W Brandstätter, G Bachler, and R Pucher. Comparison of Newtonian and Non-Newtonian Blood Flow in Stenotic Vessels using Numerical Simulation.

In Dieter W Liepsch, editor, *Biofluid Mechanics*, pages 479–485, Berlin, Heidelberg, 1990. Springer.

[25] Hannes Orelma, Ilari Filpponen, Leena-Sisko Johansson, Janne Laine, and Orlando J Rojas. Modification of cellulose films by adsorption of CMC and chitosan for controlled attachment of biomolecules. *Biomacromolecules*, 12(12):4311–4318, 2011.

[26] Sergei Zaitsev. Dynamic surface tension measurements as general approach to the analysis of animal blood plasma and serum. *Advances in colloid and interface science*, 235:201–213, 2016.

[27] S. Yu Zaitsev. Interfacial tensiometry method for the analysis of model systems in comparison with blood as the most important biological liquid. *Moscow University Chemistry Bulletin*, 71(3):205–208, 2016.

[28] B. Sobac and D. Brutin. Desiccation of a sessile drop of blood: Cracks, folds formation and delamination. *Colloids and Surfaces A: Physicochemical and Engineering Aspects*, 448(1):34–44, 2014.

[29] Yu Yu Tarasevich, I. V. Vodolazskaya, and O. P. Bondarenko. Modeling of spatial-temporal distribution of the components in the drying sessile droplet of biological fluid. *Colloids and Surfaces A: Physicochemical and Engineering Aspects*, 432:99–103, 2013.

[30] J Rosina, E Kvasnak, D Suta, H Kolarova, J Malek, and L Krajci. Temperature dependence of blood surface tension. *Physiological research*, 56:S93, 2007.

[31] Karl Landsteiner. On Agglutination Phenomena of Normal Human Blood. *Wien Klin Wochenschr*, 14, 1901.

[32] Friedrich Schwarz, Hans Peter and Dorner. Karl Landsteiner and his major contributions to haematology. *British Journal of Haematology*, 121(4):556–565, 2003.

[33] Geoff Daniels and Imelda Bromilow. *Essential Guide to Blood Groups*. Wiley Blackwell, 2014.

[34] Peter D. Issitt and David J. Anstee. *Applied Blood Group Serology*. Montgomery Scientific Publications, 1998.

[35] Yoshihito Yawata. *Cell membrane: the red blood cell as a model*. John Wiley & Sons, 2006.

[36] Theodore L Steck. The organization of proteins in the human red blood cell membrane. *Journal of cell biology*, 62:1–19, 1974.

[37] Ivan M Delves, Peter J and Roitt. The Immune system. *New England journal of medicine*, 343(1):37–49, 2000.

[38] Wim Malomgré and Birgid Neumeister. Recent and future trends in blood group typing. *Analytical and Bioanalytical Chemistry*, 393(5):1443–1451, 2009.

[39] Daniela Proverbio, E. Spada, L. Baggiani, and R. Perego. Assessment of a gel column technique for feline blood typing. *Veterinary Research Communications*, 33(SUPPL. 1):201–203, 2009.

[40] Melur K. Ramasubramanian and Stewart P. Alexander. An integrated fiberoptic-microfluidic device for agglutination detection and blood typing. *Biomedical Microdevices*, 11(1):217–229, 2009.

[41] Jun You Chen, Yi Ting Huang, Hsin Hao Chou, Cheng Po Wang, and Chien Fu Chen. Rapid and inexpensive blood typing on thermoplastic chips. *Lab on a Chip*, 15(24):4533–4541, 2015.

[42] Denise M Harmening. *Modern blood banking and transfusion practices*. FA Davis, 2018.

[43] Krishna M. Pillai. Modeling the unsaturated flow in liquid composite molding processes: A review and some thoughts. *Journal of Composite Materials*, 38(23):2097–2118, 2004.

[44] C W Rose. Water transport in soil with a daily temperature wave. *Australian Journal of Soil Research*, (1965):45–57, 1968.

[45] Musaddaq Azeem, Amal Boughattas, Jakub Wiener, and Antonin Havelka. Mechanism of liquid water transport in fabrics; a review. *Fibres and Textiles*, 24(4):58—-65, 2017.

[46] Max M. Gong and David Sinton. Turning the page: Advancing paper-based microfluidics for broad diagnostic application. *Chemical Reviews*, 117(12):8447–8480, 2017.

[47] Christopher J Biermann. *Handbook of pulping and papermaking*. Elsevier, 1996.

[48] Paul Joos. *Dynamic Surface Phenomena*. VSP, 1999.

[49] David L. Hu, Brian Chan, and John W.M. Bush. The hydrodynamics of water strider locomotion. *Nature*, 424(6949):663–666, 2003.

[50] Daniel Bonn, Jens Eggers, Joseph Indekeu, Jacques Meunier, and Etienne Rolley. Wetting and spreading. *Reviews of modern physics*, 81(2):739, 2009.

[51] Thomas Young. An essay on the cohesion of fluids. *Philosophical Transactions of the Royal Society of London*, 95:65–87, 1805.

[52] Victor M Starov and Manuel G Velarde. *Wetting and Spreading Dynamics*. CRC press, 2019.

[53] Hanyang Gu, Chi Wang, Shengjie Gong, Yong Mei, Huang Li, and Weimin Ma. Investigation on contact angle measurement methods and wettability transition of porous surfaces. *Surface and Coatings Technology*, 292:72–77, 2016.

[54] R S Hebbar, A M Isloor, and A F Ismail. Contact Angle Measurements. In Nidal Hilal, Ahmad Fauzi Ismail, Takeshi Matsuura, and Darren B T Membrane Characterization Oatley-Radcliffe, editors, *Membrane Characterization*, pages 219–255. Elsevier, 2017.

[55] David Brutin. *Droplet wetting and evaporation: from pure to complex fluids*. Academic Press, 2015.

[56] R Lucas. The time law of the capillary rise of liquids. *Kolloid-Zeitschrift*, 23(1):15–22, 1918.

[57] Edward W Washburn. The dynamics of capillary flow. *Physical Review*, 17(3):273–283, 1921.

[58] J. Soriano, A. Mercier, R. Planet, A. Hernández-Machado, M. A. Rodríguez, and J. Ortín. Anomalous roughening of viscous fluid fronts in spontaneous imbibition. *Physical Review Letters*, 95:104501, 2005.

[59] Jacob Bear. *Dynamics of fluids in porous media*. Courier Corporation, 2013.

[60] Kewen Li, Danfeng Zhang, Huiyuan Bian, Chao Meng, and Yanan Yang. Criteria for applying the Lucas-Washburn law. *Scientific Reports*, 5:14085, 2015.

[61] R. Lenormand, C. Zarcone, and A. Sarr. Mechanisms of the displacement of one fluid by another in a network of capillary ducts. *Journal of Fluid Mechanics*, 135:337–353, 1983.

[62] Tim J Senden, M A Knackstedt, and M B Lyne. Droplet penetration into porous networks: Role of pore morphology. *Nordic Pulp & Paper Research Journal*, 15(5):554–563, 2000.

[63] R. Lenormand. Liquids in porous media. *Journal of Physics: Condensed Matter*, 2, 1990.

[64] Ran Chen, Yi-Feng and Fang, Shu and Wu, Dong-Sheng and Hu. Visualizing and quantifying the crossover from capillary fingering to viscous fingering in a rough fracture. *Water Resources Research*, 53(9):7756–7772, 2017.

[65] Noosheen Walji and Brendan D. MacDonald. Influence of geometry and surrounding conditions on fluid flow in paper-based devices. *Micromachines*, 7(5):73, 2016.

[66] A M Miranda, I L Menezes-Sobrinho, and M S Couto. Spontaneous Imbibition Experiment in Newspaper Sheets. *Physical Review Letters*, 104(8):086101, 2010.

[67] Raymond Roberts, Timothy Senden, Mark Knackstedt, and M B Lyne. Spreading of aqueous liquids in unsized papers is by film flow. *Journal of pulp and paper science*, 29(4):123—-131, 2003.

[68] Eduardo N. De Azevedo, Lars R. Alme, M. Engelsberg, Jon Otto Fossum, and Paul Dommersnes. Fluid imbibition in paper fibers: Precursor front. *Physical Review E - Statistical, Nonlinear, and Soft Matter Physics*, 78(6):066317, 2008.

[69] Zhi Liu, Xiaocong He, Jiaxiu Han, Xiuhai Zhang, Fei Li, Ang Li, Zhiguo Qu, and Feng Xu. Liquid wicking behavior in paper-like materials: mathematical models and their emerging biomedical applications. *Microfluidics and Nanofluidics*, 22(11):132, 2018.

[70] Reza Masoodi and Krishna M Pillai. *Wicking in Porous Materials : Traditional and Modern Modeling Approaches*. CRC Press, 2012.

[71] Becky Lavi, Abraham Marmur, and Joerg Bachmann. Porous media characterization by the two-liquid method: Effect of dynamic contact angle and inertia. *Langmuir*, 24(5):1918–1923, 2008.

[72] C.H. Bosanquet. LV. On the flow of liquids into capillary tubes. *The London, Edinburgh, and Dublin Philosophical Magazine and Journal of Science*, 45(267):525–531, 1923.

[73] G. Martic, F. Gentner, D. Seveno, D. Coulon, J. De Coninck, and Terry D. Blake. A molecular dynamics simulation of capillary imbibition. *Langmuir*, 18(21):7971–7976, 2002.

[74] C. M. Reed and N. Wilson. Fundamentals of absorbency of fibres, textile structures and polymers. I: the rate of rise of a liquid in glass capillaries. *Journal of Physics D: Applied Physics*, 26(9):1378, 1993.

[75] B. V. Zhmud, F. Tiberg, and K. Hallstensson. Dynamics of capillary rise. *Journal of Colloid and Interface Science*, 228(2):263–269, 2000.

[76] N. Fries and M. Dreyer. An analytic solution of capillary rise restrained by gravity. *Journal of Colloid and Interface Science*, 320(1):259–263, 2008.

[77] N. Fries and M. Dreyer. Dimensionless scaling methods for capillary rise. *Journal of Colloid and Interface Science*, 338(2):514–518, 2009.

[78] T. D. Blake and J. M. Haynes. Kinetics of liquid liquid displacement. *Journal of Colloid And Interface Science*, 30(3):421–423, 1969.

[79] Yulii D. Shikhmurzaev. Moving contact lines in liquid/liquid/solid systems. *Journal of Fluid Mechanics*, 334:211–249, 1997.

[80] Benjamin J. Mullins, Roger D. Braddock, and Gerhard Kasper. Capillarity in fibrous filter media: Relationship to filter properties. *Chemical Engineering Science*, 62(22):6191–6198, 2007.

[81] RG Cox. The dynamics of the spreading of liquids on a solid surface. Part 1. Viscous flow. *Journal of fluid mechanics*, 168:169—-194, 1986.

[82] A. M. Cazabat. Wetting from macroscopic to microscopic scale. *Advances in Colloid and Interface Science*, 42:65–87, 1992.

[83] Sooyoung Chang, Jaedeok Seo, Seokbin Hong, Duck Gyu Lee, and Wonjung Kim. Dynamics of liquid imbibition through paper with intra-fibre pores. *Journal of Fluid Mechanics*, 845:36–50, 2018.

[84] W. B. Palmer. The advance of a liquid front along a glass yarn. *Journal of the Textile Institute Transactions*, 44(8-9):T391–T400, 1953.

[85] David R Schuchardti and John C Berg. Liquid transport in composite cellulose-superabsorbent fiber networks. *Wood and Fiber Science*, 23(3):342–357, 1991.

[86] John S. Lioumbas, Angelos Zamanis, and Thodoris D. Karapantsios. Towards a wicking rapid test for rejection assessment of reused fried oils: Results and analysis for extra virgin olive oil. *Journal of Food Engineering*, 119(2):260–270, 2013.

[87] Seokbin Hong and Wonjung Kim. Dynamics of water imbibition through paper channels with wax boundaries. *Microfluidics and Nanofluidics*, 19(4):845–853, 2015.

[88] Elain Fu, Stephen A. Ramsey, Peter Kauffman, Barry Lutz, and Paul Yager. Transport in two-dimensional paper networks. *Microfluidics and Nanofluidics*, 10(1):29–35, 2011.

[89] Shivani Dharmaraja, Lisa Lafleur, Samantha Byrnes, Peter Kauffman, Josh Buser, Bhushan Toley, Elain Fu, Paul Yager, and Barry Lutz. Programming paper networks for point of care diagnostics. *Microfluidics, BioMEMS, and Medical Microsystems XI*, 8615:86150X, 2013.

[90] Bhushan J. Toley, Brittney McKenzie, Tinny Liang, Joshua R. Buser, Paul Yager, and Elain Fu. Tunable-delay shunts for paper microfluidic devices. *Analytical Chemistry*, 85(23):11545–11552, 2013.

[91] Sergio Mendez, Erin M. Fenton, Gil R. Gallegos, Dimiter N. Petsev, Scott S. Sibbett, Howard A. Stone, Yi Zhang, and Gabriel P. López. Imbibition in porous membranes of complex shape: Quasi-stationary flow in thin rectangular segments. *Langmuir*, 26(2):1380–1385, 2010.

[92] Junfeng Xiao, Howard A. Stone, and Daniel Attinger. Source-like solution for radial imbibition into a homogeneous semi-infinite porous medium. *Langmuir*, 28(9):4208–4212, 2012.

[93] Emanuel Elizalde, Raúl Urteaga, and Claudio L. A. Berli. Rational design of capillary-driven flows for paper-based microfluidics. *Lab on a Chip*, 15(10):2173–2180, 2015.

[94] L. A. Richards. Capillary conduction of liquids through porous mediums. *Journal of Applied Physics*, 1(5):318–333, 1931.

[95] Henk Huinink. *Fluids in Porous Media*. Morgan & Claypool Publishers, 2016.

[96] Angel Perez-Cruz, Ion Stiharu, and Aurelio Dominguez-Gonzalez. Two-dimensional model of imbibition into paper-based networks using Richards' equation. *Microfluidics and Nanofluidics*, 21(5):98, 2017.

[97] A. Ashari, T. M. Bucher, H. Vahedi Tafreshi, M. A. Tahir, and M. S.A. A Rahman. Modeling fluid spread in thin fibrous sheets: Effects of fiber orientation. *International Journal of Heat and Mass Transfer*, 53(9-10):1750–1758, 2010.

[98] Sudhakar Jaganathan, Hooman Vahedi Tafreshi, and Behnam Pourdeyhimi. A realistic modeling of fluid infiltration in thin fibrous sheets. *Journal of Applied Physics*, 105(11):113522, 2009.

[99] R. D. Hazlett. Simulation of capillary-dominated displacements in microtomographic images of reservoir rocks. *Transport in Porous Media*, 20(1-2):21–35, 1995.

[100] A. Ashari and H. Vahedi Tafreshi. A two-scale modeling of motion-induced fluid release from thin fibrous porous media. *Chemical Engineering Science*, 64(9):2067–2075, 2009.

[101] Volker P. Schulz, Eric A. Wargo, and Emin C. Kumbur. Pore-Morphology-Based Simulation of Drainage in Porous Media Featuring a Locally Variable Contact Angle. *Transport in Porous Media*, 107(1):13–25, 2015.

[102] H.-J. Vogel, J. Tölke, V. P. Schulz, M. Krafczyk, and K. Roth. Comparison of a Lattice-Boltzmann Model, a Full-Morphology Model, and a Pore Network Model for Determining Capillary Pressure-Saturation Relationships. *Vadose Zone Journal*, 4(2):380–388, 2005.

[103] Herbert Giesche. Mercury porosimetry: A general (practical) overview. *Particle and Particle Systems Characterization*, 23(1):9–19, 2006.

[104] Dharitri Rath, N. Sathishkumar, and Bhushan J. Toley. Experimental Measurement of Parameters Governing Flow Rates and Partial Saturation in Paper-Based Microfluidic Devices. *Langmuir*, 34(30):8758–8766, 2018.

[105] L. Durlofsky and J. F. Brady. Analysis of the Brinkman equation as a model for flow in porous media. *The Physics of Fluids*, 30(11):3329–3341, 1987.

[106] Claudio Parolo, Mariana Medina-Sánchez, Alfredo De La Escosura-Muñiz, and Arben Merkoçi. Simple paper architecture modifications lead to enhanced sensitivity in nanoparticle based lateral flow immunoassays. *Lab on a Chip*, 13(3):386–390, 2013.

[107] Lourdes Rivas, Mariana Medina-Sánchez, Alfredo De La Escosura-Muñiz, and Arben Merkoçi. Improving sensitivity of gold nanoparticle-based lateral flow assays by using wax-printed pillars as delay barriers of microfluidics. *Lab on a Chip*, 14(22):4406–4414, 2014.

[108] Jane Ru Choi, Zhi Liu, Jie Hu, Ruihua Tang, Yan Gong, Shangsheng Feng, Hui Ren, Ting Wen, Hui Yang, Zhiguo Qu, Belinda Pingguan-Murphy, and Feng Xu. Polydimethylsiloxane-Paper Hybrid Lateral Flow Assay for Highly Sensitive Point-of-Care Nucleic Acid Testing. *Analytical Chemistry*, 88(12):6254–6264, 2016.

[109] V. M. Starov, S. R. Kosvintsev, V. D. Sobolev, M. G. Velarde, and S. A. Zhdanov. Spreading of liquid drops over saturated porous layers. *Journal of Colloid and Interface Science*, 246(2):372–379, 2002.

[110] Fei Jiang and Takeshi Tsuji. Changes in pore geometry and relative permeability caused by carbonate precipitation in porous media. *Physical Review E - Statistical, Nonlinear, and Soft Matter Physics*, 90(5):053306, 2014.

[111] Hu Dong and Martin J. Blunt. Pore-network extraction from micro-computerized-tomography images. *Physical Review E - Statistical, Nonlinear, and Soft Matter Physics*, 80(3):036307, 2009.

[112] Christos D. Tsakiroglou and Alkiviades C. Payatakes. Characterization of the pore structure of reservoir rocks with the aid of serial sectioning analysis, mercury porosimetry and network simulation. *Advances in Water Resources*, 23(7):773–789, 2000.

[113] Martin J. Blunt. Flow in porous media pore-network models and multiphase flow. *Current Opinion in Colloid & Interface Science*, 6:197–207, 2001.

[114] Jinfang Gao, Huilin Xing, Zhiwei Tian, and Hans Muhlhaus. Lattice Boltzmann modeling and evaluation of fluid flow in heterogeneous porous media involving multiple matrix constituents. *Computers and Geosciences*, 62:198–207, 2014.

[115] AA Mohamad. *Lattice Boltzmann Method*. Springer, 2011.

[116] Cathy J. Ridgway, Joachim Schoelkopf, G. Peter Matthews, Patrick A.C. Gane, and Philip W. James. The effects of void geometry and contact angle on the absorption of liquids into porous calcium carbonate structures. *Journal of Colloid and Interface Science*, 239(2):417–431, 2001.

[117] M. Prat. Recent advances in pore-scale models for drying of porous media. *Chemical Engineering Journal*, 86(1-2):153–164, 2002.

[118] B. Markicevic and H. K. Navaz. Primary and Secondary Infiltration of Wetting Liquid Sessile Droplet into Porous Medium. *Transport in Porous Media*, 85(3):953–974, 2010.

[119] X. Yin, H. Aslannejad, E. T. de Vries, A. Raoof, and S. M. Hassanizadeh. Droplet Imbibition into Paper Coating Layer: Pore-Network Modeling Simulation. *Transport in Porous Media*, 125(2):239–258, 2018.

[120] Vinay R. Gopala and Berend G.M. van Wachem. Volume of fluid methods for immiscible-fluid and free-surface flows. *Chemical Engineering Journal*, 141(1-3):204–221, 2008.

[121] H. Aslannejad, H. Fathi, S. M. Hassanizadeh, A. Raoof, and N. Tomozeiu. Movement of a liquid droplet within a fibrous layer: Direct pore-scale modeling and experimental observations. *Chemical Engineering Science*, 191:78–86, 2018.

[122] Ken Palakurthi, Nikhil Kumar and Konangi, Santosh and Ghia, Urmila and Comer. Micro-scale simulation of unidirectional capillary transport of wetting liquid through 3D fibrous porous media: Estimation of effective pore radii. *International Journal of Multiphase Flow*, 77:48–57, 2015.

[123] Abraham Marmur. Penetration and displacement in capillary systems of limited size. *Advances in Colloid and Interface Science*, 39:13–33, 1992.

[124] Dganit Danino and Abraham Marmur. Radial capillary penetration into paper: limited and unlimited liquid reservoirs. *Journal of Colloid and Interface Science*, 166(1):245–250, 1994.

[125] E M D'albe and M S Hidayetulla. The break-up of large water drops falling at terminal velocity in free air. *Quarterly Journal of the Royal Meteorological Society*, 81(350):610–613, 1955.

[126] T. Gillespie. The spreading of low vapor pressure liquids in paper. *Journal of Colloid Science*, 13(1):32–50, 1958.

[127] Erik Kissa. Capillary sorption in fibrous assemblies. *Journal of Colloid and Interface Science*, 83(1):265–272, 1981.

[128] A. Borhan and K. K. Rungta. On the radial spreading of liquids in thin porous substrates. *Journal of Colloid And Interface Science*, 154(1):295–297, 1992.

[129] Tokuzo Kawase, Sakiko Sekoguchi, Tomiko Fujii, and Motoi Minagawa. Spreading of Liquids in Textile Assemblies Part I: Capillary spreading of liquids. *Textile Research Journal*, 56(7):409–414, 1986.

[130] KK Borhan, Ali and Rungta. An experimental study of the radial penetration of liquids in thin porous substrates. *Journal of Colloid and Interface Science*, 158(2):403–411, 1993.

[131] Abraham Marmur. The radial capillary. *Journal of Colloid and Interface Science*, 124(1):301–308, 1988.

[132] O. Peschel, S. N. Kunz, M. A. Rothschild, and E. Mützel. Blood stain pattern analysis. *Forensic Science, Medicine, and Pathology*, 7(3):257–270, 2011.

[133] B Karger, S P Rand, and B Brinkmann. Experimental bloodstains on fabric from contact and from droplets. *International journal of legal medicine*, 111(1):17–21, 1998.

[134] Therese De Castro, Tania Nickson, Debra Carr, and Clare Knock. Interpreting the formation of bloodstains on selected apparel fabrics. *International Journal of Legal Medicine*, 127(1):251–258, 2013.

[135] Therese C. de Castro, Debra J. Carr, Michael C. Taylor, Jules A. Kieser, and Warwick Duncan. Drip bloodstain appearance on inclined apparel fabrics: Effect of prior-laundering, fibre content and fabric structure. *Forensic Science International*, 266:488–501, 2016.

[136] Jingyao Li, Xingyu Li, and Stephen Michielsen. Alternative method for determining the original drop volume of bloodstains on knit fabrics. *Forensic science international*, 263:194–203, 2016.

[137] George M. Whitesides. The origins and the future of microfluidics. *Nature*, 442(7101):368–373, 2006.

[138] Luc Gervais, Nico De Rooij, and Emmanuel Delamarche. Microfluidic chips for point-of-care immunodiagnostics. *Advanced Materials*, 23(24):H151–H176, 2011.

[139] Eric K. Sackmann, Anna L. Fulton, and David J. Beebe. The present and future role of microfluidics in biomedical research. *Nature*, 507(7491):181–189, 2014.

[140] Xiao Wang, Joshua A. Hagen, and Ian Papautsky. Paper pump for passive and programmable transport. *Biomicrofluidics*, 7(1):014107, 2013.

[141] Whui Lyn Then and Gil Garnier. Paper diagnostics in biomedicine. *Reviews in Analytical Chemistry*, 32(4):269–294, 2013.

[142] Yong He, Yan Wu, Jian Zhong Fu, and Wen Bin Wu. Fabrication of paper-based microfluidic analysis devices: a review. *RSC Advances*, 5(95):78109–78127, 2015.

[143] Elain Fu and Corey Downs. Progress in the development and integration of fluid flow control tools in paper microfluidics. *Lab on a Chip*, 17(4):614–628, 2017.

[144] Tugce Akyazi, Lourdes Basabe-Desmonts, and Fernando Benito-Lopez. Review on microfluidic paper-based analytical devices towards commercialisation. *Analytica Chimica Acta*, 1001:1–17, 2018.

[145] Mahdi Naseri, George P. Simon, and Warren Batchelor. Development of a Paper-Based Microfluidic System for a Continuous High-Flow-Rate Fluid Manipulation. *Analytical Chemistry*, 92(10):7307–7316, 2020.

[146] Ana C. Glavan, Ramses V. Martinez, E. Jane Maxwell, Anand Bala Subramaniam, Rui M.D. Nunes, Siowling Soh, and George M. Whitesides. Rapid fabrication of pressure-driven open-channel microfluidic devices in omniphobic RF paper. *Lab on a Chip*, 13(15):2922–2930, 2013.

[147] Meital Reches, Katherine A. Mirica, Rohit Dasgupta, Michael D. Dickey, Manish J. Butte, and George M. Whitesides. Thread as a Matrix for Biomedical Assays. *ACS Applied Materials and Interfaces*, 2(6):1722–1728, 2010.

[148] Xu Li, Junfei Tian, and Wei Shen. Thread as a versatile material for low-cost microfluidic diagnostics. *ACS Applied Materials and Interfaces*, 2(1):1–6, 2010.

[149] Herman Yagoda. Applications of Confined Spot Tests in Analytical Chemistry: Preliminary Paper. *Industrial and Engineering Chemistry - Analytical Edition*, 9(2):79–82, 1937.

[150] Ralph H. Müller and Doris L. Clegg. Automatic paper chromatography. *Analytical Chemistry*, 21(9):1123–1125, 1949.

[151] J. P. Comer. Semiquantitative Specific Test Paper for Glucose in Urine. *Analytical Chemistry*, 28(11):1748–1750, 1956.

[152] Marek Bialkower, Heather McLiesh, Clare A. Manderson, Rico F. Tabor, and Gil Garnier. Rapid, hand-held paper diagnostic for measuring Fibrinogen Concentration in blood. *Analytica Chimica Acta*, 1102:72–83, 2020.

[153] Brittany A. Rohrman, Veronica Leautaud, Elizabeth Molyneux, and Rebecca R. Richards-Kortum. A Lateral Flow Assay for Quantitative Detection of Amplified HIV-1 RNA. *PLoS ONE*, 7(9), 2012.

[154] S. A. Byrnes, J. D. Bishop, L. Lafleur, J. R. Buser, B. Lutz, and P. Yager. One-step purification and concentration of DNA in porous membranes for point-of-care applications. *Lab on a Chip*, 15(12):2647–2659, 2015.

[155] Katarzyna M. Koczula and Andrea Gallotta. Lateral flow assays. *Essays in Biochemistry*, 60(1):111–120, 2016.

[156] Jinghua Yu, Lei Ge, Jiadong Huang, Shoumei Wang, and Shenguang Ge. Microfluidic paper-based chemiluminescence biosensor for simultaneous determination of glucose and uric acid. *Lab on a Chip*, 11(7):1286–1291, 2011.

[157] Xu Li, Junfei Tian, and Wei Shen. Quantitative biomarker assay with microfluidic paper-based analytical devices. *Analytical and Bioanalytical Chemistry*, 396(1):495–501, 2010.

[158] Yanyan Xia, Jin Si, and Zhiyang Li. Fabrication techniques for microfluidic paper-based analytical devices and their applications for biological testing: A review. *Biosensors and Bioelectronics*, 77:774–789, 2016.

[159] Elain Fu, Barry Lutz, Peter Kauffman, and Paul Yager. Controlled reagent transport in disposable 2D paper networks. *Lab on a Chip*, 10(7):918–920, 2010.

[160] Andres W. Martinez, Scott T. Phillips, Manish J. Butte, and George M. Whitesides. Patterned Paper as a Platform for Inexpensive, Low-Volume, Portable Bioassays. *Angewandte Chemie*, 119(8):1340–1342, 2007.

[161] Rao Lu, Weiwei Shi, Lei Jiang, Jianhua Qin, and Bingcheng Lin. Rapid prototyping of paper-based microfluidics with wax for low-cost, portable bioassay. *Electrophoresis*, 30(9):1497–1500, 2009.

[162] Xu Li, Junfei Tian, Thanh Nguyen, and Wei Shen. Paper-based microfluidic devices by plasma treatment. *Analytical Chemistry*, 80(23):9131–9134, 2008.

[163] Longfei Cai, Chunxiu Xu, Shuo Hong Lin, Jiating Luo, Meidie Wu, and Fan Yang. A simple paper-based sensor fabricated by selective wet etching of silanized filter paper using a paper mask. *Biomicrofluidics*, 8(5):056504, 2014.

[164] Barry Lutz, Tinny Liang, Elain Fu, Sujatha Ramachandran, Peter Kauffman, and Paul Yager. Dissolvable fluidic time delays for programming multi-step assays in instrument-free paper diagnostics. *Lab on a Chip*, 13(14):2840–2847, 2013.

[165] Jared Houghtaling, Tinny Liang, Gregory Thiessen, and Elain Fu. Dissolvable bridges for manipulating fluid volumes in paper networks. *Analytical Chemistry*, 85(23):11201–11204, 2013.

[166] Ruihua Tang, Hui Yang, Yan Gong, Zhi Liu, Xiu Jun Li, Ting Wen, Zhi Guo Qu, Sufeng Zhang, Qibing Mei, and Feng Xu. Improved Analytical Sensitivity of Lateral Flow Assay using Sponge for HBV Nucleic Acid Detection. *Scientific Reports*, 7(1):1–10, 2017.

[167] Welcome To Haemokinesis. Available at: www.haemokinesis.com [Accessed 22 July 2020].

[168] Andres W. Martinez, Scott T. Phillips, and George M. Whitesides. Three-dimensional microfluidic devices fabricated in layered paper and tape. *Proceedings of the National Academy of Sciences of the United States of America*, 105(50):19606–19611, 2008.

[169] Hong Liu and Richard M. Crooks. Three-dimensional paper microfluidic devices assembled using the principles of origami. *Journal of the American Chemical Society*, 133(44):17564–17566, 2011.

[170] A. V. Govindarajan, S. Ramachandran, G. D. Vigil, P. Yager, and K. F. Böhringer. A low cost point-of-care viscous sample preparation device for molecular diagnosis in the developing world; An example of microfluidic origami. *Lab on a Chip*, 12(1):174–181, 2012.

[171] Deidre Sechi, Brady Greer, Jesse Johnson, and Nastaran Hashemi. Three-dimensional paper-based microfluidic device for assays of protein and glucose in urine. *Analytical Chemistry*, 85(22):10733–10737, 2013.

[172] Xiao Li and Xinyu Liu. Fabrication of three-dimensional microfluidic channels in a single layer of cellulose paper. *Microfluidics and Nanofluidics*, 16(5):819–827, 2014.

[173] Christophe Renault, Jessica Koehne, Antonio J. Ricco, and Richard M. Crooks. Three-dimensional wax patterning of paper fluidic devices. *Langmuir*, 30(23):7030–7036, 2014.

[174] Seong Geun Jeong, Sang Ho Lee, Chang Hyung Choi, Jiyun Kim, and Chang Soo Lee. Toward instrument-free digital measurements: A three-dimensional microfluidic device fabricated in a single sheet of paper by double-sided printing and lamination. *Lab on a Chip*, 15(4):1188–1194, 2015.

[175] Andres W. Martinez, Scott T. Phillips, Zhihong Nie, Chao Min Cheng, Emanuel Carrilho, Benjamin J. Wiley, and George M. Whitesides. Programmable diagnostic devices made from paper and tape. *Lab on a Chip*, 10(19):2499–2504, 2010.

[176] Hong Liu, Xiang Li, and Richard M. Crooks. Paper-based SlipPAD for high-throughput chemical sensing. *Analytical Chemistry*, 85(9):4263–4267, 2013.

[177] Kwi Nam Han, Jong Soon Choi, and Joseph Kwon. Three-dimensional paper-based slip device for one-step point-of-care testing. *Scientific Reports*, 6(1):1–7, 2016.

[178] ChenLg Guo Li, Hyou Arm Joung, Hyungrye Noh, Mun Bum Song, Min Gon Kim, and Hyungil Jung. One-touch-activated blood multidiagnostic system using a minimally invasive hollow microneedle integrated with a paper-based sensor. *Lab on a Chip*, 15(16):3286–3292, 2015.

[179] Mohidus Samad Khan, George Thouas, Wei Shen, Gordon Whyte, and Gil Garnier. Paper diagnostic for instantaneous blood typing. *Analytical chemistry*, 82(10):4158–4164, 2010.

[180] Mohammad Al-Tamimi, Wei Shen, Rania Zeineddine, Huy Tran, and Gil Garnier. Validation of paper-based assay for rapid blood typing. *Analytical Chemistry*, 84(3):1661–1668, 2012.

[181] Purim Jarujamrus, Junfei Tian, Xu Li, Atitaya Siripinyanond, Juwadee Shiowatana, and Wei Shen. Mechanisms of red blood cells agglutination in antibody-treated paper. *Analyst*, 137(9):2205–2210, 2012.

[182] Temsiri Songjaroen and Wanida Laiwattanapaisal. Simultaneous forward and reverse ABO blood group typing using a paper-based device and barcode-like interpretation. *Analytica Chimica Acta*, 921:67–76, 2016.

[183] Natasha Yeow, Heather McLiesh, Liyun Guan, Wei Shen, and Gil Garnier. Paper-based assay for red blood cell antigen typing by the indirect antiglobulin test. *Analytical and Bioanalytical Chemistry*, 408(19):5231–5238, 2016.

[184] W L Then, Miaosi Li, Heather McLiesh, Wei Shen, and Gil Garnier. The detection of blood group phenotypes using paper diagnostics. *Vox Sanguinis*, 108(2):186–196, 2015.

[185] Jasmina Casals-Terré, Josep Farré-Lladós, Joan A. López, Teresa Vidal, and Maria Blanca Roncero. Enhanced fully cellulose based forward and reverse blood typing assay. *Journal of Biomedical Materials Research - Part B Applied Biomaterials*, 108(2):439–450, 2020.

[186] A. Caesar, S. Meyer, N. Trost, K. Neuenschwander, C. Geisen, B. M. Frey, C. Gassner, and P. Schwind. A uniform method for the simultaneous blood group phenotyping of Fya, Fyb, Jka, Jkb, S, $\bar{s}$, P1, k applying lateral-flow technique. *Vox Sanguinis*, 113(2):177–184, 2018.

[187] Natasha Yeow, Heather McLiesh, and Gil Garnier. Indirect antiglobulin paper test for red blood cell antigen typing by flow-through method. *Analytical Methods*, 7(11):4645–4649, 2015.

[188] Miaosi Li, Junfei Tian, Mohammad Al-Tamimi, and Wei Shen. Paper-based blood typing device that reports patient's blood type "in writing". *Angewandte Chemie - International Edition*, 51(22):5497–5501, 2012.

[189] Temsiri Songjaroen, Vitsarut Primpray, Thawintra Manosarn, Witsanuwat Khumchanta, Tasanee Sakuldamrongpanich, Suntree Kulkeratiyut, and Wanida Laiwattanapaisal. A simple and low-cost portable paper-based ABO blood typing device for point-of-care testing. *Journal of Immunoassay and Immunochemistry*, 39(3):292–307, 2018.

[190] Kuniaki Anachi, Eiki and Dimitrov, Antony S and Nagayama. Stripe Patterns Formed on a Glass Surface during Droplet Evaporation. *Langmuir*, 11(4):1057–1060, 1995.

[191] Robert D Deegan, Olgica Bakajin, Todd F Dupont, Greb Huber, Sidney R Nagel, and Thomas A Witten. Capillary flow as the cause of ring stains from dried liquid drops. *Nature*, 389(6653):827–829, 1997.

[192] Ruoyang Chen, Liyuan Zhang, Duyang Zang, and Wei Shen. Wetting and Drying of Colloidal Droplets: Physics and Pattern Formation. *Advances in Colloid Science*, pages 3–25, 2016.

[193] Dileep Mampallil and Huseyin Burak Eral. A review on suppression and utilization of the coffee-ring effect. *Advances in Colloid and Interface Science*, 252:38–54, 2018.

[194] Duyang Zang, Sujata Tarafdar, Yuri Yu Tarasevich, Moutushi Dutta Choudhury, and Tapati Dutta. Evaporation of a Droplet: From physics to applications. *Physics Reports*, 804:1–56, 2019.

[195] Anne-marie Cazabat and Geoffroy Gu. Evaporation of macroscopic sessile droplets. *Soft Matter*, 6(12):2591–2612, 2010.

[196] H Yildirim Erbil. Evaporation of pure liquid sessile and spherical suspended drops : A review. *Advances in Colloid and Interface Science*, 170(1-2):67–86, 2012.

[197] D Starov, V and Brutin. Recent advances in droplet wetting and evaporation. *Chemical Society Reviews*, 47(2):558–585, 2018.

[198] Maryam Parsa, Souad Harmand, and Khellil Se. Mechanisms of pattern formation from dried sessile drops. *Advances in Colloid and Interface Science*, 254:22–47, 2018.

[199] N M Kovalchuk, A Trybala, and V M Starov. Evaporation of sessile droplets. *Current Opinion in Colloid & Interface Science*, 19(4):336–342, 2014.

[200] Ronald G Larson. Transport and deposition patterns in drying sessile droplets. *AIChE Journal*, 60(5):1538–1571, 2014.

[201] F. Giorgiutti-Dauphiné and L. Pauchard. Drying drops: Drying drops containing solutes: From hydrodynamical to mechanical instabilities. *European Physical Journal E*, 41(3):1–5, 2018.

[202] R G Picknett and R Bexon. The evaporation of sessile or pendant drops in still air. *Journal of Colloid and Interface Science*, 61(2):336–350, 1977.

[203] K S Birdi and D T Vu. Wettability and the evaporation rates of fluids from solid surfaces. *Journal of Adhesion Science and Technology*, 7(6):485–493, 2012.

[204] H Yildirim Erbil, G Mchale, and M I Newton. Drop Evaporation on Solid Surfaces : Constant Contact Angle Mode. *Langmuir*, 18(7):2636–2641, 2002.

[205] Tzyy-Shyang Lin, Yi-Hong Zeng, Ruey-Yug Tsay, and Shi-Yow Lin. Roughness-induced strong pinning for drops evaporating from polymeric surfaces. *Journal of the Taiwan Institute of Chemical Engineers*, 62:54–59, 2016.

[206] Alexander F Routh. Drying of thin colloidal films. *Reports on Progress in Physics*, 76(4):46603, 2013.

[207] Xuehua Zhang. Mixed mode of dissolving immersed nanodroplets at a solid–water interface. *Soft Matter*, 11(10):1889–1900, 2015.

[208] J. Ross Moffat, Khellil Sefiane, and Martin E.R. Shanahan. Effect of TiO2 nanoparticles on contact line stick-slip behavior of volatile drops. *Journal of Physical Chemistry B*, 113(26):8860–8866, 2009.

[209] HengAn Wang, FengChao and Wu. Molecular origin of contact line stick-slip motion during droplet evaporation. *Scientific reports*, 5:17521, 2015.

[210] Yuri O Popov and S Ellis Ave. Evaporative Deposition Patterns Revisited : Spatial Dimensions of the Deposit. *Physical Review E*, 71(3):036313, 2005.

[211] Hua Hu and Ronald G Larson. Evaporation of a Sessile Droplet on a Substrate. *The Journal of Physical Chemistry B*, 106(6):1334–1344, 2002.

[212] S F Chini and A Amirfazli. Resolving an ostensible inconsistency in calculating the evaporation rate of sessile drops. *Advances in Colloid and Interface Science*, 243:121–128, 2017.

[213] Robert D. Deegan, Olgica Bakajin, Todd F. Dupont, Greg Huber, Sidney R. Nagel, and Thomas A. Witten. Contact line deposits in an evaporating drop. *Physical Review E*, 62(1):756, 2000.

[214] Benjamin J. Fischer. Particle convection in an evaporating colloidal droplet. *Langmuir*, 18(1):60–67, 2002.

[215] Adam D Eales, Alexander F Routh, Nick Dartnell, and Simon Goddard. Evaporation of pinned droplets containing polymer – an examination of the important groups controlling final shape. *AIChE Journal*, 61(5):1759–1767, 2015.

[216] Søren Kiil. Drying of latex films and coatings: Reconsidering the fundamental mechanisms. *Progress in Organic Coatings*, 57(3):236–250, 2006.

[217] V. D. Ta, R. M. Carter, E. Esenturk, C. Connaughton, T. J. Wasley, J. Li, R. W. Kay, J. Stringer, P. J. Smith, and J. D. Shephard. Dynamically controlled deposition of colloidal nanoparticle suspension in evaporating drops using laser radiation. *Soft Matter*, 12(20):4530–4536, 2016.

[218] Hua Hu and Ronald G Larson. Marangoni effect reverses coffee-ring depositions. *The Journal of Physical Chemistry B*, 110(14):7090–7094, 2006.

[219] Hua Hu and Ronald G. Larson. Analysis of the effects of marangoni stresses on the microflow in an evaporating sessile droplet. *Langmuir*, 21(9):3972–3980, 2005.

[220] Hua Hu and Ronald G. Larson. Analysis of the microfluid flow in an evaporating sessile droplet. *Langmuir*, 21(9):3963–3971, 2005.

[221] Tim Still, Peter J. Yunker, and Arjun G. Yodh. Surfactant-induced Marangoni eddies alter the coffee-rings of evaporating colloidal drops. *Langmuir*, 28(11):4984–4988, 2012.

[222] Wouter Sempels, Raf De Dier, Hideaki Mizuno, Johan Hofkens, and Jan Vermant. Auto-production of biosurfactants reverses the coffee ring effect in a bacterial system. *Nature Communications*, 4:1–8, 2013.

[223] Jung Hoon Kim, Sang Byung Park, Jae Hyun Kim, and Wang Cheol Zin. Polymer transports inside evaporating water droplets at various substrate temperatures. *Journal of Physical Chemistry C*, 115(31):15375–15383, 2011.

[224] Mainak Majumder, Clint S. Rendall, J. Alexander Eukel, James Y.L. Wang, Natnael Behabtu, Cary L. Pint, Tzu Yu Liu, Alvin W. Orbaek, Francesca Mirri, Jaewook Nam, Andrew R. Barron, Robert H. Hauge, Howard K. Schmidt, and Matteo Pasquali. Overcoming the "coffee-stain" effect by compositional marangoni-flow-assisted drop-drying. *Journal of Physical Chemistry B*, 116(22):6536–6542, 2012.

[225] Alexander F. Routh and William B. Russel. Horizontal drying fronts during solvent evaporation from latex films. *AIChE Journal*, 44(9):2088–2098, 1998.

[226] Lucas Goehring, William J. Clegg, and Alexander F. Routh. Solidification and ordering during directional drying of a colloidal dispersion. *Langmuir*, 26(12):9269–9275, 2010.

[227] Irvin M. Krieger and Thomas J. Dougherty. A mechanism for non-Newtonian flow in suspensions of rigid spheres. *Transactions of the Society of Rheology*, 3(1):137–152, 1959.

[228] Yongjian Zhang, Yimeng Qian, Zhengtang Liu, Zhiguang Li, and Duyang Zang. Surface wrinkling and cracking dynamics in the drying of colloidal droplets. *European Physical Journal E*, 37(9):84, 2014.

[229] Peter J Yunker, Tim Still, Matthew A Lohr, and A G Yodh. Suppression of the coffee-ring effect by shape-dependent capillary interactions. *Nature*, 476(7360):308–311, 2011.

[230] Vladimir S. Ajaev. Spreading of thin volatile liquid droplets on uniformly heated surfaces. *Journal of Fluid Mechanics*, 7(2):279–296, 2005.

[231] Adam D Eales and Alexander F Routh. Elimination of coffee-ring formation by humidity cycling: a numerical study. *Langmuir*, 32(2):505–511, 2016.

[232] Kin'ya Ozawa, Eisuke Nishitani, and Masao Doi. Modeling of the drying process of liquid droplet to form thin film. *Japanese Journal of Applied Physics*, 44(6 A):4229–4234, 2005.

[233] Yuri Yu Tarasevich, Irina V. Vodolazskaya, and Olga P. Isakova. Desiccating colloidal sessile drop: Dynamics of shape and concentration. *Colloid and Polymer Science*, 289(9):1015–1023, 2011.

[234] I. V. Vodolazskaya and Yu Yu Tarasevich. The model of drying sessile drop of colloidal solution. *Modern Physics Letters B*, 25(15):1303–1310, 2011.

[235] W. B. Zimmerman, J. M. Rees, and B. N. Hewakandamby. Numerical analysis of solutocapillary Marangoni-induced interfacial waves. *Advances in Colloid and Interface Science*, 134:346–359, 2007.

[236] V. Ya Shur, D. A. Bykov, E. A. Mingaliev, A. E. Tyurnina, G. V. Burban, R. M. Kadushnikov, and V. V. Mizgulin. Coffee ring effect during drying of colloid drop: Experiment and computer simulation. *Ferroelectrics*, 476(1):47–53, 2015.

[237] Patrice Bacchin, David Brutin, Anne Davaille, Erika Di Giuseppe, Xiao Dong Chen, Ioannis Gergianakis, Frédérique Giorgiutti-Dauphiné, Lucas Goehring, Yannick Hallez, Rodolphe Heyd, Romain Jeantet, Cécile Le Floch-Fouéré, Martine Meireles, Eric Mittelstaedt, Céline Nicloux, Ludovic Pauchard, and Marie Louise Saboungi. Drying colloidal systems: Laboratory models for a wide range of applications. *European Physical Journal E*, 41(8):94, 2018.

[238] Alexander F. Routh and William B. Zimmerman. Distribution of particles during solvent evaporation from films. *Chemical Engineering Science*, 59(14):2961–2968, 2004.

[239] Shunto Arai and Masao Doi. Anomalous drying dynamics of a polymer solution on a substrate. *European Physical Journal E*, 36(6), 2013.

[240] Jian Lin Liu and Xi Qiao Feng. On elastocapillarity: A review. *Acta Mechanica Sinica/Lixue Xuebao*, 28(4):928–940, 2012.

[241] E. Lintingre, F. Lequeux, L. Talini, and N. Tsapis. Control of particle morphology in the spray drying of colloidal suspensions. *Soft Matter*, 12(36):7435–7444, 2016.

[242] L. Pauchard and Y. Couder. Invagination during the collapse of an inhomogeneous spheroidal shell. *Europhysics Letters*, 66(5):667–673, 2004.

[243] Ludovic Pauchard and Catherine Allain. Mechanical instability induced by complex liquid desiccation. *Comptes Rendus Physique*, 4(2):231–239, 2003.

[244] Fanlong Meng, Masao Doi, and Zhongcan Ouyang. Cavitation in drying droplets of soft matter solutions. *Physical Review Letters*, 113(9):098301, 2014.

[245] Céline Sadek, Hervé Tabuteau, Pierre Schuck, Yannick Fallourd, Nicolas Pradeau, Cécile Le Floch-Fouéré, and Romain Jeantet. Shape, shell, and vacuole formation during the drying of a single concentrated whey protein droplet. *Langmuir*, 29(50):15606–15613, 2013.

[246] Lucas Goehring. *Desiccation cracks and their patterns : formation and modelling in science and nature*. Statistical physics of fracture and breakdown. John Wiley & Sons, first edit edition, 2015.

[247] Ram Weinberger. Initiation and growth of cracks during desiccation of stratified muddy sediments. *Journal of Structural Geology*, 21(4):379–386, 1999.

[248] E. R. Dufresne, E. I. Corwin, N. A. Greenblatt, J. Ashmore, D. Y. Wang, A. D. Dinsmore, J. X. Cheng, X. S. Xie, J. W. Hutchinson, and D. A. Weitz. Flow and fracture in drying nanoparticle suspensions. *Physical Review Letters*, 91(22):224501, 2003.

[249] R. C. Chiu, T. J. Garino, and M. J. Cima. Drying of Granular Ceramic Films: I, Effect of Processing Variables on Cracking Behavior. *Journal of the American Ceramic Society*, 76(9):2257–2264, 1993.

[250] H. Lei, L. F. Francis, W. W. Gerberich, and L. E. Scriven. Stress development in drying coatings after solidification. *AIChE Journal*, 48(3):437–451, 2002.

[251] C. Allain and L. Limat. Regular patterns of cracks formed by directional drying of a collodial suspension. *Physical Review Letters*, 74(15):2981–2984, 1995.

[252] Karnail B. Singh and Mahesh S. Tirumkudulu. Cracking in drying colloidal films. *Physical Review Letters*, 98(21):218302, 2007.

[253] Wai Peng Lee and Alexander F Routh. Why Do Drying Films Crack. *Langmuir*, 20(23):9885–9888, 2004.

[254] Ludovic Pauchard, Bérengère Abou, and Ken Sekimoto. Influence of mechanical properties of nanoparticles on macrocrack formation. *Langmuir*, 25(12):6672–6677, 2009.

[255] Mahesh S. Tirumkudulu and William B. Russel. Cracking in drying latex films. *Langmuir*, 21(11):4938–4948, 2005.

[256] Rong Cao, Zhirong Pan, Hua Tang, Jing Wu, Junfei Tian, Azadeh Nilghaz, and Miaosi Li. Understanding the coffee-ring effect of red blood cells for engineering paper-based blood analysis devices. *Chemical Engineering Journal*, 391:123522, 2020.

[257] Azadeh Nilghaz, Liyuan Zhang, and Wei Shen. Coffee stains on paper. *Chemical Engineering Science*, 129:34–41, 2015.

[258] Yurii Yu Tarasevich. Mechanisms and models of the dehydration self-organization in biological fluids. *Physics-Uspekhi*, 47(7):717–728, 2004.

[259] Tatyana V. Kulyabina, Roman A. Drajevsky, Vyacheslav I. Kochubey, and Dmitry A. Zimnyakov. Coherent optical analysis of crystal- like patterns induced by human blood plasma desiccation. *Saratov Fall Meeting 2000: Coherent Optics of Ordered and Random Media*, 4242:282–285, 2001.

[260] E. Rapis. A change in the physical state of a nonequilibrium blood plasma protein film in patients with carcinoma. *Technical Physics*, 47(4):510–512, 2002.

[261] Leila Bahmani, Mahdi Neysari, and Maniya Maleki. The study of drying and pattern formation of whole human blood drops and the effect of thalassaemia and neonatal jaundice on the patterns. *Colloids and Surfaces A: Physicochemical and Engineering Aspects*, 513:66–75, 2017.

[262] Tatiana A. Yakhno, Vladimir G. Yakhno, Anatoly G. Sanin, Olga A. Sanina, Artem S. Pelyushenko, Natalia A. Egorova, Igor G. Terentiev, Svetlana V. Smetanina, Olga V. Korochkina, and Elena V. Yashukova. The informative-capacity phenomenon of drying drops. *IEEE Engineering in Medicine and Biology Magazine*, 24(2):96–104, 2005.

[263] Frank Ramsthaler, J. Schlote, C. Wagner, J. Fiscina, and M. Kettner. The ring phenomenon of diluted blood droplets. *International Journal of Legal Medicine*, 130(3):731–736, 2016.

[264] Stéphanie Devineau, Manos Anyfantakis, Laurent Marichal, Laurent Kiger, Mathieu Morel, Sergii Rudiuk, and Damien Baigl. Protein Adsorption and Reorganization on Nanoparticles Probed by the Coffee-Ring Effect: Application to Single Point Mutation Detection. *Journal of the American Chemical Society*, 138(36):11623–11632, 2016.

[265] Yu Yu Tarasevich and A. K. Ayupova. Effect of diffusion on the separation of components in a biological fluid upon wedge-shaped dehydration. *Technical Physics*, 48(5):535–540, 2003.

[266] S. N. Shatokhina, V. N. Shabalin, M. E. Buzoverya, and V. T. Punin. Bio-liquid morphological analysis. *TheScientificWorldJournal*, 4:657–661, 2004.

[267] L. Pauchard, F. Parisse, and C. Allain. Influence of salt content on crack patterns formed through colloidal suspension desiccation. *Physical Review E - Statistical Physics, Plasmas, Fluids, and Related Interdisciplinary Topics*, 59(3):3737–3740, 1999.

[268] T. A. Yakhno, V. G. Yakhno, A. G. Sanin, O. A. Sanina, and A. S. Pelyushenko. Protein and salt: Spatiotemporal dynamics of events in a drying drop. *Technical Physics*, 49(8):1055–1063, 2004.

[269] Guofang Chen and Gideon J. Mohamed. Complex protein patterns formation via salt-induced self-assembly and droplet evaporation. *European Physical Journal E*, 33(1):19–26, 2010.

[270] T. A. Yakhno, V. V. Kazakov, O. A. Sanina, A. G. Sanin, and V. G. Yakhno. Drops of biological fluids drying on a hard substrate: Variation of the morphology, weight, temperature, and mechanical properties. *Technical Physics*, 55(7):929–935, 2010.

[271] M. E. Buzoverya, Yu P. Shcherbak, and I. V. Shishpor. Experimental investigation of the serum albumin fascia microstructure. *Technical Physics*, 57(9):1270–1276, 2012.

[272] Tatiana Yakhno. Salt-induced protein phase transitions in drying drops. *Journal of Colloid and Interface Science*, 318(2):225–230, 2008.

[273] W. Bou Zeid and D. Brutin. Influence of relative humidity on spreading, pattern formation and adhesion of a drying drop of whole blood. *Colloids and Surfaces A: Physicochemical and Engineering Aspects*, 430:1–7, 2013.

[274] Viral H. Chhasatia, Abhijit S. Joshi, and Ying Sun. Effect of relative humidity on contact angle and particle deposition morphology of an evaporating colloidal drop. *Applied Physics Letters*, 97:231909, 2010.

[275] W. Bou Zeid, J. Vicente, and D. Brutin. Influence of evaporation rate on cracks' formation of a drying drop of whole blood. *Colloids and Surfaces A: Physicochemical and Engineering Aspects*, 432:139–146, 2013.

[276] Z. Néda, K. T. Leung, L. Józsa, and M. Ravasz. Spiral cracks in drying precipitates. *Physical Review Letters*, 88(9):95502, 2002.

Chapter 3

High Throughput Blood Typing

Preface

In this chapter, a new and scalable paper-based blood group test is introduced based on the radial wicking of a droplet. The stain growth rate and final size are analysed to determine the presence or absence of agglutination after combination with different antibodies. This test introduces stain analysis as a simple and informative measure of fluid properties. This technique shows high reproducibility and sensitivity for forward blood group testing and for reverse testing is also demonstrated. This chapter contains a submitted manuscript and an appendix section where the concept developed for reverse testing is used with functionalised red blood cells to detect COVID-19 antibodies in patient plasma.

A rapid paper-based blood typing method from droplet wicking

Michael J. Hertaeg, Rico F. Tabor, Heather Mcliesh, Gil Garnier

Submitted: ACS Sensors

Keywords: Blood typing, antibody, rapid, paper, kinetic test, stain, drop wicking

Abstract

Paper-based diagnostics are leading the field of low-cost, point of care diagnostics. However, large scale testing facilities such as hospitals are still primarily using the gel column agglutination technique. This is because paper-based systems are single use tests that are generally more time consuming and less automatable than traditional methods. Here, we present a novel, rapid and scalable, paper-based blood typing method that can produce test results in under 10 seconds. We believe this is the fastest blood typing test. The test consists of placing a drop of antibody solution on paper, followed by a drop of blood on the same locus, and measuring the evolution of blood stain area as a function of time. Positive reactions for both forward and reverse tests have significantly slower growth rates and smaller final stain sizes when compared to negatives. We analyse the effect paper type, red blood cell concentration, antibody specificity (A, B and D) and antibody concentration have on the diagnostic sensitivity and reproducibility. A high sensitivity is found in papers with a low density and thickness. The optimum red blood cell concentration is determined from a balance between wicking rate, strength of reaction and optical contrast. A and B antibodies give more sensitive results than D; however, the D antigen can still be successfully identified. This technique has the potential to significantly cut down the time and cost (both initial and ongoing) of blood typing tests and enable design of a new high throughput and fully automatable system.

3.1 Introduction

Blood transfusion is a common medical procedure required in the treatment of major haemorrhages, cancer and complications during birth. Before each transfusion, blood typing or grouping is performed to ensure the donor's blood is compatible with the patient. Of the many blood types, the most clinically relevant are A, B and D [1]. These types correspond to the presence of specific antigens that exist on the red blood cell membrane. The O blood type is simply the absence of A or B antigens. Blood also contains antibodies in the plasma phase. Exposing red blood cells (RBC) to any specific antibody leads to a series of events. First, the antibody adsorbs onto its specific antigen, located on the membrane of the RBC. Second, should the antibody be an Immunoglobulin M (IgM), RBC agglutination directly proceeds. IgM antibodies are large star shape pentamer immunoglobulins, commonly used for A, B and D typing [1]. They are able to bind multiple RBCs into agglutinates by overcoming the cell-cell electrostatic repulsion; this is because the radius of IgM antibodies is higher than the Debye length of a red cell [2, 3].

Hundreds of typing tests are required every day in medical centres. These are usually performed in large scale laboratories using automated processes. A large range of techniques can be used, including spin-tube [1], microplate [4], flow cytometry [1], gel column [5], microfluidic methods [6, 7] and many more [8]. Despite significant advances, this step remains an expensive and time-consuming process.

Most typing methods are based on the detection of specific antibody-antigen reactions. Diagnostics operate by detecting and reporting this agglutination (positive) or this lack of agglutination (negative) using various principles. Many tests detect RBC agglutination by measuring the corresponding change in rheological properties. However, most tests take between 5 and 10 minutes to complete and require sensitive and expensive equipment such as a centrifuge or pump that makes the remote application of these tests impractical. This limitation has created interest in paper-based methods that can be done in remote locations and with minimum training and equipment. Paper-based diagnostics take advantage of passive flows that occur spontaneously when a wetting fluid comes into contact with a porous material. This process has been studied in detail for simple fluids and has been applied to biodiagnostics in a variety of ways [9–14].

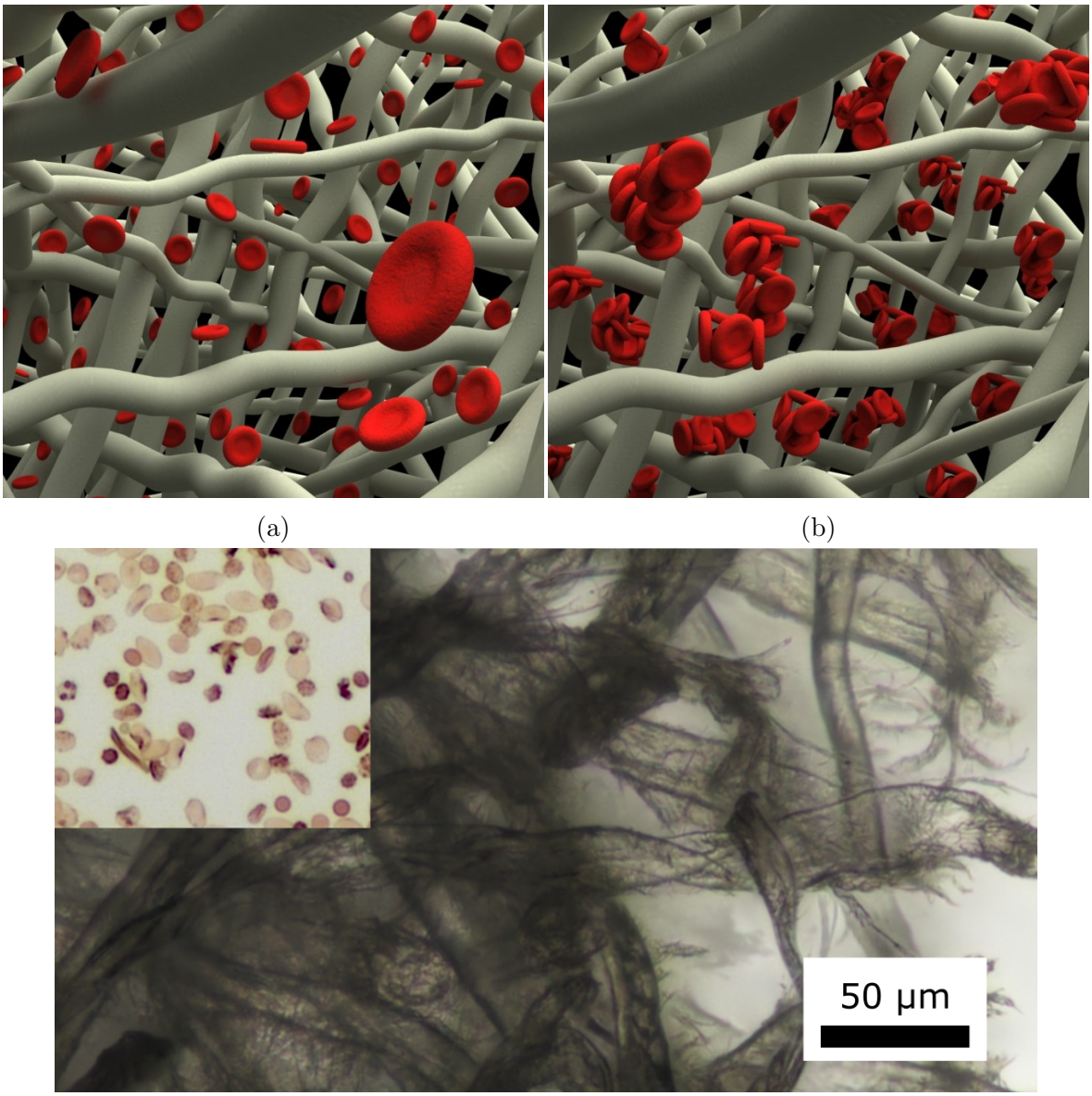

(a) (b)

(c)

Figure 3.1: Schematic representation of the mechanism behind the kinetic wicking blood typing. RBCs flowing through paper when (a) individualised (high mobility) and (b) agglutinated (low mobility). (c) image of the torn edge of Whatman 41 filter paper, inset shows human RBCs at the same magnification.

Different paper-based blood typing methods have been developed. Most involve spotting a droplet of blood onto paper previously soaked in an antibody solution. The area is then flushed with saline, whether by direct application [15–19] or with an elution bath [3, 20–23]. The saline in this system serves as a carrier fluid that transports RBCs away from the initial stain. If the cells are agglutinated, there is significant resistance to this transport. This mechanism is illustrated in Figure 3.1 where individualised and

agglutinated RBCs are sketched in a paper fibre matrix. An image of filter paper fibers showing the relative size of human red cells is represented in Figure 3.1c. Agglutination occurs due to reaction with both antibodies free in the bulk solution and adsorbed onto the paper fibres [17]. This causes the difference between a positive and negative reaction to be easily seen by eye. This style of test is useful for low-cost point of care diagnostics as they give clear and robust results. However, current paper diagnostics are all multi step processes that are difficult to automate and are therefore, not practical for high volume applications. Khan et al. [2] developed a method where a blood droplet was deposited onto a strip of paper soaked in antibody solution. The final wicked length was shorter after a positive antigen-antibody reaction had occurred. Although this result is not as clearly seen by eye as other paper-based methods, this demonstrates that a washing step is not required to produce accurate results. These observations also suggest that the kinetics of the wicking process can be insightful.

In this study, we aim to quantify the kinetics of antibody-RBC stain formation for blood typing diagnostics. Previous studies have solely focused on the final appearance of stains and ignored the kinetics and mechanism of stain growth from 2 sequential droplets on paper. We develop a new but simple, two drop methodology and analyse the stain growth kinetics. We raise the hypothesis that the wicking kinetics can provide a clear and reproducible difference between positive and negative RBC-antibody reactions after a short wicking time. We hope this difference can be used to engineer a robust blood typing diagnostic device, where the size of the stain seconds after blood deposition is indicative of test results. Such a concept could lead to an automatable and scalable diagnostic that would be significantly faster than any current method. This methodology also has the potential to be generalised to the detection of any IgM antibody-antigen reaction. This study investigates the effects paper type, RBC concentration, forward/reverse tests, antibody specificity, antibody concentration and drop size have on the kinetics of antibody-RBC stain size for positive and negative systems.

3.2 Methods

To perform tests, a pipette was used to manually deposit a droplet of antibody solution onto a paper surface suspended horizontally. After a 10 second delay a droplet of RBC solution is deposited in the center of the antibody stain. A timer was used to keep delay consistent. The evolution of the blood stain size as a function of time was captured by a bottom mounted Point Grey Flea3 camera shooting at 120 frames per second. A

shortpass filter with a 600 nm cutoff wavelength filter was purchased from Thorlabs and was held in the optical path to selectively image the growth of blood rather than that of the antibody solution. The area of the stain in each image was determined with an ImageJ macro script. This involved determining a threshold intensity to binarise the image. The intensity was determined manually for each set of experiments. However, the intensity was kept constant between positive and negative samples on the same paper and at the same concentration. The fill holes and analyze particles tools were then used to identify the area of the largest individual object in the image. The scale of the image was determined by placing a ruler in the same focal plane as the imaged paper and measuring the mm/pixel ratio.

A schematic of the test methodology is shown in Figure 3.2. RBC solutions are made with whole blood provided by the Red Cross Australia with EDTA anticoagulant. RBCs were washed 3 times by centrifugation, removing the supernatant and then re-suspending in phosphate buffered saline (PBS). The pellet left after centrifugation was assumed to be 100 vol% cells. This was combined with more PBS to the required concentration. PBS solutions were used instead of whole blood as protein content was shown to influence wicking in paper [24, 25]. Antibody solutions used in tests were monoclonal grouping reagents; B and D solutions were purchased from Immulab, where A was purchased from Sequris. Tests were completed on two types of

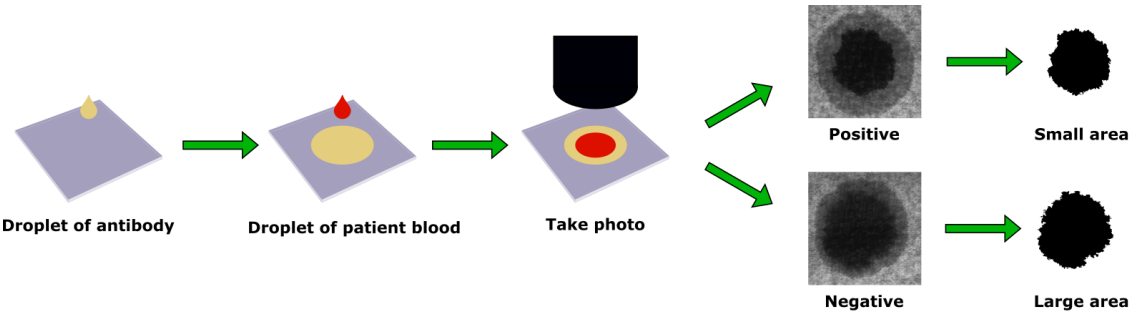

Figure 3.2: Methodology for stain monitoring. 1) - A droplet of antibody is placed on paper. 2) - A droplet of patient RBC is placed at the same location after a specified time. 3) - Camera records stain growth dynamics.

paper; Whatman 41 filter paper and Kimberly Clark Scott hand towel (4419). Each paper was tested with A and B antibodies using cell solutions at 45%, 30% and 15% concentrations by volume. For A and B tests (Figure 3.3 and 3.4); red blood cells from six donors, (3 of type A and 3 of type B) were washed in PBS and tested.

Tests with D antibodies were performed only on paper towel and at 45% concentration (Figure 3.5). This test used blood from 6 donors (3 of D positive, 3 of D negative) and were prepared in the same manner as the tests describes with A and B antibodies.

Reverse group tests were performed using patient plasma in the place of an antibody solution. This was prepared by collecting the supernatant (plasma) after the first centrifuge of the blood washing process. RBC solutions were prepared in the same way as other tests. 6 samples of blood where used (three of type A and three of type B). Each RBC solution was tested twice, once with a sample of A type plasma and once with B, giving 12 measurements in total (Figure 3.7).

Most forward group tests were completed with 10 µL of antibody solution and 10 µL of RBC suspension. However, clearer results were found in reverse group tests using 20 µL of antibody solution and 10 µL of RBC suspension. Tests with D antibody tests were completed with both methods (Figure 3.5).

Dilution experiments were also only completed on paper towel and at 45% RBC concentration for the two different antibody droplet sizes, 10 µL and 20 µL. These were performing with diluted A antibody solutions in PBS. Each dilution was tested six times with blood from 6 different donors for each dilution (three positive and three negative). The critical dilution over which there was no longer a clear distinction between positive and negative results was recorded. A dilution experiment using the same antibody concentrations using a traditional gel card test was also completed. This was performed with 0.8 vol% concentration of washed cells in PBS, a Haemokinesis neutral gel card and centrifuging at 1270 relative centrifugal force for 5.5 minutes. Three replicates were tested using RBCs from different donors.

3.3 Results

The kinetics and final stain area are investigated by varying RBC concentration, antibody specificity, antibody concentration and paper structure. Here, an antibody droplet is first deposited on paper and allowed to wick for 10 seconds. A droplet of RBC suspension is then deposited on the same locus. The time interval between deposition of the two droplets is kept constant in this study.

Figure 3.3 shows the evolution of stain area as a function of time for droplets of 3

different concentrations for type A and B red blood cell (RBCs) suspensions on Whatman 41 filter paper. Four systems are studied: A RBCs spreading on A (positive) and B (negative) antibodies, and B RBCs on A (negative) and B (positive) antibodies. Three replicates are shown for each case. The stain reached equilibrium size typically in around 5 sec, always within 10 sec. The consistent scale used in Figure 3.3 shows an inverse relationship between concentration of RBCs and stain area. The droplets with the higher RBC concentrations also wick slower. The lower RBC concentrations display a clear difference between positive and negative results indicating a successful test. However, at 45% RBC concentration, filter paper is not able to discriminate a positive from a negative test. Here the variation between tests is dominated by experimental error. There is a slight decrease in stain size at the later times for the positive 15% case. This is because the stain partially lightens or degrades at the later times, leading to a decreased stain size as calculated by the constant intensity threshold algorithm used to analyse images.

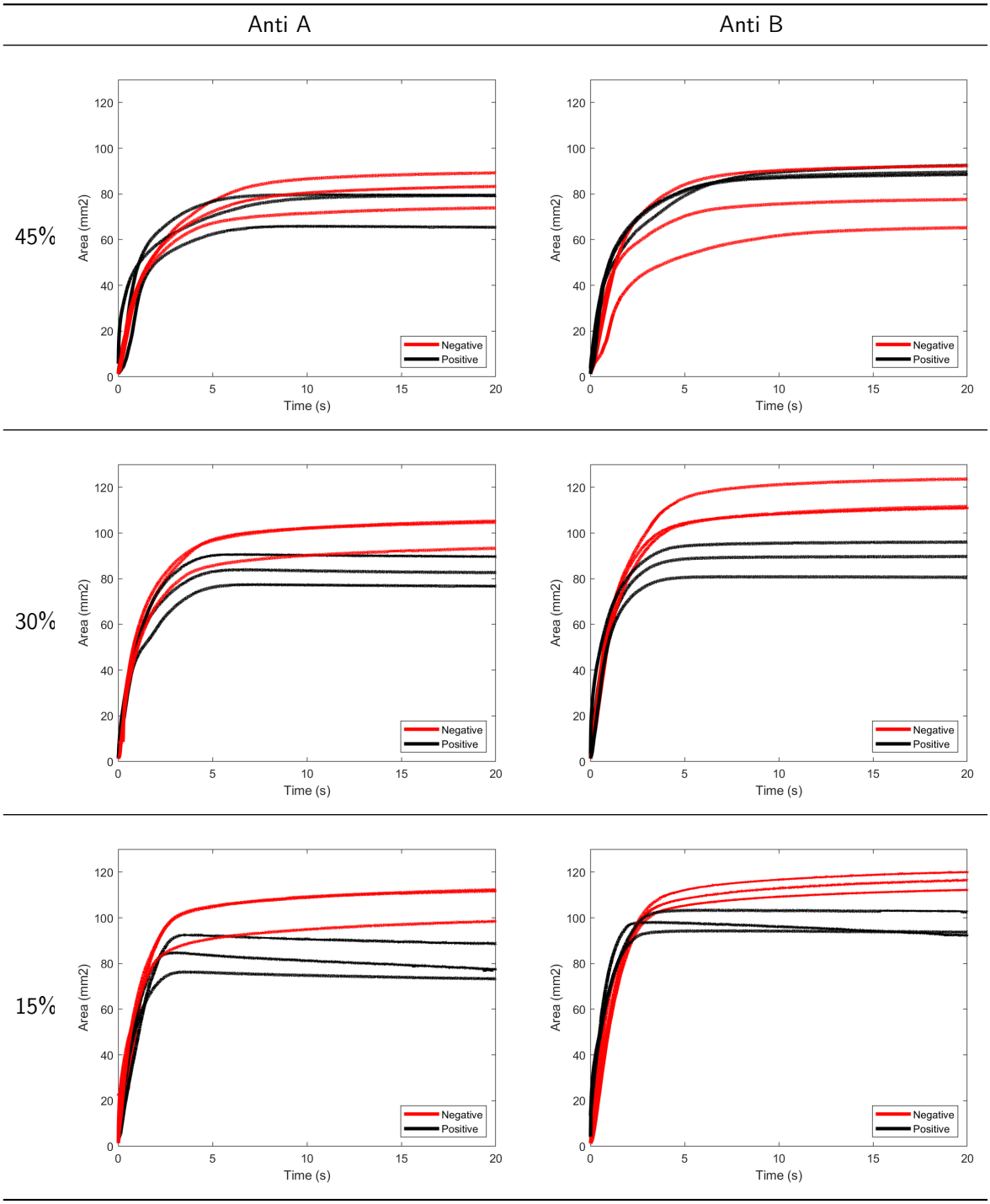

Figure 3.3: Effect of red blood cell concentration and type/specificity of antibody on the evolution of the stain size with time of blood droplets spreading on a filter paper (Whatman 41) previously wet with anti A or anti B antibody. Positive and negative test were performed 3 times; in some cases variability was less than the thickness of a line and is therefore hidden.

Figure 3.4 shows the results of the same test but performed on paper towel. The stain

size and growth rate for this paper is much higher than for filter paper. Here, there is clear separation between positive and negative tests in all cases. Tests at 15% RBC suffered from contrast issues particularly at the later times. This is partially due to the stain lightening that occurs at the late times in all papers, and partially due to contrast issues that are present in paper towel because of the increased profile roughness. This can be seen in the noisy data at the later times in Figure 3.4. Contrast issues are only present at low RBC concentrations as the colour is much weaker.

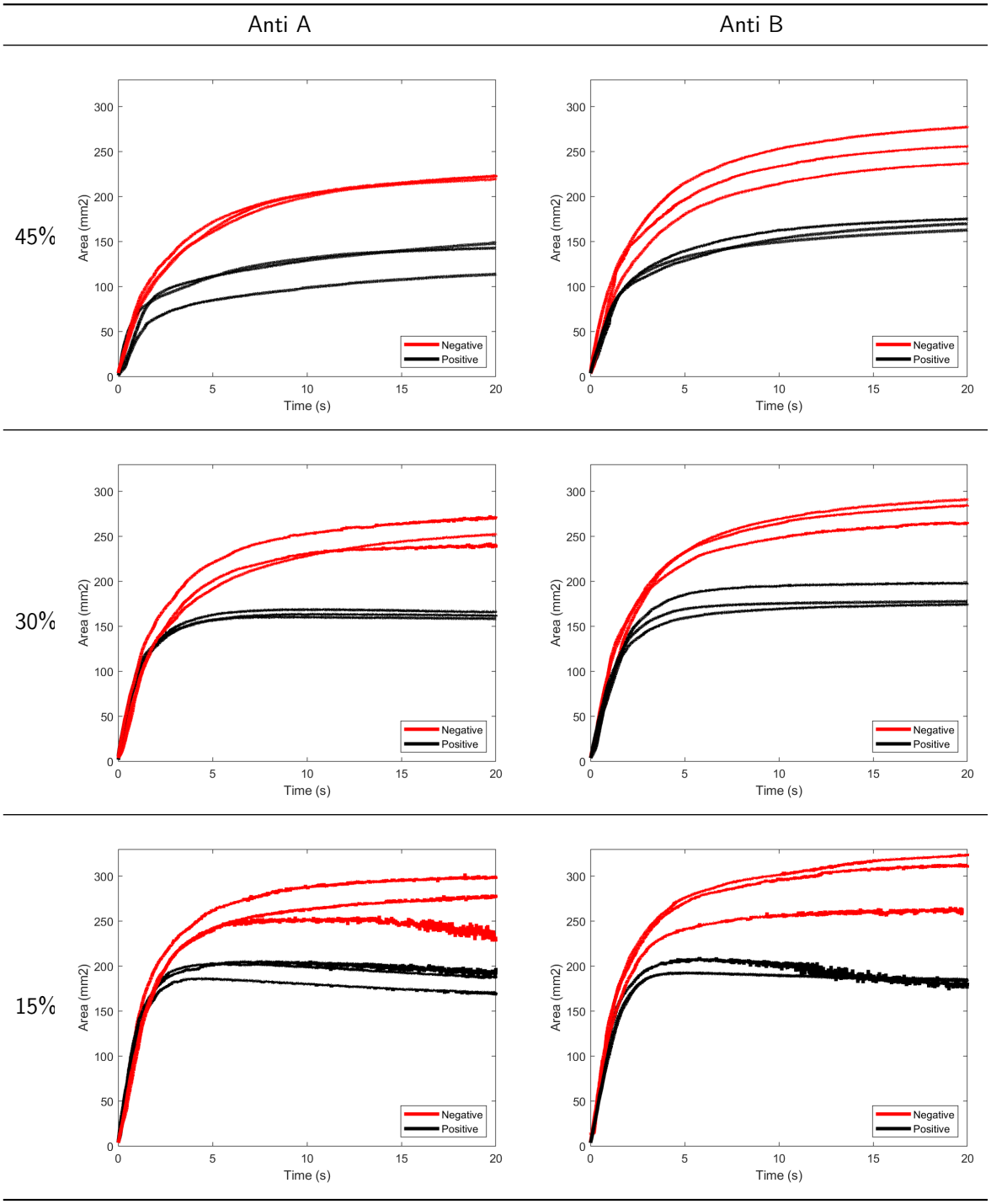

Figure 3.4: Effect of red blood cell concentration and the type/specificity of antibody on the evolution of the stain size with time for blood droplets spreading on a paper towel previously wet with anti A or anti B antibody. Positive and negative test were performed 3 times; in some cases variability was less than the thickness of a line and is therefore hidden.

The absorption properties of 100cm^2 samples of filter paper and paper towel were

Table 3.1: Paper properties for 100cm^2 samples

Paper	O.D Weight (g/m^2 ± SD)	Wet Weight (g/m^2 ± SD)	Dry Thickness (m ± SD)	Wet Thickness (m ± SD)	Dry Density (kg/m^3)	Water Capacity (g/m^2)
Towel	25.6 ± 0.3[24]	55.4 ± 1.8[24]	98 ± 2[24]	76 ± 2[24]	261.0	29.8
Filter	85.4 ± 0.7 [24]	180.9 ± 2.1[24]	226 ± 5[24]	218 ± 5[24]	391.6	95.5

measured using TAPPI standards and presented in our previous study[24]. The findings are reproduced here and summarised in Table 3.1. Paper dry density is calculated using the oven dried (O.D) weight and the dry thickness. Water capacity is calculated by subtracting the wet and dry weights. Filter paper is significantly denser and thicker than paper towel, leading to a higher water capacity.

Figure 3.5 displays the evolution of stain size as a function of time for a 45% RBC suspension on paper towel with D (IgM) antibodies. Two methods are compared, using droplets of 10 µL and 20 µL antibody solution but with the same volume of RBC suspension. Although there is a small difference in the variability, both tests can discriminate a positive from a negative result. Both positive and negative stains spread significantly further and faster than those tested with A or B antibodies.

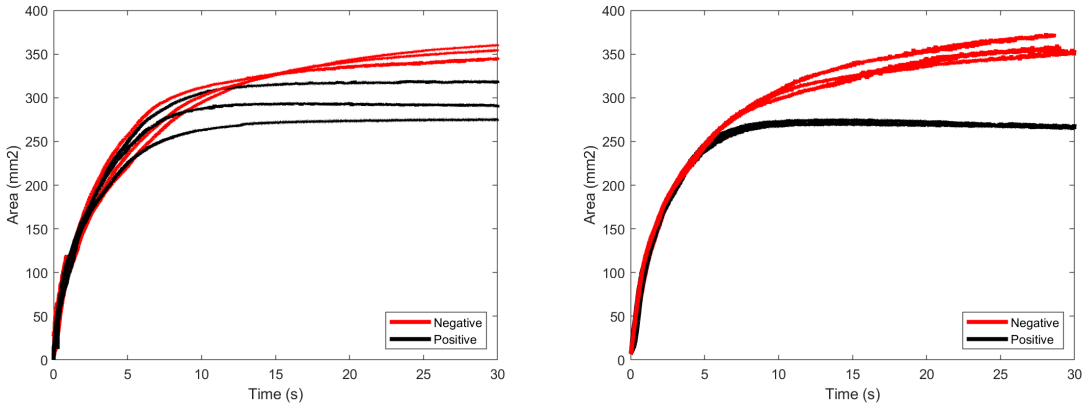

(a) (b)

Figure 3.5: Tests with 45% RBC for the D antigen was performed with (a) 10 µL and (b) 20 µL drop of antibody solution. Each test was performed 3 times, in some cases variability was less than the thickness of a line and is therefore hidden.

A dilution experiment was also performed using A antibodies to assess the sensitivity of the test. This compares the effect of antibody volume/ratio. Figure 3.6 displays the evolution of stain size with time for dilution experiments for droplets of 10 µL antibody solution at 4 different antibody dilutions 1:2, 1:8, 1:16, 1:32. Figure 3.6a shows the

difference between positive results at each dilution. As expected, the stain size is larger with a more severe dilution. Figure 3.6b displays the difference in negative tests between dilutions. These results follow the same trend as the positives, where a lower concentration of antibodies produces a larger stain. Despite this, a separation between positive and negative results was found consistently in all tests down to a dilution of 1:8. A dilution test was also performed with the second protocol where a 20 µL droplet of antibody solution was used. This yielded similar finding where a reliable result was found down to a dilution of 1:8, indicating the same sensitivity. The critical dilution of a traditional gel column test using the same antibody solution was also performed (Figure 3.6c). The gel columns indicate a positive reaction when RBCs are present at the top of the column and negative when the RBCs are at the bottom [5]. Therefore, the sensitivity can be determined by identifying the threshold antibody dilution over which a false negative is found. The critical dilutions for the gel card test were 1:256, 1:256 and 1:512 for the three samples of RBC tested.

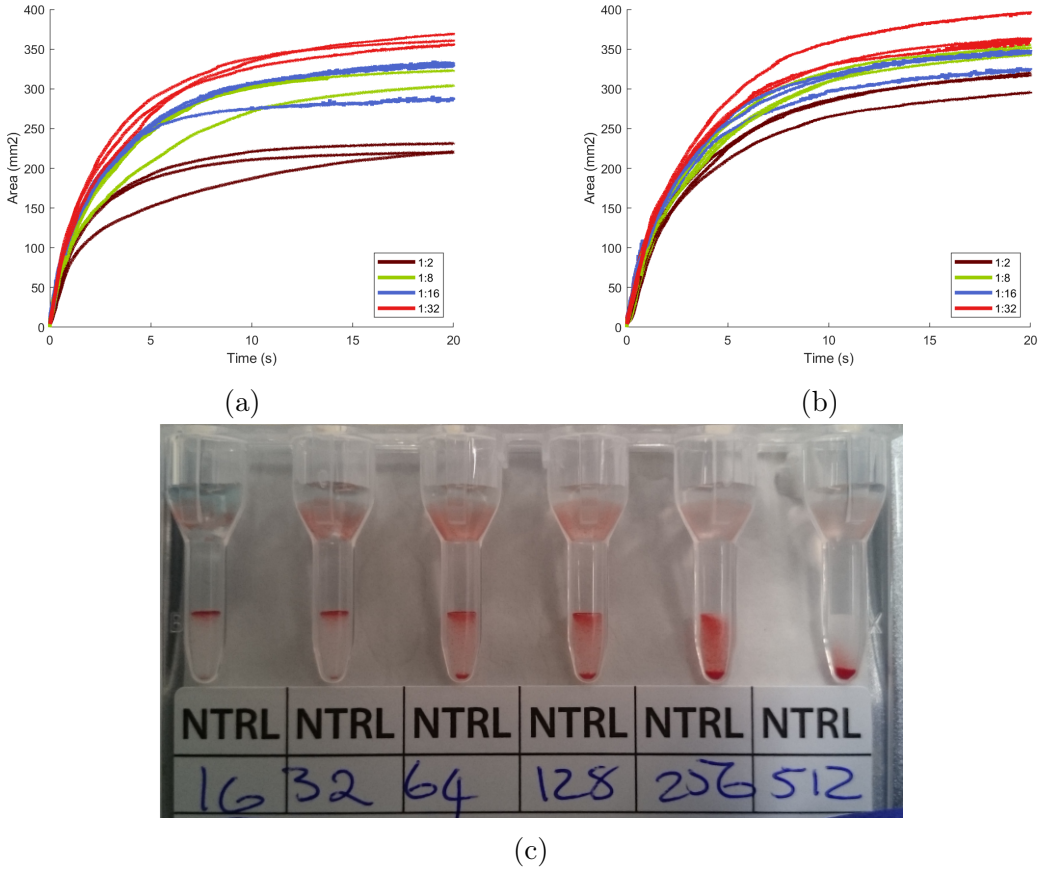

Figure 3.6: Stain growth evolution for tests with (a) positive and (b) negative reactions with serial dilutions of antibody. Each dilution is tested 3 times, in some cases variability was less than the thickness of a line and is therefore hidden. (c) test performed using serial dilutions of the same antibodies using the gel column technique.

Robust blood typing involves forward testing, (detecting antigens on RBCs), combined with reverse testing (detecting antibodies in plasma). Figure 3.7 displays the results of reverse group tests performed using 20 µL droplets of patient plasma and 10 µL of 45% RBC solution. Figure 3.7 combines the results from 4 systems: A plasma with A RBC (negative), A plasma with B RBCs (positive), B plasma with B RBCs (negative) and B plasma with A RBCs (positive). The stain sizes and growth rates of reverse group tests are larger than those from forward group tests with commercial antibodies. Although some overlap exists, it is clear that positive and negative results have different stain sizes on average. A two sample T-test performed with stain areas at 27 seconds shows a statistically significant difference between the positive and negative samples ($P = 0.028$). This demonstrates potential for this test. However, optimisation of paper structure and RBC concentration is required to perfectly segregate positive from negative with no overlap.

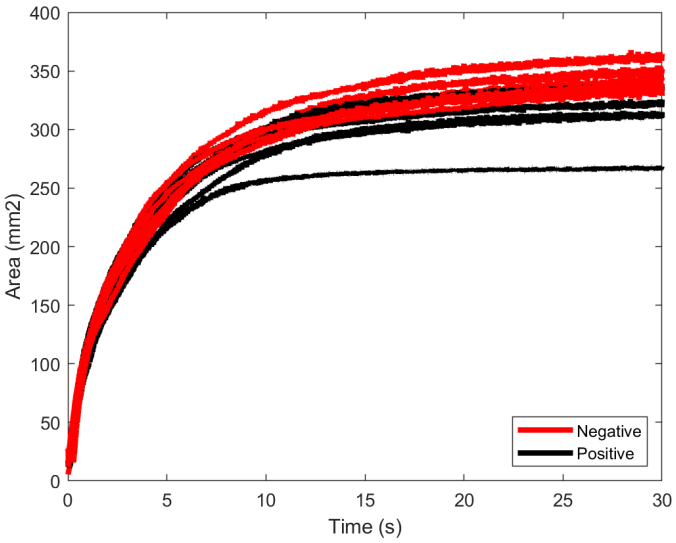

Figure 3.7: Stain growth evolution for reverse blood typing test.

3.4 Discussion

This study aims to develop a rapid blood typing diagnostic that can easily be scaled up. We raised the hypothesis that there is a difference in wicking kinetics of blood in paper wetted with specific (slow kinetics) and non-specific (fast kinetics) antibody. Measuring this difference could lead to a fast, reliable and reproducible diagnostic. This concept can provide an attractive alternative to existing large-scale blood typing systems due to its faster speed of detection and possible cost benefits.

3.4.1 Reproducibility

Reproducibility of results is critical as the variability between replicates must be well below the difference between a positive and a negative test. There are several sources of inconsistency in this experiment that affect results. As each replicate was performed with blood from a different donor, stain growth is expected to be slightly different. This is because there are many inconsistencies in blood taken from different individuals [26, 27]; these include RBC concentration and biochemistry (protein levels, hormones, cholesterol/lipids, ionic strength). However, wicking of blood on the same paper but without the presence of antibodies is quite reproducible [24, 25]. The discrepancy here may be caused by differences in antigen expression between individuals or by the manual method used here to deposit droplets. Differences in antigen density or expression in the RBC membrane affects binding strength and rate, therefore affecting agglutinate

size [28, 29]. The hand pipette method selected introduces some variability in the relative position and timing of successive droplets. Each of these individual causes will influence stain area values and compounds errors. It is also a challenge to deliver each blood droplet at the same rate. These issues would disappear in a fully automated blood diagnostic device as the deposition of droplets would be completed precisely.

Despite slight reproducibility issues with the simple methodology used, forward group test results are shown in under 10 seconds after the deposition of the RBC solution for A, B and D antibodies. Stain growth evolution of positive results generally reaches a plateau very quickly while negative tests continue to spread for longer. This difference highlights the chromatography-like mechanism which was introduced for paper-based blood tests by Khan et al. [2]. The increase in particle size due to agglutination causes an increased extrinsic viscosity of the suspension and a higher likelihood of physical blockages forming in the paper network (Figure 3.1). This causes resistance to the movement of RBCs and bulk solution, which leads to decreased wicking and a chromatography-like separation of agglutinated RBCs. Phase separation was not detectable here due to the paper already being wet with antibody solution. To increase test sensitivity the area difference between positive and negative results must be maximised. Here, 5 variables are investigated: paper type, forward/reverse testing, RBC concentration, antibody specificity and antibody concentration. Each of these variables are analysed below.

3.4.2 Reverse Typing

Figure 3.7 shows that variability between reverse tests is currently too high and sensitivity too low to reliably test reverse groups with the current method. However, it is clear that positive and negative results on average present different stain sizes, showing the potential of the method. With further optimisation to increase sensitivity and decrease variability, reverse testing may be improved to the level needed for safe blood banking. Reverse blood typing was previously accomplished on paper using the elution method [20, 23]. This produced reliable results and is useful for small scale and remote application. However, the requirement of separate reaction and elution steps, make these tests difficult to scale up. Also, the total time required for these multistep processes is comparable to conventional testing methodologies. While not yet optimised, the kinetic diagnostic introduced here has the potential to be faster and simpler than all previous reverse group tests.

3.4.3 Paper Type

The exact effect of paper structure and property is difficult to predict as the dynamics of a droplet soaking radially into paper is a complex process. The radial wicking of a single droplet of simple and biological fluids was discussed and modelled elsewhere [25, 30]. However, the radial wicking of a subsequent droplet has never been studied. Despite these complications, the Lucas-Washburn equation [31, 32] provides a simplified model of wicking in a saturated linear system that can be used to demonstrate the effect of paper type on wicking length.

$$L = \sqrt{\frac{t\gamma r cos\theta}{2\mu}} \tag{3.1}$$

Where t is time, γ is surface tension, θ is contact angle, μ is viscosity, r is average pore radius and L is the wicked length. This equation demonstrates how a change in viscosity produces a change in wicked length and therefore affects the primary mechanism of the studied test. To increase sensitivity the effect of changing viscosity must be maximised. The high density of filter paper (Table 3.1) indicates that it has a lower porosity when compared to paper towel. The Lucas-Washburn equation simplifies paper structure to a single variable (r) that is representative of the average pore size. Although in reality there is a distribution of pore sizes (Figure 3.1), the value of r can be shown to increase with porosity.

The large thickness and water capacity of filter paper also decreases wicked length due to volume conservation. This analysis provides a simple explanation of why dense and thick papers such as filter paper have a decreased wicking length, and therefore a lower sensitivity. The same trend with paper properties is observed in elution [3] and flow through [33] style paper-based blood tests. The wicked area from many different fluids on these two papers are presented elsewhere [24, 30] and indicate the expected trends in wicking rate and length for paper towel and filter paper.

3.4.4 Red Blood Cell Concentration

Sensitivity is also determined by RBC concentration. The effect RBC concentration has on the wicking of blood droplets in untreated paper was studied previously[25, 34]. An increased RBC concentration causes a decrease in wicking length. This is due to a combined effect of an increase in viscosity with haematocrit, a decreasing surface tension and an increased pinning effect. When analysing paper type the highest sensitivity

was found when the fluid had the greatest wicking length. This analysis implies that the lowest concentration of RBC will be optimum. However, a very low concentration of RBCs will not have enough contrast for the stain boundary to be detected accurately by image processing. To overcome this, a dye or other visualisation aid could be incorporated, or a more sophisticated image processing algorithm implemented. However, there is still a lower limit to the test as a very low concentration does not have enough RBCs to make their agglutination induce significant rheological change. Therefore, selecting the optimum RBC concentration for a test involves a balance between wicking rate, strength of agglutination and contrast. The location of this optimum is dependent on paper type. This balance is achieved somewhere around 15% concentration for filter paper. However, with the significant increase to wicking rate and length seen in paper towel this is increased to above 45%. With current analysis, contrast is lost before results are affected by a lack of RBCs.

3.4.5 Antibody Specificity

All tested antibodies were able to distinguish a positive from a negative result. Although a general trend of increased sensitivity with increased wicking length was seen with other parameters, D antibody tests had the lowest sensitivity despite their large wicking lengths. See change of horizontal and vertical scale between Figure 3.4 and 3.5. As the antibody solutions used are commercial products, their exact compositions and concentrations are not known. Although they likely contain a combination of proteins, salts and preservatives. As the wicking lengths of D tests are larger than A or B in both positive and negative cases, this discrepancy is likely caused by differences in the avidity or concentration of the antibody solutions. The decreased sensitivity of D tests could be also caused by a decrease in antigen strength or density when compared to A or B.

3.4.6 Antibody Strength

Dilution experiments were performed using serial dilutions of A antibody solution in PBS. Figure 3.6 shows that there is an inverse relationship between antibody concentration and stain area. This trend is also observed, but to a lesser extent, for negative results where no agglutination is present. This relationship with antibody concentration for negative results is expected as a previous study showed the presence of protein to cause a decrease in stain area [24]. This was due to an increased contact angle because of protein adsorption. The variation of negative tests with antibody concentration could

lead to misinterpretation, as Figure 3.6a suggests that the positive test show variation between concentrations down to a dilution of 1:32. However, the variation of stain size with antibody concentration in the negative test (Figure 3.6b) shows that stain size is not solely determined by agglutination. The test is successful only if the stain size of a positive test is consistently lower than a negative. This occurs with antibody dilutions at and above 1:8 for both 10 µL and 20 µL droplets of antibody solution, indicating that both volumes of antibody solution produce tests of identical sensitivity.

Comparison with gel column tests in Figure 3.6c indicates that although the method proposed here is significantly faster than traditional methods, it has a much lower sensitivity. This is likely the reason that reverse tests were not fully reproducible. Antibody concentration and binding strength varies significantly between individuals and although the test methodology can detect the presence of strongly expressed antibodies, weak ones are missed.

3.5 Conclusion

The identification of red blood cell antigens for blood typing is an everyday process performed at high volumes in hospitals and blood banks around the world. In this study, the evolution of wicked stain area from red blood cell suspensions on paper wetted with an antibody solution was monitored for a series of specific and non-specific antibody-RBC systems. The test concept relies on an increase in the effective viscosity of the suspension and a chromatography-like separation of red blood cells in agglutinated samples.

A clear and reproducible difference was observed between positive and negative reactions for all forward group tests for type A, B and D on paper towel and for lower red blood cell concentrations on filter paper (requires dilution). Positive/negative results are achieved within 10 sec. Low paper density and thickness were found to increase sensitivity. Optimum red blood cell concentration was dependent on a balance between wicking rate, strength of reaction and optical contrast. Potential for reverse group testing is also demonstrated, although currently, sensitivity is insufficient to detect weakly expressed antibodies.

The kinetic paper-based test presented here is significantly faster than any method currently in use. Due to the simple methodology, this technique can be easily scaled

up to produce a high throughput system capable of handling the demands of a modern blood banking facility. This device would function similarly to an office inkjet printer where a drop of antibody is deposited onto the paper and shortly after, the RBC suspension at the same location. Within 10 seconds of the RBC deposition, a single photo could be taken and analysed to determine the size of the stain and therefore the presence of agglutination. The ongoing costs associated with this technique would be very low as each test only consumes 10 µL of antibody solution, 10 µL of patient RBC suspension and conservatively 10cm^2 of paper towel. The introduction of such a low-cost device can increase access to blood banking equipment as well as save considerable time, resources and lives.

3.6 Acknowledgement

This research was funded by an ARC Linkage grant (LP160100544), Haemokinesis and an Australian Government Research Training Program (RTP) Scholarship. Thanks to the Red Cross Australia for supplying blood products.

3.7 References

[1] Geoff Daniels and Imelda Bromilow. *Essential Guide to Blood Groups*. Wiley Blackwell, 2014.

[2] Mohidus Samad Khan, George Thouas, Wei Shen, Gordon Whyte, and Gil Garnier. Paper diagnostic for instantaneous blood typing. *Analytical chemistry*, 82(10):4158–4164, 2010.

[3] Mohammad Al-Tamimi, Wei Shen, Rania Zeineddine, Huy Tran, and Gil Garnier. Validation of paper-based assay for rapid blood typing. *Analytical Chemistry*, 84(3):1661–1668, 2012.

[4] Wim Malomgré and Birgid Neumeister. Recent and future trends in blood group typing. *Analytical and Bioanalytical Chemistry*, 393(5):1443–1451, 2009.

[5] Daniela Proverbio, E. Spada, L. Baggiani, and R. Perego. Assessment of a gel column technique for feline blood typing. *Veterinary Research Communications*, 33(SUPPL. 1):201–203, 2009.

[6] Melur K. Ramasubramanian and Stewart P. Alexander. An integrated fiberoptic-microfluidic device for agglutination detection and blood typing. *Biomedical Microdevices*, 11(1):217–229, 2009.

[7] Jun You Chen, Yi Ting Huang, Hsin Hao Chou, Cheng Po Wang, and Chien Fu Chen. Rapid and inexpensive blood typing on thermoplastic chips. *Lab on a Chip*, 15(24):4533–4541, 2015.

[8] Denise M Harmening. *Modern blood banking and transfusion practices*. FA Davis, 2018.

[9] Whui Lyn Then and Gil Garnier. Paper diagnostics in biomedicine. *Reviews in Analytical Chemistry*, 32(4):269–294, 2013.

[10] Yong He, Yan Wu, Jian Zhong Fu, and Wen Bin Wu. Fabrication of paper-based microfluidic analysis devices: a review. *RSC Advances*, 5(95):78109–78127, 2015.

[11] Max M. Gong and David Sinton. Turning the page: Advancing paper-based microfluidics for broad diagnostic application. *Chemical Reviews*, 117(12):8447–8480, 2017.

[12] Elain Fu and Corey Downs. Progress in the development and integration of fluid flow control tools in paper microfluidics. *Lab on a Chip*, 17(4):614–628, 2017.

[13] Tugce Akyazi, Lourdes Basabe-Desmonts, and Fernando Benito-Lopez. Review on microfluidic paper-based analytical devices towards commercialisation. *Analytica Chimica Acta*, 1001:1–17, 2018.

[14] Zhi Liu, Xiaocong He, Jiaxiu Han, Xiuhai Zhang, Fei Li, Ang Li, Zhiguo Qu, and Feng Xu. Liquid wicking behavior in paper-like materials: mathematical models and their emerging biomedical applications. *Microfluidics and Nanofluidics*, 22(11):132, 2018.

[15] Natasha Yeow, Heather McLiesh, and Gil Garnier. Indirect antiglobulin paper test for red blood cell antigen typing by flow-through method. *Analytical Methods*, 7(11):4645–4649, 2015.

[16] Miaosi Li, Junfei Tian, Mohammad Al-Tamimi, and Wei Shen. Paper-based blood typing device that reports patient's blood type "in writing". *Angewandte Chemie - International Edition*, 51(22):5497–5501, 2012.

[17] Purim Jarujamrus, Junfei Tian, Xu Li, Atitaya Siripinyanond, Juwadee Shiowatana, and Wei Shen. Mechanisms of red blood cells agglutination in antibody-treated paper. *Analyst*, 137(9):2205–2210, 2012.

[18] Temsiri Songjaroen, Vitsarut Primpray, Thawintra Manosarn, Witsanuwat Khumchanta, Tasanee Sakuldamrongpanich, Suntree Kulkeratiyut, and Wanida Laiwattanapaisal. A simple and low-cost portable paper-based ABO blood typing device for point-of-care testing. *Journal of Immunoassay and Immunochemistry*, 39(3):292–307, 2018.

[19] A. Caesar, S. Meyer, N. Trost, K. Neuenschwander, C. Geisen, B. M. Frey, C. Gassner, and P. Schwind. A uniform method for the simultaneous blood group phenotyping of Fya, Fyb, Jka, Jkb, S, $\bar{s}$, P1, k applying lateral-flow technique. *Vox Sanguinis*, 113(2):177–184, 2018.

[20] Temsiri Songjaroen and Wanida Laiwattanapaisal. Simultaneous forward and reverse ABO blood group typing using a paper-based device and barcode-like interpretation. *Analytica Chimica Acta*, 921:67–76, 2016.

[21] Natasha Yeow, Heather McLiesh, Liyun Guan, Wei Shen, and Gil Garnier. Paper-based assay for red blood cell antigen typing by the indirect antiglobulin test. *Analytical and Bioanalytical Chemistry*, 408(19):5231–5238, 2016.

[22] W L Then, Miaosi Li, Heather McLiesh, Wei Shen, and Gil Garnier. The detection of blood group phenotypes using paper diagnostics. *Vox Sanguinis*, 108(2):186–196, 2015.

[23] Jasmina Casals-Terré, Josep Farré-Lladós, Joan A. López, Teresa Vidal, and Maria Blanca Roncero. Enhanced fully cellulose based forward and reverse blood typing assay. *Journal of Biomedical Materials Research - Part B Applied Biomaterials*, 108(2):439–450, 2020.

[24] Michael J Hertaeg, Rico F Tabor, and Gil Garnier. Effect of protein adsorption on the radial wicking of blood droplets in paper. *Journal of Colloid And Interface Science*, 528:116–123, 2018.

[25] Michael J Hertaeg, Rico F Tabor, Joseph Berry, and Gil Garnier. Radial Wicking of Biological Fluids in Paper. *Langmuir*, 36:8209–8217, 2020.

[26] Cinzia Sala, Marina Ciullo, Carmela Lanzara, Teresa Nutile, Silvia Bione, Roberto Massacane, Pio D'Adamo, Paolo Gasparini, Daniela Toniolo, and Clara Camaschella. Variation of hemoglobin levels in normal Italian populations from genetic isolates. *Haematologica*, 93(9):1372–1375, 2008.

[27] Benjamin J. Ravenhill, Usheer Kanjee, Ambroise Ahouidi, Luis Nobre, James Williamson, Jonathan M. Goldberg, Robin Antrobus, Tandakha Dieye, Manoj T. Duraisingh, and Michael P. Weekes. Quantitative comparative analysis of human erythrocyte surface proteins between individuals from two genetically distinct populations. *Communications Biology*, 2(1):1–9, 2019.

[28] Natasha Yeow, Rico F. Tabor, and Gil Garnier. Direct measurement of IgM—Antigen interaction energy on individual red blood cells. *Colloids and Surfaces B: Biointerfaces*, 155:373–378, 2017.

[29] Natasha Yeow, Rico F. Tabor, and Gil Garnier. Mapping the distribution of specific antibody interaction forces on individual red blood cells. *Scientific Reports*, 7:41956, 2017.

[30] Michael J. Hertaeg, Rico F. Tabor, Joseph D. Berry, and Gil Garnier. Dynamics of stain growth from sessile droplets on paper. *Journal of Colloid and Interface Science*, 541:312–321, 2019.

[31] Von Richard Lucas. Ueber das zitgesetz des kapillaren aufstiegs von flüssigkeiten. *Kolloid-Zeitschrift*, 23(1):15–22, 1918.

[32] Edward W Washburn. The dynamics of capillary flow. *Physical Review*, 17(3):273–283, 1921.

[33] Jielong Su, Mohammad Al-Tamimi, and Gil Garnier. Engineering paper as a substrate for blood typing bio-diagnostics. *Cellulose*, 19(5):1749–1758, 2012.

[34] Jingyao Li, Xingyu Li, and Stephen Michielsen. Alternative method for determining the original drop volume of bloodstains on knit fabrics. *Forensic science international*, 263:194–203, 2016.

3.8 Appendix - Rapid COVID-19 serology test

During this doctoral candidature, the COVID-19 pandemic, caused by the SARS-CoV-2 virus, has caused significant disruption to global populations. As of August 12, 2020, there are more than 20 million confirmed cases, and over 700,000 deaths globally associated with the disease [1]. Since the outbreak, there have been many new diagnostic techniques proposed to detect SARS-CoV-2 infection [2–4]. These diagnostics test for active viruses (PCR), their antigens, or the antibodies (IgM and IgG) realeased by the body as immunologic response which can be used to diagnose patients. Serology tests, that detect the presence of SARS-CoV-2 antibodies are critical for rapid and global pandemic management in a population as well as to study the body's immune response [5]. The most common method for serological testing is laboratory-based indirect enzyme-linked immunosorbent assay (ELISA) [6]. However, this process is not suited to high throughput application because it is time consuming, difficult to perform and requires many different antigens and reagents. To address this, researchers at Monash University developed an agglutination assay by binding a peptide-antibody bioconjugate onto the membrane of red blood cells [7]. These funtionalised cells cross-link and agglutinate in the presence of plasma containing SARS-CoV-2 antibodies. A gel column agglutination test could then be used to quickly and easily determine the presence of SARS-CoV-2 antibodies in patient plasma.

Here, the same functionalised cells used by Alves et al. [7] are selected and incorporated into the testing methodology introduced in this chapter to create a rapid and automatable diagnostic for SARS-CoV-2 antibodies. Human plasma or serum samples were provided by Monash Pathology and the Australian Red Cross Lifeblood, obtained with written informed consent in accordance with the recommendations of Blood Service Human Research Ethics Committee (BSHREC) and the Monash University Human Research Ethics Committee (MUHREC).

Figure 3.8 shows the evolution of stain area as a function of time of functionised RBCs spreading on paper wetted with patient plasma samples donated by confirmed SARS-CoV-2-positive and negative patients. Functionalised cells were washed and combined with PBS at 45% concentration. A 10 µL droplet of RBC suspension was deposited 10 seconds after plasma droplet in an identical process as in the reverse blood typing tests presented in this chapter. Two plasma droplet sizes were tested, 10 µL and 20 µL. Both tests are shown in Figure 3.8 and display comparable sensitivity. Results in

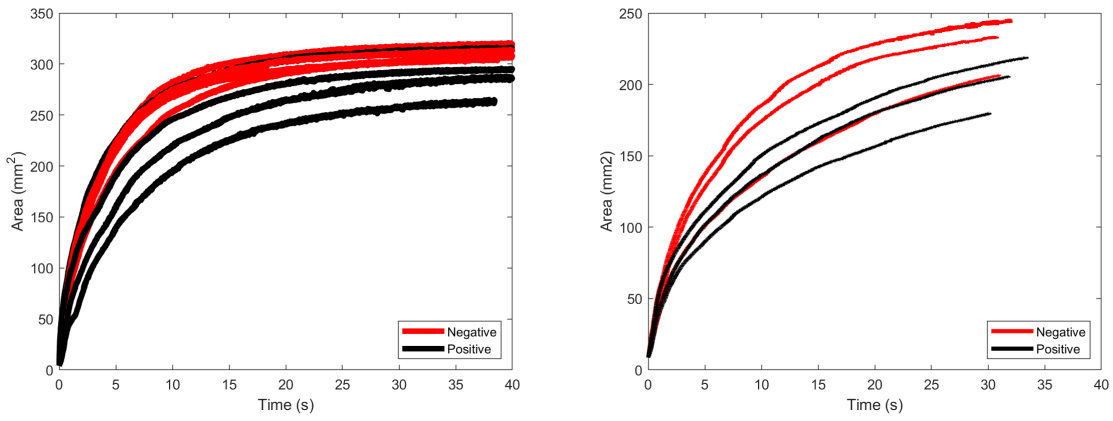

(a) (b)

Figure 3.8: Spreading of functionalised RBC suspension on paper wet with patient plasma. Positive tests were completed using plasma from confirmed SARS-CoV-2-positive patients.

Figure 3.8a were gathered using positive samples from 3 individuals, 1 of these samples was tested twice to make 4 replicates. This was compared with 4 negative samples from 4 different individuals. Results in Figure 3.8b were gathered by testing a single positive sample 3 times and comparing this to 3 different negative samples. With both plasma droplet sizes used, there is a clear average difference in stain size between the positive and negative tests. However, the variation due to agglutination is not large enough to overcome the variability between samples in all cases. Despite sensitivity issues, this is the fastest SARS-CoV-2 serology test and can be easily automated and scaled up. With further development, this technique has the potential to drastically reduce testing time and cost.

3.8.1 References

[1] Worldometer. Coronavirus Update (Live). www.worldometers.info/coronavirus.

[2] Linda J. Carter, Linda V. Garner, Jeffrey W. Smoot, Yingzhu Li, Qiongqiong Zhou, Catherine J. Saveson, Janet M. Sasso, Anne C. Gregg, Divya J. Soares, Tiffany R. Beskid, Susan R. Jervey, and Cynthia Liu. Assay Techniques and Test Development for COVID-19 Diagnosis. *ACS Central Science*, 6:591–605, 2020.

[3] Giwan Seo, Geonhee Lee, Mi Jeong Kim, Seung Hwa Baek, Minsuk Choi, Keun Bon Ku, Chang Seop Lee, Sangmi Jun, Daeui Park, Hong Gi Kim, Seong Jun Kim, Jeong O. Lee, Bum Tae Kim, Edmond Changkyun Park, and Seung Il Kim. Rapid

Detection of COVID-19 Causative Virus (SARS-CoV-2) in Human Nasopharyngeal Swab Specimens Using Field-Effect Transistor-Based Biosensor. *ACS nano*, 14(4):5135–5142, 2020.

[4] Guangyu Qiu, Zhibo Gai, Yile Tao, Jean Schmitt, Gerd A. Kullak-Ublick, and Jing Wang. Dual-Functional Plasmonic Photothermal Biosensors for Highly Accurate Severe Acute Respiratory Syndrome Coronavirus 2 Detection. *ACS Nano*, 14(5):5268–5277, 2020.

[5] Rosanna W Peeling, Catherine J Wedderburn, Patricia J Garcia, Debrah Boeras, Noah Fongwen, John Nkengasong, Amadou Sall, Amilcar Tanuri, and David L Heymann. Serology testing in the COVID-19 pandemic response. *The Lancet Infectious Diseases*, 2020.

[6] Wei Zhang, Rong Hui Du, Bei Li, Xiao Shuang Zheng, Xing Lou Yang, Ben Hu, Yan Yi Wang, Geng Fu Xiao, Bing Yan, Zheng Li Shi, and Peng Zhou. Molecular and serological investigation of 2019-nCoV infected patients: implication of multiple shedding routes. *Emerging Microbes and Infections*, 9(1):386–389, 2020.

[7] Diana Alves, Rodrigo Curvello, Edward Henderson, Vidhishri Kesarwani, Julia A Walker, Samuel C Leguizamon, Heather McLiesh, Vikram Singh Raghuwanshi, Hajar Samadian, Erica M Wood, Zoe K McQuilten, Maryza Graham, Megan Wieringa, Tony M Korman, Timothy F Scott, Mark M Banaszak Holl, Gil Garnier, and Simon R Corrie. Rapid Gel Card Agglutination Assays for Serological Analysis Following SARS-CoV-2 Infection in Humans. *ACS sensors*, 2020.

Chapter 4

Paper-Based Reverse Blood Typing

4.1 Introduction

In chapter 3, a rapid paper-based reverse blood group test was demonstrated. However, the sensitivity must be improved before it can be used in medical applications. Here, an alternate paper-based agglutination diagnostic to detect reverse groups is introduced. This test is capable of sensitively and accurately performing reverse group tests by depositing a pre-combined and incubated droplet of red blood cells and plasma onto paper. Results are determined by the appearance of stains 3 minutes after deposition, making this test much slower than the high throughput technique introduced in chapter 3. However, the test presented here remains simple enough to be automated and shows a high reproducibility and sensitivity with manual methods. An image processing algorithm was also developed capable of identifying results from an image of the stain. Two types of paper are compared, the paper towel used in chapter 3 and a custom handsheet paper.

4.1.1 Method

Patient plasma was separated from whole blood donations from the Red Cross Australia with EDTA anticoagulant by centrifugation. This was was combined with an equal amount of undiluted reagent red blood cells. The reagent cells used were Seracell reagent purchased from Imulab; the exact concentration and components in these are not known. However, the appearance and behaviour is similar to whole blood implying a similar RBC concentration. The plasma and cells were mixed by shaking lightly in a 1.5 mL tube and incubated at approximately 4°C for 7 minutes. This temperature was achieved with an iced insulated box. The plasma, reagent cells and empty tubes

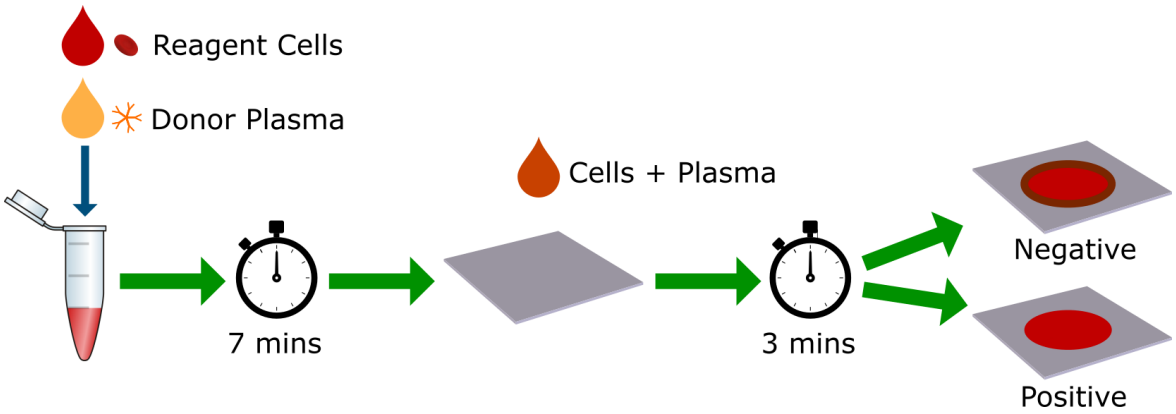

Figure 4.1: Test methodology. 1) - plasma and reagent cells are combined. 2) - mixture is incubated at approx 4°C. 3) - 20 µL droplet is deposited on paper. 4 - After 3 minutes results can be identified. Ring stains in figure correspond to paper towel tests.

were placed in a rack resting on top of the ice 10 minutes before tests were performed. Reactants were combined in a pre-chilled tube and then returned to the ice box for the incubation period. The temperature at the location of the tubes in the rack was measured with a thermometer.

After incubation, 20 µL of the cell-plasma mixture was then deposited onto paper and after 3 minutes, a photograph was taken of the stain. All tests were performed at 23°C 50% relative humidity. Figure 4.1 depicts the test methodology. 2 different papers were used with this method, Kimberly Clark Scott hand towel (4419) and a 30 grams per square meter custom paper made with a British Handsheet Maker. This paper was engineered to have a very slow initial wicking rate, but a large final wicked area. The paper was made using NIST hardwood pulp and 10 mg/g Nopcobond 1213 PAE (polyamidoamine epichlorohydrin) wet strength agent. Tests on paper towel were repeated using plasma from 3 different individuals from each blood group (A, B, O) and each test was repeated twice. This meant that 18 tests were completed with plasma from 9 different donors. For handsheet paper, 2 different plasma samples were tested for each blood group and each sample was tested twice, making 12 tests in total from 6 different donors.

4.2 Results and Discussion

Due to antibodies that are present in plasma [1], a positive agglutination reaction was expected when A type cells were combined with either B or O type plasma, and when

B type cells were combined with either A or O plasma. The 9 images in Figures 4.2 and 4.3 show every combination of red cells and plasma for 3 blood groups (A, B and O) on both papers. A clear difference between positive and negative results can be identified on both papers; although, each displayed results very differently. For paper towel (Figure 4.2), a negative result for A, B and O blood is identified by the presence of a dark ring around the outside of the stain. I_{mid} and p_{max} are quantitative parameters determined by an image processing step discussed in section 4.3. A positive result is indicated when the position of maximum intensity (p_{max}) is below 0.8 or when the normalised intensity of the midpoint is above 0.8. For handsheet paper (Figure 4.3), agglutination causes a severe chromatographic separation of RBCs from the diluent, which is clearly observed 3 minutes after droplet deposition. This observation is consistent across A, B and O blood types. Repeated experiments using plasma from different donors produced slight variation in both papers. However, this difference was small enough for results to be readable by both eye and image processing in all but one of the 15 tested plasma samples. The one erroneous plasma sample demonstrated false negative results for all replicates on both papers (not shown). This error is likely caused by weak antibody expression which is a persistent complication of reverse testing [1].

	A cells	B cells	O cells
A plasma	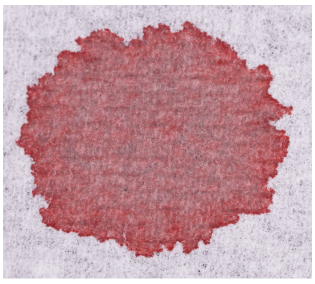 I_{mid} = 0.70 p_{max} = 0.92	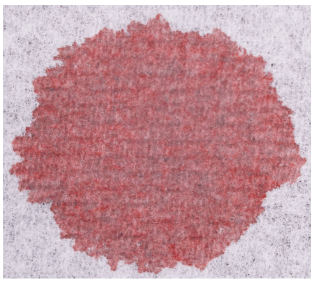 I_{mid} = 0.81 p_{max} = 0.70	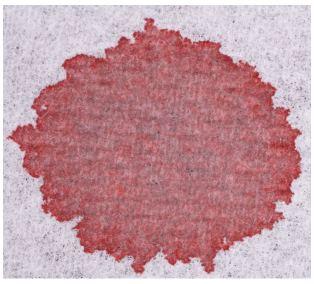 I_{mid} = 0.72 p_{max} = 0.90
B plasma	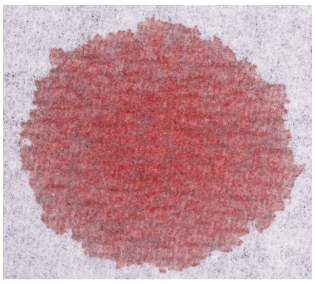 I_{mid} = 0.91 p_{max} = 0.22	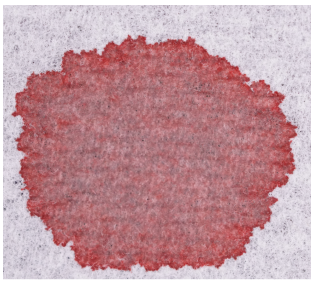 I_{mid} = 0.65 p_{max} = 0.94	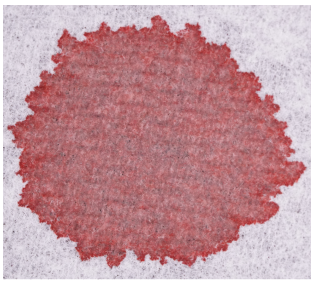 I_{mid} = 0.73 p_{max} = 0.92
O plasma	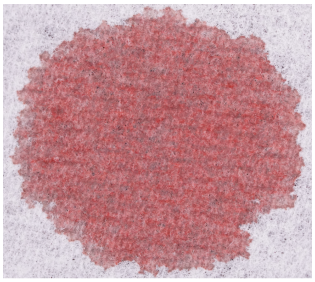 I_{mid} = 0.85 p_{max} = 0.37	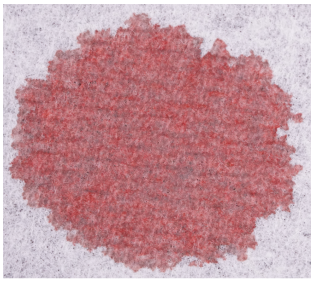 I_{mid} = 0.84 p_{max} = 0.49	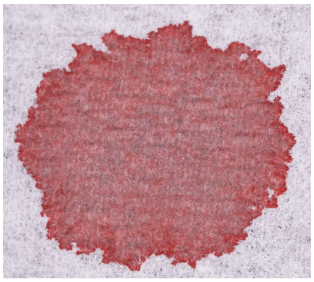 I_{mid} = 0.69 p_{max} = 0.92

Figure 4.2: Stain appearance 3 minutes after droplet deposition on paper towel. Results of image processing (p_{max} and I_{mid}) are given below each image.

The evolution of stain appearance for both positive and negative tests is displayed in Figure 4.4. The equilibrium diameter is reached soon after 15 seconds; however, it is not until much later (approximately 100 s) that ring stains can be clearly identified by eye and image processing. This is demonstrated by the image processing parameters p_{max} and I_{mid}. Each parameter can independently identify results after 3 minutes and further time after this point increases the difference in parameter values. This could indicate that sensitivity could be increased by allowing more time. However, more testing is required to fully optimes this diagnostic technique. Similar ring stains were

observed in paper previously for stains of simple colloids [2] and whole blood [3]. They are caused by an evaporation driven flow that carries RBCs outwards toward a pinned boundary. This is a similar mechanism to ring formation in droplet systems [4, 5]. Ring formation in paper has not been studied in detail, and therefore the governing mechanisms are not fully understood. However, the dominance of chromatographic effects has been identified as a governing factor [2]. When there is a large separation between the solvent front and the migration distance of the analyte, this is referred to as having a low chromatographic mobility or a low retardation factor. Nilghaz et al. [2] determined that systems with low chromatographic mobility are unlikely to form ring deposits, and vice versa for a high mobility. This is because ring formation requires a significant amount of the non-volatile component to be transported to the edge of the stain. This is likely the mechanism leading to the absence of ring structures in positive tests on paper towel, as agglutination decreases the chromatographic mobility of RBCs [6].

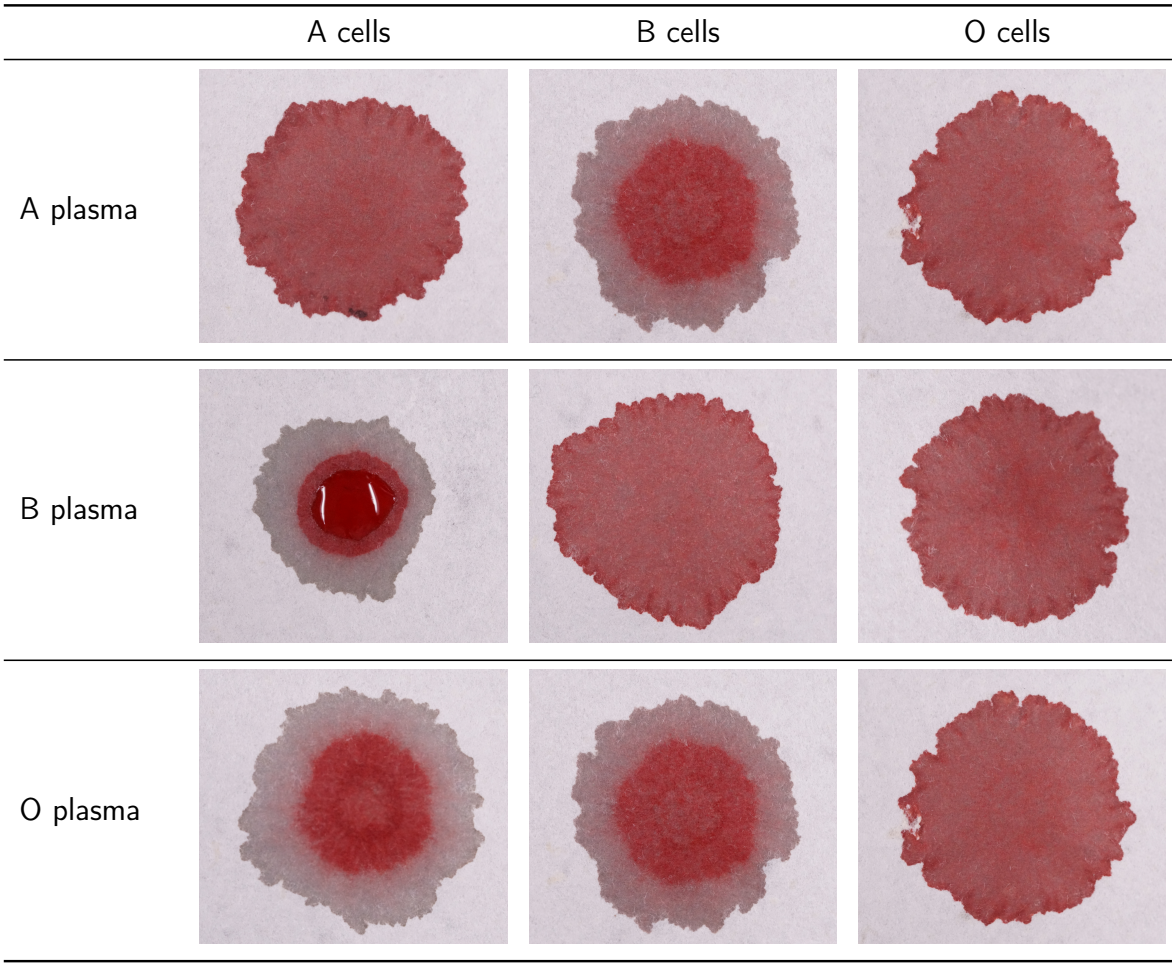

Figure 4.3: Stain appearance 3 minutes after droplet deposition on handsheet paper.

Although tests on paper towel can discriminate positive and negative results, there is little variation in the final stain sizes between them two groups. This implies that agglutination does not affect initial wicking dynamics as the solvent flow velocity from initial wicking is much higher than in the later evaporation driven flow. The agglutination of RBCs is only able to affect transport of RBCs in low velocity flows, such as the evaporation driven flow in drying stains and wicking in less absorbent papers (handsheet). A possible explanation of this is that high shear flows breakup the weak agglutinates that form in reverse group tests. This process is poorly understood for agglutinated RBCs, although a similar process is observed in RBCs under normal conditions. Low shear rate flows allow RBCs to form meso structures such as rouleaux aggregates which are very weakly bonded together by surface forces [7]. At high shear rates the aggregates breakup, leading to a significant decrease in the effective viscosity. This change is primarily due to the variation in average particle size, which has a large influence on viscosity [7–10].

The decreased absorbance of the handsheet paper when compared to paper towel is caused by two factors. A smaller pore size and the small amount of PAE wet strength agent that is likely to increase the pore scale contact angle. The effects of these factors are both demonstrated with the Lucas-Washburn equation [11, 12] (Equation 2.5) and result in a lower wicking rate. The smaller pore size in handsheets also results in more effective exclusion of the aggregated RBC's due to blockages in small pores. This is the cause of the central red regions in Figure 4.3.

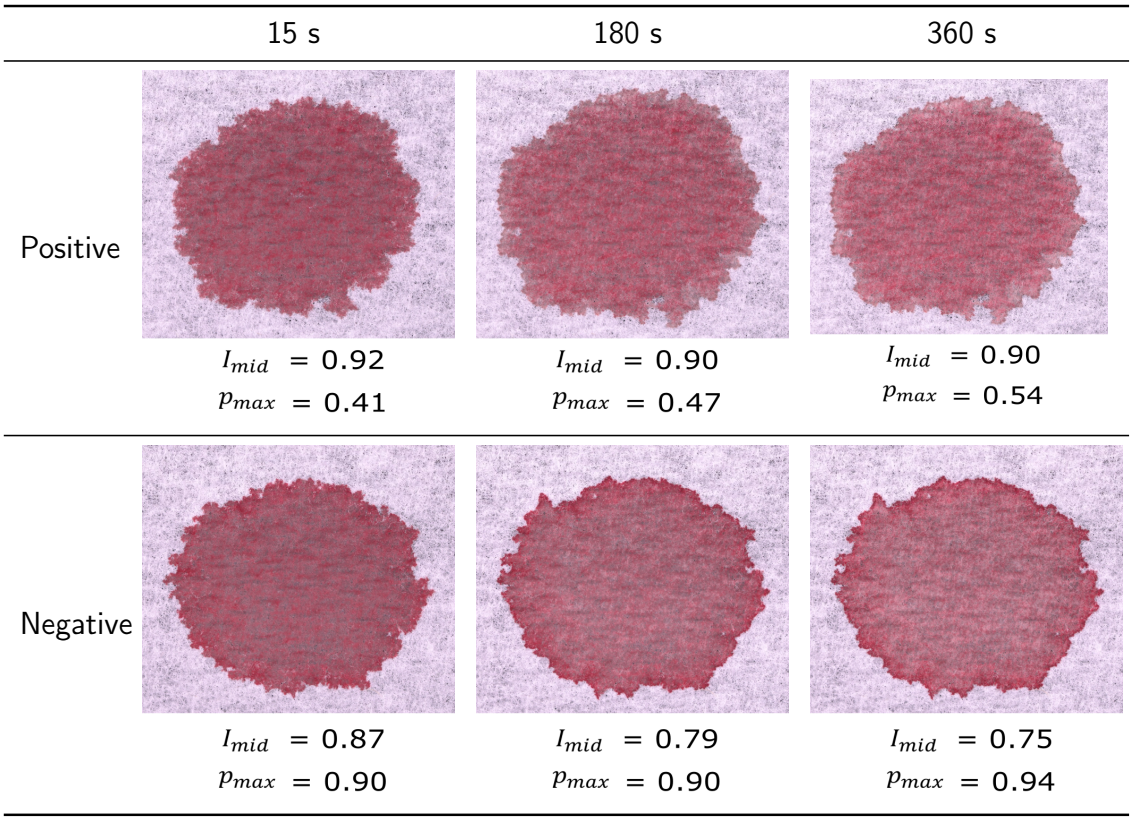

Figure 4.4: Evolution of ring stain with time. Results of image processing (p_{max} and I_{mid}) are given below each image.

4.3 Image Processing

In chapter 3, image analysis was used to determine the size of the stain and therefore test results. This method can be used to automate the interpretation of results on handsheet paper by selectively measuring the size of the red area of the stains. However, the detection of ring formation in paper towel tests required the development of a new image processing algorithm. This is because stain size is not indicative of results in

this case. The algorithm utilises the intensity distribution along the centre line of the stain and was implemented in Matlab. The methodology and representative intensity distributions for positive and negative tests are shown in Figure 4.5. Two important characteristics of these intensity distributions are the position of the maximum value (p_{max}) and the normalised intensity at the midpoint (I_{mid}). The calculation of these parameters from intensity distribution curves is shown in Figures 4.5b and c. The analysis algorithm measures these quantities and can identify a positive or negative result based on whether they are above or below a critical value.

Quantification is achieved by first converting to a grey-scale image by selecting the blue channel. The blue channel was chosen as this gave the best contrast. Next, the intensity along a vertical line that intersects with the centre point is measured and a linear function is subtracted to ensure both the start and end points of the line have a magnitude of zero. Also, the intensity at each point is divided by the maximum value giving normalised intensity. This is how the graphs in Figure 4.5 were generated. The position of maximum intensity is calculated and divided by the radius of the stain giving a dimensionless value that is independent of the size of the stain. The midpoint intensity relative to maximum intensity can be directly measured as the intensity of the midpoint as all intensity values are scaled by the maximum value. Using these relative parameters is advantageous as the calculated values are not significantly influenced by image resolution or light intensity. To increase accuracy, the algorithm was run 10 times on each stain, with each run following a 18° rotation of the image. After this, the calculated parameters are averaged over all rotations.

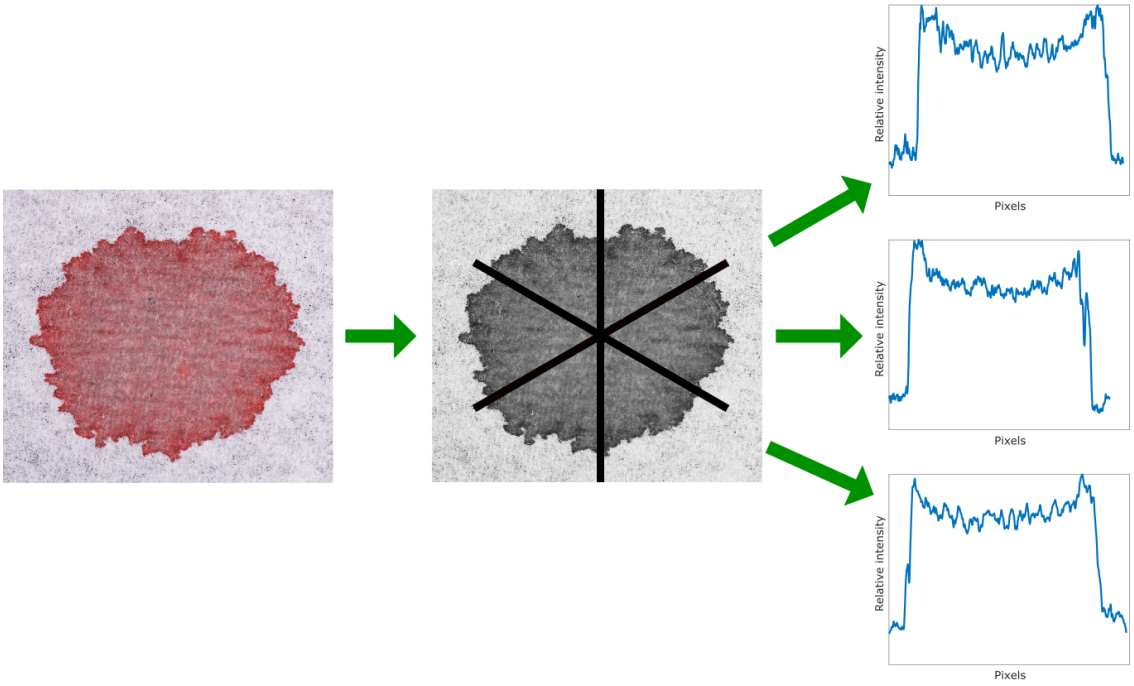

(a)

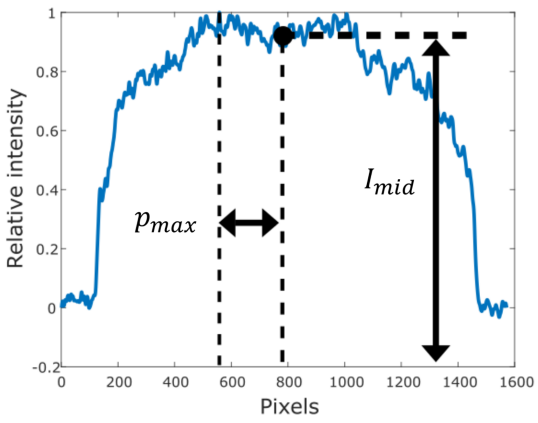

(b)

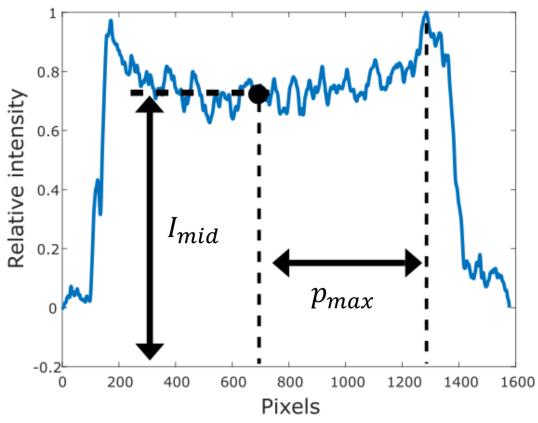

(c)

Figure 4.5: a) Steps involved in image analysis. b) Relative intensity distributions along lines of interest for positive and c) negative tests. Measurements show the two parameters: position of maximum and intensity at centre.

In all positive tests that showed agglutination the average relative position of maximum intensity was above 0.8 and the average relative intensity of the midpoint was below 0.8. This trend is demonstrated in Figures 4.2 and 4.4. This implies that either of the two parameters can be used to identify results. However, the use of both is more robust.

4.4 Conclusion

In this chapter a robust paper-based reverse group test is presented. Here, a droplet of reagent RBCs mixed with patient plasma, and a droplet of this mixture is deposited on paper. The appearance of the stain created indicates a positive or a negative agglutination reaction, which is used to determine the reverse blood groups. Two different papers, varying in structure (pore size) and surface chemistry (hydrophobicity) were tested with nine combination of plasma- reagent RBC. The test concept relies on a similar chromatography-like mechanism as the technique presented in chapter 3. This is caused by an additional resistance to the transport of agglutinated RBCs. However, in this case, a greater reproducibility and sensitivity is observed.

A clear result is identifiable within 3 minutes of droplet deposition for both tested papers. However, each paper displayed results differently. For handsheet paper a positive reaction is identified by a significant separation of RBCs from the bulk solution, causing a small red area inside the larger stain. For paper towel, a negative result is identified by a dark ring around the stain's edge. An image processing algorithm was also developed to automatically identify positive and negative results from the appearance of stains.

This test is more reproducible and sensitive than the method presented in chapter 3. This is becuase the slower flow is less likely to breakup weak agglutinates. However, the additional time required makes the test less suitable for automated applications. The high reproducibility with manual methods show potential for remote and small scale applications, where all that is required is a piece of paper towel, reagent RBCs and patient plasma. Although results are clearly readable by eye, inexperienced users may require the use of the developed analysis algorithm that can be easily be implemented with the use of a smart phone. This concept can be engineered into a robust hand held and easy to use paper diagnostics where only the addition of a drop blood is required.

4.5 References

[1] Geoff Daniels and Imelda Bromilow. *Essential Guide to Blood Groups*. Wiley Blackwell, 2014.

[2] Azadeh Nilghaz, Liyuan Zhang, and Wei Shen. Coffee stains on paper. *Chemical Engineering Science*, 129:34–41, 2015.

[3] Rong Cao, Zhirong Pan, Hua Tang, Jing Wu, Junfei Tian, Azadeh Nilghaz, and Miaosi Li. Understanding the coffee-ring effect of red blood cells for engineering paper-based blood analysis devices. *Chemical Engineering Journal*, 391:123522, 2020.

[4] Robert D Deegan, Olgica Bakajin, Todd F Dupont, Greb Huber, Sidney R Nagel, and Thomas A Witten. Capillary flow as the cause of ring stains from dried liquid drops. *Nature*, 389(6653):827–829, 1997.

[5] Duyang Zang, Sujata Tarafdar, Yuri Yu Tarasevich, Moutushi Dutta Choudhury, and Tapati Dutta. Evaporation of a Droplet: From physics to applications. *Physics Reports*, 804:1–56, 2019.

[6] Mohidus Samad Khan, George Thouas, Wei Shen, Gordon Whyte, and Gil Garnier. Paper diagnostic for instantaneous blood typing. *Analytical chemistry*, 82(10):4158–4164, 2010.

[7] H. Bäumler, B. Neu, E. Donath, and H. Kiesewetter. Basic phenomena of red blood cell rouleaux formation. *Biorheology*, 36(5-6):439–442, 1999.

[8] A L Copley and G Stainsby. *Flow Properties of Blood*. Pergamon Press, 1960.

[9] Mark Thiriet. *The Biology and Mechanics of Blood Flows*. Springer, 2008.

[10] G. Barshtein, D. Wajnblum, and S. Yedgar. Kinetics of linear rouleaux formation studied by visual monitoring of red cell dynamic organization. *Biophysical Journal*, 78(5):2470–2474, 2000.

[11] Von Richard Lucas. Ueber das zitgesetz des kapillaren aufstiegs von flüssigkeiten. *Kolloid-Zeitschrift*, 23(1):15–22, 1918.

[12] Edward W Washburn. The dynamics of capillary flow. *Physical Review*, 17(3):273–283, 1921.

Chapter 5

Equilibrium Stain Size

Preface

To better understand and further optimise the diagnostics presented in Chapters 3 and 4, the fundamental mechanisms leading to stain formation of biological fluids must be investigated. In this chapter, the phenomena that determine the final stain size in paper were studied. The final stain size is shown to be representative of fluid properties, and therefore is highly relevant for the design of a variety of low-cost diagnostics. This chapter was published in the Journal of Colloid and Interface Science in 2018. The text was reformatted to be consistent with the remaining sections; no other changes have been made. The article as published is provided in Appendix A.

Effect of protein adsorption on the radial wicking of blood droplets in paper

Michael J Hertaeg, Rico Tabor, Gil Garnier

Published: Journal of Colloid and Interface Science, 528:116–123, 2018

Abstract

Hypotheses: 1) The equilibrium size and characteristics of a radially wicked fluid on porous material such as paper is expected to be dependent on the fluid properties and therefore could serve as a diagnostic tool. 2) The change in wicked stain size between biological fluids is dependent on a change in solid-liquid surface interfacial energy due to protein adsorption.

Experiments: Sessile droplets of increasing volume of blood, its components, and model fluids were deposited onto paper and the equilibrium stain size after coming to a halt was recorded. The contact angle of fluid droplets on model cellulose surfaces was measured to quantify the effect that blood protein adsorption at the solid-liquid interface has on radially wicked equilibrium size. Finally the significance of droplet evaporation for the time scale of interest was analysed.

Findings: The final stain area of all fluids tested on paper scales remarkably linearly with droplet volume. Different fluids were compared and the gradient of this linear relation was measured. Model fluids varying in surface tension and viscosity all behave similarly and exhibit a constant gradient. Blood and its components produce smaller stains, demonstrated by lower gradients. The gradient is a function of protein concentration, thus the mechanism of this phenomenon was identified as protein adsorption at the cellulose-liquid interface. The slope of the area/volume relationship for droplets is an important quantitative mechanistic variable.

Keywords: Blood, Protein, Radial wicking, Protein adsorption, Stain area, Paper, Biodiagnostic

5.1 Introduction

The wicking of fluids through porous media is of fundamental importance in many processes and applications such as printing, textiles, agriculture and more recently the medical field for its applications in paper based blood diagnostic tools [1, 2].

Blood is a suspension of cells that are weakly electrostatically stabilised in plasma, the liquid component of blood. Plasma consists mostly of water (90 wt%), proteins (approximately 6% wt) and a small amount of lipids, carbohydrates and electrolytes [3]. There are different types of proteins in blood of which the most abundant are albumin (38.7 g/L) [4], globulin (25 g/L) and fibrinogen (3 g/L) [3]. The composition and protein concentrations in blood vary greatly as a function of health as well as natural variation among populations [3, 5, 6]. Many blood proteins are surface active and readily adsorb onto surfaces [7]. There are three main types of cells in blood: erythrocytes (red cells), lymphocytes (white cells) and platelets. The majority of cells in blood are red blood cells. Healthy red blood cells are biconcave disks approximately 8 µm in diameter and 3 µm in thickness [8]. The shape, abundance and mechanical properties (deformation) of these cells are responsible for the unique viscoelastic and shear thinning behavior of blood [9]. By centrifugation the majority of cells can be removed from blood allowing the analysis of solely the plasma component. Although plasma exhibits weak viscoelastic properties [10], most analyses assume Newtonian behavior to no significant loss in accuracy. By testing plasma instead of whole blood the effect of protein adsorption can be isolated from the non-Newtonian properties of blood cells as a suspension (shear thinning, viscoelasticity and granularity).

The radial wicking of a drop has been studied previously [11–15]. However all previous studies have considered highly idealised systems ignoring evaporation and the complex properties of multicomponent systems. This study aims to identify the parameters and phenomena controlling the final stain area achieved by a single droplet of blood radially wicking onto paper. This is of direct interest in the development of blood diagnostics for several reasons. The surprising reproducibility and sensitivity of results suggest that drop stain analysis can serve as a convenient and inexpensive method to identify fluid properties. Whether these property changes are caused by protein content, specific antibody-antigen reaction or hematocrit levels will determine the nature of the sensor. The effect of protein concentration is examined here; however, this type of analysis is applicable to many sensing applications. Further a robust fundamental

knowledge of the blood stain/volume relationship on paper/porous media will allow more sensitive, faster and more accurate diagnostic methods to be developed and guide the optimisation of existing devices. This study is also relevant to any system involving the contact or deposition of a wetting liquid over a porous material.

5.2 Experimental Section

5.2.1 Materials

Tests were performed on Kimberly Clark Scott hand towel (4419) and Whatman 41 filter paper. Wet, dry and oven dried (O.D) weights of 100cm^2 sections of paper are given in Table 5.1. The wet and dry thicknesses were also measured. Analytical grade glycerol, and ethanol were purchased from Merck, and Thermo Fisher Scientific, respectively. BSA (bovine serum albumin) solutions were diluted from 30% (wt/v) solutions from BioCSL, PBS (phosphate buffered saline) was made to 0.9 wt% with tablets from Sigma. Human blood with EDTA anti-coagulant was provided by the Australian Red Cross following established best ethics practice. Deionized water for tests and dilutions was purified from tap water with a Direct-Q water purification system to a minimum resistivity of 18.2 MΩcm.

Table 5.1: Paper Properties

Paper	O.D Weight (g)	Std Dev (g)	Dry Weight (g)	Std Dev (g)	Wet Weight (g)	Std Dev (g)	Dry Thickness (µm)	Std Dev (µm)	Wet Thickness (µm)	Std Dev (µm)
Towel	0.2558	0.0030	0.2671	0.0031	0.5537	0.0180	98	2	76	2
Filter	0.8537	0.0065	0.8794	0.0174	1.8086	0.0208	226	5	218	5

5.2.2 Methods

Paper Characterisation

Paper oven dry (O.D) weight was measured using TAPPI standard 412 by placing samples in a 105 °C oven until weight stabilised. The weight at this point was recorded. The given values are the mean of 3 recordings for each type of paper. Dry weight was measured using TAPPI standard 402, where the weight of the samples after equilibration in 23°C 50% relative humidity (RH) conditions for at least 24 hours was measured. The values reported are the mean of 6 recordings for each type of paper. Wet weight was determined using a variation of testing standard TAPPI 441. This involved submersing

the paper in water for 2 hours, then pressing each between two pieces of blotting paper with 2 passes of a 10kg roller to remove excess water. The paper was then weighed. This process was repeated until weight stabilised. The values for wet weight presented in Table 5.1 are the mean of 3 recordings for each type of paper. Wet and dry thicknesses were measured using a L & W micrometer. Thickness values are the mean of 10 measurements.

Equilibrium Stain Size

Reproducible droplets of volume ranging from 2 to 40 µL were created with an adjustable needle and a syringe pump (Figure 5.1a). The syringe pump was used to provide a constant flow rate to the needle which created repeatable small drops. Drop size could be controlled by needle geometry. These droplets were directed onto a paper surface that was suspended in 23°C 50% relative humidity (RH) air. Setup took sufficient time to assume fluids were at room temperature during tests. The paper was then imaged using an Epson perfection V370 office scanner and analysed to give the area of each stain. Droplets were recorded in groups of at least 7 onto one piece of paper that was moved between each drop. The volume of the created droplets was measured 4 times before and after being directed onto paper to ensure the drops' volume remained a constant. Prior to tests with biological fluids, needles were soaked for at least 2 hours in the fluid to be tested. This was to ensure protein adsorption onto the needle's surface was at equilibrium which improved the uniformity of drops. The difference in area between stains and the variation in measured drop volume is given as error bars in Figures 5.2a and b. All property values were found in literature [16–20], except the viscosity and surface tension of blood plasma and BSA solutions, these were measured with an Ostwald viscometer and a pendant drop surface tensiometer [21]. The density of BSA solutions, plasma and PBS were measured using a Mettler Toledo TLE balance and Eppendorf Pipette.

Surface tension results were complicated by the dynamic surface tension of plasma and BSA [22]. This surface tension variation with time has not been well studied and it is unclear how the surface tension of blood and blood components will change during wicking. For the purpose of this study, highly accurate surface tension data was not required, therefore the average recorded surface tension over a relevant time scale (10-15 seconds) is reported.

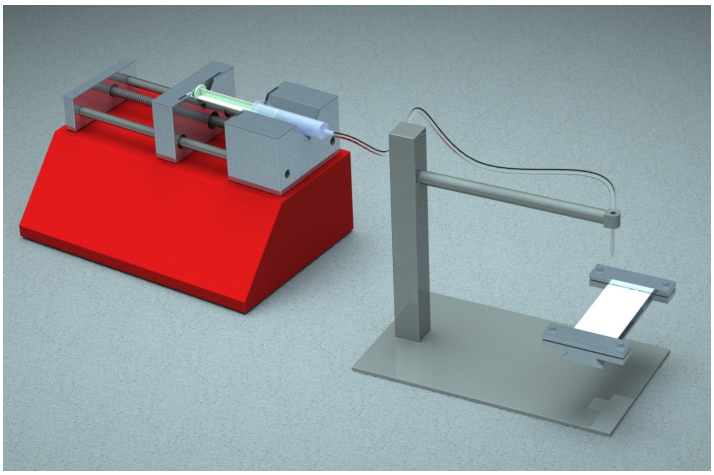

(a)

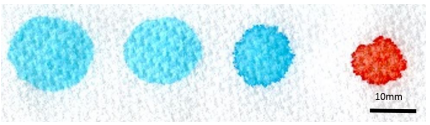

(b)

Figure 5.1: a) Diagram of the experimental system depositing sessile droplets of controlled volume on paper. b) Stains produced from
8 µL droplets of different fluids on paper at identical ambient conditions. From left to right: 25% glycerol, 20% Ethanol, plasma and whole blood. Colourless fluids have blue dye (3wt%) added to aid visualisation.

Contact Angle Measurements

Cellulose thin films were prepared by regenerating spin coated cellulose acetate as previously described [23, 24]. A 0.5 wt% solution of cellulose acetate was spin coated onto a plasma cleaned glass slides at 2000 RPM for 20 seconds. These slides were then regenerated from cellulose acetate to cellulose by soaking in a 0.5% sodium methoxide solution for 10 hours. The advancing contact angle was determined using a DataPhysics OCA35 contact angle instrument by taking measurements at several points as liquid was pumped into the drop at a rate of 20 µL/s. For each batch of cellulose films, this test was repeated at least three times for each fluid, and three batches of cellulose films were tested. Roughness measurements using a JPK Nanowizard 3 atomic force microscope were completed on 4 of the cellulose surfaces; the roughness value reported is the mean of these 4 values.

Drying Time Measurement

Tests were completed by suspending a paper towel sample in a digital scale and recording the weight as a function of time. This allowed the rate of evaporation to be measured. The drop size used was 8 µL and the tests were performed at 23°C 50% relative humidity (RH). The fluids tested were PBS (phosphate buffered saline), 10% BSA (bovine serum albumin), water and plasma.

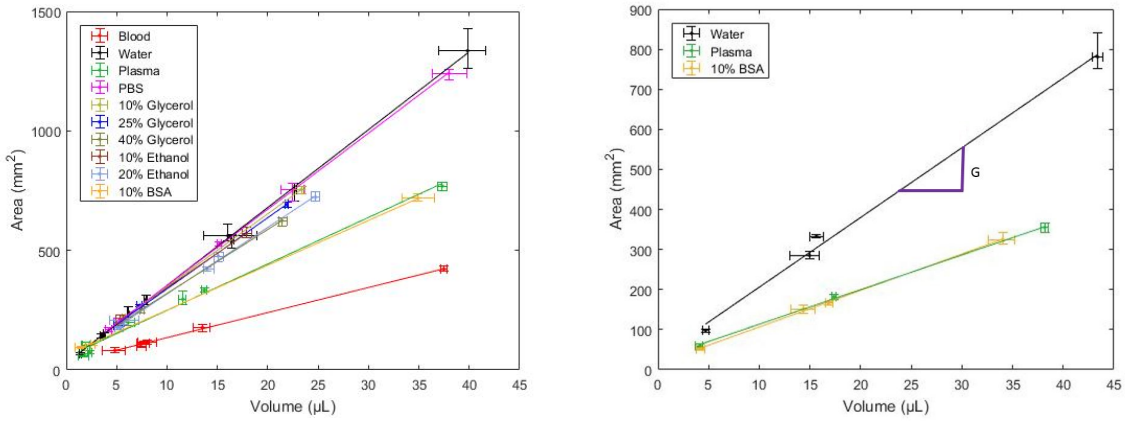

(a) (b)

Figure 5.2: Effect of initial droplet volume on equilibrium stain area on paper hand towel for blood components and model fluids. The average, minimum and maximum area/volume of at least 7 droplets are shown. All measurements were performed at 23 °C 50% RH. (a) All fluids on paper hand towel and (b) a selection of fluids on filter paper.

5.3 Results

Droplets varying in volume were deposited on paper and the area of the stain at equilibrium was measured for a series of fluids. Blood, blood components and model fluids varying in viscosity and surface tension were tested under standard humidity and temperature conditions. The size, shape, perimeter fractal and colour intensity distribution of the stains on paper vary among the different fluids of the same volume (Figure 5.1b). However, size is the most important variable of these stains. The average, maximum and minimum values for stain size and drop volume for a minimum of 7 replicates are shown in Figures 5.2a and b. Linear trend lines are fitted for reference.

5.3.1 Equilibrium Stain Size

Figure 5.2a shows the equilibrium stain size for all tested fluids deposited on paper hand towel, where Figure 5.2b shows a selection of these fluids on filter paper. The stain area of a droplet on paper is surprisingly reproducible and scales linearly with volume. All fluids tested show a similar linear trend however with a shift in slope or gradient. At constant drop volume, whole blood creates the smallest stain, followed by plasma. The stain area at equilibrium can be expressed as:

$$A = GV + C \tag{5.1}$$

Where A is the equilibrium area (mm^2), V is the drop volume (µL), G is the gradient of stain area to drop volume ($\frac{1}{m}$) and C is a constant (mm^2). The calculated value of C range between 74 and 20 mm^2. This value is slightly larger than the average error in area measurements and is always positive.

The gradient G varies significantly between the different fluids and papers. The gradient values for the model fluids on hand towel as well as the fluid properties are presented in Table 5.2. The gradient value does not correlate with the fluid surface tension or viscosity significantly.

5.3.2 Effect of Protein Concentration

Figure 5.3a shows the gradient values for solutions of different concentrations of BSA on the paper hand towel. These results were collected in the same way as results in 5.2a and b. The gradient of the lines is plotted against BSA concentration. The gradient decreases in a roughly inverse square root fashion with BSA concentration. A faster changing gradient is seen at lower BSA concentrations. This might indicate some adsorption surface saturation mechanism.

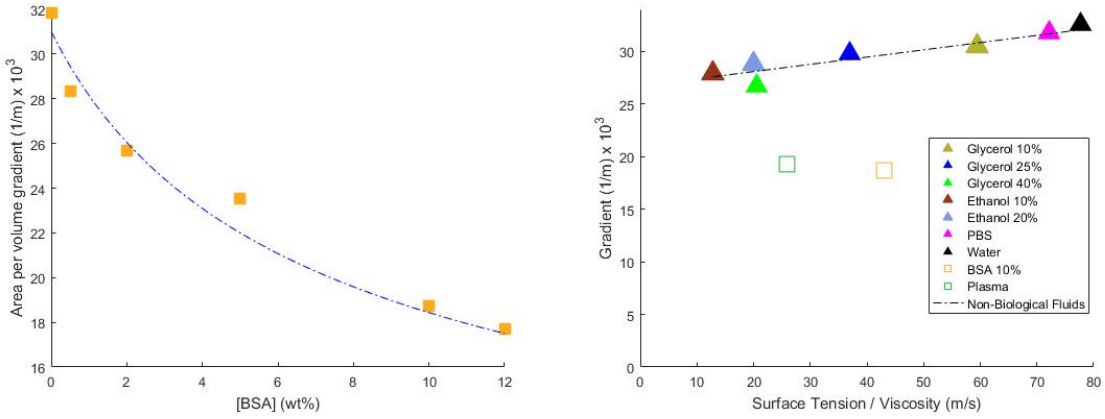

(a) (b)

Figure 5.3: (a) The droplet area/volume gradient plotted as a function of protein concentration for a series of BSA solutions. A trend line has been drawn to guide the eye. (b) Effect of surface tension to viscosity ratio on the stain area to drop volume gradient. A linear trend line is fitted for non-biological fluids. Biological fluids do not follow this trend.

5.3.3 Contact Angle Measurements

As different and lower gradients are only seen with biofluids on paper, wetting experiments were performed on smooth cellulose films to understand the effect of wetting. Figure 5.4 shows the advancing contact angle of a series of selected fluids on model cellulose surfaces. Histograms are presented to visually highlight a statistically significant shift in the mean contact angle despite a high amount of variability in results. This variability has a physical meaning as it quantifies both the chemical and physical heterogeneity of the cellulose films. There is a similar increase in the mean contact angle for biological fluids when compared to non biological fluids.

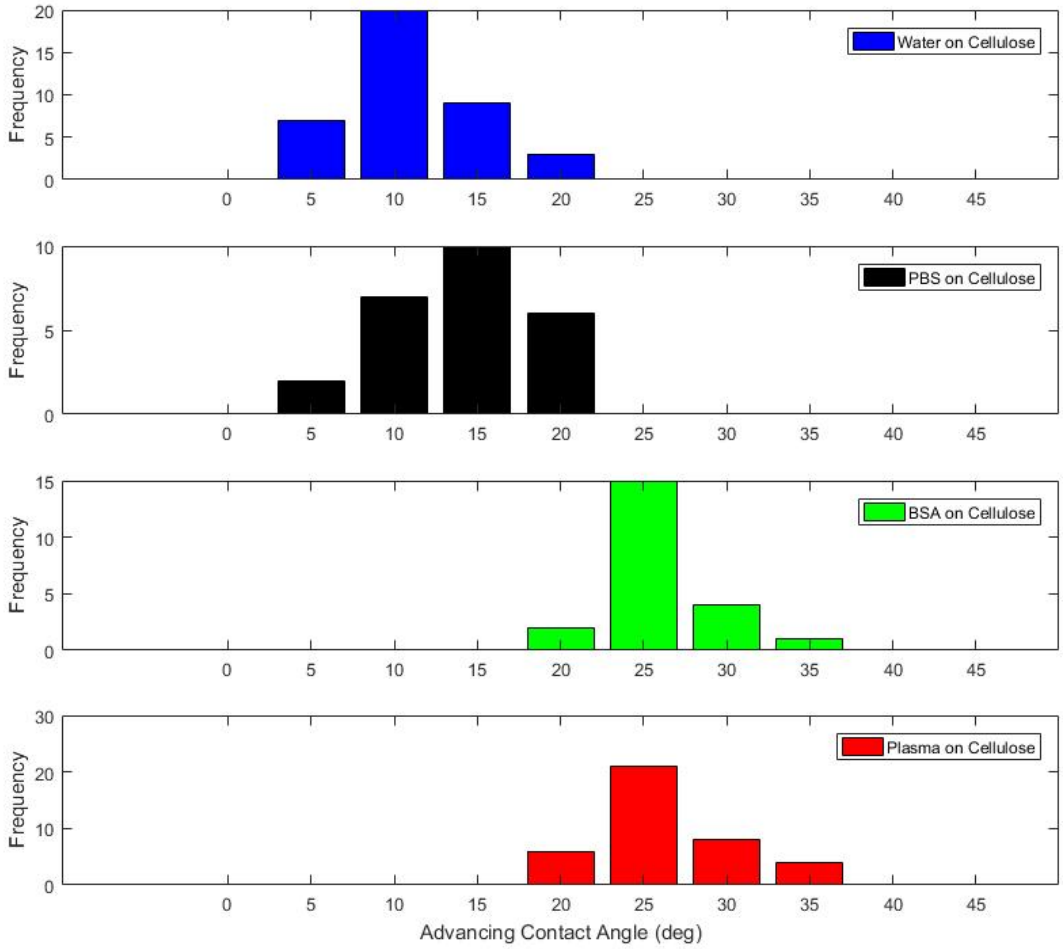

Figure 5.4: Histogram of advancing contact angle measurements for water, PBS and biological fluids on cellulose films.

5.3.4 Time Scale of Evaporation

To simplify matters it was intended to study wicking under conditions independent of liquid evaporation. This was achieved by testing in a conditioned laboratory at 23° C and 50% relative humidity (RH). The effect of droplet evaporation was analysed by measuring the relative weight of a drop deposited onto paper during evaporation. For the time period required for stain growth to fully stop (5-15 seconds) all fluids had evaporated by less than 10%. Water and PBS evaporate at the same rate, while plasma and BSA solutions evaporate similarly but at a slower rate (Figure 5.5).

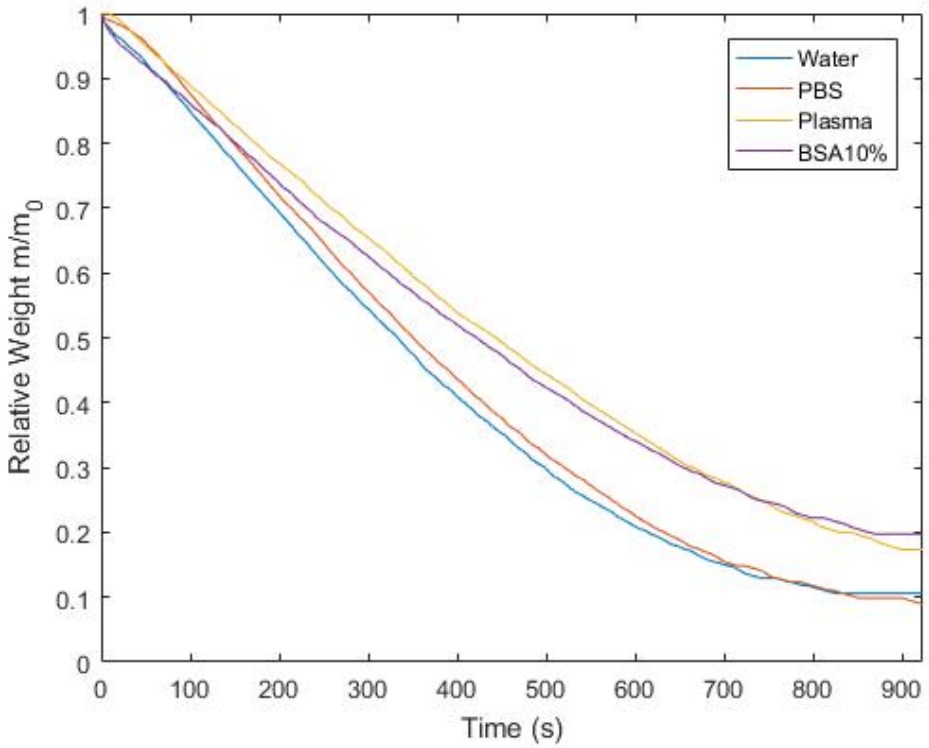

Figure 5.5: Weight of 8 µL drops of tested fluids on paper in 23°C 50% relative humidity air. Y axis is normalised by initial drop weight. All show limited drying at a time where the stain growth was observed to stop, approximately 11 seconds.

5.4 Discussion

5.4.1 Equilibrium Stain Size

Figures 5.2a and b show a clear distinction between the wicking behavior of biological and non-biological fluids on paper. Despite large variations in both surface tension and

viscosity between water, ethanol and glycerol solutions, there is no significant change in gradient. This is surprising as previous research on non-equilibrium radial spreading has shown a strong dependency on the ratio $\frac{\gamma}{\eta}$ [12, 14], although this is not directly comparable to equilibrium results. Figure 5.3b shows the effect of the $\frac{\gamma}{\eta}$ ratio on the gradient of the equilibrium stain area to drop volume curve with all fluid properties presented in Table 5.2. There is a slight dependence of the gradient on the $\frac{\gamma}{\eta}$ ratio for non-biological fluids and a linear function was arbitrarily fitted. Plasma and 10% BSA solution do not follow the trend of model fluids. Table 5.2 also shows that the gradient parameter does not directly scale with either viscosity or surface tension. Although there may be a slight dependence of the stain area/drop volume gradient with the $\frac{\gamma}{\eta}$ ratio, there is another property that presents itself in blood plasma that is far more dominant. This extreme variation in stain sizes between plasma and model fluids was not reported by Li et al. in their experiments with porcine plasma on cotton 'T-shirt' fabric [25]. The gradient for blood is significantly smaller than all tested fluids. The stain area of blood is on average 55% that of plasma using droplets of identical volumes. This finding corroborates the study of Li et al. with porcine blood/plasma who further reported the blood to plasma stain ratio to be equal to one minus the average hematocrit value of blood [25]. The authors relied on this observation to justify the assumption that it is only the volume of the plasma component that determines stain size. Although the value of this repeatable stain size ratio between blood and plasma is intriguing, it is unlikely that the red blood cells have no effect on the wicking process. Other causes of the smaller stain size for blood could include blood cells form blockages in the smaller pores of paper, or electrostatic repulsion between the negatively charged red blood cells [26] and the anionic cellulose [27]; however this is unlikely to be significant due to the micro scale of red blood cells.

Table 5.2: Fluid Properties at 23°C effecting wicking behavior [16–20]

Solution	wt%	Density (kg/m^3x 10^3)	γ (mN/m)	η (mPa.s)	γ/η (m/s)	Gradient ($1/mx10^3$)
Water	100%	1.00 [16]	72.31 [28]	0.93 [16]	77.75	32.6
Glycerol	10%	1.02 [18]	71.97 [19]	1.21[18]	59.48	30.5
Glycerol	25%	1.06 [18]	70.95 [19]	1.92[18]	36.95	29.8
Glycerol	40%	1.10 [18]	69.61 [19]	3.40[18]	20.47	26.7
Ethanol	10%	0.96 [17]	39.29[17]	1.96[17]	20.0	28.8
Ethanol	20%	0.93 [17]	32.27[17]	2.52[17]	12.8	27.9
Plasma	100%	1.01	45	1.74	25.9	19.4
BSA	10%	1.01	40	0.93	43.0	18.7
PBS		1.00	72.2 [20]	1.00 [20]	72.2	31.8

Stains on different papers can be compared by defining a new variable, the paper ratio factor (PRF). This is calculated as the gradient of the stain area to volume relationship on a certain paper, divided by the gradient of the same fluid on a different reference paper (equation 5.2). Table 5.3 compares the PRF values on hand towel and filter paper for 3 fluids. If the two papers were to behave identically, simple volume conservation analysis reveals that the PRF should be equal to the ratio of the two paper thicknesses. This ratio was measured by micrometer and found to be 2.26.

$$PRF = G_{HandTowel}/G_{FilterPaper} \tag{5.2}$$

Table 5.3: Paper Ratio Factor (no unit). Filter paper is used as reference paper.

Fluid	PRF
Water	1.87
Plasma	2.25
10% BSA	2.06

Although plasma and BSA have PRF factors close to 2.26, water shows a slightly lower than expected ratio. This implies that water and biological fluids are affected differently by the change in paper properties.

Schuchard et al. reported fiber swelling to be an important parameter to consider for wicking in cellulose networks [29]. All fluids used in this study are water-based and therefore will swell cellulose; however, it is not clear if there is a difference in swelling among fluids and whether this would cause a change in stain area. This could be the cause of the shifts in PRF value between fluids as paper type may affect the extent of fiber swelling.

5.4.2 Effect of Evaporation

The linearity of the equilibrium stain area with drop volume relationship (Figure 5.2a) implies the absence of any significant evaporation. If evaporation was taking place, a plateau would be expected at the higher drop sizes. This is further shown by drying time experiments in which the weight after fluid contact with paper was measured with time. No significant drying occurs in the time frame of wicking, which range between 5 and 15 s in this study. Therefore evaporation is insignificant for the system studied. Measurements with water, plasma, PBS and BSA solutions all show similar behavior.

This differs from expectations from literature. Gilespie [13] predicted that a wicked stain equilibrium area would only be detectable when evaporation is significant. It might be possible that the measured apparent equilibrium position is actually a state where the front is moving so slowly that its motion is unobservable and the final position is the effect of drying after a significant time.

Nilghaz et al. [30] demonstrated that coffee rings [31] form on paper in some situations. As the mechanism of coffee ring formation is dependent on a pinned outer edge [32], and the effects of surface pinning are not included in models that predict indefinite spreading, pinning may be a determining factor in stain equilibrium size.

5.4.3 Wetting Mechanism

Advancing contact angle measurements were performed on model cellulose films. The contact angle data can be used with the Young equation [33] (equation 5.3), to determine the interfacial energy at the solid liquid interface. Equation 5.4 accounts for surface roughness [34]. The value for the cellulose-air interfacial energy γ_{sv} used is 69.0 mN/m. This value is the mean of the two testing methods for the surface energy of untreated cellulose fibers by Westerlind and Berg [35] and is very close to the value also found by Niegelhell et al. [36]. The roughness used in calculations was measured by atomic force microscopy to be 1.16. Roughness is defined as the real surface area divided by the surface area of a smooth surface of the same dimensions.

$$\gamma_{sv} = \gamma_{sl} + \gamma_{lv} \cos\theta \tag{5.3}$$

Where γ_{sv}, γ_{sl} and γ_{lv} are the solid-vapour, solid-liquid and liquid-vapour surface tensions respectively.

$$\cos\theta_{app} = r \cos\theta_r \tag{5.4}$$

Where θ_{app} is the apparent measured contact angle, r is the roughness of the substrate and θ_r is the real contact angle that can be used in the Young equation. The solid-liquid interfacial energies calculated are presented in Table 5.4. Results from PBS are calculated to demonstrate the negligible effect of ionic strength on wetting.

Table 5.4: Liquid solid interfacial energy measured from wetting experiments for the different fluids on cellulose films

Fluid	Mean advancing contact angle ($degrees$)	Solid-liquid interfacial energy (mN/m)
Water	13.5	8.4
PBS	16.6	9.3
BSA 10%	28.4	38.6
Plasma	28.9	35.0

The equilibrium stain size of 0% BSA or 100% PBS are similar to tests with water, which shows that the effect of salinity is negligible.

5.4.4 Protein Adsorption

Surface energy measurements show the solid liquid surface energy to be significantly raised by high protein concentrations in the droplet solution. Fluids exhibiting similar stain sizes, such as 10% BSA and plasma also have very similar surface energies. This suggests a relationship between stain size and the solid-liquid interfacial energy which is affected by protein content in the fluid. This is most likely caused by protein adsorption onto the cellulose surface.

The adsorption of BSA and human immunoglobulin G onto cellulose was previously demonstrated [7]. This adsorption of blood proteins was shown to make cellulose more hydrophobic after aging and drying [23]. This augmented hydrophobicity is caused by an increase in solid-liquid interfacial energy at the cellulose interface due to a protein conformation change. The increased solid-liquid interfacial energy calculated here is likely caused by a similar mechanism although contact angle measurements were performed with the protein solution, not water after drying as in previous studies. An increase in cellulose-fluid interfacial energy would cause a decrease in stain area as the formation of such an interface is energetically unfavorable.

As a wicking system is in motion the transportation of solution components is not necessarily homogeneous due to adsorption and diffusive variations. Such variations can effect wicking of surfactant solutions [37]. The surface energies calculated for static drops in equilibrium presented may not directly translate to transient wicking analysis. It is also unknown how the addition of protein will affect fiber swelling.

Interpolating from the trend in Figure 5.3a, plasma behavior is similar to a solution having a BSA concentration of 8.3%. This value differs from the average concentration of albumin in human plasma which is 3.9% [4], with normal values ranging from 3.2% to 4.5% [5]. Although albumin concentration is likely to be a factor affecting plasma equilibrium wicked area, it is not the only factor.

Albumin represents only 60-65% by weight of blood plasma proteins [6]; there are many other blood proteins capable of adsorbing onto cellulose [7]. The concentration of all proteins in plasma is approximately 6.2%. Comparing this value to the plasma similar BSA solution concentration (8.3%) reveals that either non-albumin proteins effect equilibrium on a per weight basis more than albumin, or there is another factor that has not been investigated, such as the competitive binding of phosphate ions from PBS [38].

5.5 Conclusion

A series of small droplets of blood and model fluids were deposited onto paper and the stain area to drop volume was measured for droplets of increasing volume. The model fluids studied consist of a selection of simple fluids varying in surface tension and viscosity, as well as blood plasma and protein solutions of different concentrations. The stain area-droplet volume relationship was studied. This was performed under controlled conditions (23 °C and 50% RH) under which evaporation was negligible. To better distinguish the effect of wetting from radial wicking in a porous material, the contact angle of plasma and water were measured over smooth cellulose films.

The area of the stain achieved by the radial wicking of a droplet of controlled volume deposited onto paper is very reproducible. Stain area scales linearly with droplet volume. The slope of the stain area-droplet volume relationship (gradient) is indicative of the fluid composition and the paper structure. The gradient is however nearly independent of fluid viscosity and surface tension. Blood has the lowest gradient, followed by plasma, protein solutions and the model simple fluids each having nearly identical slopes. This different behaviour was attributed to the adsorption of protein onto paper, affecting the solid-liquid (γ_{sl}) interfacial energy. The protein content of BSA solutions and blood was found to strongly effect the gradient and therefore the equilibrium stain size. This is due to the increase in surface energy that occurs after protein adsorption onto the cellulose fluid interface. Previous studies have shown that the ratio of surface

tension to viscosity is a critical parameter for situations under non-equilibrium wicking conditions [12–14]. However, our results were found to be almost independent of the ratio. The paper ratio factor (PRF) is proposed as a new measure of the relative stain sizes in different papers and is compared to the ratio of thicknesses to identify effects from paper structure.

The reproducibility of stain area-droplet volume on paper, its ease of measurement combined with the slope (gradient) being a function of fluid properties all make blood stain analysis very attractive for diagnostic applications. Blood stain analysis could become the basis for a new generation of high throughput and very fast blood diagnostic systems.

5.6 Acknowledgments

This research was funded by an ARC Linkage grant (LP160100544) and Haemokinesis.

5.7 References

[1] Mohammad Al-Tamimi, Wei Shen, Rania Zeineddine, Huy Tran, and Gil Garnier. Validation of paper-based assay for rapid blood typing. *Analytical Chemistry*, 84(3):1661–1668, 2012.

[2] W L Then, Miaosi Li, Heather McLiesh, Wei Shen, and Gil Garnier. The detection of blood group phenotypes using paper diagnostics. *Vox Sanguinis*, 108(2):186–196, 2015.

[3] Ruoyang Chen, Liyuan Zhang, Duyang Zang, and Wei Shen. Blood drop patterns: Formation and applications. *Advances in colloid and interface science*, 231:1–14, 2016.

[4] David J. Greenblatt. Reduced Serum Albumin Concentration in the Elderly: A Report from the Boston Collaborative Drug Surveillance Program. *Journal of the American Geriatrics Society*, 27(1):20–22, 1979.

[5] Basem N Azab, Vijaya R Bhatt, Steven Vonfrolio, Rana Bachir, Vladimir Rubinshteyn, Homam Alkaied, Ayman Habeshy, Jignesh Patel, Antonio I Picon, and Scott W Bloom. Value of the pretreatment albumin to globulin ratio in predicting

long-term mortality in breast cancer patients. *The American Journal of Surgery*, 206(5):764–770, 2013.

[6] Masaki Otagiri and Victor Tuan Giam Chuang. *Albumin in Medicine: Pathological and Clinical Applications*. Springer, 2016.

[7] Hannes Orelma, Ilari Filpponen, Leena-Sisko Johansson, Janne Laine, and Orlando J Rojas. Modification of cellulose films by adsorption of CMC and chitosan for controlled attachment of biomolecules. *Biomacromolecules*, 12(12):4311–4318, 2011.

[8] Mark Thiriet. *The Biology and Mechanics of Blood Flows*. Springer, 2008.

[9] A L Copley and G Stainsby. *Flow Properties of Blood*. Pergamon Press, 1960.

[10] M Brust, C Schaefer, R Doerr, L Pan, M Garcia, P E Arratia, and C Wagner. Rheology of human blood plasma: Viscoelastic versus Newtonian behavior. *Physical Review Letters*, 110(7):78305, 2013.

[11] KK Borhan, Ali and Rungta. An experimental study of the radial penetration of liquids in thin porous substrates. *Journal of Colloid and Interface Science*, 158(2):403–411, 1993.

[12] Dganit Danino and Abraham Marmur. Radial capillary penetration into paper: limited and unlimited liquid reservoirs. *Journal of Colloid and Interface Science*, 166(1):245–250, 1994.

[13] T. Gillespie. The spreading of low vapor pressure liquids in paper. *Journal of Colloid Science*, 13(1):32–50, 1958.

[14] Erik Kissa. Capillary sorption in fibrous assemblies. *Journal of Colloid and Interface Science*, 83(1):265–272, 1981.

[15] Abraham Marmur. Penetration and displacement in capillary systems of limited size. *Advances in Colloid and Interface Science*, 39:13–33, 1992.

[16] Joseph Kestin, Mordechai Sokolov, and William A Wakeham. Viscosity of liquid water in the range -8 C to 150 C. *Journal of Physical and Chemical Reference Data*, 7(3):941–948, 1978.

[17] Ibrahim Sadek Khattab, Farzana Bandarkar, Mohammad Amin Abolghassemi Fakhree, and Abolghasem Jouyban. Density, viscosity, and surface tension of water

+ ethanol mixtures from 293 to 323K. *Korean Journal of Chemical Engineering*, 29(6):812–817, 2012.

[18] Madison L Sheely. Glycerol viscosity tables. *Industrial & Engineering Chemistry*, 24(9):1060–1064, 2013.

[19] Koichi Takamura, Herbert Fischer, and Norman R Morrow. Physical properties of aqueous glycerol solutions. *Journal of Petroleum Science and Engineering*, 98:50–60, 2012.

[20] Hossein Tavana, Chuan-Hsien Kuo, Qian Yi Lee, Bobak Mosadegh, Dongeun Huh, Paul J Christensen, James B Grotberg, and Shuichi Takayama. Dynamics of liquid plugs of buffer and surfactant solutions in a micro-engineered pulmonary airway model. *Langmuir*, 26(5):3744–3752, 2009.

[21] Joseph D. Berry, Michael J. Neeson, Raymond R. Dagastine, Derek Y.C. C Chan, and Rico F. Tabor. Measurement of surface and interfacial tension using pendant drop tensiometry. *Journal of Colloid and Interface Science*, 454:226–237, 2015.

[22] Sergei Zaitsev. Dynamic surface tension measurements as general approach to the analysis of animal blood plasma and serum. *Advances in colloid and interface science*, 235:201–213, 2016.

[23] Ziwei Huang, Vikram Singh Raghuwanshi, and Gil Garnier. Functionality of immunoglobulin g and immunoglobulin M antibody physisorbed on cellulosic films. *Frontiers in bioengineering and biotechnology*, 5:41, 2017.

[24] Jielong Su, Christopher J Garvey, Stephen Holt, Rico F Tabor, Bjorn Winther-Jensen, Warren Batchelor, and Gil Garnier. Adsorption of cationic polyacrylamide at the cellulose–liquid interface: A neutron reflectometry study. *Journal of Colloid and Interface Science*, 448:88–99, 2015.

[25] Jingyao Li, Xingyu Li, and Stephen Michielsen. Alternative method for determining the original drop volume of bloodstains on knit fabrics. *Forensic science international*, 263:194–203, 2016.

[26] Hsueh-Chia Chang. Electrokinetic transport of red blood cells in microcapillaries. *Electrophoresis*, 23:2165–2173, 2002.

[27] Chuantao Zhu, Illia Dobryden, Jens Ryde n, Sven Oberg, Allan Holmgren, and Aji Mathew. Adsorption behavior of cellulose and its derivatives toward Ag (I) in aqueous medium: An AFM, spectroscopic, and DFT study. *Langmuir*, 31(45):12390–12400, 2015.

[28] Gonzalo Vazquez, Estrella Alvarez, and Jose M Navaza. Surface tension of alcohol water+ water from 20 to 50. degree. C. *Journal of chemical and engineering data*, 40(3):611–614, 1995.

[29] David R Schuchard and John C Berg. Liquid transport in composite cellulose—superabsorbent fiber networks. *Wood and Fiber Science*, 23(3):342–357, 2007.

[30] Azadeh Nilghaz, Liyuan Zhang, and Wei Shen. Coffee stains on paper. *Chemical Engineering Science*, 129:34–41, 2015.

[31] Robert D Deegan, Olgica Bakajin, Todd F Dupont, Greb Huber, Sidney R Nagel, and Thomas A Witten. Capillary flow as the cause of ring stains from dried liquid drops. *Nature*, 389(6653):827–829, 1997.

[32] Ruoyang Chen, Liyuan Zhang, Duyang Zang, and Wei Shen. Wetting and Drying of Colloidal Droplets: Physics and Pattern Formation. *Advances in Colloid Science*, pages 3–25, 2016.

[33] Thomas Young. An essay on the cohesion of fluids. *Philosophical Transactions of the Royal Society of London*, 95:65–87, 1805.

[34] David Brutin. *Droplet wetting and evaporation: from pure to complex fluids*. Academic Press, 2015.

[35] Bo S Westerlind and John C Berg. Surface energy of untreated and surface-modified cellulose fibers. *Journal of Applied Polymer Science*, 36(3):523–534, 1988.

[36] Katrin Niegelhell, Michael Sussenbacher, Jurgen Sattelkow, Harald Plank, Yonggui Wang, Kai Zhang, and Stefan Spirk. How Bound and Free Fatty Acids in Cellulose Films Impact Nonspecific Protein Adsorption. *Biomacromolecules*, 18(12):4224–4231, 2017.

[37] Kevin T Hodgson and John C Berg. The effect of surfactants on wicking flow in fiber networks. *Journal of colloid and interface science*, 121(1):22–31, 1988.

[38] Zhengpeng Yang and Chunjing Zhang. Adsorption/desorption behavior of protein on nanosized hydroxyapatite coatings: a quartz crystal microbalance study. *Applied Surface Science*, 255(8):4569–4574, 2009.

Chapter 6

Transient Stain Growth

Preface

Many paper-based diagnostic techniques and devices use droplet deposition as a simple method to introduce reagents or carrier fluids. This is a complex process because it involves the transition from a saturated system (droplet in contact with paper) and unsaturated (droplet absorbed) characterised by different mechanisms leading to varying behaviour. In this chapter, the radial wicking of a droplet of fluid varying in viscosity and surface tension is characterised on paper. The dynamics of the stage transition is highlighted and a numerical model capable of predicting behaviour before and after stage transition is derived. This chapter was published in the Journal of Colloid and Interface Science in 2019. The text was reformatted to be consistent with the remaining sections; no other changes have been made. The article as published is provided in Appendix A.

Dynamics of stain growth from sessile droplets on paper

Michael J. Hertaeg, Rico F. Tabor, Joseph D. Berry, Gil Garnier

Published: Journal of Colloid and Interface Science, 541:312-321, 2019

Abstract

Hypothesis: The rate of stain growth of a sessile droplet deposited on paper has been previously studied [1–4] but is not fully understood. In particular, the mechanism by which the abrupt decrease in growth rate occurs is unknown. This process is expected to follow a model where the disappearance of the droplet is represented by a change to the boundary condition at the droplet-paper interface when the volume of the fluid inside the paper is equal to the volume of the simulated droplet.

Experiments: The stain size of sessile droplets on paper was monitored against time. A series of fluids varying in surface tension and viscosity was studied. The kinetics of stain growth was modelled and compared with experiments and existing models of stain growth.

Findings: The measured stain area formed by a sessile droplet deposited on paper follows a two regime mechanism [2]. In the initial regime, the dynamics are governed by the filling of pores. However, in the later stage, the process is influenced by the emptying/redistribution of fluid. Simulations show that experimental results are well described by a model that identifies the change in boundary conditions after the droplet is no longer present above the paper, coupled with the change to a redistribution dominated mechanism.

Keywords: Radial wicking, Stain area, Paper, Wetting, Kinetics, Modelling, Sessile droplets

6.1 Introduction

Wicking has been described for many years by the Lucas-Washburn equation [5, 6]. This model assumes the substrate material to be a collection of cylindrical capillaries and gives fairly good correlation with experimental results in a variety of porous materials [7, 8]. However, there are several critical and restrictive simplifications required that prevent generalisation of the model to all wicking applications. The two most notable assumptions of the Lucas-Washburn equation are: i) the unidirectional requirements and ii) the definition of a sharp interface where the material transitions from 100% saturated to 0% saturated at the wicking front. These two assumptions do not apply for many systems including droplets wicking on paper. To overcome these simplifications, previous researchers have derived relations based on Darcy's law for flow through porous media. These approaches allow for the description of wicking in complex geometries and semi-saturated media and are used in the design of many paper-based diagnostic devices [9].

The deposition of a droplet of liquid onto the surface of a thin porous material like paper is a special wicking case that has received particular attention. Droplets wicking on porous media and the kinetics of stain growth play a critical role in many industrial applications, including printing for communication and functional uses such as biodiagnostic manufacturing. Fundamentally, modelling the kinetics of droplet wicking, from sessile droplet to stain at equilibrium, has remained a complex and elusive task. This process is different from the case of a infinite reservoir system because at some finite time after deposition, the droplet will completely be absorbed by the paper, changing the nature of the process significantly. These two stages are usually referred to as stage one (droplet disappearing from the surface of the paper) and stage two (absorbed droplet redistributing/wicking in paper). As stage two is much longer than stage one, most of the models have been focused there. Many models based on Darcy's law have been proposed. However, all have relied on many empiricisms to fit results [1, 2, 10, 11]. All of these relations can be broadly expressed in the functional form:

$$A \propto t^m, \tag{6.1}$$

where A is the wetted area, t the time after deposition and m is a constant. The evolution of the stain area produced by a wicking droplet is quite well represented by this power law. However, the value of m is higher in the first stage than in the second stage. The stated values of m for each stage vary but are in the range of 0.39 - 0.50 for

the first stage and 0.10 - 0.33 for the second stage [1–4]. These discrepancies have been attributed to differences between fluids, droplet sizes, absorption by fibers, temperature and humidity; however, no model has been able to explain the large variation reported.

Marmur [12] presented an analytical model for radial wicking where the material is modelled as a gap between two plates with liquid being introduced from a hole in the center of the top plate. Marmur's equation expressed in terms of area [4] is given as:

$$\frac{A}{A_o}(\ln\frac{A}{A_o}-1) = -1 + (\frac{2\pi d\gamma\cos\theta}{3A_o\mu})t. \tag{6.2}$$

Here A is wetted area, A_o is the area of the inlet, d is the separation of the two plates, γ is the liquid-vapour surface tension of the liquid, θ is the contact angle and μ is the viscosity. This approach is similar to that of Lucas and Washburn as it also assumes a sharp interface. Despite this, the equation predicts radial wicking behavior from infinite reservoirs quite well [2, 4] and results from Danino and Marmur [2] imply that it also can be used to model stage one of droplet wicking. For the droplet wicking case, it is not clear what value to use for A_o; however, the fitted values are physically reasonable.

The effectiveness of Marmur's equation in predicting stage one behavior implies that the distribution of fluid creates an abrupt transition between fully saturated and dry paper. However, after the consumption of the reservoir (stage two), liquid motion is primarily driven by the redistribution effect [13] which is why Marmur's equation is no longer appropriate. The redistribution effect is the emptying of initially filled large pores into smaller pores due to the higher capillary pressures there. Our previous work has identified that this motion will continue until a position is reached that is determined by the system's solid-liquid interfacial energy [14].

Several numerical studies have predicted wicking behavior from infinite reservoirs using Richards' equation, developed to determine liquid distribution in soils [15–18]. Some of these studies simulate radial wicking and correlate well with both experimental results and Marmur's relation (equation 6.2). The present work applies previously developed numerical schemes to model the radial wicking of fluid from a sessile droplet. This is done by applying the same Dirichlet (saturated) boundary conditions [19] used for infinite systems at the droplet interface until the simulated droplet is consumed. After this a Neumann (no flux) boundary condition [19] is used.

It is the objective of this study to measure and model the wicking dynamics of a sessile droplet deposited onto paper. We also aim to identify and quantify the mechanisms controlling the stain growth in paper. This knowledge is required to engineer accurate and predictive paper diagnostics for biomedical applications [20]. A secondary objective of the study is to develop a rigorous, accurate and physically meaningful alternative to the Lucas-Washburn equation.

6.2 Methods

6.2.1 Simulation

Model Development

Richards' equation can be described as Darcy's law with allowances for mass conservation where the permeability of the porous material is proportional to the local volume fraction [21],

$$\frac{\partial \phi}{\partial t} = \nabla \cdot \left(\frac{K(\phi)}{\mu} \nabla P \right) \tag{6.3}$$

here ϕ is the relative volume fraction expressed relative to maximum saturation $\phi = \epsilon/\epsilon_s$, ϵ is the volume fraction expressed in volume of fluid per volume of paper and ϵ_s is the saturated volume fraction, $K(\phi)$ is the permeability as a function of volume fraction, μ is viscosity and P is pressure.

In a wicking situation where there is no externally applied pressure gradient and gravitational effects can be ignored, pressure variation is caused solely by Laplace pressure at liquid-vapour interfaces. This pressure will be a function of volume fraction as the liquid-vapour interfaces will be in small pores with higher Laplace pressures at low volume fractions, and will move to large pores with lower Laplace pressures at high volume fractions. With this, equation 6.3 becomes the diffusion equation where diffusivity is a simple function of pressure, permeability and viscosity:

$$\frac{\partial \phi}{\partial t} = \nabla \cdot \left(\frac{D(\phi)}{\mu} \nabla \phi \right), \tag{6.4}$$

$$D(\phi) = K(\phi) \frac{\partial P(\phi)}{\partial \phi}. \tag{6.5}$$

This approach was verified by several previous studies [15–18]. However, each of those used a different function for permeability and pressure distribution. One of the simplest

systems of constitutive equations for permeability and pressure was implemented by Perez-Cruz [15] and is reproduced here. This model expresses the combined effects of varying pressure and permeability as an effective scaled diffusivity. Due to the factor of viscosity in equation 6.4, $D(\phi)$ is not a true diffusivity and therefore does not have the units m^2/s. This scaled diffusivity can be expressed as a power law relation with volume fraction [15]:

$$D(\phi) = D_0\phi^n \tag{6.6}$$

Where D_0 is the viscosity scaled diffusivity at saturation and n is a constant calculated from a substrate's pore size distribution index [22]. Perez-Cruz fit n to results. However, pore size distribution index (λ), and therefore n, can be calculated by fitting equation 6.7 to experimental porosimetry data (Figure 6.3):

$$\phi = (\frac{P(\phi)}{P_c})^{-\lambda}, \tag{6.7}$$

$$n = 2 + \frac{2}{\lambda}, \tag{6.8}$$

where P_c is atmospheric pressure. These relations are based on the Brooks Corey model for water penetration in soils [22].

Model Implementation

The solution of equation 6.4 was carried out in arb, an open source finite volume solver [23] on a two-dimensional axisymmetric domain (Figure 6.1). Boundary conditions were initially no flux on all external edges, except the top region covered by the droplet at $0 > r > R_0$. Here, the value of phi was fixed at the saturation value of the material until the total volume of liquid in the domain reaches the volume of the simulated droplet at $t = t_{abs}$. For $t > t_{abs}$ the boundary condition at the droplet interface was changed to the zero flux condition. This procedure simulates the transition from stage one to stage two radial wicking where the droplet disappears from the surface of the paper. This process ignores the changes in droplet radius discussed in previous literature [24] as the effects on larger scale behavior are secondary. A structured mesh was used to better capture the sharp front that is created, with four divisions used in the vertical direction as the problem is essentially one-dimensional. This is because the small thickness of the paper relative to its length means that vertical equilibrium occurs so quickly that a one-dimensional simulation would have also been appropriate. A two-dimensional domain was however investigated to make the initial surface saturation boundary condition where the droplet resides more intuitive. The results of a mesh refinement study are

shown in supplementary information for an n value of 8. This value was chosen as it is higher than any n value used in results and therefore represents a worst case, where the simulation would be most dependent on mesh quality. This is because higher n values cause a sharper interface to form. A mesh spacing of $\delta x = 0.02R_0$ was chosen as this kept simulations to a reasonable time and corresponded to less than a 5% variation from the finest mesh tested. To simulate the first stage a time step $\delta t = 0.01$ s was chosen to ensure that t_{abs} was calculated to sufficient accuracy. During the second stage the time step was increased incrementally to a maximum of 0.04 s to save computational time. Time step sensitivity analysis of the same test case as the mesh resolution study was carried out, showing that the choice of $\delta t = 0.01$ s - 0.04 s was sufficient for accuracy and stability of the numerical solution.

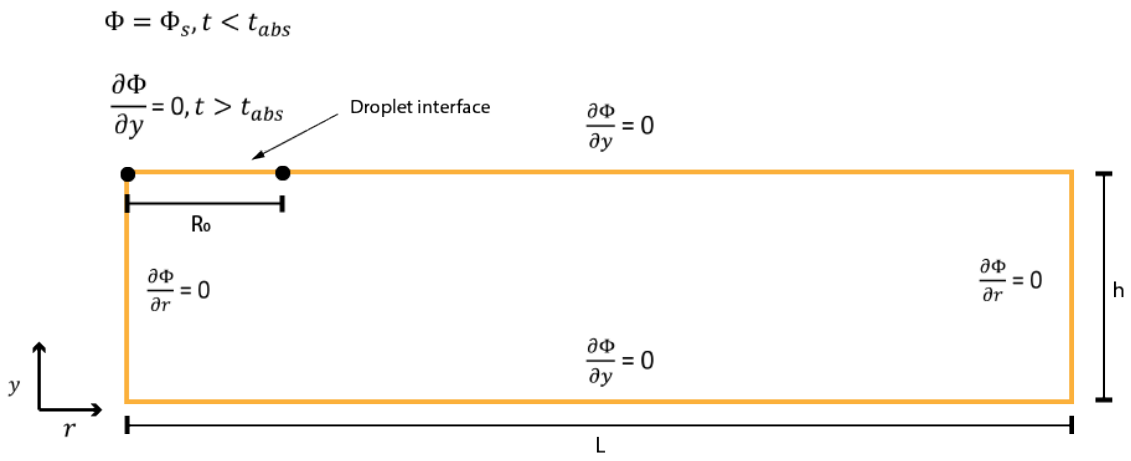

Figure 6.1: Diagram of simulation domain with implemented boundary conditions.

Stain boundary was calculated by identifying a radial position that corresponded to a relative volume fraction (ϕ) of 0.01. As volume fraction decreases extremely quickly near the edge of a stain, the criterion of stain front definition did not affect results. This model uses 7 input parameters: V_D droplet volume, μ viscosity, h paper thickness, D_0 diffusivity at maximum saturation, n linear function of pore distribution index, A_0 initial droplet area and ϵ_s saturation volume fraction. While some of these parameters can be directly measured and some must be fitted, all have a physical meaning in the first stage of the simulation. As n is only based on pore distribution index in the first stage it is an empirical fitting parameter in the second.

6.2.2 Experimental

Materials

Analytical grade glycerol, decane and ethanol were purchased from Merck, Sigma and Thermo Fisher Scientific, respectively. Densities of glycerol, decane and ethanol solutions were interpolated from data measured by Sheely [25], Liu et. al [26] and Khattab et. al [27] respectively. Tests were performed on Whatman 41 filter paper and Advantec GA-55 glass fiber filters. Deionized water for tests and dilutions was purified from tap water with a Direct-Q water purification system to a minimum resistivity of 18.2 MΩ·cm. Queens blue food dye was used to dye water soluble fluids.

Methods

Droplets were produced with an adjustable needle and a syringe pump in the same way as our previous study [14]. The syringe pump provided a constant flow rate to the needle which causes droplets of repeatable size to detach and periodically fall from the needle. Droplet size was quantified using a Mettler Toledo TLE balance before the needle was directed onto the paper surface. The average weight of 4 previous droplets divided by the density of the fluid was used to estimate the volume of the droplet that fell onto the paper. Droplet size was controlled by altering needle size. Stain size data were recorded by a Point Grey Flea3 camera mounted on a track that captured the reflected bottom view of the paper. The images were captured at 120 frames per second. A diagram of the experimental setup is shown in Figure 6.2. All tests were performed in a 23°C 50% relative humidity environment. To improve contrast, 3 wt% of food dye solution was added to the aqueous solutions. Tests were performed to ensure the dye at the concentration studied did not affect results. Although the dynamic wicking measurements without dye were prone to noise, there was no significant differences between dyed and not dyed fluids. This dye was assumed to have the same properties as water and was included in solution concentration calculations. Droplet disappearance times were found using a side mounted Phantom VEO 410L high speed camera recording at 4000 fps. No adequate dye was found for decane as all dyes separated chromatographically due to their affinity for cellulose. Due to this, no contrast agent was used and as a result there is more noise in the decane recordings.

Porosimetry

Porosimetry measurements were performed with a mercury porosimeter (Micrometrics AutoPore IV 9500). This characterises the infiltration against pressure. To convert this

into data that can be compared to equation 6.7, the infiltration values were divided by their maximum value; this gave infiltration data relative to maximum saturation. The pressures were converted to a radius and then back to a pressure using the Young-Laplace equation applied on circular capillaries using the surface tension of mercury and then back with the surface tension of water. The values of surface tension and contact angle used are shown in Table 6.1.

Table 6.1: Fluid properties used

Fluid	wt%	Density ($kg/m^3 x10^3$)	Surface Tension (mN/m)	Viscosity (mPa·s)	Advancing contact angle (deg)
Mercury	100%		485[28]		130[28]
Water	100%	1.00[29]	72.31[30]	0.93[29]	13.5[14]
Glycerol	10%	1.02[25]	71.97[31]	1.21[25]	
Glycerol	20%	1.05[25]	71.4 [31]	1.63 [25]	
Glycerol	40%	1.10[25]	69.6[31]	3.40[25]	
Glycerol	60%	1.15[25]	68.1 [31]	9.63[25]	
Ethanol	20%	0.93[27]	32.27[27]	2.52[27]	
Ethanol	40%	0.89[27]	27.65[27]	2.49[27]	
Ethanol	90%	0.80[27]	23.09[27]	1.38 [27]	
Decane	100%	0.73 [26]	24.47[26]	0.85 [26]	

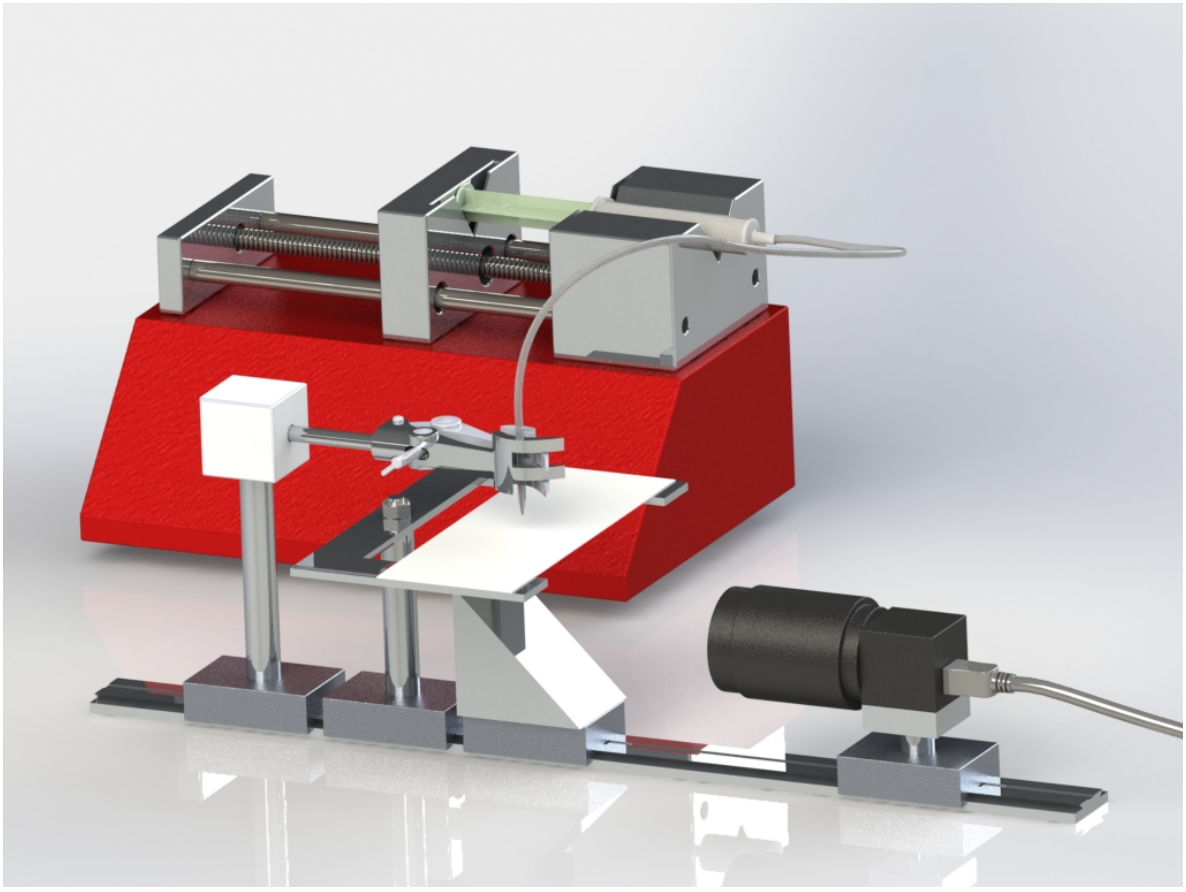

Figure 6.2: Syringe pump and needle experimental setup. The side mounted camera and 45 degree mirror are shown.

6.3 Results

6.3.1 Porosimetry

To verify the use of equation 6.6, porosimetry measurements were carried out. This allowed the fitting of model pressure curves (equation 6.7) to porosimetry data to determine the pore distribution index and therefore the value of n. Figure 6.3 shows the comparison between porosimetry data calculated using the surface tension and contact angle of water. A pressure curve corresponding to an n value of 2.2 is fitted, with good correlation between model and experimental data.

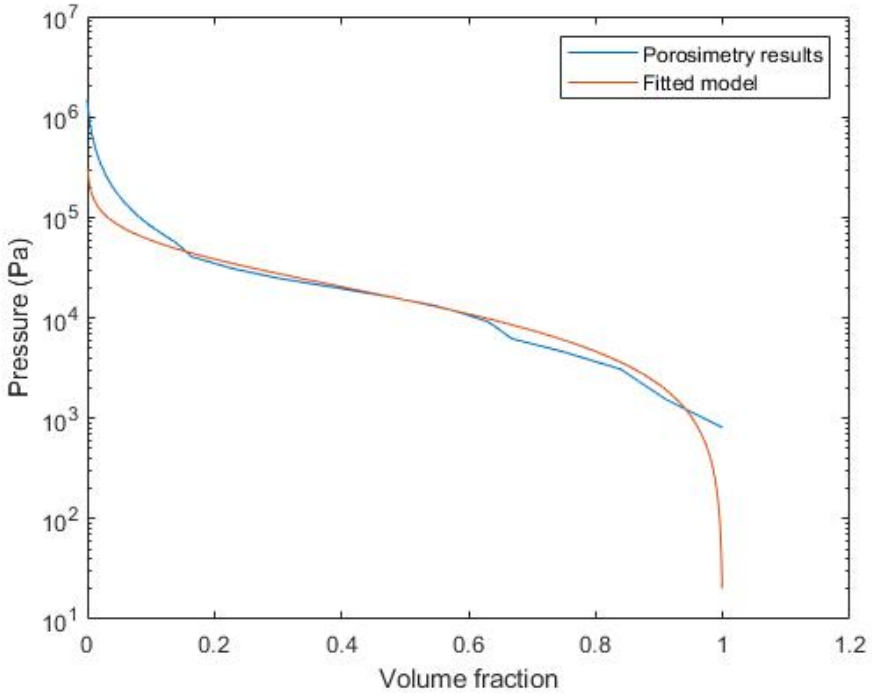

Figure 6.3: Comparison of the theoretical model (equation 6.7) with the mercury porosimetry measurement on Whatman 41 filter paper. Volume fraction is calculated as the volume of fluid in the paper divided by the volume at maximum saturation.

6.3.2 Initial Penetration

Simultaneously recording the side and bottom views of the paper substrate allowed the delay between droplet impact and stain appearance to be measured on all types of paper tested. A high-speed recording of this imaged at 8000fps is given in supplementary information. This recording shows that the vertical penetration of the droplet into paper occurs so quickly as to be considered instantaneous over the time scale of the stain growth. This finding was consistent for all types of paper tested. This very short time scale of vertical penetration also shows that the vertical variation of fluid will be insignificant in this study. This, combined with ignoring the variation between the paper machine (MD) and cross (CD) directions that is known to cause slightly elliptical stains [32] allows the process to be considered as one dimensional.

6.3.3 Stain Growth

The stain sizes with time for a series of model fluids on Whatman 41 paper are shown in Figure 6.4. The stain size data was recorded over different time intervals. The main

focus was on the early to mid stages and longer recordings took up significant hard disk space and were minimised. Due to this, the relative length of the curves in Figure 6.4 vary and are only indicative of the recording time. The wicking behaviour of droplets of water, ethanol and glycerol solutions on paper was studied. These liquids were selected to provide a variety of viscosity and surface tension conditions for a homologous series of fluids. Droplets of different diameter were deposited on paper and the stain area was recorded as a function of time. Results show that the larger droplets cause larger stain area; however, these area kinetics measurements are not scalable by any simple function of droplet volume. In some cases, droplets of slightly larger volumes created smaller stain sizes or vice versa (Figure 6.4d); the droplet volume difference over which this occurs gives an indication of experimental error. Fluids of high surface tension wick faster than fluids of low surface tension. Fluids of high viscosity wick slower than fluids of low viscosity. These trends are consistent with Marmur's equation [12] (equation 6.2) as well as the Lucas-Washburn equation [6].

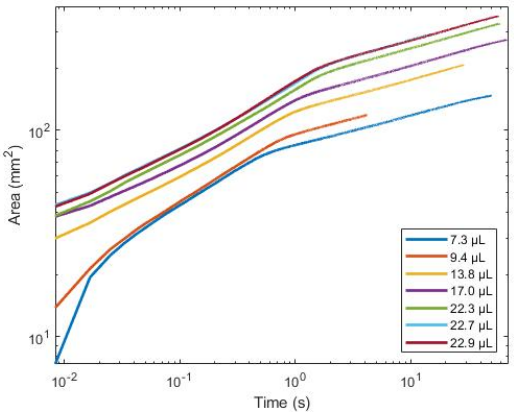

(a) Water

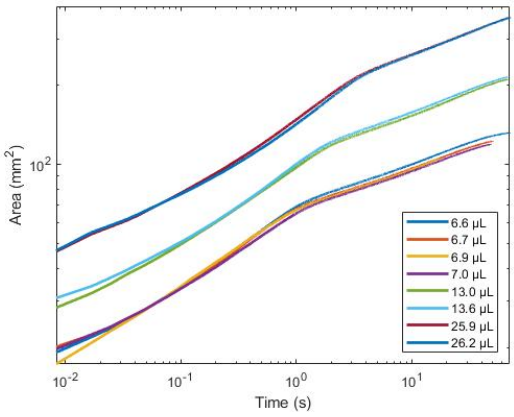

(b) 20% ethanol

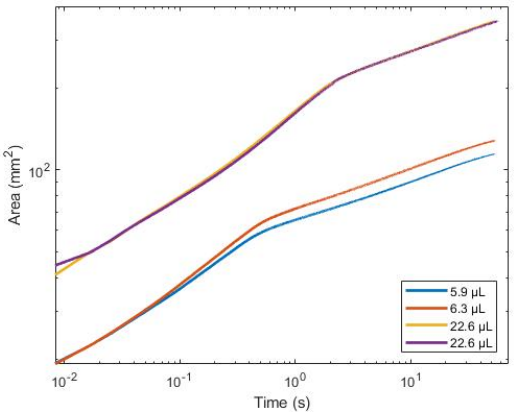

(c) 10% glycerol

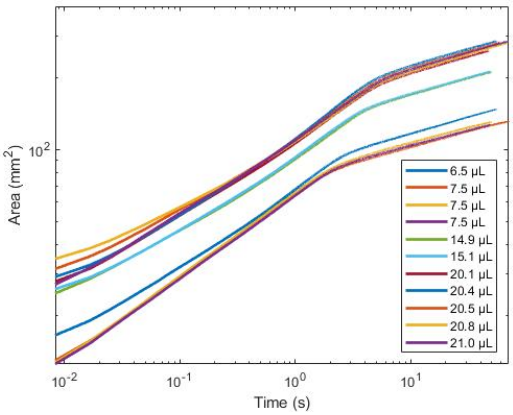

(d) 40% glycerol

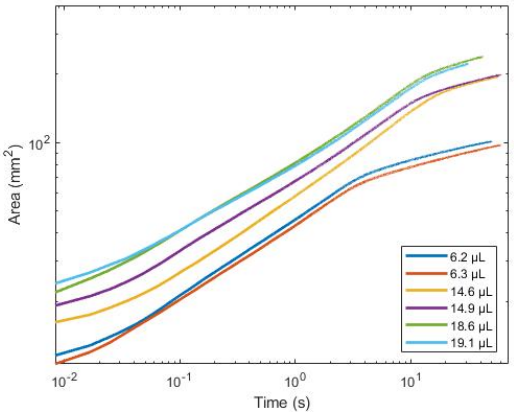

(e) 60% glycerol

Figure 6.4: Evolution of stain size with time for a variety of fluids and droplet sizes on Whatman 41 filter paper.

6.3.4 Transition Point

A two-stage wicking behaviour becomes clearly apparent on a log-log scale for all fluids tested. The linear counterparts to the data in Figure 6.4 are shown in supplementary information. The transition point between the two stages was identified from the sudden change in the gradient in the log-log curves. The questions to address are therefore whether these two stages have a physical meaning, and what are the mechanisms driving the phenomena.

From the gradient of the log-log curves, the exponent m (equation 6.1) can be calculated before and after transition. For all aqueous solutions tested on paper, the value of m for each system ranged between 0.26-0.44 for the first stage and between 0.12-0.20 for the second stage. These values are slightly lower than those reported in most previous studies on radial wicking [1, 2, 10].

Figure 6.5 shows the results of the same test with decane. In this case there is no clearly defined transition point, and the stains are much larger than those from similar volumes of aqueous solutions at all times. This size difference is highlighted by the plot utilising the same axis dimensions as those in Figure 6.4.

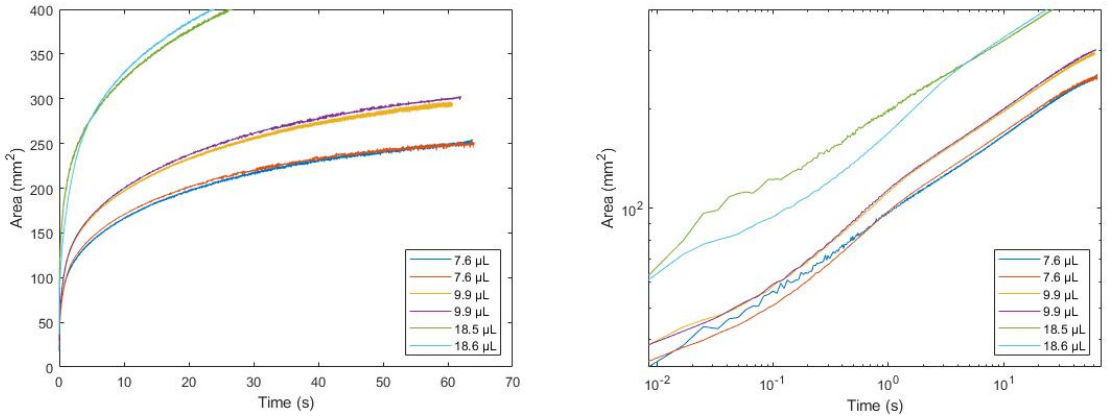

(a) (b)

Figure 6.5: Stain size with time for decane on filter paper.

Before stain growth data for different fluids can be compared (Figure 6.4), several droplets of similar size but from different fluids must be compared. Unfortunately, due to varying densities and surface tensions of fluids, any needle of a given diameter produced droplets of different size for different fluids. This meant it was not always possible to accurately predict the size of the droplet. Reproducing identically sized

droplets proved challenging for the different fluids. To overcome this issue, the data was fitted to a function of volume at every frame to determine the area's dependence on droplet volume at that time. This function could then be interpolated to a desired droplet volume to estimate the stain area at any volume for each frame. By combining these interpolated area values, an estimate of the spreading dynamics could be calculated. The results from interpolation agree with experimental data extremely well and all areas were found to be strongly linear with droplet volume at any given time. This means that the dynamics of stain growth of a droplet of any size can be predicted accurately using the results of two droplet sizes. This linearity was also demonstrated in our previous study [14], where the area to droplet volume relationship at equilibrium was found to be linear.

Using the data in Figure 6.4, the area of the stain at the transition can be plotted as a function of droplet volume. This is shown in Figure 6.6a. This demonstrates that the stain transition area forms a linear relation with droplet volume and is independent of fluid properties. Aqueous solutions at high concentrations of ethanol and glycerol deviate from this trend slightly.

Figure 6.6b illustrates the timing of the stain transition point relative to the timing of droplet disappearance above the surface of the paper for water, 40% ethanol and 60% glycerol solutions. The same figure with data from all water solutions is in supplementary information. Figure 6.6b also shows that linear fits are reasonable for both stain size transition and droplet disappearance. Using these linear fits for all fluids, the timing of stain size transition and droplet disappearance of a 10 µL droplet is interpolated and compared in Figure 6.6c. It shows that the timing of the two phenomena is related; as one gets longer, the timing of the other generally follows proportionally. The figure also shows that droplet disappearance always occurs before the stain growth transition.

6.4 Discussion

6.4.1 Stain Growth

Figure 6.7 shows the results of an interpolation for the wetting area produced by a 10 µL droplet of several model fluids on Whatman 41 filter paper for the beginning of the wicking period. There are minor differences in the transient behavior of the stain area

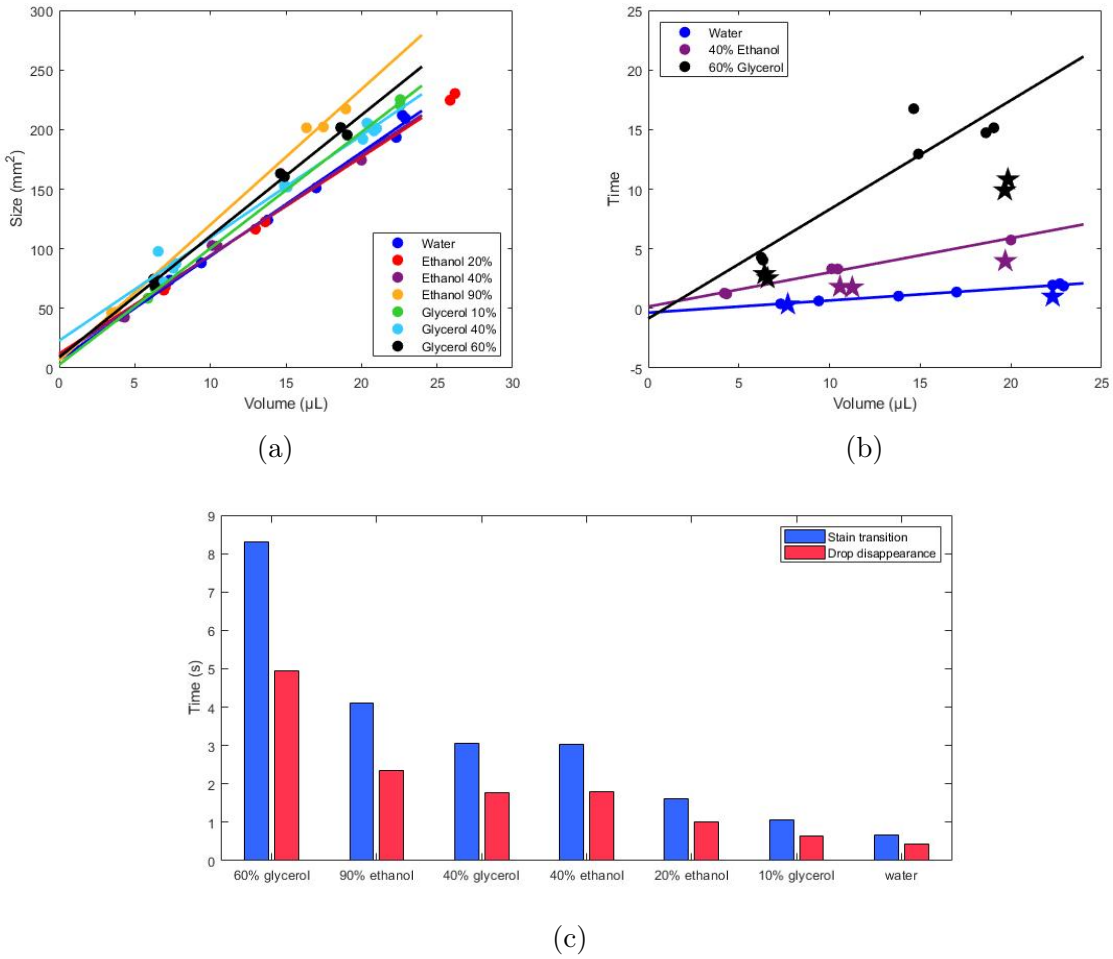

Figure 6.6: a) Area at which stain transition occurs with droplet volume for all model fluids. b) Time at which the stain wicking transition occurs as a function of droplet volume for 3 representative fluids. Stars represent the time at which each droplet disappears from the surface of paper. c) Interpolated stain size transition and drop disappearance time data at 10 µL.

kinetics among the various aqueous solution droplets. However, the late stages appear to converge. This late stage convergence was discussed in our previous study [14] where the equilibrium stain size was analysed for a series of fluids. Here, decane produces a much larger stain size than those from the other fluids tested, despite having a similar surface tension to the 90% ethanol solution. The viscosity of decane is slightly lower than that of any other fluids studied (Table 6.1). However, based on the relatively low sensitivity to viscosity found with the other measurements, it is unlikely that the slightly lower viscosity of decane is responsible for the huge discrepancy in stain behaviour observed. The high stain size of decane was previously attributed to the purely non-polar behaviour of the fluid, preventing any swelling of the cellulose fibers through

relaxation of the intra and inter hydrogen bonding among fibers [3]. Swelling of fibers results in a smaller amount of fluid available, therefore effectively decreasing the liquid volume available to wick out. The swelling fibers will also physically become larger, decreasing pore size [33]. Neither the effect of pore size change or liquid consumption has been thoroughly quantified. Schuchard and Berg [33] studied the effect of swelling fibers on vertical imbibation from an infinite reservoir. They reported the difference between a swelling and a non-swelling fluid could be accounted for by a reduction of the effective capillary radius in the Lucas-Washburn equation [5, 6] for normal paper fibers.

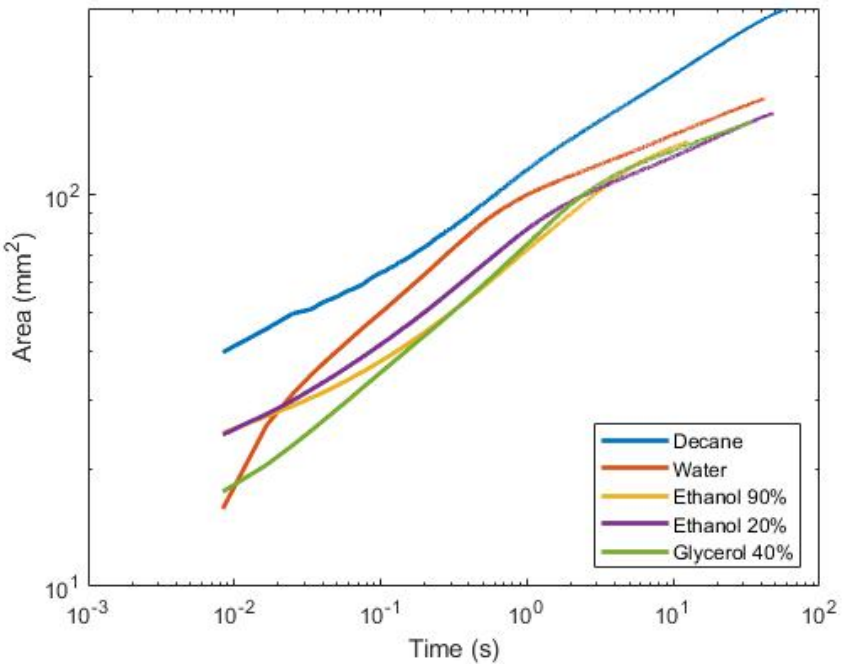

Figure 6.7: Interpolated data showing the spreading of 10µL droplets on a loglog scale.

6.4.2 Mechanism of the Stage Transition

A two-stage wicking regime is clearly seen on the log-log scale of stain size as a function of time (Figure 6.4). These regimes are very reproducible and were systematically observed for all fluids except for decane on paper. Several explanations for this two-stage process were investigated. First, as decane is known not to swell cellulose fibers [33] the transition could indicate the time at which the fibers have swollen by an amount that would affect wicking. Tests on filter papers performed with glass fibers (non-swelling) are given in supplementary information and also revealed a two-stage process,

very similar to that observed on cellulosic fibers. This observation reveals that swelling is unlikely to be responsible. A second possible explanation is the absorption of the droplet into the paper. This process is likely to affect results as its timing correlates with the stain transition (Figure 6.6b). However, as this absorption also occurs with decane droplets, it is unlikely to be a dominant mechanism. Third, the transition could represent a transition from wicking through a fully saturated to a partially saturated substrate. This is likely to affect results; however, as there is little previous work on the subject, the dominance of this mechanism is unknown and needs to be further probed. This was achieved here by modelling.

The transition from a fully saturated to a semi saturated mechanism also explains the delay seen between stain transition and droplet disappearance shown in Figure 6.6b. It is reasonable to assume that the propagation of the effect of the droplet disappearance (lowering of the local volume fraction), requires a finite period of time to reach the outside of the stain. Also, the decreased volatility of decane, compared to aqueous solutions, is unlikely to be responsible for the change in transition phenomena as it would result in a smaller amount of evaporation occurring. Our previous study demonstrated [14] that even with the more volatile fluids, no significant evaporation occurs over the time scale studied. Therefore, lowering the evaporation further is expected to have no effect.

6.4.3 Simulation Results

The model developed predicts the wicking behavior of sessile droplets onto a porous surface. It requires 7 input parameters to calculate stain size as a function of time: droplet volume (V_D), viscosity (μ), paper thickness (h), scaled diffusivity at saturation (D_0), pore distribution index (λ), initial wet area (A_0) and saturation volume fraction (ϵ_s). Each of these variables has a clear physical meaning and most can be identified experimentally [16]. Although the choice for droplet volume, paper thickness and viscosity is trivial, the selection of the remaining variables is more difficult. For the given case, a value for n and therefore λ was extrapolated from porosimetry measurement in Figure 6.3, and a value for A_0 was found by scaling the stage one data with Marmur's equation (equation 6.2). The value of A_0 that results in a linear relation with time is chosen as the A_0 for that situation. An estimation for ϵ_s can be found by measuring the difference between the dry weight and the wet weight of a paper sample. This was reported for Whatman 41 filter paper previously [14] and the volume fraction of water in wet paper can be calculated to be 0.62. The testing standard used (TAPPI 441)

for wet weight characterisation includes a rolling step between blotting papers that is designed to remove excess water. However, this rolling method might also remove some excess water that will otherwise remain in a droplet wicking case. For these reasons, the actual saturated value is likely to be slightly higher than measured. A value of ϵ_s=0.7 best fits our results. The results of a simulation with these calculated parameters and fitting just the D_0 value is shown in Figure 6.8. Parameter used in this simulation are shown in Table 6.2. Viscosity of water is taken from literature [29].

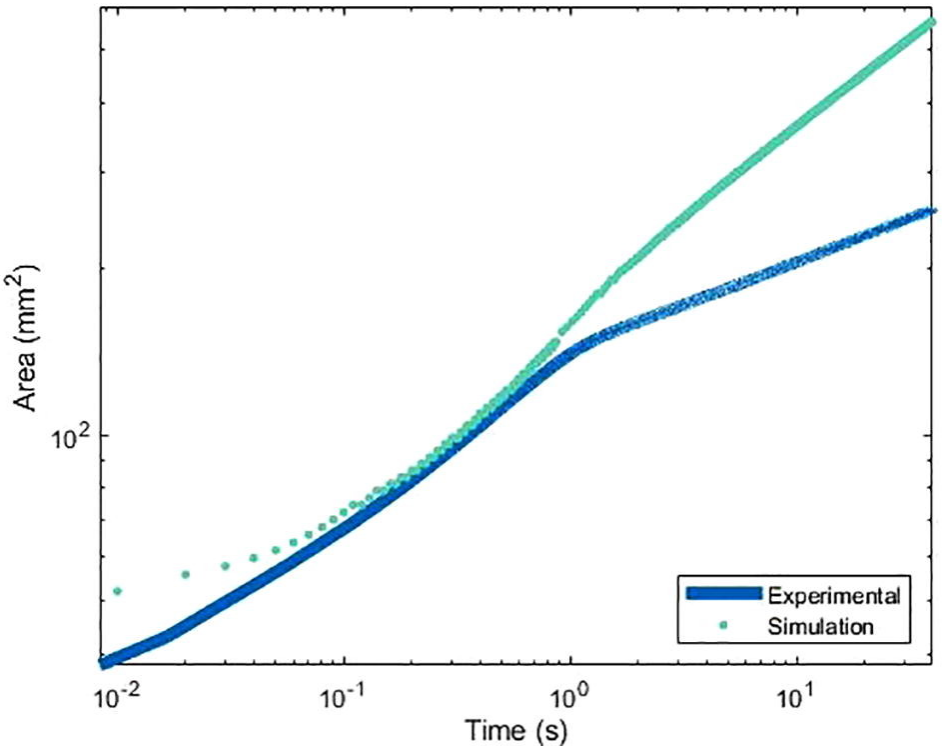

Figure 6.8: Comparison of experimental versus calculated values of area as a function of time on a log-log scale.

Table 6.2: Parameters used for Figure 6.8

Parameter	Value
V_D	17 µL
μ	0.93 mPa·s
h	226 µm
D_0	12.09 nPa·m^2
A_0	43.01 mm^2
ϵ_s	0.7
n	2.2

Although modelling well represents experiments in the first stage, poor agreement is

observed for the second stage. It is clear that the 7 parameters chosen do not fit the second stage. This is not surprising, as only infusion porosimetry data was used to calculate n. Hysteresis in porosimetry experiments is well documented [34] and its relevance to wicking reported [35]. As the liquid redistribution (second) phase is dominated by the emptying of pores, it is not surprising that a single value of n cannot capture both the first and second stages. Figure 6.9 shows the results of a simulation with a value of n that changes for the second stage. This value was found by fitting the stain area data. This value could not be externally calculated because it is an effective n for the specific combination of infiltration and redistribution occurring in the second stage which is rather complex. Both experimental and simulation results are also shown for a 17 µL droplet of water and 40% glycerol solution in Figure 6.9. The only difference between these two simulations is a change in the viscosity parameter and a refitted second stage n value. Parameters used are given in Table 6.3. The viscosity of a 40% glycerol solution was interpolated from results of Sheely [25]. The fitted value for second stage n was different between the two fluids, with each requiring a different fitted n value for the second stage. The fitted value for n during the second stage is 5 and 4 for water and glycerol respectively. The experimental results for glycerol are interpolated from data in 6.4d as a droplet of exactly 17 µL droplet was not tested. The water case is very well described by the model except for a slight deviation at later times. This is most likely because evaporation and swelling become more dominant in the later stages and are not included in this model. The glycerol simulation predicts behavior very well in the first stage; however, it deviates more than water in the second. This implies that higher viscosities slightly invalidate the assumption that the redistribution of fluid can be represented by a simple constant exponent n. Although the broad behavior is still represented. Simulations of different droplet sizes with appropriate changes to V_D and A_0 and keeping all else constant also fit experimental data. However, small droplets (<10 µL) are not well described by the model. This is likely because the small reservoir results in a larger fraction of the stain having never achieved full saturation. This would make redistribution more dominant through the whole process, and would mean that both the calculated n value for the first stage and the fitted value of n for larger droplets for the second stage may not be an appropriate choice. The constant size of the fully saturated boundary condition in the first stage would also be less appropriate for a small droplet [24].

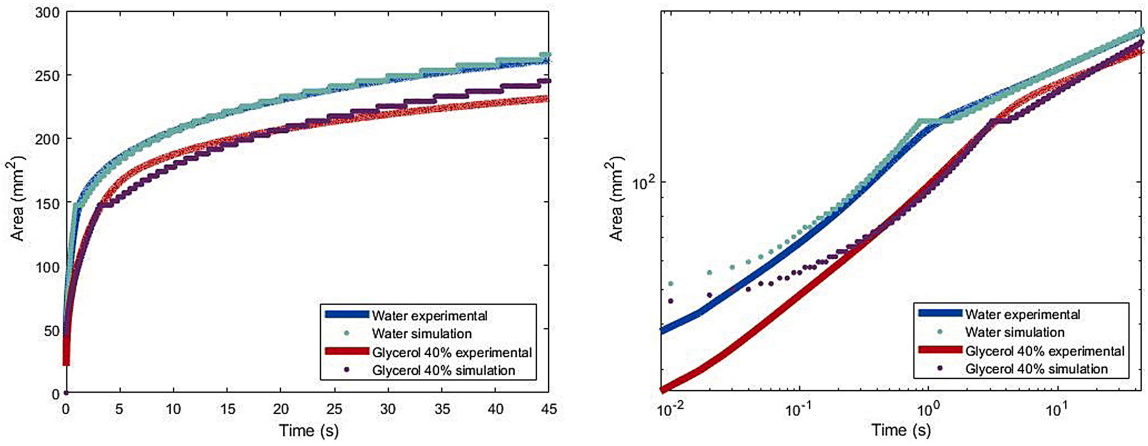

(a) (b)

Figure 6.9: Simulation and experimental results for water and 40% glycerol solution on a linear and log-log scale.

Table 6.3: Parameters used for Figure 6.9

Parameter	Water Case	40% Glycerol Case
V_D	17 µl	17 µL
μ	0.93 mPa·s	3.40 mPa·s
h	226 µm	226 µm
D_0	12.09 nPa·m^2	12.09 nPa·m^2
A_0	43.01 mm^2	43.01 mm^2
ϵ_s	0.7	0.7
n stage 1	2.2	2.2
n stage 2	5	4

The abrupt transition from stage one to stage two and the flat region immediately after is caused by the sudden shift in n at the stage transition of the simulation. In reality, both the transition from saturated to a no flux boundary condition and the change in n value happens gradually as the droplet is consumed and the dominant spreading mechanism changes from infiltration to redistribution. This is a simplification and a more complete model would account for this gradual shift. Not enough is known about porosimetry hysteresis and how it is affected by local volume fraction history to account for this effect. However, the broad effects are well described by the simplification introduced here. It is also relevant that the simulation results for the no hysteresis case (Figure 6.8) look very similar to results with decane in that no significant transition is observable. The simulation can be made to fit decane results with a single value of n, however this requires new fitted values for A_0, D_0 and n. This may be because the

wetting characteristics of decane on cellulose are such that the diffusivity experiences no significant hysteresis, and this affects the calculated parameters.

Although surface tension and contact angle of the fluid are used in calculating n from porosimetry data, these are also likely to effect A_0 and D_0; these were not included as input parameters in the model. Both of these quantities for water and glycerol are very similar [31], which explains why the model still fits experimental data between these two fluids.

The results of these simulations show that there are two dominant driving mechanisms behind the two-stage transition. First, the change from saturated to non-saturated boundary conditions at the center of the stain. Second, a change in how pressure and permeability vary as functions of volume fraction between systems that are dominated by pore filling and pore emptying.

6.5 Conclusion

The evolution in time of the stain area produced by a sessile droplet deposited on paper was measured, modelled and analysed. A series of fluids varying in surface tension and viscosity was examined. A new model to describe the data has been developed based on Richards' equation [21] and is easily resolved numerically in one dimension using experimentally measured boundary conditions and input parameters. This expands on previous work [10–12, 15, 18] where imbibation into linear and radial systems from an infinite reservoir has been investigated and modeled.
Radial wicking kinetics with all tested liquids besides decane showed two-stages, with a fast initial growth regime followed by a slower regime. The first regime corresponds to the liquid absorbing into the paper by wicking, while the second represents liquid redistribution [2]. This work identifies the cause of the transition between the two regimes to be the disappearance of the droplet coupled with the shift in mechanism due to the redistribution occurring in the second phase. This modeling technique also describes well the experimental results for both regimes. Further, the 7 parameters of the model have all a physical meaning and can be either measured experimentally or calculated.
This research contributes to the fundamental understanding of the wicking mechanism. The proposed modeling technique allows the quantification and prediction of stain dynamics in a variety of industrially relevant situations that were previously deemed too complex. The wicking of a finite reservoir is a common process in the printing, textile,

agriculture and medical industries, and the development of a method of prediction will assist in the design and optimisation of new technologies. This study also provides a rigorous and physically meaningful alternative to the semi-empirical Lucas-Washburn equation to describe the wicking kinetics of droplets in real porous media.

6.6 Acknowledgments

This research was funded by an ARC Linkage grant (LP160100544) and Haemokinesis.

6.7 References

[1] Erik Kissa. Capillary sorption in fibrous assemblies. *Journal of Colloid and Interface Science*, 83(1):265–272, 1981.

[2] Dganit Danino and Abraham Marmur. Radial capillary penetration into paper: limited and unlimited liquid reservoirs. *Journal of Colloid and Interface Science*, 166(1):245–250, 1994.

[3] Tokuzo Kawase, Sakiko Sekoguchi, Tomiko Fujii, and Motoi Minagawa. Spreading of Liquids in Textile Assemblies Part I: Capillary spreading of liquids. *Textile Research Journal*, 56(7):409–414, 1986.

[4] KK Borhan, Ali and Rungta. An experimental study of the radial penetration of liquids in thin porous substrates. *Journal of Colloid and Interface Science*, 158(2):403–411, 1993.

[5] Von Richard Lucas. Ueber das zitgesetz des kapillaren aufstiegs von flüssigkeiten. *Kolloid-Zeitschrift*, 23(1):15–22, 1918.

[6] Edward W Washburn. The dynamics of capillary flow. *Physical Review*, 17(3):273–283, 1921.

[7] Kewen Li, Danfeng Zhang, Huiyuan Bian, Chao Meng, and Yanan Yang. Criteria for applying the Lucas-Washburn law. *Scientific Reports*, 5:14085, 2015.

[8] Max M. Gong and David Sinton. Turning the page: Advancing paper-based microfluidics for broad diagnostic application. *Chemical Reviews*, 117(12):8447–8480, 2017.

[9] Emanuel Elizalde, Raúl Urteaga, and Claudio L. A. Berli. Rational design of capillary-driven flows for paper-based microfluidics. *Lab on a Chip*, 15(10):2173–2180, 2015.

[10] T. Gillespie. The spreading of low vapor pressure liquids in paper. *Journal of Colloid Science*, 13(1):32–50, 1958.

[11] A. Borhan and K. K. Rungta. On the radial spreading of liquids in thin porous substrates. *Journal of Colloid And Interface Science*, 154(1):295–297, 1992.

[12] Abraham Marmur. The radial capillary. *Journal of Colloid and Interface Science*, 124(1):301–308, 1988.

[13] Abraham Marmur. Penetration and displacement in capillary systems of limited size. *Advances in Colloid and Interface Science*, 39:13–33, 1992.

[14] Michael J Hertaeg, Rico F Tabor, and Gil Garnier. Effect of protein adsorption on the radial wicking of blood droplets in paper. *Journal of Colloid And Interface Science*, 528:116–123, 2018.

[15] Angel Perez-Cruz, Ion Stiharu, and Aurelio Dominguez-Gonzalez. Two-dimensional model of imbibition into paper-based networks using Richards' equation. *Microfluidics and Nanofluidics*, 21(5):98, 2017.

[16] Dharitri Rath, N. Sathishkumar, and Bhushan J. Toley. Experimental Measurement of Parameters Governing Flow Rates and Partial Saturation in Paper-Based Microfluidic Devices. *Langmuir*, 34(30):8758–8766, 2018.

[17] Sudhakar Jaganathan, Hooman Vahedi Tafreshi, and Behnam Pourdeyhimi. A realistic modeling of fluid infiltration in thin fibrous sheets. *Journal of Applied Physics*, 105(11):113522, 2009.

[18] A. Ashari, T. M. Bucher, H. Vahedi Tafreshi, M. A. Tahir, and M. S.A. A Rahman. Modeling fluid spread in thin fibrous sheets: Effects of fiber orientation. *International Journal of Heat and Mass Transfer*, 53(9-10):1750–1758, 2010.

[19] Steven C Chapra and Raymond P Canale. *Numerical Methods For Engineers*. Mcgraw-hill New York, 1998.

[20] W L Then, Miaosi Li, Heather McLiesh, Wei Shen, and Gil Garnier. The detection of blood group phenotypes using paper diagnostics. *Vox Sanguinis*, 108(2):186–196, 2015.

[21] L. A. Richards. Capillary conduction of liquids through porous mediums. *Journal of Applied Physics*, 1(5):318–333, 1931.

[22] Henk Huinink. *Fluids in Porous Media*. Morgan & Claypool Publishers, 2016.

[23] Dalton James Eric Harvie. An implicit finite volume method for arbitrary transport equations. *ANZIAM Journal*, 52(0):1126–1145, 2010.

[24] V.D. Sobolev V.M. Starov, S.A. Zhdanov , S.R. Kosvintsev and M.G.Velardec. Spreading of liquid drops over porous substrates. *Advances in Colloid and Interface Science*, 105:123–158, 2003.

[25] Madison L Sheely. Glycerol viscosity tables. *Industrial & Engineering Chemistry*, 24(9):1060–1064, 2013.

[26] Yi Liu, Rocco Difoggio, Kerry Sanderlin, Louis Perez, and Jinsong Zhao. Measurement of density and viscosity of dodecane and decane with a piezoelectric tuning fork over 298-448 K and 0.1-137.9 MPa. *Sensors and Actuators, A: Physical*, 167(2):347–353, 2011.

[27] Ibrahim Sadek Khattab, Farzana Bandarkar, Mohammad Amin Abolghassemi Fakhree, and Abolghasem Jouyban. Density, viscosity, and surface tension of water + ethanol mixtures from 293 to 323K. *Korean Journal of Chemical Engineering*, 29(6):812–817, 2012.

[28] Herbert Giesche. Mercury porosimetry: A general (practical) overview. *Particle and Particle Systems Characterization*, 23(1):9–19, 2006.

[29] Joseph Kestin, Mordechai Sokolov, and William A Wakeham. Viscosity of liquid water in the range -8 C to 150 C. *Journal of Physical and Chemical Reference Data*, 7(3):941–948, 1978.

[30] Gonzalo Vazquez, Estrella Alvarez, and Jose M Navaza. Surface tension of alcohol water+ water from 20 to 50. degree. C. *Journal of chemical and engineering data*, 40(3):611–614, 1995.

[31] Koichi Takamura, Herbert Fischer, and Norman R Morrow. Physical properties of aqueous glycerol solutions. *Journal of Petroleum Science and Engineering*, 98:50–60, 2012.

[32] Noosheen Walji and Brendan D. MacDonald. Influence of geometry and surrounding conditions on fluid flow in paper-based devices. *Micromachines*, 7(5):73, 2016.

[33] David R Schuchard and John C Berg. Liquid transport in composite cellulose—superabsorbent fiber networks. *Wood and Fiber Science*, 23(3):342–357, 2007.

[34] J. Kloubek. Hysteresis in porosimetry. *Powder Technology*, 29(1):63–73, 1981.

[35] M. Landeryou, I. Eames, and A. Cottenden. Infiltration into inclined fibrous sheets. *Journal of Fluid Mechanics*, 529:173–193, 2005.

6.8 Supplementary

Mesh refinement

Divisions per drop radius, $R_0/\delta x$	Droplet absorption time (s)
25	2.15
50	2.19
100	2.20
150	2.20
200	2.21

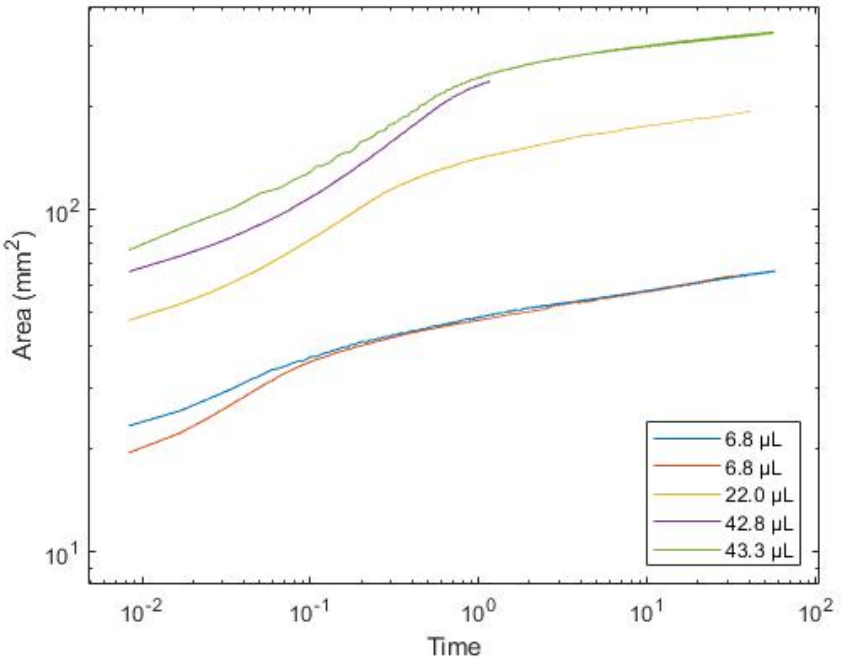

Stain size with time for water on glass fibers. Shows stage transition.

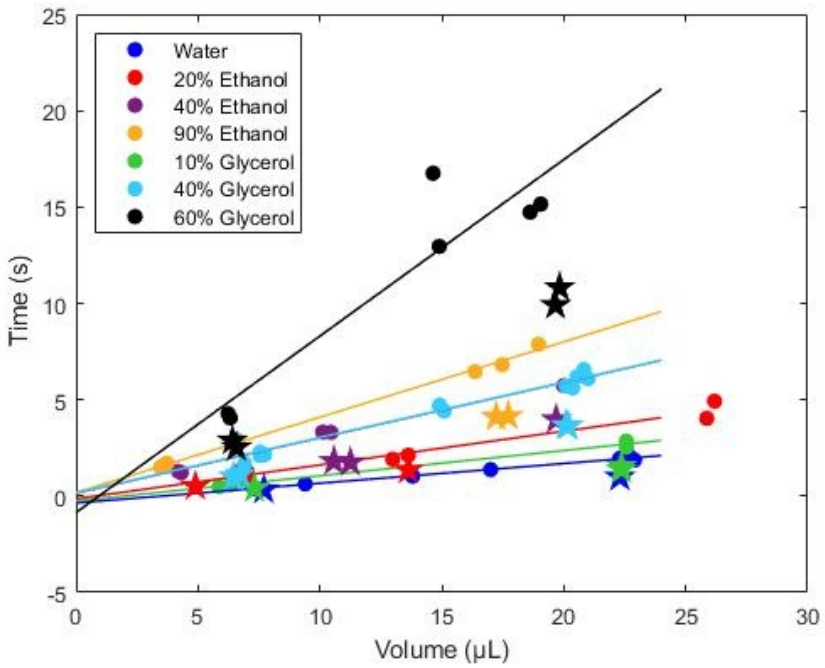

Stain transition and droplet disappearance time for all tested water solutions. Linear fit lines overlap for 40% ethanol and 40% glycerol.

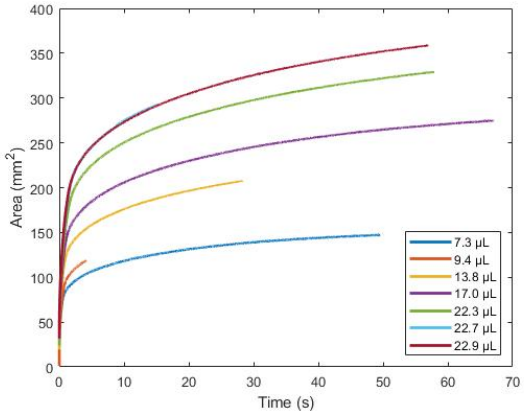

(a) Water

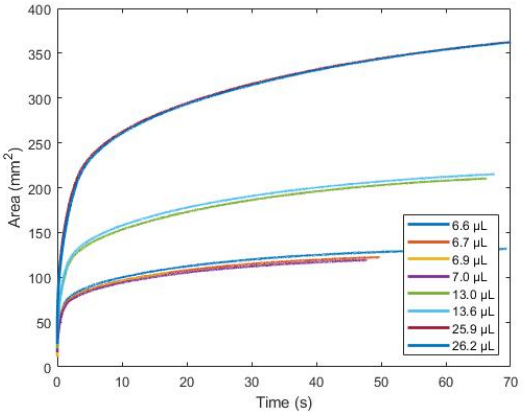

(b) 20% ethanol

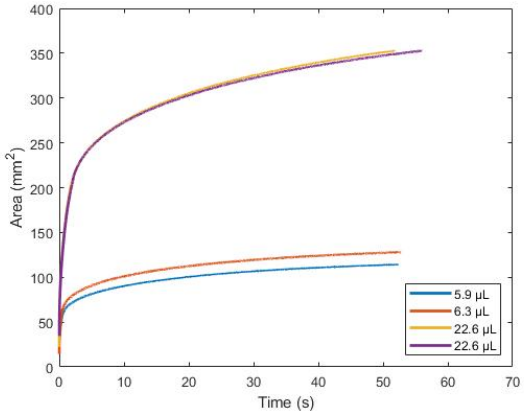

(c) 10% glycerol

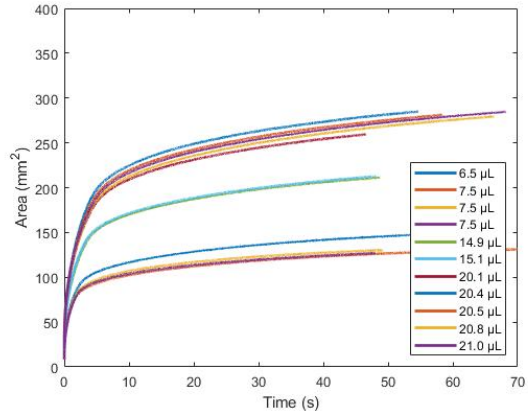

(d) 40% glycerol

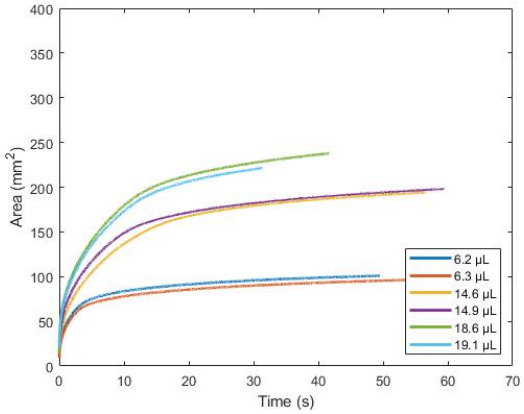

(e) 60% glycerol

Linear plots of stain size with time data.

Chapter 7

Wicking of Biological Fluids

Preface

As the droplet deposition mechanism is used commonly in the operation of paper-based diagnostics, radial wicking from a single droplet of complex fluids is critical. The previous chapters identified the importance of this phenomenon as a fast and easy measure of many properties that can be used in diagnostics. The dominance of hysteresis in second stage stain growth after the drop is absorbed by the paper was also highlighted. In this chapter, the dynamics of a droplet of blood and other biological fluids spreading on paper is analysed and the model introduced in chapter 6 is expanded to include the effect of biological components. This chapter was published in Langmuir in 2020. The text was reformatted to be consistent with the remaining sections; no other changes have been made. The article as published is provided in Appendix A.

Radial wicking of biological fluids in paper

Michael J. Hertaeg, Rico F. Tabor, Joseph D. Berry, Gil Garnier

Published: Langmuir, 36:8209-8217, 2020

Abstract

In this study, we analyze stain growth kinetics from droplets of biological fluids such as blood, plasma, and protein solutions on paper both experimentally and numerically. The primary difference of biological fluids from a simple fluid is a significant wetting/dewetting hysteresis in paper. This becomes important in later stages of droplet wicking, after the droplet has been completely absorbed into paper. This is shown by anomalous power dependence of area with time in the later stages of radial wicking. At early stages, current numerical wicking models can predict stain growth of biological fluids. However, at later stages, the introduction of hysteresis complicates modeling significantly. We show that the cause of the observed hysteresis is due to contact angle effects and that this is the dominant mechanism that leads to the anomalous stain growth kinetics measured uniquely in biological fluids. Results presented will streamline the design process of paper-based diagnostics, allowing a modeling approach instead of a trial and error method.

7.1 Introduction

Paper-based diagnostics are integral in an industry-wide shift toward low-cost, point-of-care medical devices. Paper is a flexible platform for these devices because of its low cost and capacity to easily induce passive flows through wicking phenomena caused by capillary forces. Current devices on the market are typically reliant on a trial and error design process because not enough is known about wicking phenomena in paper. While wicking of simple fluids has been well studied as it is integral to many industrial applications including, textiles, printing, agricultural, and medicine, [1–6], wicking of complex fluids has not been studied in depth. This is required for the design of paper-based diagnostics as it will allow the efficient optimization of parameters such as paper properties and geometry. Also, as paper-based devices often involve reactions inside a wicking fluid, a thorough understanding of wicking phenomena is required before any sophisticated reaction optimization can take place. There are critical and distinct differences in the behavior of simple fluids when compared to complex biological fluids and suspensions. Also, the mechanism behind stain growth transition in droplet wicking remains unknown as it has been poorly studied. This lack of understanding is particularly acute for human blood on paper. Much of the literature on the topic is in the field of forensics and is focused on applications rather than fundamental understanding. [7–9].

Biological fluids have many different components that cause complexities. The cell component of blood introduces rheological changes such as a shear-thinning viscosity and granularity caused by the presence of highly deformable red blood cells (RBCs)[10]. Also, the significant protein content and lipid component of blood plasma will adsorb onto both solid–liquid and liquid–vapor interfaces, affecting the contact angle, surface tension, and viscosity of the system nonuniformly [11, 12]. The most abundant protein in blood is albumin [13] and has been shown to significantly impact wicking in paper [11].

Wicking is caused by a negative pressure produced by the curved meniscus at the air–liquid interface between pores. The pressure developed in a pore can be approximated with the Young–Laplace equation applied for a capillary with a circular cross section and setting the atmospheric pressure to zero (equation 7.1)

$$P = -\frac{2\gamma cos\theta}{R} \tag{7.1}$$

where P is the pressure on the liquid side of the meniscus, γ is the surface liquid-vapor surface tension, R is the radius of the capillary and θ is the contact angle. This negative pressure causes Poiseuille flow toward the meniscus, drawing further fluid into the capillary and moving the interface. In a complex porous material like paper, the pore radius changes depending on position. Therefore, the capillary pressure is not constant and depends on the pore radius. The contact angle at the meniscus is also a critical parameter affecting the driving force.

The radial wicking of a droplet on paper is an example of a complex wicking scenario, and several studies have analyzed stain growth as a function of time [14–17]. In this situation, stain growth continues well after the droplet has absorbed into the paper and disappeared from the surface. The absorption of the drop a finite time after deposition causes a decrease in the spreading rate, which can be clearly identified from the stain growth kinetics plotted on a log-log scale. The two stages observed are referred to as stage one, where the drop is still present above the paper, and stage two, where the drop has been completely consumed. Before the transition, spreading is driven only by the infiltration of pores near the edge of the stain. After the transition, the reservoir of fluid is consumed and any further stain growth is caused by the redistribution of fluid from the large pores in the center to the unfilled small pores at the edge of the stain. This causes voids to form in the central region, creating receding air interfaces and therefore negative capillary pressures to form within large pores at the center of the stain. This effect causes impedance to further stain growth. At first, the small radius of the filling pores near the edge of the stain dominates and stain growth continues [18]. This becomes less dominant at later times as the meniscus in the center region moves into incrementally smaller pores. Stain growth transition was shown to depend on a hysteresis effect presenting as a difference between infiltration and emptying porous networks [19]. Our previous numerical study showed that including hysteresis is essential to produce clear second-stage transitions and that an increase of hysteresis severity results in a more drastic stage transition [20]. This reveals that the stain growth transition is not caused directly by the consumption of the droplet reservoir. Instead, the stage transition occurs because of a pore hysteresis that only becomes relevant once the droplet is consumed; this is because until this point there are no emptying pores. The cause of this hysteresis is poorly understood and is likely to be material dependent. However, the most likely causes are entrapment due to decreased pore interconnectivity, contact angle hysteresis, and fiber swelling.

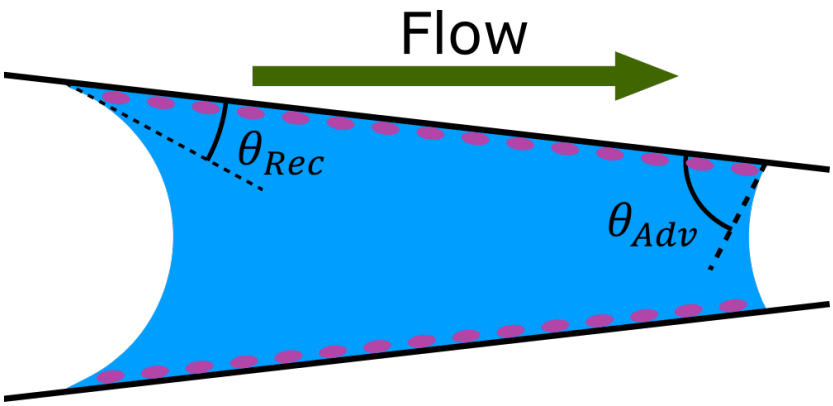

Figure 7.1: Advancing and receding contact angle in a model capillary with adsorbed biomolecules.

It is the objective of this study to elucidate the cause of wetting/dewetting hysteresis in paper and the effect that biological components have on the radial wicking process (Figure 7.1). This is achieved through experimental analysis of stain growth of biological fluids, contact angle experiments, full-morphology numerical analysis [21], and continuum scale modeling using the Richards equation [22]. This work enables the prediction of the wicking behavior of biological fluids for the efficient development of paper diagnostics.

7.2 Experimental Section

7.2.1 Materials

Cellulose films for contact angle experiments were prepared in the same way as several previous studies [11, 23, 24]. Here a 0.5 wt % solution of cellulose acetate (Sigma-Aldrich) in acetone (analytical reagent, Thermo Fisher Scientific) was spin-coated onto glass and then soaked in a 0.5 wt % solution of sodium methoxide (Sigma-Aldrich) in methanol (analytical reagent, Thermo Fisher Scientific). Whatman 41 filter paper was used for wicking tests, and the blood used was collected with consent by the Red Cross Blood Service Australia following strict ethics requirements. Blood was mixed with ethylenediaminetetraacetic acid (EDTA) as an anticoagulant at collection to prevent coagulation.

7.2.2 Methods

Experimental Process

Stain growth data were gathered by monitoring the stain size as a function of time after droplet deposition with the same setup as in our previous study [20]. The bottom view of the paper is captured using a Point Grey Flea3 camera directed onto a 45 degree mirror positioned underneath the paper. Examples of captured images are shown in Figure 7.2. Images were taken at a rate of 120 frames/s and analyzed in ImageJ to give area as a function of time. Droplets were created by pumping at a constant flow rate through a needle; this caused droplets of constant size to fall periodically. The size of the droplet was calculated from weight measured using a Mettler Toledo TLE balance before the needle was positioned above the paper. The average weight of the previous four droplets was divided by the fluid's density to estimate the volume of the droplet. The size of the droplet was altered using needles of varying outer diameters. Needles were made by hand by drawing out heated glass capillary tubes. Protein adsorption onto the needle resulted in varying drop volumes. To overcome this, the needles were submersed in the test fluid for 30 min prior to create a saturated layer of adsorbed biomolecules.

Contact angles were measured with an OCA35 Dataphysics contact angle instrument. For advancing and receding measurements, a pump rate of 20 µL/s was used. The presented values are the mean of at least six measurements, and the same batch of cellulose films was used to decrease variability. The static contact angles of blood, plasma and water on silicon wafers were also measured. Advancing contact angles of water and plasma on cellulose have been previously reported [11]. These were measured and are presented again as a comparison with these new receding measurements with blood components. All wicking and contact angle tests were performed at 23 °C and 50% relative humidity.

The internal structure of the paper used was imaged with a Zeiss Xradia 520 Versa high-resolution x-ray computed tomography scanner. The size of the scan was 150 µm x 150 µm x 205 µm with a resolution of 0.46 µm (voxel volume = 0.46 µm x 0.46 µm x 0.46 µm). The images were binarised in ImageJ using ANKAphase plugin [25]. This plugin implements a phase-contrast algorithm [26] which was required due to the low absorption of x-rays by cellulose. For analysis the imaged section is required to be representative of the bulk. For this to be true, the size of the image must be larger than

the length scale of heterogeneities in the material. This was confirmed by cropping the image to different sizes and calculating the average volume fraction of the fibers in the new image. As the image size was increased, the average volume fraction plateaued to a constant, indicating that the taken image was large enough to be representative of the bulk properties of the paper.

Numerical Methods

The model selected adopts a similar approach to that of several previous studies [20, 27–29]. The Richards equation (equation 7.2) is used to relate volume fraction time and pressure.

$$\frac{\partial \phi}{\partial t} = \nabla \cdot \left(\frac{K(\phi)}{\mu} \nabla P \right) \tag{7.2}$$

where ϕ is the volume fraction divided by the maximum saturation in the material (ϵ_s), K is the permeability, μ is viscosity, P is pressure, and t is time. In most wicking systems, pressure is a function of only the volume fraction. Due to this, the simpler equation 7.3 can be used.

$$\frac{\partial \phi}{\partial t} = \nabla \cdot \left(\frac{D(\phi)}{\mu} \nabla \phi \right) \tag{7.3}$$

where $D(\phi)$ is given by:

$$D(\phi) = K(\phi) \frac{\partial P(\phi)}{\partial \phi} \tag{7.4}$$

$$K(\phi) = K_0 \phi^{\frac{3\lambda+2}{\lambda}} \tag{7.5}$$

$$\frac{\partial P(\phi)}{\partial \phi} = \frac{\gamma cos\theta P_m}{\lambda} \phi^{\frac{-1-\lambda}{\lambda}} \tag{7.6}$$

Expressions for $K(\phi)$ and $\frac{\partial P(\phi)}{\partial \phi}$ (equations 7.5 and 7.6) can be derived using the Brooks-Coorey model [30]. Equation 7.6 has been altered to include a linear relationship with surface tension and the cosine of the contact angle. This relationship is predicted from equation 7.1. These expressions are substituted into equation 7.4 to give equations 7.7 and 7.8.

λ is the pore distribution index derived from mercury porosimetry or full morphology. In the typical expression derived from the Brooks-Coorey analysis, the product $\frac{\gamma cos\theta P_m}{\lambda}$ is represented as a single constant, usually defined as the capillary pressure at maximum saturation. This is sometimes set to atmospheric pressure and sometimes left as an empirical constant depending on best fit to data. Here, contributions from surface

tension and contact angle on this constant are separated from the contribution from material choice P_m and λ. The effect of P_m is indistinguishable from K_0 in equation 7.8, so the estimation of this value is not possible. However, both of these constants should be properties of the paper and therefore constant between fluids. Therefore, the product $K_0 P_m$ can be calculated from experimental data using a single fluid and then used for all fluids on that same paper.

$$D(\phi) = D_0 \phi^{\frac{2\lambda+1}{\lambda}} \tag{7.7}$$

$$D_0 = \frac{K_0 P_m \gamma cos\theta}{\lambda} \tag{7.8}$$

Once all substitutions have been made, equation 7.3 is solved using an implicit finite volume method using the open source PDE solver arb [31] over a two-dimensional axisymmetric domain. The same uniform structured mesh and temporal resolution were used as validated in our previous study [20]. $\delta r = 0.02 r_c$ and $\delta t = 0.01$ s where r_c is the droplet radius. No flux boundary conditions are used on all external faces except for a small region where the droplet is in contact with the paper. Here, a saturated boundary condition is used. The simulation is stopped when the total volume of fluid inside the domain equals the specified volume of the initial droplet. This introduces three additional parameters: the thickness of the paper h, the volume of the droplet V and the radius of the contact patch r_c. The radius of contact can be estimated using the following equation

$$r_c^3 \approx \frac{3V}{\pi} \left[\frac{sin^3\theta}{2 - 3cos\theta + cos^3\theta} \right] \tag{7.9}$$

This equation is derived assuming spherical cap geometry on a solid surface. This is not rigorously exact on paper because some of the liquid is absorbed and the instantaneous contact angle over paper will be different to that calculated on other cellulose surfaces due to porosity and roughness. The simplifications introduced in the model mean that the real contact area differs slightly from the effective contact area used in simulations. This is likely caused by ignoring the effects of inertia and dynamic contact angle. Both these effects have been shown to influence some wicking systems particularly at early times when velocities are high [32–34]. Despite this, equation 7.9 provides a robust approximation.

Fiber interconnectivity is analyzed with a full-morphology processing step. This is a quasi-static simulation technique to predict the pressure variation in a porous material at various levels of infiltration. It was first developed by Hazlett [21] and has since

been used widely to analyze a variety of porous materials, including paper [28, 35]. The method uses a three dimentional (3D) geometry and relies on fitting spheres of constant diameter inside the void space in the geometry. These spheres are allowed to intersect each other but not with the fibers. As the Laplace equation (equation 7.1) can be used to relate the radius of these spheres to a pressure, the level of infiltration can be calculated as the original nonfiber volume in the paper minus the volume occupied by the overlapping spheres. This is achieved by labeling all voxels occupied by spheres and then adding the volume of all labeled voxels. In this way, the overlap between spheres can be overcome and the true volume of the nonwetting phase calculated accurately. Varying the size of the spheres allows the level of infiltration corresponding to each capillary pressure to be calculated.

Most previous studies have used a commercial implementation of the full-morphology algorithm called GeoDict by Math2Market. For this study, a custom full morphology implementation was developed and written with Matlab. The code used can be found at https://github.com/MHertaeg/Full-Morpholology.git.

7.3 Results

Figure 7.2 demonstrates the stain progression at different times after droplet deposition on the same paper for similar volumes of blood, plasma, and water. Achieving identically sized droplets of different fluids was not possible because fluid surface tension and viscosity affect the volume of droplets generated with a needle. Even from the very early stages of stain growth, blood has a very small stain size followed by plasma and then water. Differences in stain size are highlighted by the change in scale bar length between fluids. There is also a difference between the roughness of the stain boundary of different fluids, clearly forming different fractal dimensions. The highest roughness is seen in blood followed by plasma and water. All stains are slightly elliptical, with the major axis aligned with the paper's machine direction, indicating the expected slight fiber alignment in that direction.

Figure 7.3 shows the growth of stain area with time from droplets of plasma and blood wicking on filter paper. The log-scale plots are presented, as the gradient of these indicates the power dependence of area with time. These log-scale plots clearly display two typically delineated linear regions [20]. These two regions identify the first and

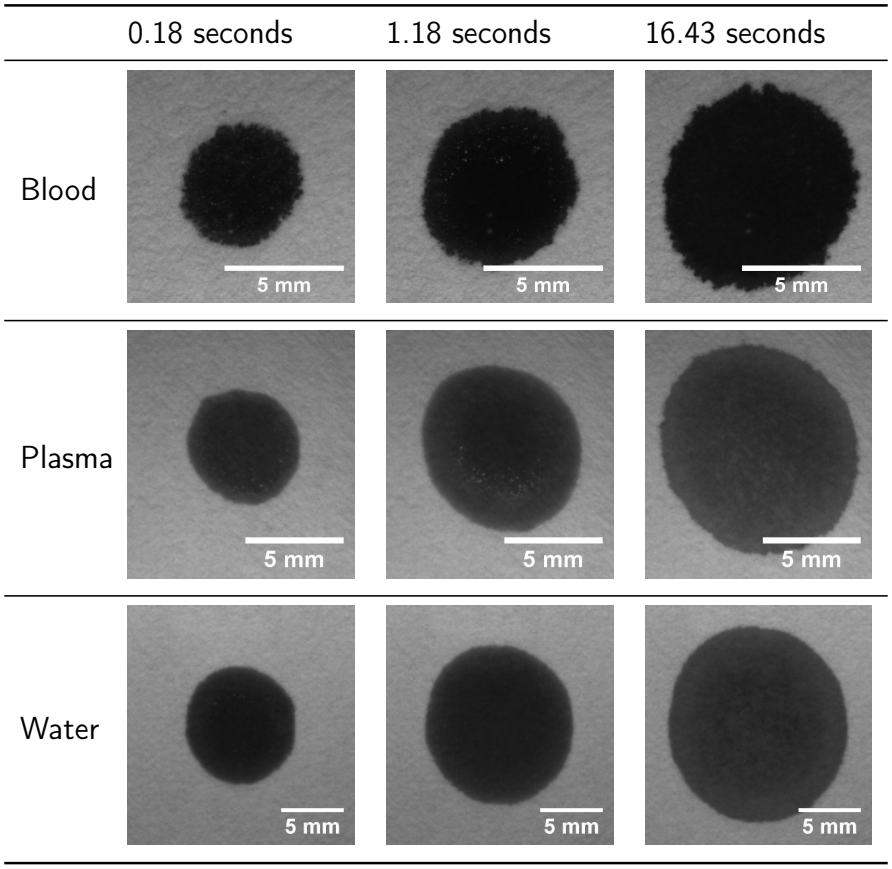

Figure 7.2: Progression of stains from similar volumes of blood, plasma, and water after droplet deposition on the same paper. Note the different sized scale bars for the different fluids. Droplet volumes: blood 12.9 µL, plasma 13.5 µL and water 13.8 µL.

second stages of radial wicking. Although similar in form, blood wicks more slowly than plasma; this is shown by the different vertical scale used to plot the two fluids. It can also be seen that the stage transition occurs much later in blood than in plasma. Discrepancies in blood wicking show that variability is higher between donors with whole blood compared to plasma. This is due to differences in red blood cells between individuals [36, 37]. Figure 7.6 in the supplementary section shows the variability caused by different donors.

Stain growth tests were also performed with bovine serum albumin (BSA) solution, red cells suspended in phosphate-buffered saline (PBS) and water. This was undertaken to identify the effect cells and protein have on the wicking process. Cells combined with water were tested as this was anticipated to cause a significant number of cells to lyse (burst) driven by a high osmotic pressure difference between the cell and the bulk solution. Albumin is the most abundant protein in blood [13] and therefore serves as a simplified model of plasma. A BSA concentration of 83 g/L BSA in PBS was chosen

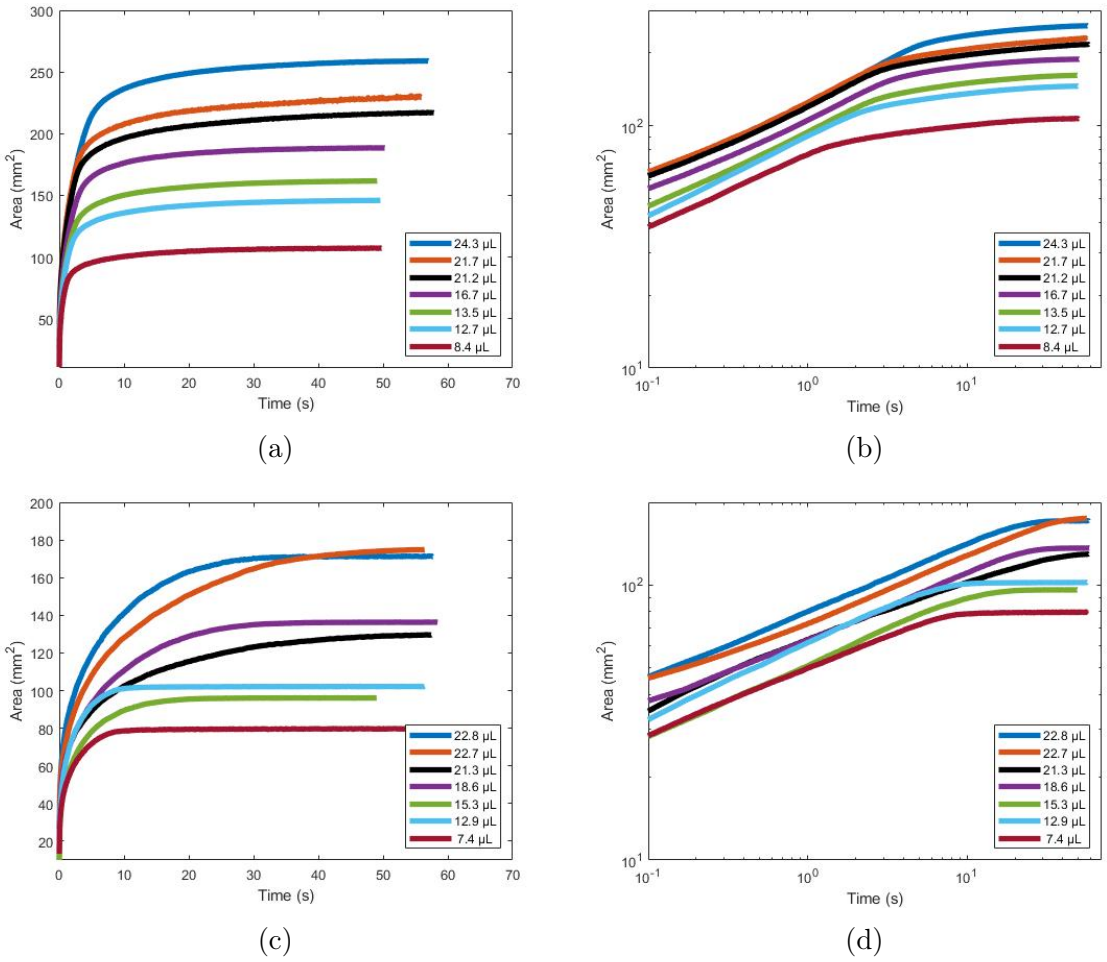

Figure 7.3: Evolution of stain growth with time for droplets of varying volumes. (a) Plasma linear scale, (b) plasma log scale, (c) blood linear scale, and (d) blood log scale.

as it is close to the protein concentration in plasma and has been shown to mimic the wicking behavior of plasma [11]. All red blood cell solutions were prepared at a concentration of 45% by volume to be similar to blood [38]. Stain growth kinetics from all of these fluids are compared to water [20] in Figure 7.4. As experimental limitations prevented measuring the stain growth from identically sized drops of different fluids, interpolated data must be used. This interpolation was achieved by finding the stain size at every time point and fitting to a linear function of drop volume. Then, using this function, the stain size at any drop volume could be estimated. By combining interpolated stain area data at each time point, the full stain growth plot of any sized droplet could be determined. Figures 7.6 and 7.7 in supplementary information show the fit of results to linear functions of drop volume for plasma and blood 30 s after droplet deposition. These can be used to demonstrate the small error introduced by this interpolation.

Table 7.1: Experimental Contact Angles and Stain Area powers of Biofluids

Fluid	Advancing θ_{adv}	Receding θ_{rec}	Hysteresis $\cos(\theta_{rec}) - cos(\theta_{adv})$	First Stage Power	Second Stage Power
Water	15	5	0.03	0.33 ± 0.11	0.15 ± 0.04
Plasma	28	12	0.09	0.32 ± 0.02	0.06 ± 0.01
Blood	46	3	0.30	0.24 ± 0.04	≈ 0

Figure 7.4 displays a significant difference between the stain growths of the different blood components and water. Pure water wicks very quickly followed by plasma, red blood cell solutions, and then whole blood. Stains from suspensions of blood cells in water and red blood cells in PBS achieve the same equilibrium size. However, red blood cells in water are slightly slower to reach equilibrium. As expected, the behavior of blood plasma is mimicked with the 83 g/L BSA solution. Comparing the gradient of a log-log plot reveals the power dependence of the relationship with time. This value has been quoted in previous studies [15, 16] and is very reproducible between results of the same fluid and substrate. The calculated power values for different fluids are shown in Table 7.1. All first-stage powers are similar, but second-stage powers vary significantly. The second-stage power for blood is effectively zero as the stains come to an abrupt halt after a short transition region.

Table 7.1 also shows advancing and receding contact angles of water, plasma and blood on cellulose films. The biological fluids have significantly higher advancing contact angles when compared to water; however, receding angles do not show this trend. The receding angle for blood is lower than all other tested fluids although its difference from water is not significant, particularly considering the inaccuracies in measuring very low contact angles. Contact angle hysteresis is usually presented as a difference in angles. Here, the differences between cosines of the advancing and receding contact angles are displayed in Table 7.1 as this is how the contact angle is included in equation 7.1. This metric is presented to indicate the severity of contact angle hysteresis for these fluids. Plasma produces 3 times the contact angle hysteresis as that of water on cellulose; for blood, it is 10 times. These results demonstrate that there is a correlation between a severe contact angle hysteresis and a low second-stage power. Contact angle measurements for sessile droplets of water, plasma, and blood on silicon wafers were also performed. In this case, all fluids were found to have a similar contact angle of approximately 61 degrees.

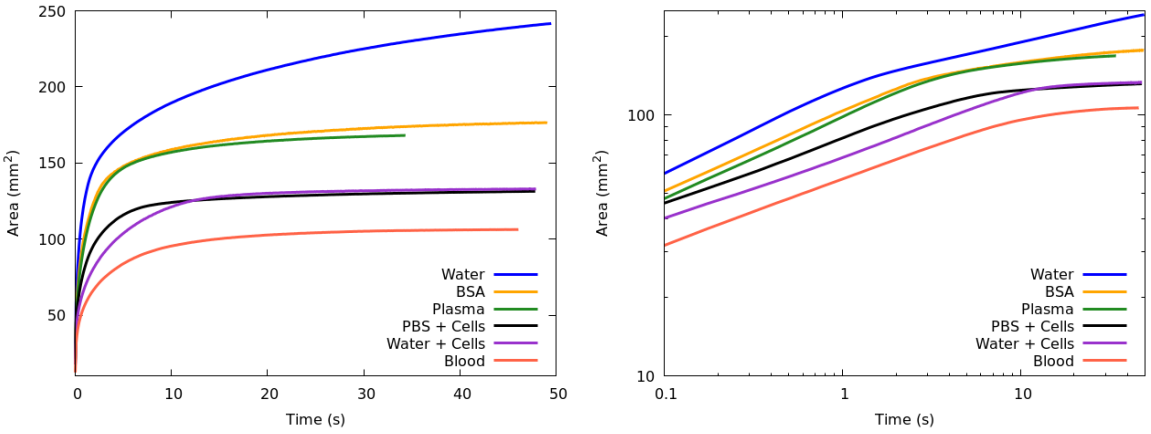

Figure 7.4: Stain growth of several biofluids interpolated to 15 µL.

7.3.1 Numerical Results

Results of numerical simulations compared to experimental wicking in the first stage for water, plasma, and blood are shown in Figure 7.5. Good agreement is found apart from the very early stages and the region right before stage transition. The simulations also predict well the timing of the first to second stage transition as the end of simulation results correlates to the position of the change of gradient in the log-log experimental data. The parameters used for each result are shown in Table 7.2. h is the thickness of the paper, ϵ_s is the saturation volume fraction, λ is the pore distribution index, μ is the dynamic viscosity of the fluids, θ is the contact angle and r_c is the radius of the contact patch of the droplet.

h, ϵ_s and λ are properties of the paper and are calculated or measured in our previous study [20]. The value for $K_0 P_m$ was calculated with equation 7.8 using apreviously reported value of D_0 [20]. Viscosities are found from the literature. Both blood and plasma have been shown to be shear-thinning; [10] however, as the shear rate in wicking is likely to be very small, a constant viscosity is assumed. θ is the advancing contact angle from Table 7.1.

A few studies have reported the surface tension of blood and plasma. However, the reported values vary significantly [39–41]. This variability could be caused by a number of factors: differences between individuals, use of different anticoagulants in blood collection, different storage conditions, or longer delays between donation and measurement. Variability is also caused by a dynamic surface tension due to a transient

adsorption of proteins that is rarely considered [42]. Pendant drop surface tensiometry [43] was performed on the samples of whole blood and plasma used in measurements. Due to the quickly changing surface tension right after droplet formation and its dependence on interface dynamics, results were variable. Representative measurements over a large time interval are presented in Figure 7.8 in supplementary information. These correlate with the range of values previously reported. The complex interfacial behavior of such systems means that the surface tension of these fluids will be a function of geometry and diffusion dynamics. Therefore, the effective surface tension in any particular system is difficult to estimate without precise measurements. For this reason, surface tension was fit to data, although the fitted values are within measured ranges for both plasma and blood. Values for r_c are also found by fitting to data. The fitted values are within 20% of the approximate values calculated from equation 7.9 using the volume of the droplet and the measured contact angle on cellulose.

Table 7.2: Parameters used in Figure 7.5

Parameter	Water	Plasma	Blood
V (µL)	15	15	15
μ (mPa·s)	0.93 [44]	1.74[11]	4 [10]
γ (mN/m)	72.31 [45]	60	50
θ (deg)	15	28	46
h (µm)	226 [11]	226 [11]	226 [11]
K_0P_m	8.61x10-7	8.61x10-7	8.61x10-7
r_c (mm)	3.4	3.4	3.1
ϵ_s	0.7 [20]	0.7 [20]	0.7 [20]
λ	5.0 [20]	5.0 [20]	5.0 [20]

Full-morphology analysis was performed to assess the effect of liquid entrapment due to insufficient pore interconnectivity and whether this is a primary cause of the observed hysteresis. This is achieved by changing the algorithm to only include a wetting phase infiltration if pores are connected to a wetting phase reservoir at the edge of the domain. This step is common in full-morphology algorithms to account for entrapment of both wetting and nonwetting phases [46]. With this condition included, the current analysis shows negligible change. This implies that the paper pores are sufficiently interconnected to prevent liquid entrapment.

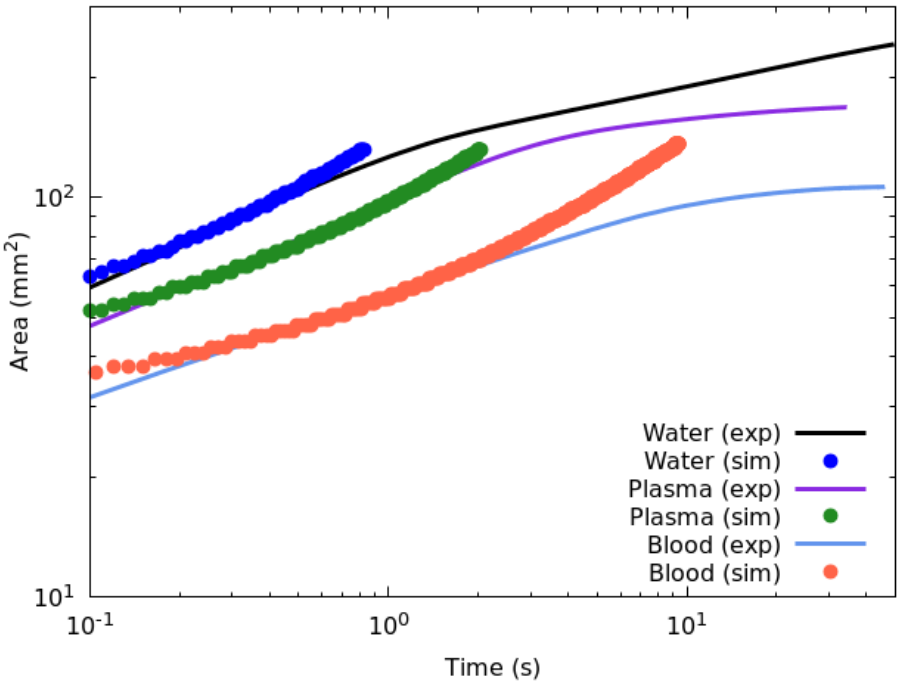

Figure 7.5: Simulation of the stain area as a function of time on log-log scale results for the first stage of wicking on paper. The parameters of Table 7.2 were used with equations 7.3, 7.7 and 7.8.

7.4 Discussion

Measurements of the stain area as a function of time from several biological fluids are shown in linear and log-log scales in Figure 7.4. A significant difference in the stain growth kinetics between biological fluids with substantial cell and protein content appears when compared to simple, pure fluids. The second-stage power is strongly system dependent for biological fluids (Table 7.1). Previous numerical research [20] attributed a change in power in the second stage to porosimetry hysteresis. This hysteresis is caused by differences in wetting/dewetting phenomena and a more severe hysteresis has been shown to cause a lower second-stage gradient. This is because de-wetting only occurs when the pores begin to empty after the droplet has been consumed. This occurs at the end of the first stage as the droplet disappears from the surface of the paper. The low second stage powers exhibited by biological fluids imply that hysteresis is more severe for these fluids. Therefore, to understand the wicking behavior of these complex fluids, the mechanism of porosimetry hysteresis is investigated.

When a droplet is deposited onto the surface of a wettable porous media made of interconnected pores, two phenomena happen concomitantly. The droplet absorbs within

the surface and starts wicking along the pores or fibers of the media. Likewise, wicking is a two-step phenomenon dictated by two distinct mechanisms [17]. In the first stage, the pores are filled with fluid provided by the droplet that is slowly being consumed. After some time, the droplet disappears, which initiates the second stage of radial wicking. In this stage, the fluid required to fill pores on the outside of the stain is provided by emptying the larger pores, causing the larger pores to be refilled with air. After the transition, the mechanism responsible for stain growth changes from wetting for the first stage (fluid moving from the droplet into the pores) to a combined wetting/dewetting mechanism for the second [20] (fluid moving from large to small pores). The advancing and receding contact angles drive each process, respectively. Should the advancing and receding angles be similar, or close, such as for decane on paper, a single wicking stage is observed [20]. For most fluids and biological fluids in particular, this is not the case. Wetting and protein adsorption change the three interfacial tensions [11], thus changing the wetting of an advancing or receding front of the liquid. This means that the advancing angle will be much higher than the receding angle. This affects the driving force behind stain growth and creates the second wicking stage discrepancy discovered in this study.

The developed model can predict the behavior in the first stage. Predictions in Figure 7.5 deviate from experimental results in the very early stages of stain growth because this region is dominated by effects that are not included in the model. These include inertial and surface impact/wetting effects. As biological fluids show more deviation from the model at early times, this is likely caused by biomolecule adsorption, which brings about dynamic changes in the contact angle, surface tension and viscosity [11, 42]. Results imply that this adsorption has a very short time scale in this system. This is why broad accuracy is achieved using constant parameters. The later stages, right before stage transition, are also not well predicted. This is because in reality, stage transition does not happen instantaneously when the drop is consumed. There is instead a finite time over which the transition occurs. During this transition, the assumptions of constant droplet contact radius and constant saturation are invalid. This is particularly true for blood as the low viscosity and surface tension combined with a high contact angle result in a very slow stage transition that is not captured by this model. Despite these discrepancies, simulation results demonstrate that differences in stain sizes between biological and simple fluids are explained solely by changes in surface tension, contact angle, and viscosity. Continuing the simulation with a shift in boundary conditions to model consumption of the droplet was previously investigated [20]. A good

agreement was found for simple fluids; however, such an agreement could not be found for biological fluids. This is likely because hysteresis of contact angles of the wicking fluid is very severe in biological fluids and the simple power law model used previously to account for this in simple fluids is no longer sufficient.

Before a more complete model of second-stage wicking can be derived, the mechanism of porosimetry hysteresis in these systems must be determined and quantified. Three hysteresis mechanisms have been investigated: (1) entrapment in a porous network, (2) fiber swelling, and (3) contact angle hysteresis. The effect of these factors is analyzed below.

In a capillary system, infiltration of the wetting phase will occur only if the non-wetting phase has an evacuation route. Similarly, if a fully wet capillary system is emptied, full evacuation of the wetting phase will not happen unless all wet regions have a path to the applied suction. In paper, the entrapment of liquid could occur during the second stage if initial stages of emptying caused the isolation of small areas of the wetting fluid in isolated areas of smaller pores. This entrapment of fluid in the second stage would produce the observed hysteresis effect.

Full-morphology analysis was used to identify the effect of liquid entrapment. Analysis shows that pores in paper are sufficiently interconnected with a large range of pore sizes such that no entrapment occurs. Thus, limited pore connectivity cannot be the primary cause of the observed hysteresis. This is particularly evident when it is considered that the resolution used would not capture the very small connections caused by fiber overlaps and intrafiber crevices. These very small channels were shown to be partially responsible for fluid transport in paper [47] and would result in a higher than calculated pore connectivity. Figure 7.9 in supplementary information shows the results from full-morphology analysis in comparison to mercury porosimetry measurements fit to the Brooks-Coorey model of pore dynamics [30]. Mercury porosimetry data and model fit are reproduced from a previous study on the same paper [20]. Our full-morphology calculation is similar to model and experimental results. Discrepancies mostly at high and low volume fractions are caused by errors in both full morphology and mercury porosimetry techniques. The true pressure against the volume fraction curve likely lies in between the two calculated values. Porosimetry results also demonstrate that the majority of the pores in paper are larger than the average size of red blood cells (6 µm) [10]. This supports the use of the Richards equation in this system as it implies that

blood can be modeled as a continuum.

Another possible cause of the observed hysteresis is paper swelling. This is because swelling fibers effectively consume fluid, removing it from the system and reducing the local pore radius and volume. This decreasing volume of fluid in the system could create a hysteresis effect. This is unlikely as this would not correspond with first-to-second stage transition unless swelling occurred suddenly a finite time after contact. Previous studies showed that the time scale of swelling in normal paper fibers is very short (less than 1 s), so this is unlikely to have an effect [48]. It was also found that a two-stage behavior is still observed in paper made with nonswelling glass fibers [20]. Therefore, swelling is also unlikely to be the cause of hysteresis.

Contact angles experience hysteresis because local physical and chemical heterogeneities produce pinning forces. This could affect the second-stage behavior significantly as the introduction of voids in the center of the stain in this stage creates receding interfaces. Any hysteresis in contact angles would alter the relative magnitude of the capillary pressures at the advancing and receding interfaces. As this is what determines the wicking rate in the second-stage, results would likely be affected significantly. Results in Table 7.1 show that these systems do experience significant contact angle hysteresis and the trend in hysteresis matches that of the second-stage powers. Therefore, contact angle hysteresis is likely to be the cause of the two-stage behavior measured in radial wicking. This also explains the reported relationship between the contact angle and equilibrium size [11]. Contact angle hysteresis defines the additional resistance to stain growth in the second stage and the anomalous stain kinetics of biological fluids.

Increased advancing contact angle of biological fluids on cellulose has previously been shown to be caused by an increase in solid-liquid interfacial energy due to protein adsorption [11]. The new results presented here show that, in most cases, the receding angle remains low due to pinning forces resisting the triple line motion. These pinning forces could be produced by adsorbed protein and cells at the contact line. This pinning due to adsorbed constituents is commonly observed in many colloid suspensions and would be more severe in blood as compared to plasma. This behavior is matched by experimental results. This implies that the primary cause of the anomalous stain growth behavior of biological fluids is a severe contact angle hysteresis (Figure 7.1). This occurs because adsorbed biomolecules cause a high advancing contact angle but do not alter the receding angle significantly.

Attempts were made to alter the developed model to incorporate the effects of contact angle hysteresis. This was achieved by including contact angle as a function of the temporal gradient of volume fraction. To do this, equation 7.3 cannot be used as pressure is no longer solely a function of the volume fraction of fluid in pores. Equation 7.2 must be selected instead, which requires pressure to be calculated at each cell. A pressure equation can be derived by integrating equation 7.6; however, this introduces two numerical difficulties. First, the equation predicts a negative infinite pressure at $\phi = 0$; this can be overcome by assuming a linear function of pressure from a threshold minimum volume fraction. This had a negligible effect on results as it maintains the required high pressure gradient over areas with a small volume fraction that was not achieved by simply setting a lower pressure limit. Second, the new pressure field is discontinuous in regions where the temporal gradient of volume fraction changes signs or where the mechanism shifts from filling to emptying. This produces convergence difficulties that could not be resolved. A more detailed numerical study is required to properly resolve the effect of contact angle hysteresis in radial wicking.

The developed model is capable of predicting results in the first stage of wicking for all tested fluids by including values of surface tension, contact angle, and viscosity. This shows that the dynamics for complex fluids in this regime are driven by the same mechanisms as simple fluids [20, 27–29]. Results highlight the role of hysteresis in these systems as it is the primary difference between the two stages. For biological fluids, wetting/dewetting hysteresis in the second stage is too severe to model with current techniques. Experimental and numerical investigations show that this hysteresis arises from contact angle effects due to the protein and cell component of the fluids. This identifies why the power relationship with time for these fluids is low.

7.5 Conclusions

In this study, the wicking of biological fluids including human blood, plasma, and protein solutions on paper was measured and modeled from first principles. This was to optimize the design of novel low-cost paper-based diagnostics. A combination of high-speed photography, image processing, and numerical modeling was used. The stain size of biological fluids on paper was recorded as a function of time. A unique second-stage behavior was discovered, differing from that of simple fluids. The two-phase wicking behavior of biological fluids on paper is best visualized by following the

stain area as a function of time on a log-log plot. The cause of the second wicking stage of biological fluids is a severe wetting/dewetting hysteresis. Wetting experiments with model systems revealed contact angle hysteresis to be the most likely cause of hysteresis. Fiber swelling and liquid entrapment in porous media were also investigated and dismissed. The difference between first stages exhibited by the different fluids tested was solely driven by differences in viscosity, surface tension, and contact angle. This was demonstrated with a good fit to numerical modeling in the first stage. These results give significant insights into the wicking of biological fluids in paper, particularly in finite reservoir systems where the investigated hysteresis will be significant. This knowledge now enables the development and optimization of a new generation of low-cost diagnostic devices with powerful tools such as computational fluid dynamics and mathematical modeling.

7.6 Acknowledgement

This research was funded by an ARC Linkage grant (LP160100544), Haemokinesis, and an Australian Government Research Training Program (RTP) Scholarship. The research was supported in part by Monash eResearch Centre and eSolutions-Research Support Services through the use of the MonARCH HPC Cluster. Thanks to David Paganin for advice on the analysis of x-ray images and the Red Cross Australia for supplying blood products.

7.7 References

[1] Tokuzo Kawase, Sakiko Sekoguchi, Tomiko Fujii, and Motoi Minagawa. Spreading of Liquids in Textile Assemblies Part I: Capillary spreading of liquids. *Textile Research Journal*, 56(7):409–414, 1986.

[2] Mohidus Samad Khan, George Thouas, Wei Shen, Gordon Whyte, and Gil Garnier. Paper diagnostic for instantaneous blood typing. *Analytical chemistry*, 82(10):4158–4164, 2010.

[3] M. Wijaya, E. C. Leong, and H. Rahardjo. Effect of shrinkage on air-entry value of soils. *Soils and Foundations*, 55(1):166–180, 2015.

[4] C. M. Reed and N. Wilson. Fundamentals of absorbency of fibres, textile structures and polymers. I: the rate of rise of a liquid in glass capillaries. *Journal of Physics D: Applied Physics*, 26(9):1378, 1993.

[5] Mohammad Al-Tamimi, Wei Shen, Rania Zeineddine, Huy Tran, and Gil Garnier. Validation of paper-based assay for rapid blood typing. *Analytical Chemistry*, 84(3):1661–1668, 2012.

[6] Zhi Liu, Xiaocong He, Jiaxiu Han, Xiuhai Zhang, Fei Li, Ang Li, Zhiguo Qu, and Feng Xu. Liquid wicking behavior in paper-like materials: mathematical models and their emerging biomedical applications. *Microfluidics and Nanofluidics*, 22(11):132, 2018.

[7] Jingyao Li, Xingyu Li, and Stephen Michielsen. Alternative method for determining the original drop volume of bloodstains on knit fabrics. *Forensic science international*, 263:194–203, 2016.

[8] Therese C. de Castro, Debra J. Carr, Michael C. Taylor, Jules A. Kieser, and Warwick Duncan. Drip bloodstain appearance on inclined apparel fabrics: Effect of prior-laundering, fibre content and fabric structure. *Forensic Science International*, 266:488–501, 2016.

[9] Frank Ramsthaler, J. Schlote, C. Wagner, J. Fiscina, and M. Kettner. The ring phenomenon of diluted blood droplets. *International Journal of Legal Medicine*, 130(3):731–736, 2016.

[10] Mark Thiriet. *The Biology and Mechanics of Blood Flows*. Springer, 2008.

[11] Michael J Hertaeg, Rico F Tabor, and Gil Garnier. Effect of protein adsorption on the radial wicking of blood droplets in paper. *Journal of Colloid And Interface Science*, 528:116–123, 2018.

[12] Tomoaki Hagiwara, Phosri Nattawut, Mario Shibata, and Takaharu Sakiyama. Monitoring of adsorption behaviors of bovine serum albumin onto a stainless steel surface by the quartz crystal microbalance based on admittance analysis. *Bioscience, Biotechnology and Biochemistry*, 81(4):783–789, 2017.

[13] David J. Greenblatt. Reduced Serum Albumin Concentration in the Elderly: A Report from the Boston Collaborative Drug Surveillance Program. *Journal of the American Geriatrics Society*, 27(1):20–22, 1979.

[14] T. Gillespie. The spreading of low vapor pressure liquids in paper. *Journal of Colloid Science*, 13(1):32–50, 1958.

[15] Erik Kissa. Capillary sorption in fibrous assemblies. *Journal of Colloid and Interface Science*, 83(1):265–272, 1981.

[16] Dganit Danino and Abraham Marmur. Radial capillary penetration into paper: limited and unlimited liquid reservoirs. *Journal of Colloid and Interface Science*, 166(1):245–250, 1994.

[17] KK Borhan, Ali and Rungta. An experimental study of the radial penetration of liquids in thin porous substrates. *Journal of Colloid and Interface Science*, 158(2):403–411, 1993.

[18] Abraham Marmur. Penetration and displacement in capillary systems of limited size. *Advances in Colloid and Interface Science*, 39:13–33, 1992.

[19] J. Kloubek. Hysteresis in porosimetry. *Powder Technology*, 29(1):63–73, 1981.

[20] Michael J. Hertaeg, Rico F. Tabor, Joseph D. Berry, and Gil Garnier. Dynamics of stain growth from sessile droplets on paper. *Journal of Colloid and Interface Science*, 541:312–321, 2019.

[21] R. D. Hazlett. Simulation of capillary-dominated displacements in microtomographic images of reservoir rocks. *Transport in Porous Media*, 20(1-2):21–35, 1995.

[22] L. A. Richards. Capillary conduction of liquids through porous mediums. *Journal of Applied Physics*, 1(5):318–333, 1931.

[23] Ziwei Huang, Vikram Singh Raghuwanshi, and Gil Garnier. Functionality of immunoglobulin g and immunoglobulin M antibody physisorbed on cellulosic films. *Frontiers in bioengineering and biotechnology*, 5:41, 2017.

[24] Jielong Su, Christopher J Garvey, Stephen Holt, Rico F Tabor, Bjorn Winther-Jensen, Warren Batchelor, and Gil Garnier. Adsorption of cationic polyacrylamide at the cellulose–liquid interface: A neutron reflectometry study. *Journal of Colloid and Interface Science*, 448:88–99, 2015.

[25] T. Weitkamp, D. Haas, D. Wegrzynek, and A. Rack. ANKAphase : software for single-distance phase retrieval from inline X-ray phase-contrast radiographs. Erratum. *Journal of Synchrotron Radiation*, 20(1):205–205, 2013.

[26] D. Paganin, S. C. Mayo, T. E. Gureyev, P. R. Miller, and S. W. Wilkins. Simultaneous phase and amplitude extraction from a single defocused image of a homogeneous object. *Journal of Microscopy*, 206(1):33–40, 2002.

[27] Angel Perez-Cruz, Ion Stiharu, and Aurelio Dominguez-Gonzalez. Two-dimensional model of imbibition into paper-based networks using Richards' equation. *Microfluidics and Nanofluidics*, 21(5):98, 2017.

[28] A. Ashari, T. M. Bucher, H. Vahedi Tafreshi, M. A. Tahir, and M. S.A. A Rahman. Modeling fluid spread in thin fibrous sheets: Effects of fiber orientation. *International Journal of Heat and Mass Transfer*, 53(9-10):1750–1758, 2010.

[29] Sudhakar Jaganathan, Hooman Vahedi Tafreshi, and Behnam Pourdeyhimi. A realistic modeling of fluid infiltration in thin fibrous sheets. *Journal of Applied Physics*, 105(11):113522, 2009.

[30] Henk Huinink. *Fluids in Porous Media*. Morgan & Claypool Publishers, 2016.

[31] Dalton James Eric Harvie. An implicit finite volume method for arbitrary transport equations. *ANZIAM Journal*, 52(0):1126–1145, 2010.

[32] Becky Lavi, Abraham Marmur, and Joerg Bachmann. Porous media characterization by the two-liquid method: Effect of dynamic contact angle and inertia. *Langmuir*, 24(5):1918–1923, 2008.

[33] C.H. Bosanquet. LV. On the flow of liquids into capillary tubes. *The London, Edinburgh, and Dublin Philosophical Magazine and Journal of Science*, 45(267):525–531, 1923.

[34] G. Martic, F. Gentner, D. Seveno, D. Coulon, J. De Coninck, and Terry D. Blake. A molecular dynamics simulation of capillary imbibition. *Langmuir*, 18(21):7971–7976, 2002.

[35] Reza Masoodi and Krishna M Pillai. *Wicking in Porous Materials : Traditional and Modern Modeling Approaches*. CRC Press, 2012.

[36] Cinzia Sala, Marina Ciullo, Carmela Lanzara, Teresa Nutile, Silvia Bione, Roberto Massacane, Pio D'Adamo, Paolo Gasparini, Daniela Toniolo, and Clara Camaschella. Variation of hemoglobin levels in normal Italian populations from genetic isolates. *Haematologica*, 93(9):1372–1375, 2008.

[37] Benjamin J. Ravenhill, Usheer Kanjee, Ambroise Ahouidi, Luis Nobre, James Williamson, Jonathan M. Goldberg, Robin Antrobus, Tandakha Dieye, Manoj T. Duraisingh, and Michael P. Weekes. Quantitative comparative analysis of human

erythrocyte surface proteins between individuals from two genetically distinct populations. *Communications Biology*, 2(1):1–9, 2019.

[38] H Billett H. *Hemoglobin and Hematocrit*. Butterworths, 3rd edition, 1990.

[39] J Rosina, E Kvasnak, D Suta, H Kolarova, J Malek, and L Krajci. Temperature dependence of blood surface tension. *Physiological research*, 56:S93, 2007.

[40] B. Sobac and D. Brutin. Desiccation of a sessile drop of blood: Cracks, folds formation and delamination. *Colloids and Surfaces A: Physicochemical and Engineering Aspects*, 448(1):34–44, 2014.

[41] Yu Yu Tarasevich, I. V. Vodolazskaya, and O. P. Bondarenko. Modeling of spatial-temporal distribution of the components in the drying sessile droplet of biological fluid. *Colloids and Surfaces A: Physicochemical and Engineering Aspects*, 432:99–103, 2013.

[42] Sergei Zaitsev. Dynamic surface tension measurements as general approach to the analysis of animal blood plasma and serum. *Advances in colloid and interface science*, 235:201–213, 2016.

[43] Joseph D. Berry, Michael J. Neeson, Raymond R. Dagastine, Derek Y.C. C Chan, and Rico F. Tabor. Measurement of surface and interfacial tension using pendant drop tensiometry. *Journal of Colloid and Interface Science*, 454:226–237, 2015.

[44] Joseph Kestin, Mordechai Sokolov, and William A Wakeham. Viscosity of liquid water in the range -8 C to 150 C. *Journal of Physical and Chemical Reference Data*, 7(3):941–948, 1978.

[45] Gonzalo Vazquez, Estrella Alvarez, and Jose M Navaza. Surface tension of alcohol water+ water from 20 to 50. degree. C. *Journal of chemical and engineering data*, 40(3):611–614, 1995.

[46] Jürgen Becker, Volker Schulz, and Andreas Wiegmann. Numerical determination of two-phase material parameters of a gas diffusion layer using tomography images. *Journal of Fuel Cell Science and Technology*, 5(2), 2008.

[47] Raymond Roberts, Timothy Senden, Mark Knackstedt, and M B Lyne. Spreading of aqueous liquids in unsized papers is by film flow. *Journal of pulp and paper science*, 29(4):123—-131, 2003.

[48] David R Schuchard and John C Berg. Liquid transport in composite cellulose—superabsorbent fiber networks. *Wood and Fiber Science*, 23(3):342–357, 2007.

7.8 Supplementary

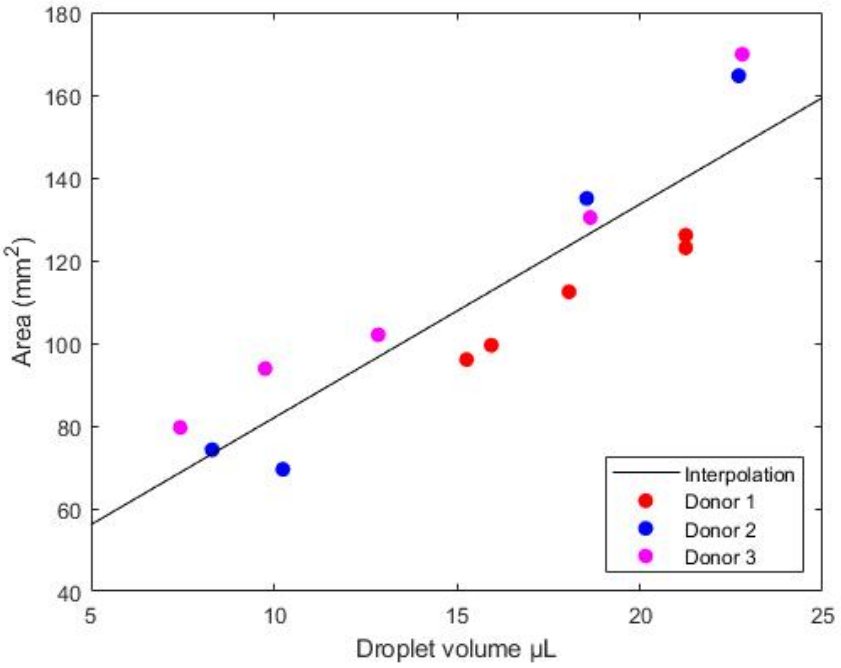

Figure 7.6: Blood stain size at 30 seconds for a range of drop volumes. Linear fit is not as accurate as plasma, this is caused by variations in blood composition between donors.

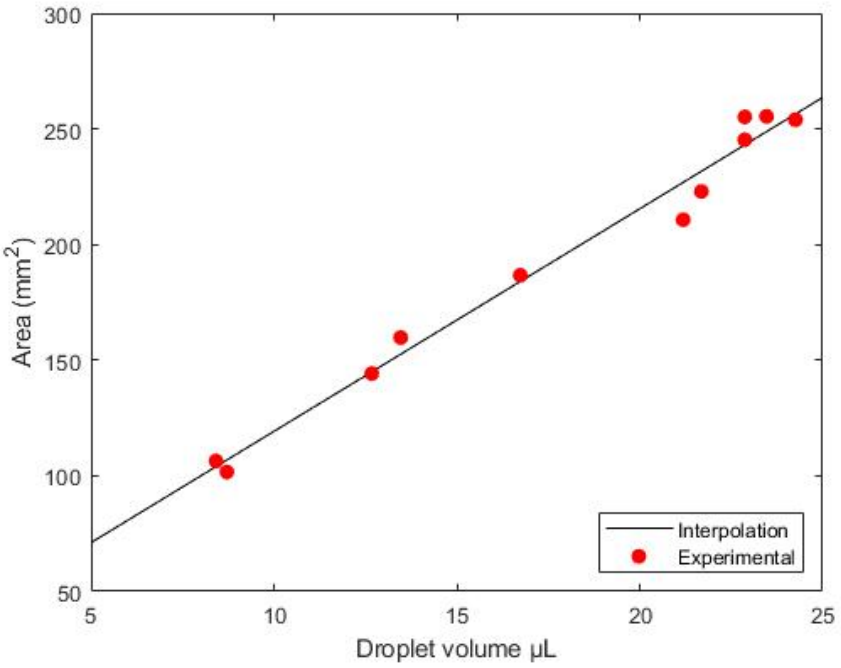

Figure 7.7: Plasma stain size at 30 seconds for a range of drop volumes. This shows the strong linear dependence.

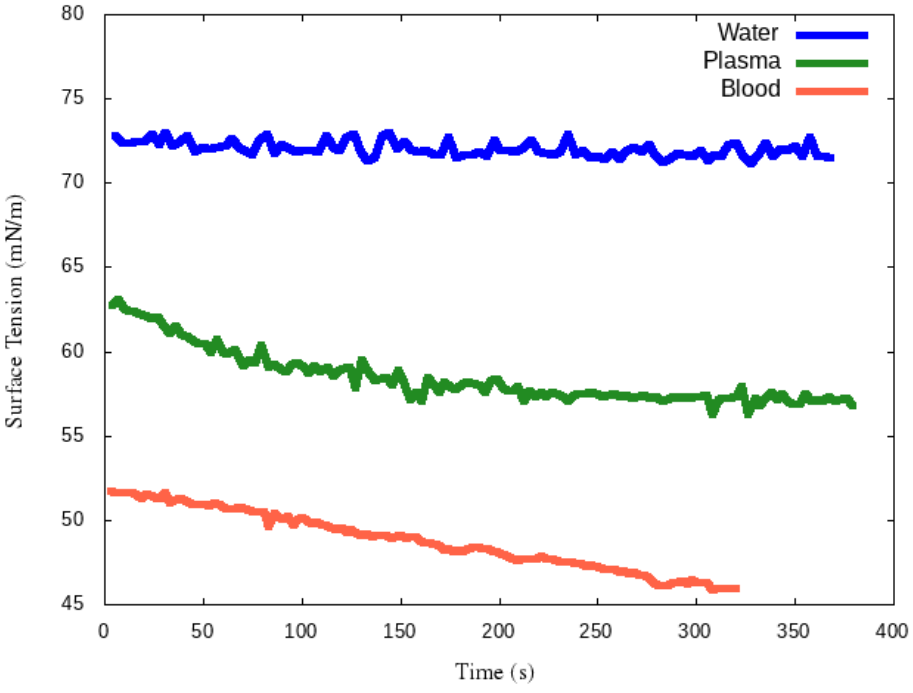

Figure 7.8: Surface tension of biological fluids measure with pendant drop surface tensiometry. Shows transient behaviour.

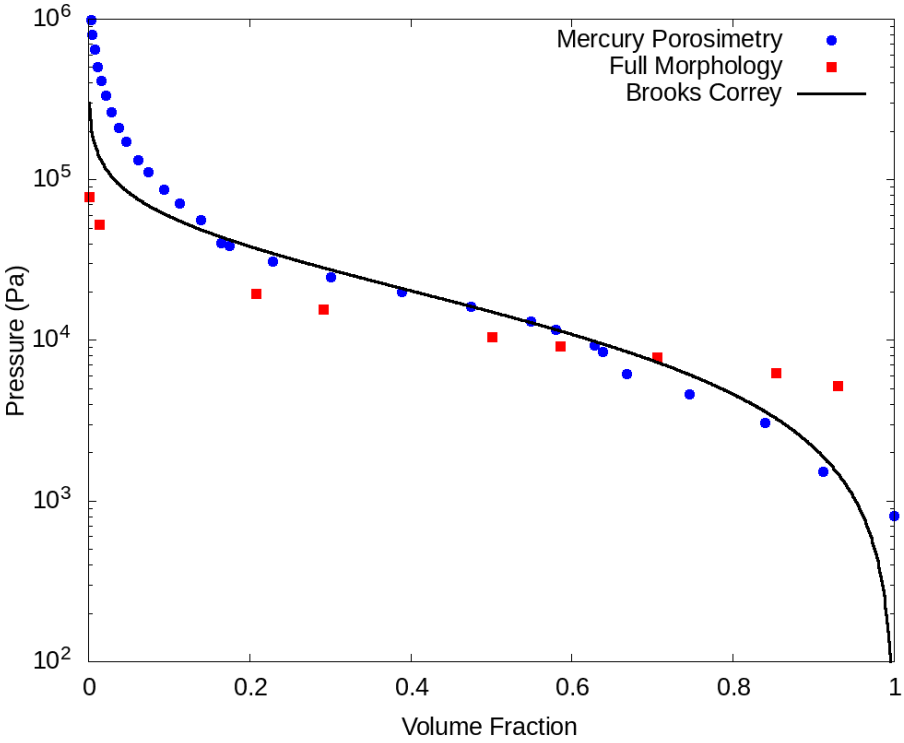

Figure 7.9: Full morphology results compared with mercury porosimetry analysis.

Chapter 8

Pattern Formation in Blood Drops

8.1 Introduction

Blood droplet analysis has been used in the field of forensics for many years [1]. It is only recently that its medical applications have received attention, where patterns produced in dried blood was indicative of several important medical conditions [2, 3]. These include carcinoma [4], anaemia, hyperlipemeia [5], thalasemia, jaundice [6] and many more [7]. These findings indicate the potential for a new generation of low-cost point of care diagnostics where all that is required is a droplet of patient blood and a standard surface. Although these techniques are promising, more research is required before robust tests can be designed, and results relied on for diagnosis. This is because the mechanisms that lead to pattern formation in drying droplets of blood is poorly understood.

Much of the previous research on the medical applications of blood droplet analysis has focused on the appearance of cracking patterns [8–10]. These are easily seen by eye and therefore have potential to be used for diagnostics. The appearance of several different concentrations of red blood cells (RBCs) in plasma are shown in Figure 8.1. Crack initiation and propagation is a complex process that is reproducible and highly dependent on the properties of the particle system [11]. This is why pattern formation can differentiate the small variations caused by disease. The concept behind these diagnostics is to visually analyse crack pattern formation in a drying droplets deposited on a model surface. Any change in RBC concentration, shape, rigidity or plasma surface tension will cause different dynamics and final appearance. Therefore relating crack patterns quantified by image analysis with pathology. There are many models that are used to predict cracking patterns in a variety of drying systems [12–16], although

complications in blood systems make their application difficult. One such complication is the redistribution of components that occurs in the early stages of drying, which is responsible for the ring-like profile that develops in most circumstances [5]. Previous literature regarding this process in simple colloids and blood are reviewed in section 2.5.

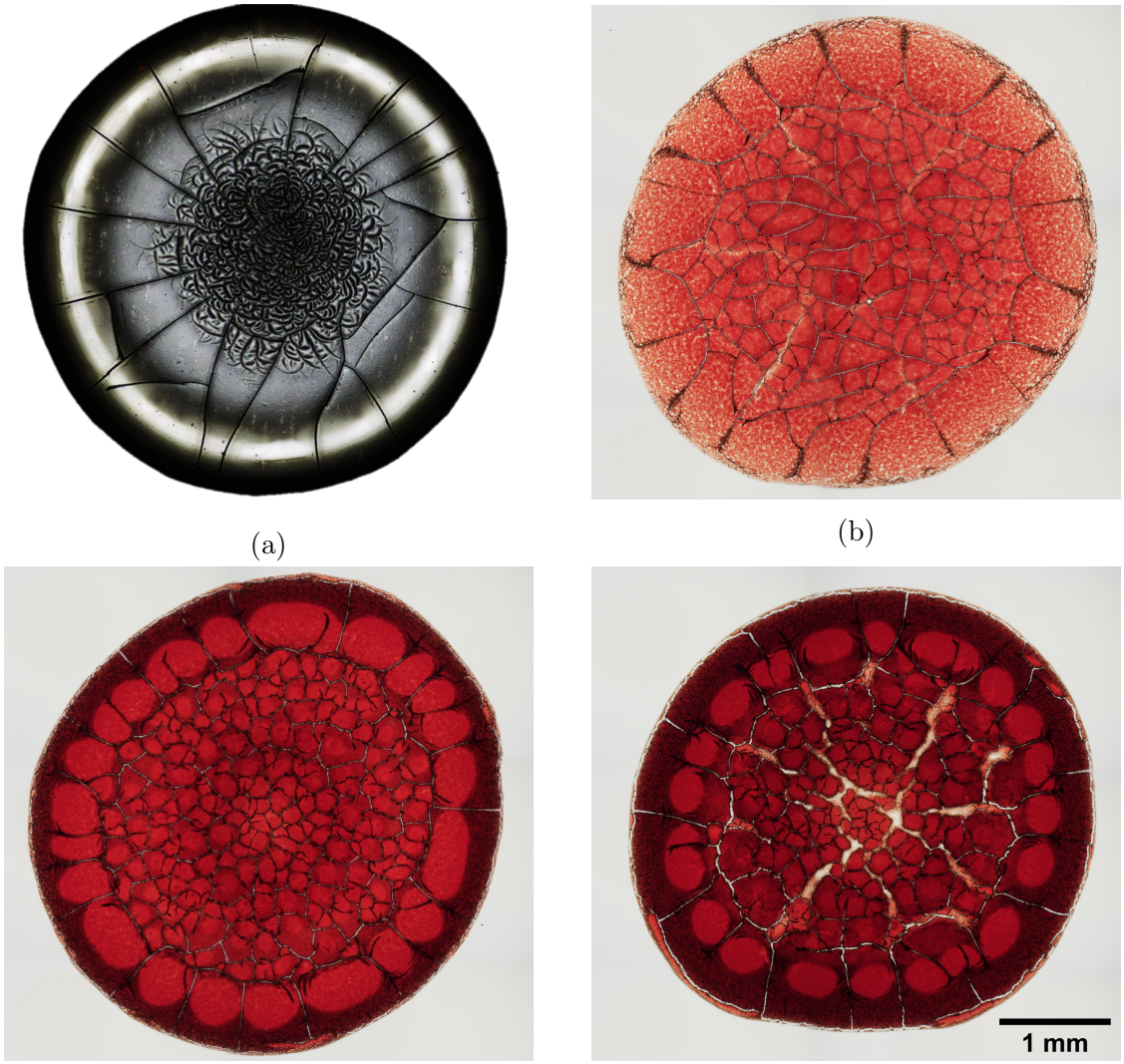

Figure 8.1: Images of droplets dried on untreated glass. Red blood cells (RBC) combined with plasma at different concentrations are shown. a) 0%, b) 15%, c) 30%, d) 45%. Scale bar applies to all images.

Here, the drying of droplets varying in red blood cell (RBC) and protein content are analysed. The drying dynamics of RBC suspensions are compared with simple colloidal particles and the dominant factors that affect the morphology of dried blood drops

are investigated. This is done by drying droplets of red blood cell suspensions at different concentrations and varying protein content on a selection of smooth treated glass surfaces providing a range of contact angles.

8.2 Methods

Model RBC suspensions were made with whole blood provided by the Red Cross Australia with EDTA as anticoagulant. RBCs were washed 3 times by centrifugation, removing the supernatant and then re-suspending in phosphate buffered saline (PBS). The pellet left after centrifugation was assumed to be 100 vol% cells, which was combined with the selected solution to the required concentration. 3 different solutions were used: Plasma, which was collected from the same sample by removing the supernatant after the first washing step. Phosphate buffered saline (PBS) purchased from Sigma and made up with water purified with a Millipore Milli-Q system. Bovine serum albumin (BSA), which was diluted in PBS from 30% (wt/v) solutions from BioCSL. 6 µL droplets of suspensions were deposited onto WestLab glass microscope slides with an Eppendorf automatic pipette and left to dry at 23°C 50% relative humidity. The wettability of glass slides was altered with a PDC-002-HP Harrik Plasma, plasma cleaner and measured by contact angle. Slides were treated for 3 minutes on the medium setting. Contact angle measurements were performed with a OCA35 DataPhysics contact angle instrument within 1 minute of depositing the droplet. The presented contact angles are the mean of at least 4 measurements over at least 2 different donors. Height profile scans were measured using an Olympus LEXT OLS5000 laser confocal microscope. 4 replicates of each test were performed, this included two result from 2 different donors. Profilometry figures show all these measurements together. 6-8 µm nominal diameter polystyrene beads were purchased from PROSCITECH and were concentrated by centrifuging at 2500 rcf for 3.5 minutes and removing supernatant. Deuterium oxide from Sigma-Aldrich was mixed with solutions to density match the particles and the fluid. Care was taken to undertake experiments in still air; however, slight directionality was seen in many tests due to a sensitivity to air circulation currents.

8.3 Results

Blood droplets of constant volume but varying in RBC concentration and eluent (plasma, PBS and BSA solutions) were deposited on model smooth glass surfaces of different extent of wettability, varied by plasma treatment. The droplet drying profile and crack

pattern were measured as a function of drying time under constant conditions (50%RH and 23°C).

Figure 8.2 shows profilometry centre line scans of dried droplets of RBCs combined with human plasma at 4 different concentrations 0%, 15%, 30% and 45% by volume. 45% is the approximate concentration of cells in human whole blood [5]. These figures show high reproducibility and a distinct relationship with concentration; however, a ring-like profile or coffee ring is always observed. A more defined ring profile is observed at high RBC concentrations. Figure 8.3 shows profilometry measurements of RBC-PBS suspensions where very different profiles are observed. Despite having the same ionic strength as plasma, dried profiles of RBC-PBS solutions demonstrated less defined ring profiles and less large cracks. Also, the lower cell concentrations of PBS solutions displayed almost uniform final height profiles. RBC suspensions in BSA solutions of similar concentration to plasma (83g/L [17]) were also tested (Figure 8.4). Suspensions with BSA produced very similar profiles to those with plasma, although results were more reproducible and slightly less large cracks were observed. All dried droplet profiles were very reproducible and characteristic of the RBC concentration and the type of eluent.

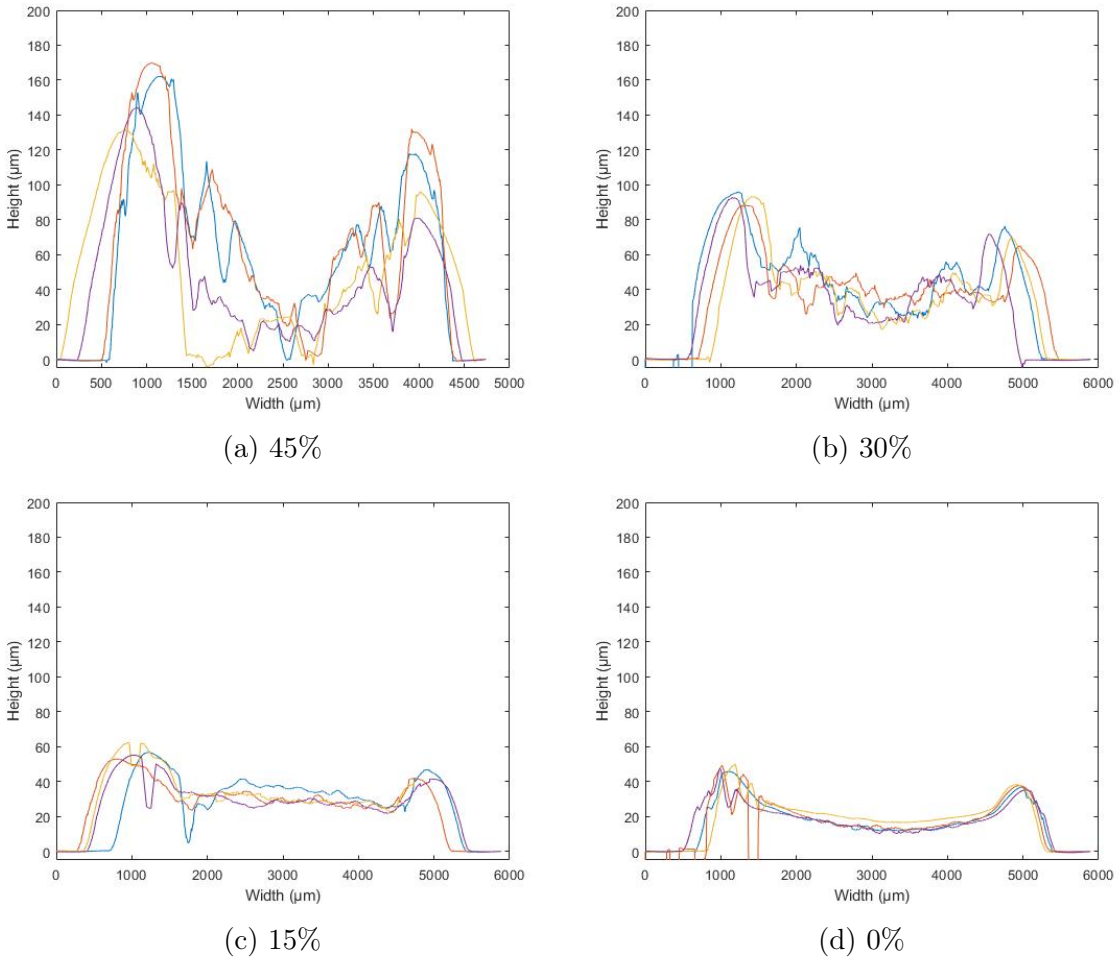

(a) 45% (b) 30%

(c) 15% (d) 0%

Figure 8.2: Profilometry centerline scans of dried 6 µL droplets of RBC-plasma suspensions on untreated glass. Effect of RBC concentration (Vol%): a) 45%, b) 30%, c) 15% and d) 0%.

In all tests, a higher initial concentration of RBCs resulted in a more defined ring profile. This is opposite to predictions by previous researchers [18] and experiments presented in Chapter 9, where a high initial concentration is observed to suppress ring deposits in simple colloid suspensions. When RBCs are suspended in a protein solution the relationship with initial concentration is less defined because protein solutions with no cells produce ring structures. However, measurements of dried profiles of RBCs suspended in PBS show a very clear relationship with initial concentration, where low RBC concentrations form near uniform profiles (8.3c).

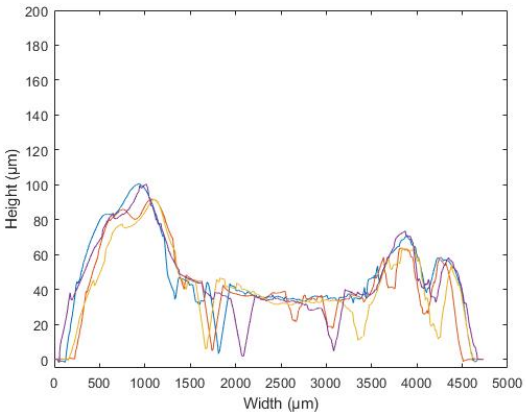

(a) 45%

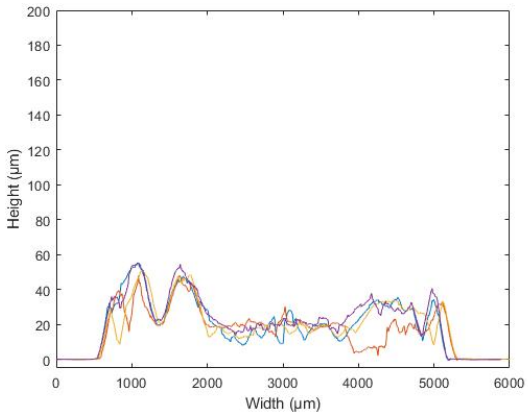

(b) 30%

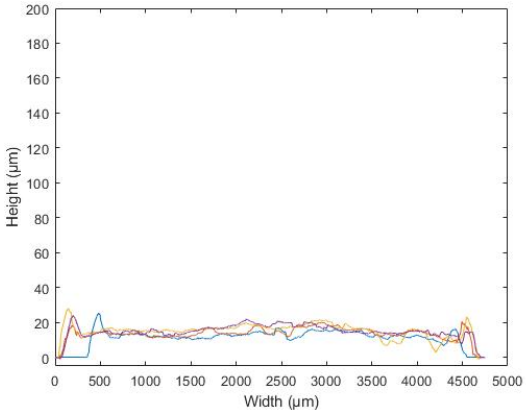

(c) 15%

Figure 8.3: Profilometry centerline scans of dried 6 µL droplets of RBC-PBS suspensions on untreated glass. Effect of RBC concentration (Vol%): a) 45%, b) 30% and c) 15%.

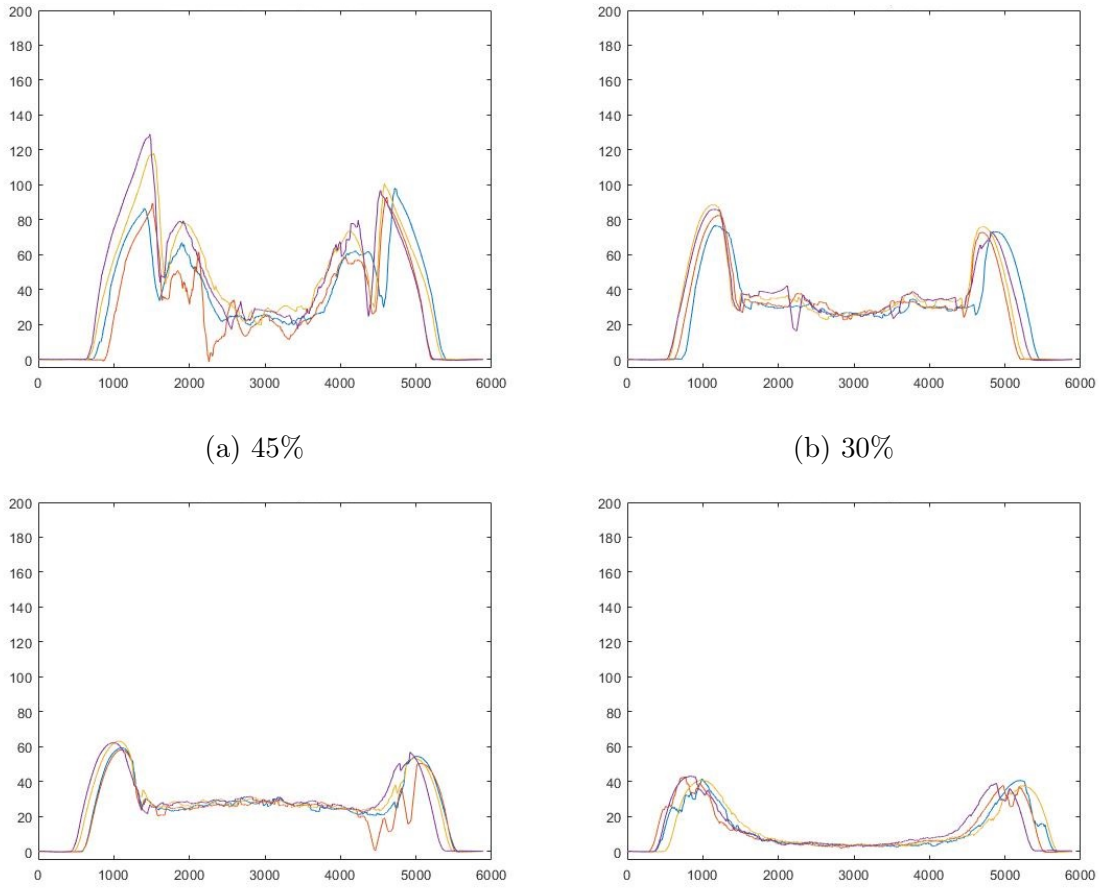

(a) 45%

(b) 30%

(c) 15%

(d) 0%

Figure 8.4: Profilometry centerline scans of dried 6 µL droplets of RBC-BSA suspensions on untreated glass. Effect of RBC concentration (Vol%): a) 45%, b) 30%, c) 15% and d) 0%.

Figure 8.5 shows a series of photographs taken at 4 minute intervals showing the drying dynamics of droplets (6 µL) of whole blood, pure plasma and a polystyrene suspension (15% by volume). Images are displayed until no visual difference was observed between subsequent images. For all systems a 'compaction' front [10] is identifiable within a short time at the outer edge, which then propagates inward. For polystyrene and plasma, this front continues until it reaches the centre. The solid front reaching the centre is marked for polystyrene by a sudden colour change and for plasma, crack initiation. Both events imply complete drying [19].

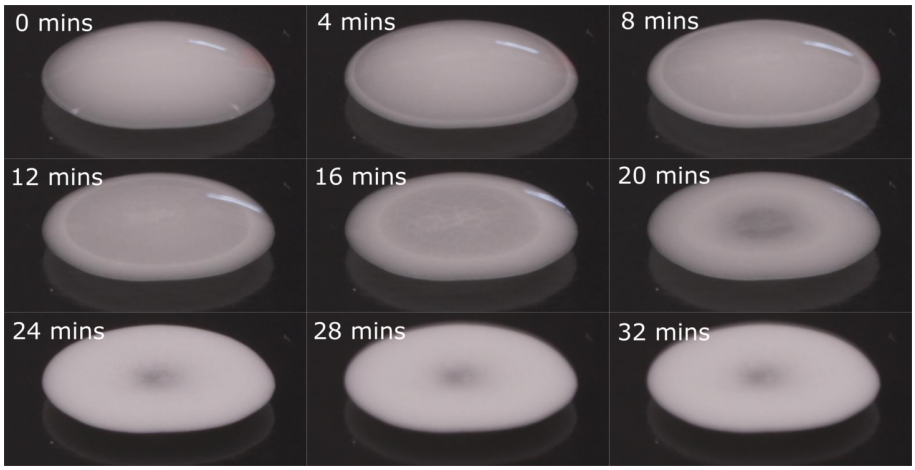

(a)

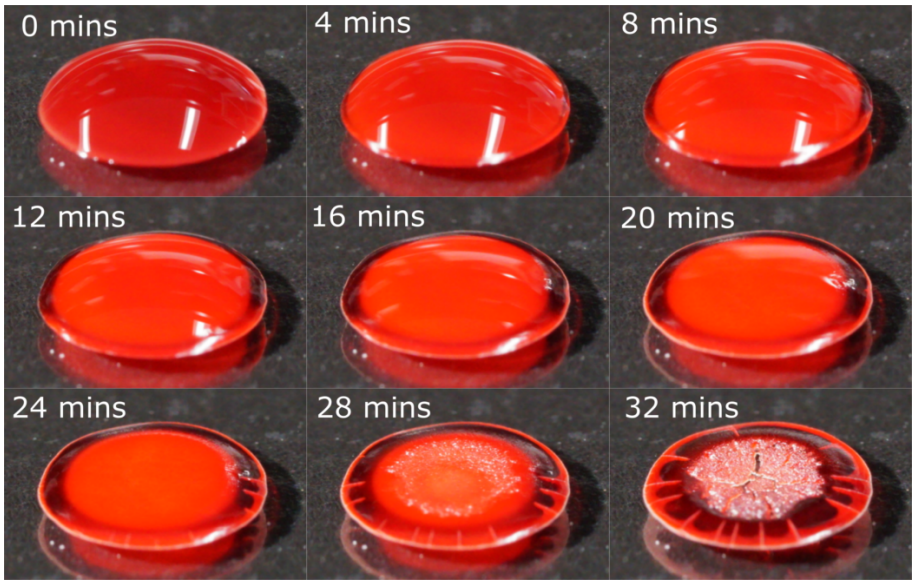

(b)

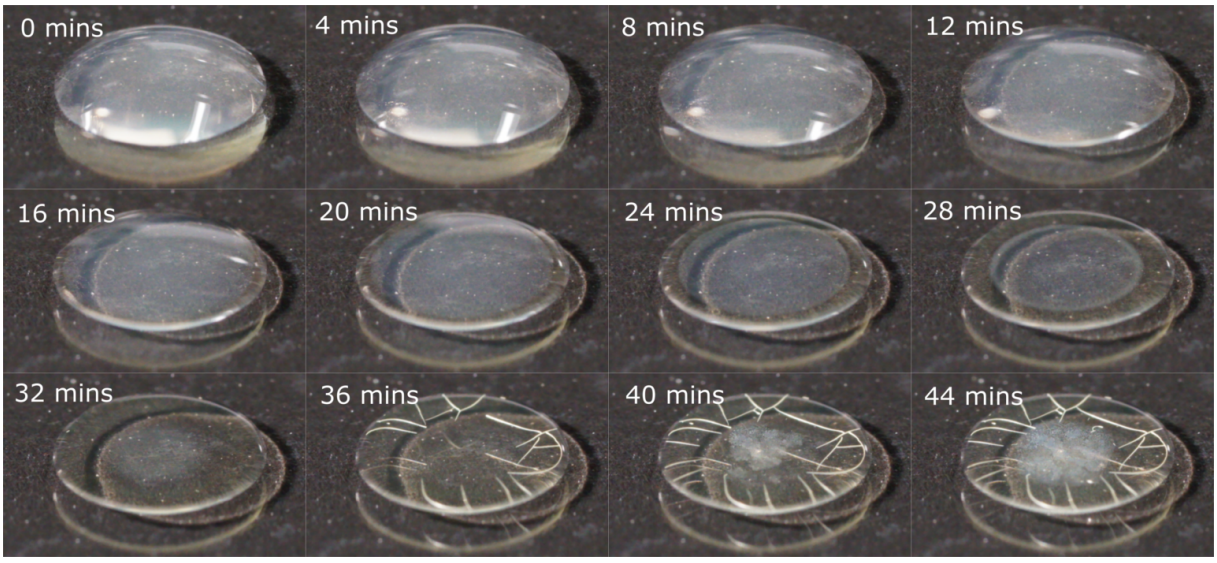

(c)

Figure 8.5: Drying 6 µL droplets of (a) polystyrene, (b) whole blood and (c) plasma on untreated glass. The pictures were taken at different intervals of drying (23°C, 50% RH).

The effect of contact angle was also investigated. Table 8.1 displays the contact angle of the suspensions used on two different surfaces, untreated glass and plasma cleaned glass. Both plasma and PBS suspensions display similar contact angles. However, results with both eluents show a decreasing contact angle with decreasing RBC concentration.

Table 8.1: Contact angle of RBC suspensions in plasma and PBS over treated glass surfaces. The statistics of at least 4 measurements from two different donors are presented.

Vol %	Plasma Glass	Std Dev	PBS Glass	Std Dev	Plasma PC Glass	Std Dev	PBS PC Glass	Std Dev
45%	45.6	7.6	38.7	6.9	9.1	0.9	7.5	0.8
30%	33.8	6.8	35.7	5.0	8.4	1.0	6.4	0.7
15%	37.8	10.6	31.0	4.9	7.9	1.1	7.0	1.2
0%	38.2	9.9	-	-	8.4	2.1	-	-

Profilometry results showed that the effect of contact angle was minimal, with many deposits being very similar in shape to their higher contact angle counterparts despite being wider and thinner. A notable exception to this is a transition that occurs at low contact angles and low RBC concentrations in PBS suspensions, where a central deposit is observed. Profilometry recordings and images of deposits around this transition are displayed in Figure 8.6.

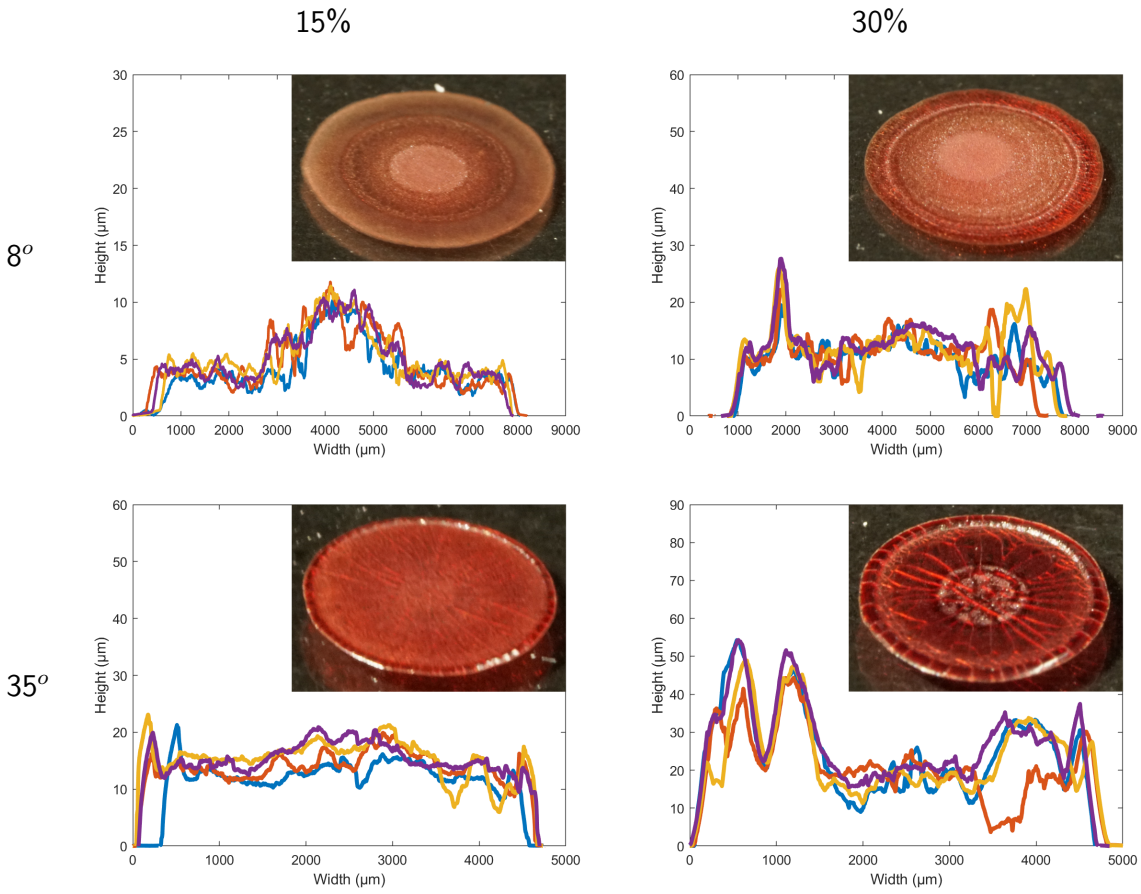

Figure 8.6: Profilometry and photographs of RBC-PBS droplets varying in concentration on treated glass, controlling contact angle.

8.4 Discussion

8.4.1 Effect of Proteins

Comparison of Figures 8.2, 8.3 and 8.4 highlights the large impact plasma has on the dried profiles of droplets and the preponderant role of protein content. The ring profile in the 0% RBC-plasma solution on glass demonstrates that plasma by itself can induce ring formations. This is due to the presence of proteins in plasma [3]. Proteins transport and deposit at the edge of the drop by a similar mechanism as particles [20–25]. Just like for suspension of solid particles there is a critical volume fraction at which the fluid solidifies as it dries. However, this mechnism is governed by gelling or crystallisation rather than by the packing mechanism previously demonstrated with latex suspensions.

Previously, drying droplets of multicomponent fluid systems were demonstrated to pref-

erentially transport the smaller elements to the edge of the drop [26]. This is because the small thickness of the film near the edge prevents the motion of larger particles by size exclusion. Also, the smaller components can flow between larger particles, and therefore can be transported past the solid front. This is especially true for proteins, as these macromolecules are dissolved in the liquid phase and transport freely to the edge of the drying droplet. This preferential deposition of proteins at the edge not only slows evaporation in this region but also hinders the development of interparticle menisci that are responsible for capillary pressure in this region. This protein induced shift in dynamics could be responsible for the observed dependence on protein content.

Initially, tests with RBCs in PBS have little to no proteins in solution, although as drying proceeds, the solution becomes increasingly hypertonic. This causes the crenation of RBCs and eventually partial haemolysis [27, 28]. This releases haemoglobin and other proteins into the bulk solution that behave similarly to the proteins in plasma. Through this mechanism, proteins are introduced in the later stages of drying. A greater amount of protein is released from suspensions of high RBC concentrations; this explains the similarities between the PBS and plasma suspensions at high RBC concentrations.

8.4.2 Mechanism

For plasma and polystyrene suspensions in Figure 8.5 the front continues to propagate until the centre is reached. This is followed by the complete drying of the whole droplet. Before this occurs, there is a significant amount of fluid in the outer region. For blood, this front slows down and effectively stops after a short time. Cracks are observed in the outer region in the early stages of drying [10], which implies that significant drying has occurred there, before the compaction front reaches the centre.

The motion of the front and the amount of fluid present in the different regions is relevant because it indicates the internal flow that is occurring. In simple colloidal systems such as polystyrene suspensions, evaporation in the outer region causes the fluid to recede into the close-packed particle network. The resulting interface deformation around immobilised particles in the network causes a negative capillary pressure, which produces an outward flow in the inner region [29]. Outflow transports particles to the front which are not able to penetrate, causing the further progression of the front and the typical ring profiles observed in drying droplets. The outflow from the inner region balances evaporation until the maximum capillary pressure of the packed particle

system is reached [19]. When this occurs, the outflow from the inner region decreases, causing the slowdown of front progression. The decrease in outflow causes evaporation to become dominant in the outer region, drying the remaining fluid. The constant progression of the compaction front and the sudden drying after the front reached the centre in polystyrene and plasma tests imply that the outer region remains saturated with fluid and an outflow continues until the very late stages. For blood, the severe slow down in front progression and cracking in the outer region imply that the outer region dries very early and there is very little outflow after this point.

This difference in drying dynamics in blood droplets causes the observed shift in profile behaviour. After drying in the outer region, further evaporation in the later stages cause the height to decrease in the inner region. This causes the shape of the interface to invert and form the concave shape seen in dried morphologies. As the inner region is drying uniformly, the local concentration is similar, producing the observed instantaneous gelation once the critical volume fraction is reached.

This a very different process of ring formation from that observed in simple colloid systems, which explains the contrary relationship with initial concentration. This mechanism also explains the abrupt change in both cracking patterns and height profile seen between the inner and outer regions. The outer corona region has regularly spaced radial cracks [5], typical of horizontal drying fronts [19]. The cracks in the inner region are more irregular, leading to a similar pattern observed from the simultaneous vertical evaporation [30]. These two regions were also observed by profilometry. The higher concentration suspensions in Figures 8.2, 8.4 and 8.3 show a discontinuity at the point where the front halted and a higher roughness in the central region. Although two regions can be identified in the image of plasma cracks in Figure 8.1d, the timing of their formation presented in Figure 8.5c identifies a different mechanism to blood as the central random cracks propagate outwards, after the solid front reaches the centre of the drop.

8.4.3 Cause of Front Slow Down

The slowing down and halting of the compaction front in drying blood droplets has a large effect on drying dynamics and final appearance. However, due to the complexity of blood, this could occur for several reasons. As red blood cells are highly deformable and biconcave in shape, they will pack very efficiently, causing the packing fraction in the consolidated region to be much higher than systems of hard spherical

particles. This causes two primary differences when compared to simple particles; First, the increased resistance to solvent flow caused by decreased interparticle space would hinder outward flow and decrease the rate of accumulation at the front. Second, the increased packing efficiency means that more bulk flow is required to produce the same volume of consolidated cells. This effect would also slow progression of the front, especially if the dehydration of the cells in this region decreases their average size, further increasing their packing efficiency. The halting of the front could also be influenced by a layer of gelled proteins at the air interface. Proteins will be preferentially transported to the droplet's edge, therefore disturbing the formation of interparticle menisci.

An alternative hypothesis leading to the slowing of the front is a gelation process occurring in the fluid region. This could occur well before a change is observable visually and would create a viscous, poroelastic matrix in the central region that would resist flow into the consolidated region. This is unlikely as the fluid region is seen to retain fluid-like properties until the very late stages of drying. This was demonstrated by the unaltered evaporation occurring in the fluid region [10] and the observation that red cells readily flow into paper strips dipped into the central region after the front has halted.

8.4.4 Effect of Surface Wettability (Contact Angle)

The effect of a significant difference in wettablilty (contact angle) on the dried deposits of blood drops was studied by Sobac et al. [10]. Droplets forming with a contact angles of 92 degrees with a surface produced a very different dried profile from those with a contact angle of 15. For the high contact angle cases, the process is dominated by skin formation followed by buckling, in a similar process to that observed in suspensions with low diffusivity [31]. For this study, the profiles were compared between smaller variations in contact angle (Table 8.1). The minimal variation between varying contact angles is contrary to experiments with polystyrene suspensions presented in Chapter 9. This further identifies the different drying mechanism of RBC suspensions.

It is not clear what mechanism leads to the central deposit observed for low contact angle droplets in Figure 8.6. However, central deposits are observed in other colloidal droplet systems and correlated with Marrangoni flows caused by temperature gradients over the drop's surface [32]. The central deposit is reproducibly observable by eye, indicating potential for such transitions to be utilised in the development of low-cost blood diagnostics. Here, the critical contact angle under which a central deposit is observed,

can indicate the volume fraction of red cells in a sample.

8.5 Conclusion

In this chapter, the dried profile of a series of RBC suspensions on smooth treated glass slides were measured and their relationship with initial cell concentration, protein content and contact angle is investigated. The drying dynamics are compared with simple latex colloidal suspensions. The primary difference between drying dynamics in droplets of RBC and that of simple colloidal suspensions is the halting of the compaction front. This occurs in RBC suspensions shortly after drying has initiated. The possible causes include increased friction due to better packing efficiency and disturbance of the interparticle menisci at the air interface. The hypothesis of gelation in the central region is rejected with wicking experiments. However, further experimental and theoretical analysis is required to elucidate this mechanism. The halting of the front in RBC suspensions causes a different mechanism of ring formation based on the drying and inversion of the fluid region after this point. This is very different to the typical ring formation mechanism in simpler suspensions where the compaction front continues until the centre of the droplet is reached. Altering the contact angle formed by a droplet with the surface (wettability) had negligible effects on the dried profile, except for RBC-PBS suspensions at low initial concentration and contact angle, where a central platform was observed. These observations highlight a series of processes occurring in drying droplets of RBC suspensions and directions for further study.

8.6 References

[1] O. Peschel, S. N. Kunz, M. A. Rothschild, and E. Mützel. Blood stain pattern analysis. *Forensic Science, Medicine, and Pathology*, 7(3):257–270, 2011.

[2] Tatyana V. Kulyabina, Roman A. Drajevsky, Vyacheslav I. Kochubey, and Dmitry A. Zimnyakov. Coherent optical analysis of crystal- like patterns induced by human blood plasma desiccation. *Saratov Fall Meeting 2000: Coherent Optics of Ordered and Random Media*, 4242:282–285, 2001.

[3] Ruoyang Chen, Liyuan Zhang, Duyang Zang, and Wei Shen. Blood drop patterns: Formation and applications. *Advances in colloid and interface science*, 231:1–14, 2016.

[4] E. Rapis. A change in the physical state of a nonequilibrium blood plasma protein film in patients with carcinoma. *Technical Physics*, 47(4):510–512, 2002.

[5] D. Brutin, B. Sobac, B. Loquet, and J. Sampol. Pattern formation in drying drops of blood. *Journal of Fluid Mechanics*, 667:85–95, 2011.

[6] Leila Bahmani, Mahdi Neysari, and Maniya Maleki. The study of drying and pattern formation of whole human blood drops and the effect of thalassaemia and neonatal jaundice on the patterns. *Colloids and Surfaces A: Physicochemical and Engineering Aspects*, 513:66–75, 2017.

[7] Tatiana A. Yakhno, Vladimir G. Yakhno, Anatoly G. Sanin, Olga A. Sanina, Artem S. Pelyushenko, Natalia A. Egorova, Igor G. Terentiev, Svetlana V. Smetanina, Olga V. Korochkina, and Elena V. Yashukova. The informative-capacity phenomenon of drying drops. *IEEE Engineering in Medicine and Biology Magazine*, 24(2):96–104, 2005.

[8] W. Bou Zeid and D. Brutin. Influence of relative humidity on spreading, pattern formation and adhesion of a drying drop of whole blood. *Colloids and Surfaces A: Physicochemical and Engineering Aspects*, 430:1–7, 2013.

[9] Viral H. Chhasatia, Abhijit S. Joshi, and Ying Sun. Effect of relative humidity on contact angle and particle deposition morphology of an evaporating colloidal drop. *Applied Physics Letters*, 97:231909, 2010.

[10] B. Sobac and D. Brutin. Desiccation of a sessile drop of blood: Cracks, folds formation and delamination. *Colloids and Surfaces A: Physicochemical and Engineering Aspects*, 448(1):34–44, 2014.

[11] Alexander F Routh. Drying of thin colloidal films. *Reports on Progress in Physics*, 76(4):46603, 2013.

[12] C. Allain and L. Limat. Regular patterns of cracks formed by directional drying of a collodial suspension. *Physical Review Letters*, 74(15):2981–2984, 1995.

[13] Wai Peng Lee and Alexander F Routh. Why Do Drying Films Crack. *Langmuir*, 20(23):9885–9888, 2004.

[14] Ludovic Pauchard, Bérengère Abou, and Ken Sekimoto. Influence of mechanical properties of nanoparticles on macrocrack formation. *Langmuir*, 25(12):6672–6677, 2009.

[15] F. Giorgiutti-Dauphiné and L. Pauchard. Drying drops: Drying drops containing solutes: From hydrodynamical to mechanical instabilities. *European Physical Journal E*, 41(3):1–5, 2018.

[16] Mahesh S. Tirumkudulu and William B. Russel. Cracking in drying latex films. *Langmuir*, 21(11):4938–4948, 2005.

[17] Michael J Hertaeg, Rico F Tabor, and Gil Garnier. Effect of protein adsorption on the radial wicking of blood droplets in paper. *Journal of Colloid And Interface Science*, 528:116–123, 2018.

[18] Adam D Eales, Alexander F Routh, Nick Dartnell, and Simon Goddard. Evaporation of pinned droplets containing polymer – an examination of the important groups controlling final shape. *AIChE Journal*, 61(5):1759–1767, 2015.

[19] Lucas Goehring, William J. Clegg, and Alexander F. Routh. Solidification and ordering during directional drying of a colloidal dispersion. *Langmuir*, 26(12):9269–9275, 2010.

[20] L. Pauchard, F. Parisse, and C. Allain. Influence of salt content on crack patterns formed through colloidal suspension desiccation. *Physical Review E - Statistical Physics, Plasmas, Fluids, and Related Interdisciplinary Topics*, 59(3):3737–3740, 1999.

[21] T. A. Yakhno, V. G. Yakhno, A. G. Sanin, O. A. Sanina, and A. S. Pelyushenko. Protein and salt: Spatiotemporal dynamics of events in a drying drop. *Technical Physics*, 49(8):1055–1063, 2004.

[22] Guofang Chen and Gideon J. Mohamed. Complex protein patterns formation via salt-induced self-assembly and droplet evaporation. *European Physical Journal E*, 33(1):19–26, 2010.

[23] T. A. Yakhno, V. V. Kazakov, O. A. Sanina, A. G. Sanin, and V. G. Yakhno. Drops of biological fluids drying on a hard substrate: Variation of the morphology, weight, temperature, and mechanical properties. *Technical Physics*, 55(7):929–935, 2010.

[24] M. E. Buzoverya, Yu P. Shcherbak, and I. V. Shishpor. Experimental investigation of the serum albumin fascia microstructure. *Technical Physics*, 57(9):1270–1276, 2012.

[25] Tatiana Yakhno. Salt-induced protein phase transitions in drying drops. *Journal of Colloid and Interface Science*, 318(2):225–230, 2008.

[26] Tak Sing Wong, Ting Hsuan Chen, Xiaoying Shen, and Chih Ming Ho. Nanochromatography driven by the coffee ring effect. *Analytical Chemistry*, 83(6):1871–1873, 2011.

[27] J Farrant and A Woolgar. Cryoprotective additives and hypertonic hemolysis. *Cryobiology*, 7(1):56–60, 1970.

[28] J Farrant and A Woolgar. Human red cells under hypertonic conditions; A model system for investigating freezing damage: 1. Sodium chloride. *Cryobiology*, 9:9–15, 1972.

[29] Ruoyang Chen, Liyuan Zhang, Duyang Zang, and Wei Shen. Wetting and Drying of Colloidal Droplets: Physics and Pattern Formation. *Advances in Colloid Science*, pages 3–25, 2016.

[30] Ram Weinberger. Initiation and growth of cracks during desiccation of stratified muddy sediments. *Journal of Structural Geology*, 21(4):379–386, 1999.

[31] Ludovic Pauchard and Catherine Allain. Mechanical instability induced by complex liquid desiccation. *Comptes Rendus Physique*, 4(2):231–239, 2003.

[32] Hua Hu and Ronald G Larson. Marangoni effect reverses coffee-ring depositions. *The Journal of Physical Chemistry B*, 110(14):7090–7094, 2006.

Chapter 9

Predictive Modelling of Coffee Rings

Preface

Pattern formation in drying droplets of blood and biological fluids have been shown to be indicative of several medical conditions. Due to this, there is increasing interest in the fundamental process of drying sessile droplets to assist the design of low-cost diagnostic techniques. Previous research has focused on characterising the presence of absence of characteristics and determining a relationship with a series of specific medical conditions. This has led to binary diagnostic processes, where the result is simplified to either a positive or negative. However, many conditions require the quantification of a parameter. This necessitates a more robust technique than the simple identification of parameters under standard conditions. Here, the fundamental mechanism for one such test is presented. In Chapter 8, the contact angle and initial volume fraction were found to affect the dried profiles of blood droplets significantly. In some cases, producing extremely different morphologies that are easily observable by eye. Therefore, noting the contact angle over/under which certain features are present, can be indicative of the initial volume fraction of cells in the blood sample. This would represent an very fast and cheap method for diagnosing conditions such as anaemia as all that is required is several standard surfaces and a drop of the patient's blood.

A similar process is observed with simple particle suspensions, where the critical contact angle over which a ring deposit is formed is determined by the initial volume fraction of the suspension. However, the underlying mechanism behind this process is poorly understood. Before the effect of contact angle on blood deposits can be understood, the mechanism in simplified systems must be elucidated. This chapter outlines the development of a numerical model predicting the onset of ring deposits at different

contact angles and initial solid volume fractions. These predictions are compared with experimental results using polystyrene particles similar in size to red blood cells. This chapter was submitted to Physical Review Letters and is at the review stage.

Predicting coffee ring formation upon drying in droplets of particle suspensions

Michael J. Hertaeg, Rico F. Tabor, Alex F. Routh, Gil Garnier

Submitted: Physcial Review Letters

Abstract

Pattern formation is a common occurrence in drying colloidal systems. The most common in droplets, is a ring distribution where the constituents have relocated to the edge, which is referred to as a coffee ring. This deposit is unfavorable in many manufacturing processes and is of fundamental interest. In this study we present a model capable of predicting when a coffee ring will be observed in hard spherical particle systems. This is found to be predicated upon the initial concentration and contact angle of the droplet. Results are in agreement with experiments using latex suspensions.

9.1 Main

Pattern formation from evaporating droplets has captivated physicists and the wider community for many years [1]. These patterns are caused by evaporation induced flows that lead to the redistribution of constituents. This often results in rings of deposited solid, referred to as coffee rings, although several other patterns are possible depending on conditions [2, 3]. Deposits left by dried droplets are critical for many industrial applications, including functional printing, coatings, biodiagnostics and surface treatments. In most of these, coffee ring-like deposits are considered defects as a uniform deposition is desirable [4]. Due to this, previous research has primarily focused on strategies for mitigating coffee rings [5, 6] and a dependence on initial volume fraction and Capillary number has been identified numerically [7]. Here, we investigate and model the effect of contact angle on the formation of ring patterns (Figure 9.1).

When a droplet is placed on a surface, it quickly reaches an apparent equilibrium

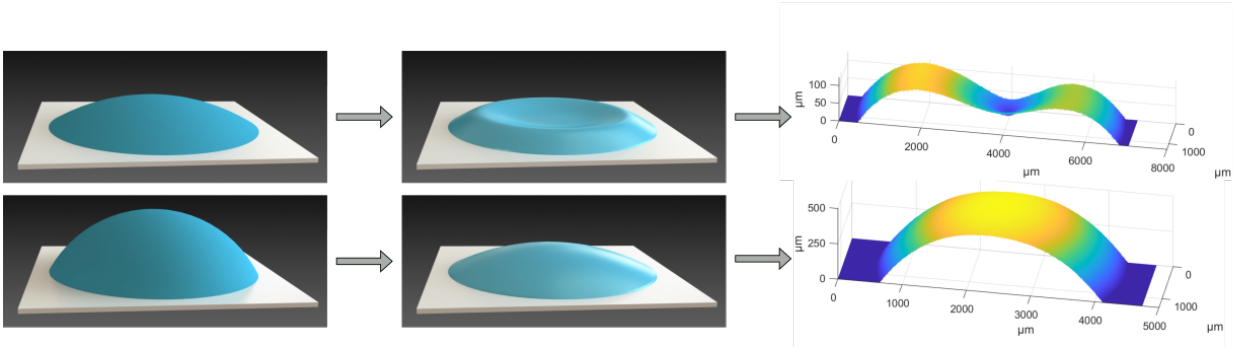

Figure 9.1: For a specified initial volume fraction, there is a critical contact angle above which a coffee ring does not form. Last set of images are optical profilometry scans of dried 6 µL droplets of 45 vol% polystyrene bead suspensions. Upper profile was dried on a glass surface with a contact angle of 10°, the lower 46°.

position that can, for small droplets, be defined solely by contact angle and radius [8]. After initial wetting to the equilibrium angle, evaporation driven effects dominate. These phenomena occur over a much longer time scale than wetting and are usually considered sequential events. The rate of evaporation and the variation of mass flux on the drop's surface is dependent on many factors including the vapor pressure of the fluid, the geometry of the droplet's surface as well as the velocity and partial pressure of the surrounding atmosphere [9, 10]. In stagnant unsaturated air, evaporation is a diffusion limited process, which can be shown to produce edge enhanced evaporation in droplets. This is because of the reduced chance of a molecule re-colliding with the liquid surface at the edge. When convection in the surrounding atmosphere is present, evaporation is instead limited by the mass transfer from the drop surface, which leads to a uniform evaporation flux. Although slight differences are produced in flow fields between edge enhanced and uniform evaporation, there is little difference in the final appearance of ring deposits. This has been demonstrated experimentally [11] and numerically [12].

Regardless of the evaporation profile, the volume of the droplet decreases during evaporation. It is common for colloid droplets to pin and therefore drying proceeds with a constant contact line and a varying contact angle. A pinned contact line is often regarded as essential for ring deposits for two reasons. First, as surface tension maintains a spherical cap, an outward flow arises to compensate for evaporation occurring near the droplet's edge [1]. Second, particle concentration in thin films increases faster when compared to thicker ones, meaning that the concentration rises faster at the droplet edge. Due to this, a close packed region quickly forms near the edge. This region is

defined as where the local concentration has risen to the critical value for liquid-solid transition in the suspension [9]. The volume fraction increases very sharply at the beginning of this region, leading to clearly delineated close packed (consolidated) and liquid regions. Although rigid, there is still evaporation in the consolidated region. This evaporation is continuous as menisci form between particles at the air interface, producing sufficient suction to draw fluid through the inter particle space in the consolidated region. Some authors have used scaling factors to represent a decrease in evaporation in the consolidated region [7] due to the high concentration of particles. However, a simple scaling analysis (supplementary section) shows that until the very late stage of drying, the maximum capillary pressure produced by menisci between particles at the air interface is orders of magnitude stronger than the viscous stress produced from the slow flow through the short consolidated region. This implies that the film-air interface remains wet and the evaporative flux is very similar to that in the liquid region. As only solvent can fit in the inter-particle space, evaporation induced flow leads to an accumulation of particles at the consolidation front causing this solid region to grow inwards. This continues until there is no fluid region left. The final shape of the dried drop is determined by a balance between the effects of surface tension and evaporative flux into the consolidated region.

Initially, the drop is modelled as an axisymmetric spherical cap defined by a quadratic profile. There is a small consolidated region at the very edge of the drop and a large fluid region in the center. The consolidated region is considered to be rigid and in the fluid region, lubrication theory is used to derive an expression for the height profile as a function of time and radius (equation 9.9). The position of the front is calculated explicitly at each time step.

Equation 9.9 is solved implicitly with a custom finite volume solver on a one-dimensional, axisymmetric domain using a uniform mesh, Newton's linearization method and Matlab's inbuilt direct linear solver. Four boundary conditions are required; symmetry and no flux are used at the center and a height and flux are calculated explicitly for the boundary at the consolidated front. The height is found from the height of the consolidated region at this point and the flux is calculated from the amount of evaporation occurring in the consolidated region. The non-dimensional equation 9.9 is derived in a similar way as several previous works [7, 12, 13]. However here, a different scaling is used so contact angle can be conveniently incorporated as a parameter:The derivation for this equation is given in the supplementary section. The key assumptions of this

equation are a constant evaporation rate, viscosity and surface tension.

$$1 + \frac{\partial h}{\partial t} + \frac{H^4\gamma}{3\mu\dot{E}R^4}\frac{1}{r}\frac{\partial}{\partial r}\left[h^3 r\frac{\partial}{\partial r}\left(\frac{1}{r}\frac{\partial}{\partial r}\left(r\frac{\partial h}{\partial r}\right)\right)\right] = 0 \tag{9.1}$$

Where h is the height of the droplet, r is the radial direction, H is the maximum initial height of the droplet, γ is surface tension, μ is viscosity, $\dot{E}$ is the evaporation rate and R is an arbitrary length scale defined by setting the value of the non-dimensional term in equation 9.9 ($\frac{H^4\gamma}{3\mu\dot{E}R^4}$) equal to unity. Setting the length R in this manner allows the maximum droplet radius to be used as an input parameter without varying the governing equation. With droplet height scaled by initial height (H) and an initial spherical cap geometry, this maximum radius is all that is required to define the system geometry, and therefore, contact angle. This is also independent of droplet volume. Each calculation can be completed at specified values of non-dimensionalized droplet radius (R_{max}) which can be related to the contact angle by $R_{max} = [\frac{1}{sin\theta} - \frac{1}{tan\theta}]^{-1}[\frac{\gamma}{3\mu\dot{E}}]^{-\frac{1}{4}}$. The derivation is provided in supplementary section. The new implementation and scaling introduced here to elucidate the dimensionless number R_{max}, provides the means to quantify the transition between viscosity and surface tension dominated behavior in drying systems. Where a high value corresponds to the dominance of viscosity and vice versa for surface tension.

To obtain an expression for solute concentration previous models [7, 12] have assumed infinite vertical diffusion and zero horizontal diffusion due to the varying length scales $H << R$. This gives the volume fraction (ϕ) as a function of radius and time (equation 9.2).

$$\frac{\partial\phi}{\partial t} = -\tilde{V_r}\left[\frac{\partial\phi}{\partial r} + \frac{\phi}{h}\frac{\partial h}{\partial r} + \frac{\phi}{r}\right] - \phi\frac{\partial\tilde{V_r}}{\partial r} - \frac{\phi}{h}\frac{\partial h}{\partial t} \tag{9.2}$$

Where $\tilde{V_r}$ is the dimensionless vertically averaged radial velocity given by: $\tilde{V_r} = h^2\left[\frac{\partial}{\partial r}\left(\frac{1}{r}\frac{\partial}{\partial r}(r\frac{\partial h}{\partial r})\right)\right]$ Solutions to equations 9.9 and 9.2 give a flat profile for volume fraction with a steep increase at the front position. This is because $\frac{\partial\phi}{\partial t}$ becomes large with increasing $\tilde{V_r}$ and diverges at small heights. At the consolidated front, $\tilde{V_r}$ is at a maximum and height a minimum. At the beginning of drying, the height at the front is very low which leads to a large spike in volume fraction near the consolidated front; however, for all other positions the volume fraction is spatially uniform. Due to this, and for simplicity, we assume a uniform concentration in the fluid region. To include the effects of evaporation, a new value for volume fraction is calculated explicitly at each time step with a simple mass balance using the total evaporation rate, volume,

concentration of the fluid region and the flow into the consolidated region.

Only the solvent can penetrate into the consolidated region and evaporate. Therefore, although the solute flux at the consolidated front is determined by evaporation in the consolidated region, the corresponding bulk velocity will be greater due to the presence of particles. This increase is dependent on the concentration in the fluid region which, in turn, determines how fast the consolidated region grows. Evaporation in the consolidated region produces flow of solvent in the fluid region; this flow transports particles towards the consolidated front where they are deposited. From this, the bulk fluid vertically averaged velocity ($\tilde{V_r}$) at the front and the front velocity can be calculated by solving a mass balance of solute and particles explicitly at each time step. $\tilde{V_r}$ is used as the boundary condition in the fluid equation for that time step and is used to calculate the new front position.

The key outcome of this simulation is determining how the relative strength of surface tension compared to viscosity affects ring pattern formation. In a physical droplet system, the relative strength of these factors is controlled by the contact angle as this determines the film thickness. As a thin film has a greater viscous resistance to flow, a low contact angle results in a large contribution of viscous effects. A high evaporation rate also contributes to a large viscous resistance. In simulations, time is scaled by the evaporation time, meaning that this effect is indistinguishable from viscosity. Due to the choice of scaling constants, R_{max} represents the combined effect of all the parameters relevant to the balance of the relative dominance of surface tension and viscosity. The calculation of contact angle from R_{max} used in the analysis of results is achieved using the parameter values of water at the experimental conditions of 23°C and 50% relative humidity. Surface tension and viscosity of water are taken from literature to be 72.3 mN/m [14] and 0.9 mPa·s [15]. The evaporation rate was measured by monitoring the weight change as a function of time from a 3 cm diameter petri dish filled with water at experimental conditions. The calculated value normalised by surface area was 0.4 cm/day. Although assuming the surface tension, viscosity and evaporation of water and no variation in these properties between different polystyrene concentrations introduces some errors, the fourth power of R and H in equation 9.9 and equivalently, the fourth root in the expression for R_{max} renders this error small. The additional parameters that must be included are, initial volume fraction and gelation point ϕ_{max}. Gelation point is set at 0.64 for simulations presented here to correspond with the random close packing of spherical particles.

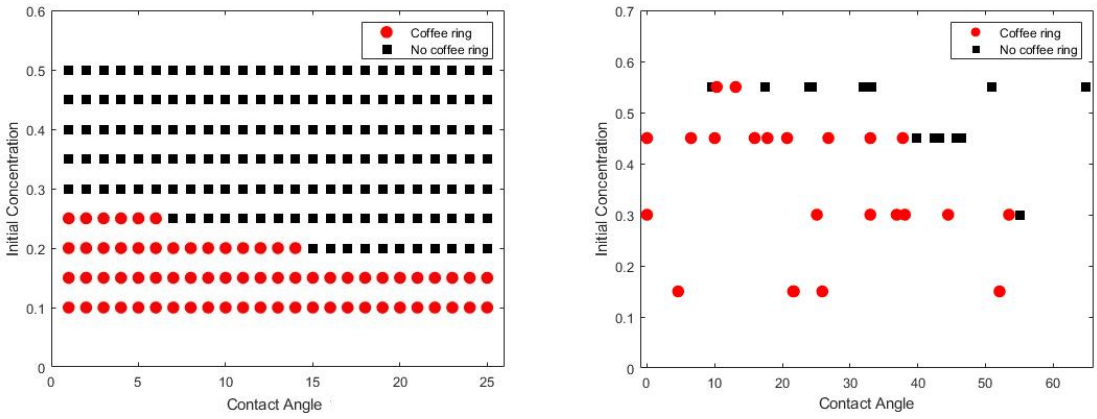

(a) (b)

Figure 9.2: Master curves predicting the formation of coffee rings as a function of initial suspension concentration and contact angle from: (a) simulation and (b) experimental results for 6 µL droplets of polystyrene bead suspension. The onset of coffee ring formation at a unique contact angle is shown for each initial volume fraction.

Results from the simulation can be used to determine a unique critical volume fraction below which ring deposits are formed for all values of contact angle. Figure 9.2 provides simulation and experimental results gathered with a suspension of 6-8 µm polystyrene beads. The presence of a positive curvature in the final height profile was used to identify a coffee ring shape and therefore provide a binary condition with which to compare experimental and simulation results. Here we show that the presence or absence of a coffee ring, can be solely predicted by the initial volume fraction of particles in a suspension and the contact angle formed by the suspension on the surface of interest. Figure 9.2 shows the broad agreement of our model with experimental results. The main finding is that there is a unique threshold volume fraction at each contact angle below which a coffee ring is observed. This value is high for low contact angles and vice versa. The position of this transition is not exactly replicated by the experimental results. However, this is likely due to ignoring particle specific properties such as surface activity that have been shown to influence patterns [6, 16].

Results from this simulation of the final height profile for a range of values of initial volume fraction and R_{max} are displayed in Figure 9.3. There is an oscillation present at low initial volume fractions and high values for R_{max}, as seen in Figure 9.3a. The results do not significantly change when the mesh and numerical scheme is altered, indicating the oscillation is caused by a physical mechanism that is damped out in most systems. The high values of R_{max} required to produce these oscillations correlate to systems with

either low contact angles ($\theta < 2$) or extremely low values of the dimensionless number $\frac{\gamma}{3\mu\dot{E}}$. Both of these conditions relate to viscosity driven phenomenon. Whilst it would be of interest to reproduce these oscillations experimentally, the conditions required are very difficult to achieve because circular droplets with very low contact angles are difficult to obtain reproducibly. The high values of R_{max} could also be replicated by using a fluid of low surface tension, high evaporation rate and high viscosity. However, we have not been able to find such a system.

Figure 9.3 shows a central minimum occurring in the film profile for all numerical cases. However, some experimental results display a more uniform deposition (Figure 9.1). As the drying front approaches the center of the droplet the flux from the fluid region is so large that the central dimple is formed. Such structures are regularly seen experimentally [17, 18], but the constant viscosity assumption accentuates the central minimum. Therefore, the morphology of this central region does not affect the occurrence or absence of a coffee ring. The 3D revolution of a simulated dried height profile is compared to that of a polystyrene bead solution in Figure 9.3.

The effect of viscosity can be included using the Krieger-Dougherty relation [19] as previously achieved in other drying studies [20]. However, viscosity changes during drying do not have a significant effect in pattern and coffee ring formation. The parameterization of viscosity was not included in our model as the purpose is to identify the underlying mechanism that spans all drying colloid systems. Although a shift in viscosity will alter the exact conditions where a coffee ring occurs, the general trends in behavior are more easily observed with as simple model as possible.

We assume Newtonian fluid behavior in the liquid region and mechanical rigidity in the consolidated region. There is a small transition region between the two where neither assumption is valid; however, as volume fraction increases very sharply at the consolidated front, this region remains small. The region only becomes large and the effect of particle interaction significant in the later stages of drying when the concentration in the fluid region is close to the gelation point. This process causes significant resistance to solvent flow in the later stages of drying which is not captured by our simulations. The relationship between concentration, flux into the consolidated region and front velocity is complex and has only received brief attention from previous researchers [21]. Further work is clearly needed to identify the relationship. However, physically reasonable final height profiles were found by including a scaling factor in the expressions for evaporation from the consolidated region. The value of the scaling

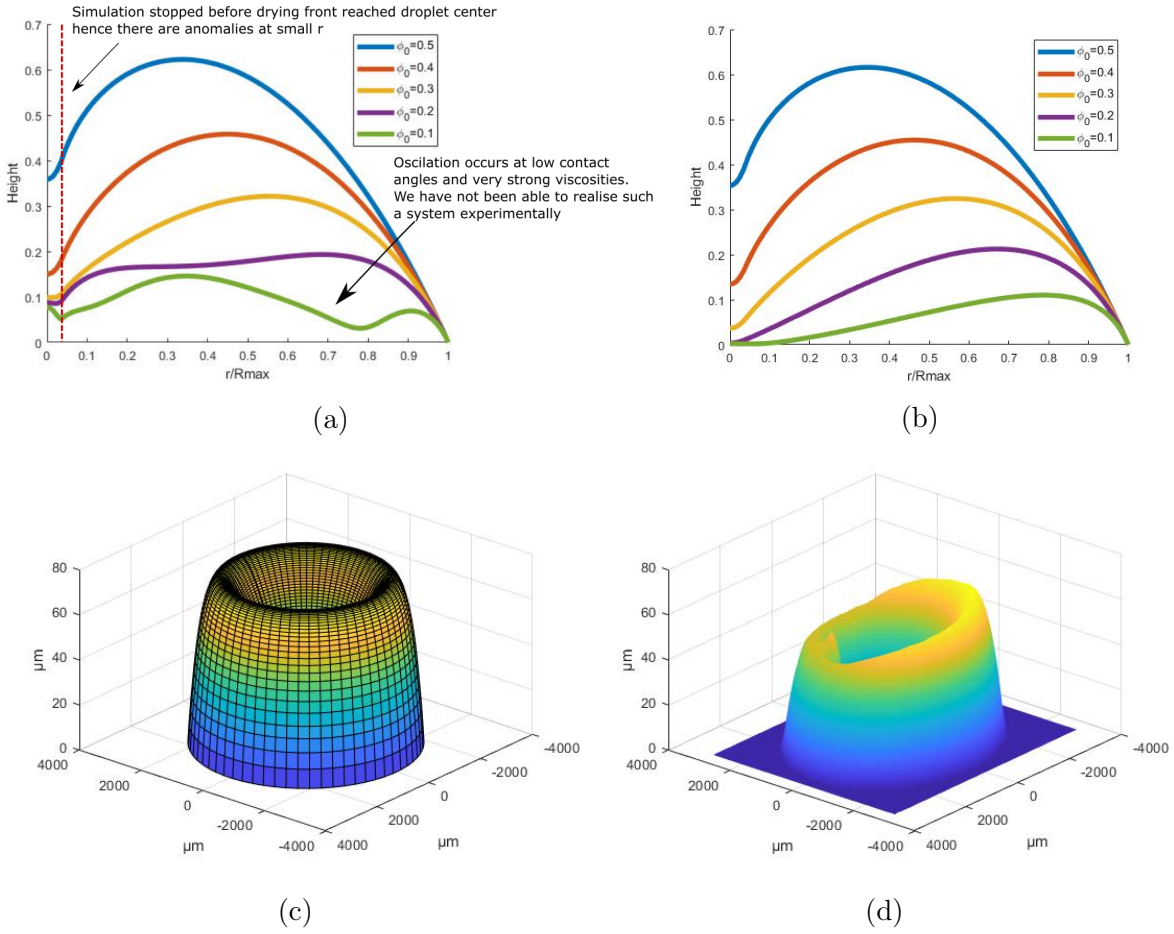

Figure 9.3: Dried height profiles at different contact angles and initial volume fractions. a) $R_{max} = 0.745$, $\theta = 1.0°$, b) $R_{max} = 0.029$, $\theta = 25.0°$. c) Revolved results for a simulated drop ($\phi_0 = 0.15$, $R_{max} = 0.042$, $\theta = 17.8°$): d) Profilometry results from for a solution of polystyrene beads ($\phi_0 = 0.15$, $\theta = 17.8°$).

factor was determined by a simple power law relationship with the bulk concentration, causing flow into the consolidated region to approach zero as the bulk concentration increases. This scaling factor was not included in the results as it is heavily dependent on particle properties and occludes the main purpose of this study. However, the analysis identifies this scaling factor as an important parameter to investigate before the behavior in the center of the drop can be realistically captured by simulations.

Figure 9.2 was produced by determining a criterion for a coffee ring which was defined as whether a positive curvature was present. This was implemented for simulation results by calculating the second derivative at all points with a radius greater than $0.05 \cdot R_{max}$, so as to ignore the effect of the small central discontinuity caused by stopping the simulation before the size of the fluid region reaches zero (Figure 9.3a). If the second derivative at any point is positive, the profile is identified as a coffee ring; if not, there is no coffee ring. The criteria to distinguish a coffee ring in experiments was whether or not there was a positive curvature anywhere on the surface of the deposit. Experiments using polystyrene latex particles near the transition values of initial volume fraction and contact angle showed a positive curvature only at very small values of r. In simulations, small values of r are hidden due to the overestimation of flux at late stages. This therefore prevents a coffee ring from being observable until a positive curvature was present outside the influence of the central minimum. This causes the threshold volume fraction values to be lower than seen in experiments.

In this study we numerically investigate a cause of ring-like patterns and its dependence on contact angle in drying droplets of colloidal suspensions. We identify the contact angle formed by the suspension on the surface and its solids content as the two governing variables. We show that for each contact angle, there is a critical initial colloid volume fraction over which no ring-like pattern will be formed. This is due to contact angle affecting the relative dominance of viscous effects over surface tension. We calculated from first principles a master-curve predicting coffee ring formation from contact angle that we corroborate experimentally for simple particles.

9.2 Methods

Drying experiments were achieved by placing a 6 µL droplet of solution onto the substrate with an Eppendorf pipette. The droplet was left to dry in a humidity and temperature controlled room held at 23°C and 50% relative humidity. Care was taken

to undertake experiments in still air however slight directionality was seen in many tests due to a sensitivity to air circulation currents. Droplets were dried on plain microscope slides and the contact angle was controlled by changing the brand of glass slide and varying levels of plasma cleaning. The two brands used were Sail and Westlab, of which Sail generally had a higher contact angle. Levels of cleaning were achieved by first using a PDC-002-HP Harrik Plasma plasma cleaner for 30 seconds on medium setting and then leaving slides in a covered container at lab conditions for between 0-24 hours. This process was not easily predictable and therefore each tested droplet was measured with a DataPhysics OCA35 contact angle instrument. Measurements were taken using an Olympus LEXT OLS5000 laser confocal microscope. 6-8 µm nominal diameter polystyrene beads were purchased from PROSCITECH and were concentrated by centrifuging at 2500 rcf for 3.5 minutes and removing supernatant. Deuterium oxide (D_20) from Sigma-Aldrich was combined with solutions to density match the particles and the fluid. This was performed by incrementally increasing the concentration of D_20 until no sedimentation was observed after centrifuging at 2500 rcf for 2 minutes. The critical solution concentration was approximately 50% water and 50% D_20. This value varied slightly between tests due to hydrogenated water uptake in D_20.

Acknowledgments

This work was funded by the Australian Research Council ARC LP160100544 with Haemokinesis and an Australian Government Research Training Program (RTP) Scholarship. Thanks to Clare Rees-Zimmerman for preliminary work. This work was supported in part by the Monash eResearch Center and eSolutions-Research Support Services for the use of the MonARCH HPC Cluster.

9.3 References

[1] Robert D Deegan, Olgica Bakajin, Todd F Dupont, Greb Huber, Sidney R Nagel, and Thomas A Witten. Capillary flow as the cause of ring stains from dried liquid drops. *Nature*, 389(6653):827–829, 1997.

[2] Kuniaki Anachi, Eiki and Dimitrov, Antony S and Nagayama. Stripe Patterns Formed on a Glass Surface during Droplet Evaporation. *Langmuir*, 11(4):1057–1060, 1995.

[3] Hua Hu and Ronald G Larson. Marangoni effect reverses coffee-ring depositions. *The Journal of Physical Chemistry B*, 110(14):7090–7094, 2006.

[4] Dileep Mampallil and Huseyin Burak Eral. A review on suppression and utilization of the coffee-ring effect. *Advances in Colloid and Interface Science*, 252:38–54, 2018.

[5] Adam D Eales and Alexander F Routh. Elimination of coffee-ring formation by humidity cycling: a numerical study. *Langmuir*, 32(2):505–511, 2016.

[6] Peter J Yunker, Tim Still, Matthew A Lohr, and A G Yodh. Suppression of the coffee-ring effect by shape-dependent capillary interactions. *Nature*, 476(7360):308–311, 2011.

[7] Adam D Eales, Alexander F Routh, Nick Dartnell, and Simon Goddard. Evaporation of pinned droplets containing polymer – an examination of the important groups controlling final shape. *AIChE Journal*, 61(5):1759–1767, 2015.

[8] Daniel Bonn, Jens Eggers, Joseph Indekeu, Jacques Meunier, and Etienne Rolley. Wetting and spreading. *Reviews of modern physics*, 81(2):739, 2009.

[9] Alexander F Routh. Drying of thin colloidal films. *Reports on Progress in Physics*, 76(4):46603, 2013.

[10] Duyang Zang, Sujata Tarafdar, Yuri Yu Tarasevich, Moutushi Dutta Choudhury, and Tapati Dutta. Evaporation of a Droplet: From physics to applications. *Physics Reports*, 804:1–56, 2019.

[11] Robert D. Deegan, Olgica Bakajin, Todd F. Dupont, Greg Huber, Sidney R. Nagel, and Thomas A. Witten. Contact line deposits in an evaporating drop. *Physical Review E*, 62(1):756, 2000.

[12] Benjamin J. Fischer. Particle convection in an evaporating colloidal droplet. *Langmuir*, 18(1):60–67, 2002.

[13] I. V. Vodolazskaya and Yu Yu Tarasevich. The model of drying sessile drop of colloidal solution. *Modern Physics Letters B*, 25(15):1303–1310, 2011.

[14] Gonzalo Vazquez, Estrella Alvarez, and Jose M Navaza. Surface tension of alcohol water+ water from 20 to 50. degree. C. *Journal of chemical and engineering data*, 40(3):611–614, 1995.

[15] Joseph Kestin, Mordechai Sokolov, and William A Wakeham. Viscosity of liquid water in the range -8 C to 150 C. *Journal of Physical and Chemical Reference Data*, 7(3):941–948, 1978.

[16] Rajneesh Bhardwaj, Xiaohua Fang, Ponisseril Somasundaran, and Daniel Attinger. Self-assembly of colloidal particles from evaporating droplets: Role of DLVO interactions and proposition of a phase diagram. *Langmuir*, 26(11):7833–7842, 2010.

[17] L. Pauchard and Y. Couder. Invagination during the collapse of an inhomogeneous spheroidal shell. *Europhysics Letters*, 66(5):667–673, 2004.

[18] Ronald G Larson. Transport and deposition patterns in drying sessile droplets. *AIChE Journal*, 60(5):1538–1571, 2014.

[19] Irvin M. Krieger and Thomas J. Dougherty. A mechanism for non-Newtonian flow in suspensions of rigid spheres. *Transactions of the Society of Rheology*, 3(1):137–152, 1959.

[20] Alexander F. Routh and William B. Russel. Horizontal drying fronts during solvent evaporation from latex films. *AIChE Journal*, 44(9):2088–2098, 1998.

[21] Lucas Goehring, William J. Clegg, and Alexander F. Routh. Solidification and ordering during directional drying of a colloidal dispersion. *Langmuir*, 26(12):9269–9275, 2010.

9.4 Supplementary

Derivation of governing equation

Applying the lubrication approximation to the Navier-Stokes equations in cylindrical polar coordinates and disregarding gravity terms leads to 3 governing equations. Horizontal distances are scaled by the characteristic radius R and vertical distances are scaled by the initial height of the droplet H. Horizontal velocities are scaled by $R\dot{E}/H$ and vertical velocities are scaled by $\dot{E}$. Time is scaled by $H/\dot{E}$, and pressure is scaled by $\mu\dot{E}R^2/H^3$. With these substitutions the governing equations can be represented in dimensionless form

$$0 = \frac{1}{r}\frac{\partial}{\partial r}(ru) + \frac{\partial w}{\partial z} \tag{9.3}$$

$$0 = -\frac{\partial p}{\partial r} + \frac{\partial^2 u}{\partial z^2} \tag{9.4}$$

$$0 = \frac{\partial p}{\partial z}. \tag{9.5}$$

Where u and w are the radial and vertical velocities respectively. At the top surface the pressure can be represented within the lubrication approximation by the dimensionless expression

$$p = -\frac{H^4\gamma}{\mu\dot{E}R^4}\frac{1}{r}\frac{\partial}{\partial r}(r\frac{\partial h}{\partial r}). \tag{9.6}$$

As equation 9.5 demonstrates that pressure does not vary in the z direction, this equation gives the pressure over the whole drop as solely a function of r.

Integrating equation 9.4, imposing zero shear at the free surface and no-slip at the substrate gives an equation for the radial velocity as a function of $\frac{\partial p}{\partial r}$. Differentiating equation 9.6 and then subbing in gives

$$u = \frac{H^4\gamma}{\mu\dot{E}R^4}\left[\frac{\partial}{\partial r}(\frac{1}{r}\frac{\partial}{\partial r}(r\frac{\partial h}{\partial r}))\right](z(h - \frac{1}{2}z)). \tag{9.7}$$

A further mass balance gives the dimensionless height evolution equation

$$\frac{\partial h}{\partial t} = -\frac{1}{r}\frac{\partial}{\partial r}(rh\tilde{V_r}) - 1. \tag{9.8}$$

Integrating equation 9.7 from 0 to h and dividing by h gives the height averaged radial velocity $\tilde{V_r}$. This term is substituted into equation 9.8 to derive the final governing equation

$$1 + \frac{\partial h}{\partial t} + \frac{H^4\gamma}{3\mu\dot{E}R^4}\frac{1}{r}\frac{\partial}{\partial r}\left[h^3 r\frac{\partial}{\partial r}\left(\frac{1}{r}\frac{\partial}{\partial r}\left(r\frac{\partial h}{\partial r}\right)\right)\right] = 0 \tag{9.9}$$

Capillary pressure against viscous losses in the consolidated region

A conservative simplified model of the droplet system is used to show that capillary pressure dominates viscous losses in the consolidated region. This is a worst case scenario where all evaporation is occurring at the droplet's edge and the droplet has a constant height. Using these assumptions, the pressure drop over the consolidated region can be calculated with Darcy's law to be

$$\Delta P = \frac{Q}{2\pi hk} log(\frac{R_2}{R_1}) \tag{9.10}$$

Where R_1 and R_2 are the radial locations of the consolidated front and the edge of the droplet respectively, and Q is calculated from the total evaporation occurring over the consolidated front;

$$Q = E\pi(R_2^2 - R_1^2) \tag{9.11}$$

The permeability (k) can be calculated using the Carmen-Kozeny equation [1];

$$k = \frac{2a^2(1-\phi)^2}{75\mu\phi^2} \tag{9.12}$$

Where a is the radius of the particles. The maximum capillary pressure at the air-liquid interface is given by

$$P_{cap} = \frac{C\gamma}{a} \tag{9.13}$$

Where γ is the surface tension and C is a geometric constant assumed unity in this circumstance. By dividing these two pressures a dimensionless number relating the relative strengths of each effect can be calculated.

$$\frac{\Delta P}{P_{cap}} = \frac{75\dot{E}\mu\phi^2(R_2^2 - R_1^2)}{4C\gamma ha(1-\phi)^2} log(\frac{R_2}{R_1}) \tag{9.14}$$

By inserting known values and conservative estimates; $E = 0.400$ cm/day = 4.62x10^{-8} m/s, $\mu = 9.3$x10^{-4} Pa·s, $\phi = 0.64$, $R_2 = 10$ mm, $R_1 = 1$ mm, $h = 1$ mm, $a = 6$ µm and γ = 72.31 mN/m the value of $\frac{\Delta P}{P_{cap}}$ is found to be 1x10^{-3}. With the conservative estimates used here, this calculation shows capillary pressure will always dominate viscous forces

due to solvent flow in the consolidated region and therefore the air interface in the consolidated region will remain wet during droplet drying.

Derivation for determining R_{max} as a function of contact angle

Assuming spherical cap geometry an expression for maximum height as a function of the droplet radius and contact angle can be found.

$$H = r\left[\frac{1}{sin(\theta)} - \frac{1}{tan(\theta)}\right] \tag{9.15}$$

The non-dimentionalized expression of this equation is,

$$\frac{H}{R} = R_{max}\left[\frac{1}{sin(\theta)} - \frac{1}{tan(\theta)}\right] \tag{9.16}$$

using $\frac{H^4\gamma}{3\mu\dot{E}R^4} = 1$ gives the calculated expression for the dimensionless R_{max} as a function of contact angle.

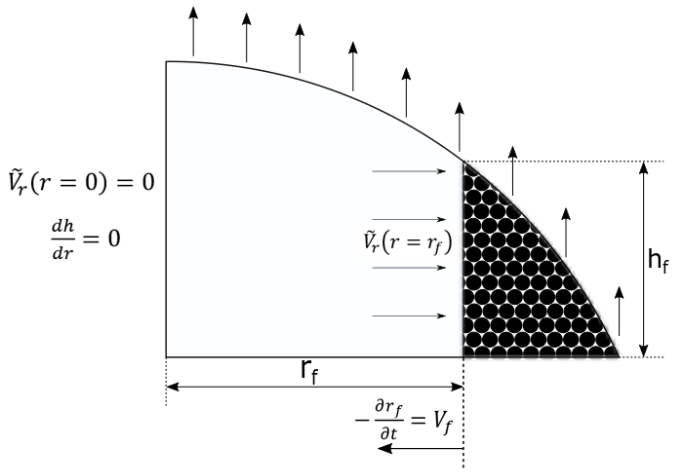

Figure 9.4: Schematic of model showing important variables and boundary conditions.

9.5 References

[1] Alexander F. Routh and William B. Russel. Horizontal drying fronts during solvent evaporation from latex films. *AIChE Journal*, 44(9):2088–2098, 1998.

Chapter 10

Conclusion and Perspective

In this thesis, the fundamental mechanisms leading to interfacial flows in low-cost blood diagnostic are investigated. Two specific systems are studied, radial wicking of droplets in paper and the evaporation induced flows in sessile droplets on impermeable surfaces. Each was quantified by numerical modelling and the dominant effects of biological components identified.

10.1 Radial wicking in paper

A radially wicking droplet of blood combined with antibodies was used to develop a rapid paper-based diagnostic technique. Based on the stain size, less than 10 seconds after deposition, the presence or absence of agglutination can be identified. Full blood typing of a sample can be determined by performing a series of wicking tests using all the antibodies of interest. This technique is the fastest of its kind and can be used to engineer new rapid, scalable diagnostic equipment capable of meeting the demands of modern blood testing facilities. This technique also demonstrated potential in the rapid identification of reverse blood groups and SARS-CoV-2 (COVID-19) antibodies. This methodology was expanded to improve sensitivity for reverse testing by premixing and incubating reactants before deposition. This showed a higher sensitivity with low velocity flows which was contrary to results from forward typing.

The radial wicking of a droplet of biological fluid is analysed systematically (Chapters 5, 6 and 7). The stage transition and the corresponding decrease in stain growth rate that occurs upon droplet absorption is analysed and a numerical model of the process was developed. Modelling shows that Newtonian viscous properties can be assumed. However, protein and other biomolecules adsorbing onto both the solid-liquid

and liquid-vapour interfaces causes an increase in contact angle and severity of contact angle hysteresis, both of which effect wicking behaviour significantly. The presence of hysteresis was identified as the cause of stain growth transition and its increase was the primary difference between the radial wicking behaviour of biological fluids and simple Newtonian fluids. The increase in contact angle and contact angle hysteresis was also identified to cause the significantly smaller final stain sizes observed in biological fluids.

10.2 Drying droplets

Pattern formation in drying blood droplets has been shown to be representative of several important medical conditions. The fundamental mechanisms that determine the final profile are analysed and compared with simple colloid suspensions (Chapter 8). For blood, there is a distinct halting of the drying front that produces different deposits when compared to simple particle suspensions. The cause of the slow down in front progression is a combination of increased viscous resistance due to particle deformation in the outer region and decreased capillary pressure due to meniscus interference from gelled proteins.

The drying of a simple colloid suspension is analysed as a model for blood (Chapter 9). A numerical model based on lubrication theory was developed to predict the relationship between ring formation, initial volume fraction and contact angle. The model probes the relationship between the effects of surface tension and viscosity. This relationship is a primary factor in determining the final dried profile. A dimensionless number is proposed based on this analysis, and the onset of ring profiles in polystyrene particle suspensions are seen to match the trends predicted by modelling.

10.3 Perspective

Current diagnostics incorporating passive interfacial flows are heavily reliant on trial and error for design and optimisation. This is because not enough is known about the fundamental mechanisms and the effect that biological components such as cells and proteins have on the process. Paper-based systems are emerging as promising platforms for the design of diagnostic devices as they are low-cost, light weight and easily produced. Many of these devices utilise droplet deposition to initiate, highlighting the importance of this style of finite reservoir wicking system. Also, this thesis introduces stain size/appearance as an informative property for medical diagnostics. The radial

wicking of a droplet on paper is extensively quantified and analysed. The reproducibility and versatility of this process demonstrate that visual stain-based diagnostic techniques can be used to create diagnostic devices with the sensitivity and accuracy required by the medical industry. Also, the modelling techniques developed allow design to go well beyond trial and error, to a more informed and optimisable approach based on fundamental understanding and computational simulations.

Similarly, the identification of the dominant mechanisms relating to pattern formation in blood and colloid droplet systems will assist in the development of further diagnostic techniques. The proposed tests in literature have not been widely utilised. This is because there is not sufficient understanding of the fundamental processes to properly optimise or design diagnostic techniques/devices. This is required before the accuracy and reliability that is required for diagnostics can be fully achieved. Here, a numerical model capable of predicting the presence or absence of patterns in final deposits was developed and the dominant effects of protein and cellular components in blood identified. Before the wide application to blood diagnostics, the developed model must be altered to include complicated and non-linear effects such as the halting of the compaction front and the dehydration of red cells.

It is the intention of this thesis to further the development of low-cost diagnostic devices by systematically characterising and modelling the relevant fundamental processes. This can now be utilised to engineer a new generation of cheap, yet sensitive diagnostic devices, increasing the accessibility of health care and ultimately saving time, cost and lives.

Appendix A

Chapters in their Published Format

Journal of Colloid and Interface Science 528 (2018) 116–123

Contents lists available at ScienceDirect

Journal of Colloid and Interface Science

journal homepage: www.elsevier.com/locate/jcis

Regular Article

Effect of protein adsorption on the radial wicking of blood droplets in paper

Michael J. Hertaeg [a], Rico F. Tabor [b], Gil Garnier [a,*]

[a] BioPRIA and Department of Chemical Engineering, Monash University, Clayton, VIC 3800, Australia
[b] School of Chemistry, Monash University, Clayton, VIC 3800, Australia

GRAPHICAL ABSTRACT

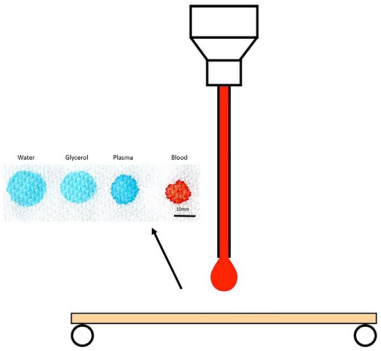

ARTICLE INFO

Article history:
Received 4 April 2018
Revised 9 May 2018
Accepted 14 May 2018
Available online 23 May 2018

Keywords:
Blood
Protein
Radial wicking
Protein adsorption
Stain area
Paper
Biodiagnostic

ABSTRACT

Hypotheses: (1) The equilibrium size and characteristics of a radially wicked fluid on porous material such as paper is expected to be dependent on the fluid properties and therefore could serve as a diagnostic tool. (2) The change in wicked stain size between biological fluids is dependent on a change in solid-liquid surface interfacial energy due to protein adsorption.
Experiments: Sessile droplets of increasing volume of blood, its components, and model fluids were deposited onto paper and the equilibrium stain size after coming to a halt was recorded. The contact angle of fluid droplets on model cellulose surfaces was measured to quantify the effect that blood protein adsorption at the solid-liquid interface has on radially wicked equilibrium size. Finally the significance of droplet evaporation for the time scale of interest was analysed.
Findings: The final stain area of all fluids tested on paper scales remarkably linearly with droplet volume. Different fluids were compared and the gradient of this linear relation was measured. Model fluids varying in surface tension and viscosity all behave similarly and exhibit a constant gradient. Blood and its components produce smaller stains, demonstrated by lower gradients. The gradient is a function of protein concentration, thus the mechanism of this phenomenon was identified as protein adsorption at the cellulose-liquid interface. The slope of the area/volume relationship for droplets is an important quantitative mechanistic variable.

* Corresponding author.
E-mail address: Gil.Garnier@monash.edu (G. Garnier).

https://doi.org/10.1016/j.jcis.2018.05.037
0021-9797/

1. Introduction

The wicking of fluids through porous media is of fundamental importance in many processes and applications such as printing, textiles, agriculture and more recently the medical field for its applications in paper based blood diagnostic tools [1,2].

Blood is a suspension of cells that are weakly electrostatically stabilised in plasma, the liquid component of blood. Plasma consists mostly of water (90 wt%), proteins (approximately 6 wt%) and a small amount of lipids, carbohydrates and electrolytes [3]. There are different types of proteins in blood of which the most abundant are albumin (38.7 g/L) [4], globulin (25 g/L) and fibrinogen (3 g/L) [3]. The composition and protein concentrations in blood vary greatly as a function of health as well as natural variation among populations [5,3,6]. Many blood proteins are surface active and readily adsorb onto surfaces [7]. There are three main types of cells in blood: erythrocytes (red cells), lymphocytes (white cells) and platelets. The majority of cells in blood are red blood cells. Healthy red blood cells are biconcave disks approximately 8 μm in diameter and 3 μm in thickness [8]. The shape, abundance and mechanical properties (deformation) of these cells are responsible for the unique viscoelastic and shear thinning behavior of blood [9]. By centrifugation the majority of cells can be removed from blood allowing the analysis of solely the plasma component. Although plasma exhibits weak viscoelastic properties [10], most analyses assume Newtonian behavior to no significant loss in accuracy. By testing plasma instead of whole blood the effect of protein adsorption can be isolated from the non-Newtonian properties of blood cells as a suspension (shear thinning, viscoelasticity and granularity).

The radial wicking of a drop has been studied previously [11–15]. However all previous studies have considered highly idealised systems ignoring evaporation and the complex properties of multicomponent systems. This study aims to identify the parameters and phenomena controlling the final stain area achieved by a single droplet of blood radially wicking onto paper. This is of direct interest in the development of blood diagnostics for several reasons. The surprising reproducibility and sensitivity of results suggest that drop stain analysis can serve as a convenient and inexpensive method to identify fluid properties. Whether these property changes are caused by protein content, specific antibody-antigen reaction or hematocrit levels will determine the nature of the sensor. The effect of protein concentration is examined here; however, this type of analysis is applicable to many sensing applications. Further a robust fundamental knowledge of the blood stain/volume relationship on paper/porous media will allow more sensitive, faster and more accurate diagnostic methods to be developed and guide the optimisation of existing devices. This study is also relevant to any system involving the contact or deposition of a wetting liquid over a porous material.

2. Experimental section

2.1. Materials

Tests were performed on Kimberly Clark Scott hand towel (4419) and Whatman 41 filter paper. Wet, dry and oven dried (O.D) weights of 100 cm^2 sections of paper are given in Table 1. The wet and dry thicknesses were also measured. Analytical grade glycerol, and ethanol were purchased from Merck, and Thermo Fisher Scientific, respectively. BSA (bovine serum albumin) solutions were diluted from 30% (wt/v) solutions from BioCSL, PBS (phosphate buffered saline) was made to 0.9 wt% with tablets from Sigma. Human blood with EDTA anti-coagulant was provided by the Australian Red Cross following established best ethics practice. Deionized water for tests and dilutions was purified from tap water with a Direct-Q water purification system to a minimum resistivity of 18.2 MΩ cm.

2.2. Methods

2.2.1. Paper characterisation

Paper oven dry (O.D) weight was measured using TAPPI standard 412 by placing samples in a 105 °C oven until weight stabilised. The weight at this point was recorded. The given values are the mean of 3 recordings for each type of paper. Dry Weight was measured using TAPPI standard 402, where the weight of the samples after equilibration in 23 °C 50% relative humidity (RH) conditions for at least 24 h was measured. The values reported are the mean of 6 recordings for each type of paper. Wet weight was determined using a variation of testing standard TAPPI 441. This involved submersing the paper in water for 2 h, then pressing each between two pieces of blotting paper with 2 passes of a 10 kg roller to remove excess water. The paper was then weighed. This process was repeated until weight stabilised. The values for wet weight presented in Table 1 are the mean of 3 recordings for each type of paper. Wet and dry thicknesses were measured using a L & W micrometer. Thickness values are the mean of 10 measurements.

2.2.2. Equilibrium stain size

Reproducible droplets of volume ranging from 2 to 40 μL were created with an adjustable needle and a syringe pump (Fig. 1a). The syringe pump was used to provide a constant flow rate to the needle which created repeatable small drops. Drop size could be controlled by needle geometry. These droplets were directed onto a paper surface that was suspended in 23°C 50% relative humidity (RH) air. Setup took sufficient time to assume fluids were at room temperature during tests. The paper was then imaged using an Epson perfection V370 office scanner and analysed to give the area of each stain. Droplets were recorded in groups of at least 7 onto one piece of paper that was moved between each drop. The volume of the created droplets was measured 4 times before and after being directed onto paper to ensure the drops' volume remained a constant. Prior to tests with biological fluids, needles were soaked for at least 2 h in the fluid to be tested. This was to ensure protein adsorption onto the needle's surface was at equilibrium which improved the uniformity of drops. The difference in area between stains and the variation in measured drop volume is given as error bars in Fig. 2a and b. All property values were found in literature [16–20], except the viscosity and surface tension of blood plasma and BSA solutions, these were measured with an Ostwald viscometer and a pendant drop surface tensiometer [21]. The

Table 1
Paper properties.

Paper	O.D weight (g)	Std Dev (g)	Dry weight (g)	Std Dev (g)	Wet weight (g)	Std Dev (g)	Dry thickness (μm)	Std Dev (μm)	Wet thickness (μm)	Std Dev (μm)
Hand towel	0.2558	0.0030	0.2671	0.0031	0.5537	0.0180	98	2	76	2
Filter paper	0.8537	0.0065	0.8794	0.0174	1.8086	0.0208	226	5	218	5

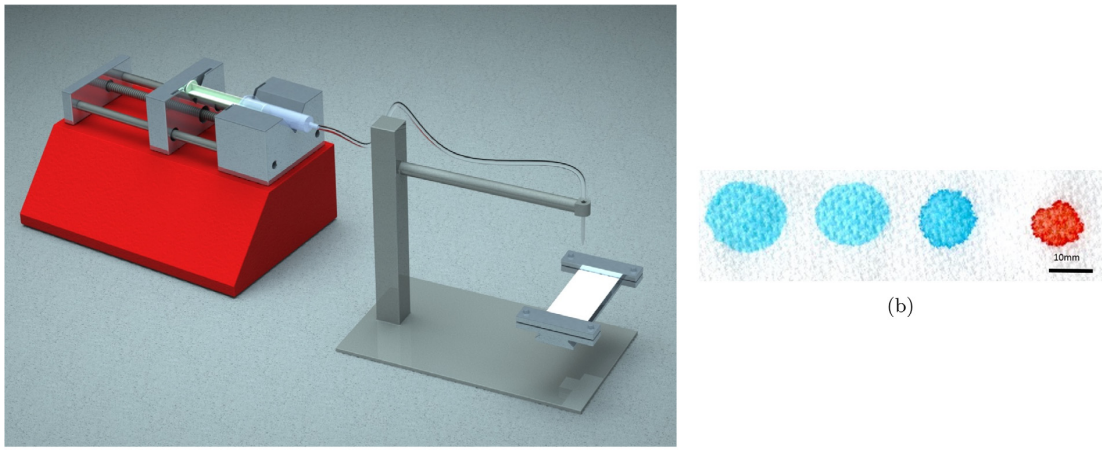

Fig. 1. (a) Diagram of the experimental system depositing sessile droplets of controlled volume on paper. (b) Stains produced from 8 μL droplets of different fluids on paper at identical ambient conditions. From left to right: 25% glycerol, 20% Ethanol, plasma and whole blood. Colourless fluids have blue dye (3 wt%) added to aid visualisation. (For interpretation of the references to colour in this figure legend, the reader is referred to the web version of this article.)

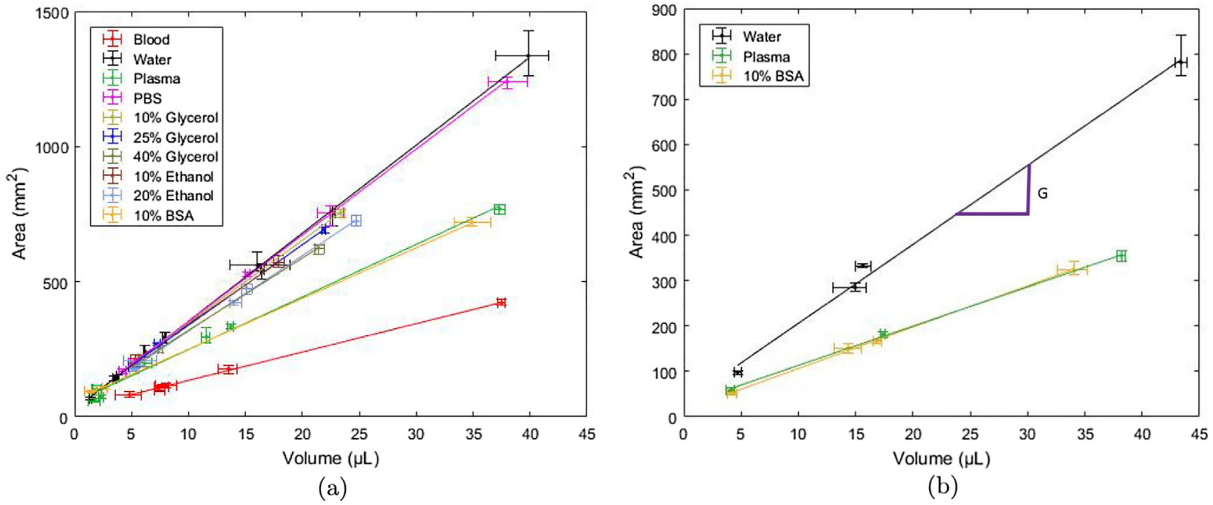

Fig. 2. Effect of initial droplet volume on equilibrium stain area on paper hand towel for blood components and model fluids. The average, minimum and maximum area/volume of at least 7 droplets are shown. All measurements were performed at 23 °C 50% RH. (a) all fluids on paper hand towel and (b) a selection of fluids on filter paper.

density of BSA solutions, plasma and PBS were measured using a Mettler Toledo TLE balance and Eppendorf Pipette.

Surface tension results were complicated by the dynamic surface tension of plasma and BSA [22]. This surface tension variation with time has not been well studied and it is unclear how the surface tension of blood and blood components will change during wicking. For the purpose of this study, highly accurate surface tension data was not required, therefore the average recorded surface tension over a relevant time scale (10–15 s) is reported.

2.2.3. Contact angle measurements

Cellulose thin films were prepared by regenerating spin coated cellulose acetate as previously described [23,24]. A 0.5 wt% solution of cellulose acetate was spin coated onto a plasma cleaned glass slides at 2000 RPM for 20 s. These slides were then regenerated from cellulose acetate to cellulose by soaking in a 0.5% sodium methoxide solution for 10 h. The advancing contact angle was determined using a dataphysics OCA35 contact angle instrument by taking measurements at several points as liquid was pumped into the drop at a rate of 20 μL/s. For each batch of cellulose films, this test was repeated at least three times for each fluid, and three batches of cellulose films were tested. Roughness measurements using a JPK Nanowizard 3 atomic force microscope were completed on 4 of the cellulose surfaces; the roughness value reported is the mean of these 4 values.

2.2.4. Drying time measurement

Tests were completed by suspending a paper towel sample in a digital scale and recording the weight as a function of time. This allowed the rate of evaporation to be measured. The drop size used was 8 μL and the tests were performed at 23 °C 50% relative humidity (RH). The fluids tested were PBS (phosphate buffered saline), 10% BSA (bovine serum albumin), water and plasma.

3. Results

Droplets varying in volume were deposited on paper and the area of the stain at equilibrium was measured for a series of fluids. Blood, blood components and model fluids varying in viscosity and surface tension were tested under standard humidity and temperature conditions. The size, shape, perimeter fractal and colour intensity distribution of the stains on paper vary among the different fluids of the same volume (Fig. 1b). However, size is the most important variable of these stains. The average, maximum and minimum values for stain size and drop volume for a minimum of 7 replicates are shown in Fig. 2a and b. Linear trend lines are fitted for reference.

3.1. Equilibrium stain size

Fig. 2a shows the equilibrium stain size for all tested fluids deposited on paper hand towel, where Fig. 2b shows a selection of these fluids on filter paper. The stain area of a droplet on paper is surprisingly reproducible and scales linearly with volume. All fluids tested show a similar linear trend however with a shift in slope or gradient. At constant drop volume, whole blood creates the smallest stain, followed by plasma. The stain area at equilibrium can be expressed as:

$$A = GV + C \quad (1)$$

where A is the equilibrium area (mm^2), V is the drop volume (μL), G is the gradient of stain area to drop volume ($\frac{1}{mm}$) and C is a constant (mm^2). The calculated value of C range between 74 and 20 mm^2. This value is slightly larger than the average error in area measurements and is always positive.

The gradient G varies significantly between the different fluids and papers. The gradient values for the model fluids on hand towel as well as the fluid properties are presented in Table 2. The gradient value does not correlate with the fluid surface tension or viscosity significantly.

3.2. Effect of protein concentration

Fig. 3a shows the gradient values for solutions of different concentrations of BSA on the paper hand towel. These results were collected in the same way as results in Fig. 2a and b. The gradient of the lines is plotted against BSA concentration. The gradient decreases in a roughly inverse square root fashion with BSA concentration. A faster changing gradient is seen at lower BSA concentrations. This might indicate some adsorption surface saturation mechanism.

3.3. Contact angle measurements

As different and lower gradients are only seen with biofluids on paper, wetting experiments were performed on smooth cellulose films to understand the effect of wetting. Fig. 4 shows the advancing contact angle of a series of selected fluids on model cellulose surfaces. Histograms are presented to visually highlight a statistically significant shift in the mean contact angle despite a high amount of variability in results. This variability has a physical

Table 2
Fluid properties at 23 °C effecting wicking behavior [16–20].

Solution	Concentration (*wt*%)	Density ($kg/m^3 \times 10^3$)	Surface tension (mN/m)	Viscosity (mPa s)	Surface tension/Viscosity (m/s)	Gradient ($1/m \times 10^3$)
Water	100%	1.00 [16]	72.31 [28]	0.93 [16]	77.75	32.6
Glycerol	10%	1.02 [18]	71.97 [19]	1.21[18]	59.48	30.5
Glycerol	25%	1.06 [18]	70.95 [19]	1.92[18]	36.95	29.8
Glycerol	40%	1.10 [18]	69.61 [19]	3.40[18]	20.47	26.7
Ethanol	10%	0.96 [17]	39.29[17]	1.96[17]	20.0	28.8
Ethanol	20%	0.93 [17]	32.27[17]	2.52[17]	12.8	27.9
Plasma	100%	1.01	45	1.74	25.9	19.4
BSA	10%	1.01	40	0.93	43.0	18.7
PBS		1.00	72.2 [20]	1.00 [20]	72.2	31.8

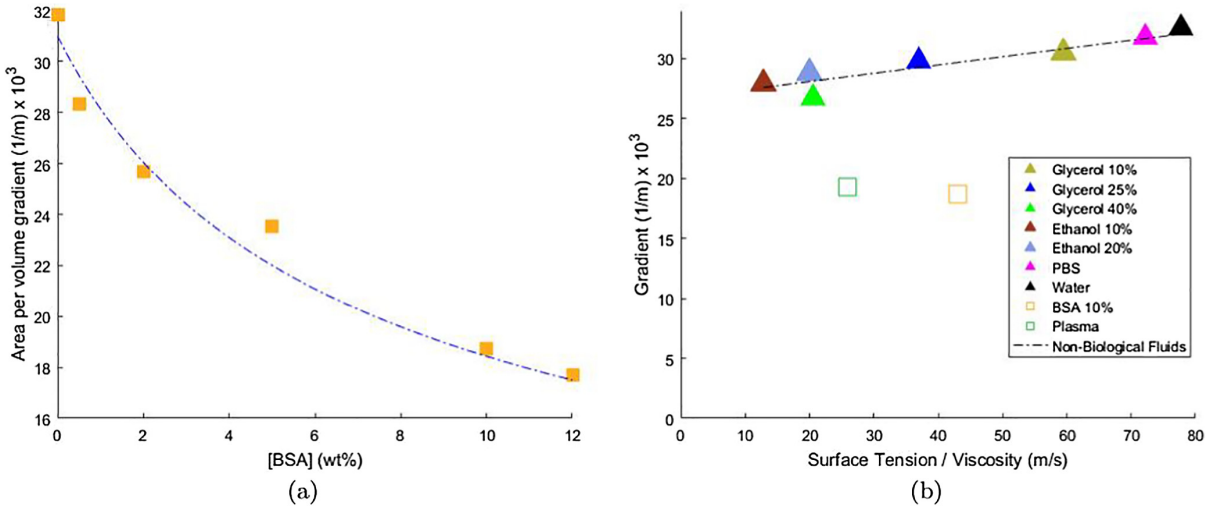

Fig. 3. (a) The droplet area/volume gradient plotted as a function of protein concentration for a series of BSA solutions. A trend line has been drawn to guide the eye. (b) Effect of surface tension to viscosity ratio on the stain area to drop volume gradient. A linear trend line is fitted for non-biological fluids. Biological fluids do not follow this trend.

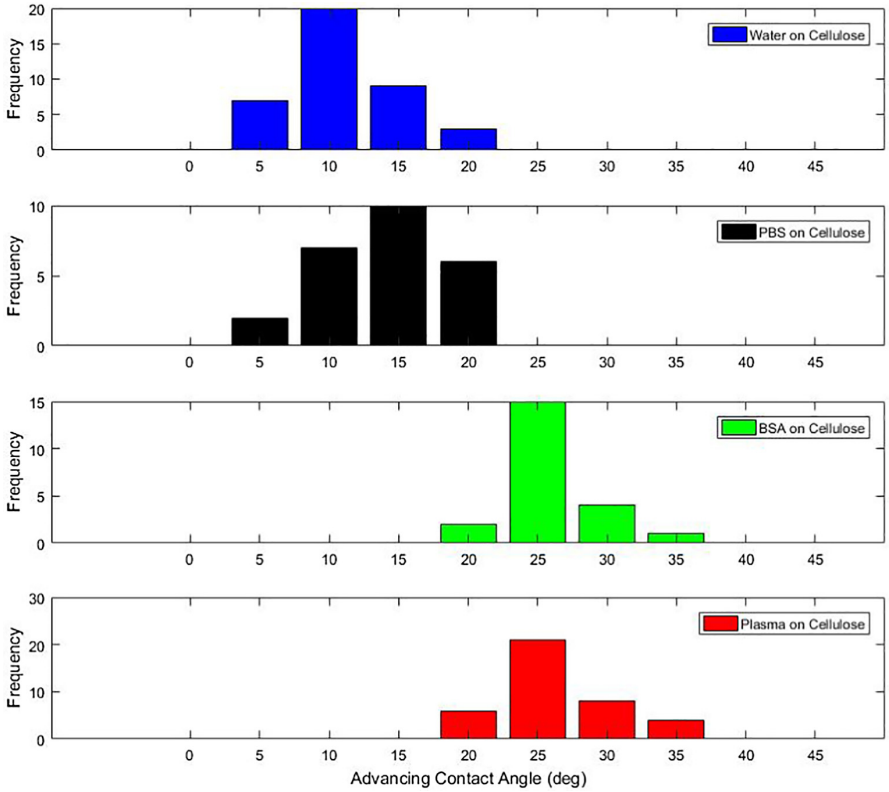

Fig. 4. Histogram of advancing contact angle measurements for water, PBS and biological fluids on cellulose films.

meaning as it quantifies both the chemical and physical heterogeneity of the cellulose films. There is a similar increase in the mean contact angle for biological fluids when compared to non biological fluids.

3.4. Time scale of evaporation

To simplify matters it was intended to study wicking under conditions independent of liquid evaporation. This was achieved by testing in a conditioned laboratory at 23 °C and 50% relative humidity (RH). The effect of droplet evaporation was analysed by measuring the relative weight of a drop deposited onto paper during evaporation. For the time period required for stain growth to fully stop (5–15 s) all fluids had evaporated by less than 10%. Water and PBS evaporate at the same rate, while plasma and BSA solutions evaporate similarly but at a slower rate (Fig. 5).

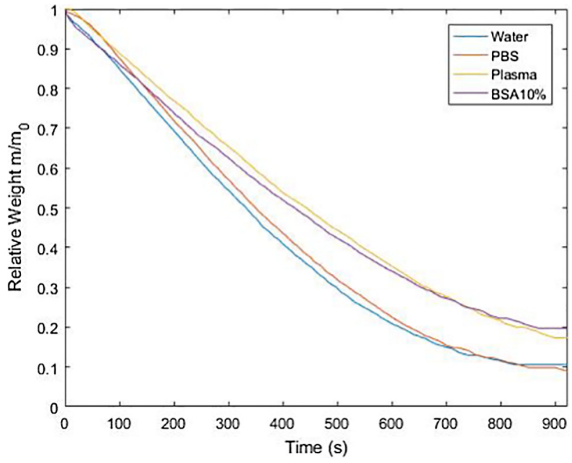

Fig. 5. Weight of 8 μL drops of tested fluids on paper in 23 °C 50% relative humidity air. Y axis is normalised by initial drop weight. All show limited drying at a time where the stain growth was observed to stop, approximately 11 s. These results are shown in Fig. 5

4. Discussion

4.1. Equilibrium stain size

Fig. 2a and b show a clear distinction between the wicking behavior of biological and non-biological fluids on paper. Despite large variations in both surface tension and viscosity between water, ethanol and glycerol solutions, there is no significant change in gradient. This is surprising as previous research on non-equilibrium radial spreading has shown a strong dependency on the ratio $\frac{\gamma}{\eta}$ [12,14], although this is not directly comparable to equilibrium results. Fig. 3b shows the effect of the $\frac{\gamma}{\eta}$ ratio on the gradient of the equilibrium stain area to drop volume curve with all fluid properties presented in Table 2. There is a slight dependence of the gradient on the $\frac{\gamma}{\eta}$ ratio for non-biological fluids and a linear function was arbitrarily fitted. Plasma and 10% BSA solution do not follow the trend of model fluids. Table 2 also shows that the gradient parameter does not directly scale with either viscosity or surface tension. Although there may be a slight dependence of the

stain area/drop volume gradient with the $\frac{\gamma}{\eta}$ ratio, there is another property that presents itself in blood plasma that is far more dominant. This extreme variation in stain sizes between plasma and model fluids was not reported by Li et al. in their experiments with porcine plasma on cotton 'T-shirt' fabric[25]. The gradient for blood is significantly smaller than all tested fluids. The stain area of blood is on average 55% that of plasma using droplets of identical volumes. This finding corroborates the study of Li et al. with porcine blood/plasma who further reported the blood to plasma stain ratio to be equal to one minus the average hematocrit value of blood [25]. The authors relied on this observation to justify the assumption that it is only the volume of the plasma component that determines stain size. Although the value of this repeatable stain size ratio between blood and plasma is intriguing, it is unlikely that the red blood cells have no effect on the wicking process. Other causes of the smaller stain size for blood could include blood cells form blockages in the smaller pores of paper, or electrostatic repulsion between the negatively charged red blood cells[26] and the anionic cellulose [27]; however this is unlikely to be significant due to the micro scale of red blood cells.

Stains on different papers can be compared by defining a new variable, the paper ratio factor (PRF). This is calculated as the gradient of the stain area to volume relationship on a certain paper, divided by the gradient of the same fluid on a different reference paper (Eq. (2)). Table 3 compares the PRF values on hand towel and filter paper for 3 fluids. If the two papers were to behave identically, simple volume conservation analysis reveals that the PRF should be equal to the ratio of the two paper thicknesses. This ratio was measured by micrometer and found to be 2.26.

$$PRF = G_{HandTowel}/G_{FilterPaper} \tag{2}$$

Although plasma and BSA have PRF factors close to 2.26, water shows a slightly lower than expected ratio. This implies that water and biological fluids are affected differently by the change in paper properties.

Schuchard et al. reported fiber swelling to be an important parameter to consider for wicking in cellulose networks [29]. All fluids used in this study are water-based and therefore will swell cellulose; however, it is not clear if there is a difference in swelling among fluids and whether this would cause a change in stain area. This could be the cause of the shifts in PRF value between fluids as paper type may affect the extent of fiber swelling.

4.2. Effect of evaporation

The linearity of the equilibrium stain area with drop volume relationship (Fig. 2a) implies the absence of any significant evaporation. If evaporation was taking place, a plateau would be expected at the higher drop sizes. This is further shown by drying time experiments in which the weight after fluid contact with paper was measured with time. No significant drying occurs in the time frame of wicking, which range between 5 and 15 s in this study. Therefore evaporation is insignificant for the system studied. Measurements with water, plasma, PBS and BSA solutions all show similar behavior.

This differs from expectations from literature. Gilespie [13] predicted that a wicked stain equilibrium area would only be detectable when evaporation is significant. It might be possible that the measured apparent equilibrium position is actually a state where the front is moving so slowly that its motion is unobservable and the final position is the effect of drying after a significant time.

Nilghaz et al. [30] demonstrated that coffee rings [31] form on paper in some situations. As the mechanism of coffee ring formation is dependent on a pinned outer edge [32], and the effects of surface pinning are not included in models that predict indefinite spreading, pinning may be a determining factor in stain equilibrium size.

4.3. Wetting mechanism

Advancing contact angle measurements were performed on model cellulose films. The contact angle data can be used with the Young equation [33] (Eq. (3)), to determine the interfacial energy at the solid liquid interface. Eq. (4) accounts for surface roughness [34]. The value for the cellulose-air interfacial energy γ_{sv} used is 69.0 mN/m. This value is the mean of the two testing methods for the surface energy of untreated cellulose fibers by Westerlind and Berg [35] and is very close to the value also found by Niegelhell et al. [36]. The roughness used in calculations was measured by atomic force microscopy to be 1.16. Roughness is defined as the real surface area divided by the surface area of a smooth surface of the same dimensions.

$$\gamma_{sv} = \gamma_{sl} + \gamma_{lv}\cos\theta \tag{3}$$

where γ_{sv}, γ_{sl} and γ_{lv} are the solid-vapour, solid-liquid and liquid-vapour surface tensions respectively.

$$\cos\theta_{app} = r\cos\theta_r \tag{4}$$

where θ_{app} is the apparent measured contact angle, r is the roughness of the substrate and θ_r is the real contact angle that can be used in the Young equation. The solid-liquid interfacial energies calculated are presented in Table 4. Results from PBS are calculated to demonstrate the negligible effect of ionic strength on wetting.

The equilibrium stain size of 0% BSA or 100% PBS are similar to tests with water, which shows that the effect of salinity is negligible.

4.4. Protein adsorption

Surface energy measurements show the solid liquid surface energy to be significantly raised by high protein concentrations in the droplet solution. Fluids exhibiting similar stain sizes, such as 10% BSA and plasma also have very similar surface energies. This suggests a relationship between stain size and the solid-liquid interfacial energy which is affected by protein content in the fluid. This is most likely caused by protein adsorption onto the cellulose surface.

The adsorption of BSA and human immunoglobulin G onto cellulose was previously demonstrated [7]. This adsorption of blood proteins was shown to make cellulose more hydrophobic after aging and drying [23]. This augmented hydrophobicity is caused

Table 3
Paper ratio factor (no unit). Filter paper is used as reference paper.

Fluid	PRF
Water	1.87
Plasma	2.25
10% BSA	2.06

Table 4
Liquid solid interfacial energy measured from wetting experiments for the different fluids on cellulose films.

Fluid	Mean advancing contact angle (degrees)	Solid-liquid interfacial energy (mN/m)
Water	13.5	8.4
PBS	16.6	9.3
BSA 10%	28.4	38.6
Plasma	28.9	35.0

by an increase in solid-liquid interfacial energy at the cellulose interface due to a protein conformation change. The increased solid-liquid interfacial energy calculated here is likely caused by a similar mechanism although contact angle measurements were performed with the protein solution, not water after drying as in previous studies. An increase in cellulose-fluid interfacial energy would cause a decrease in stain area as the formation of such an interface is energetically unfavorable.

As a wicking system is in motion the transportation of solution components is not necessarily homogeneous due to adsorption and diffusive variations. Such variations can effect wicking of surfactant solutions [37]. The surface energies calculated for static drops in equilibrium presented may not directly translate to transient wicking analysis. It is also unknown how the addition of protein will affect fiber swelling.

Interpolating from the trend in Fig. 3a, plasma behavior is similar to a solution having a BSA concentration of 8.3%. This value differs from the average concentration of albumin in human plasma which is 3.9% [4], with normal values ranging from 3.2% to 4.5% [5]. Although albumin concentration is likely to be a factor affecting plasma equilibrium wicked area, it is not the only factor.

Albumin represents only 60–65% by weight of blood plasma proteins [6]; there are many other blood proteins capable of adsorbing onto cellulose [7]. The concentration of all proteins in plasma is approximately 6.2%. Comparing this value to the plasma similar BSA solution concentration (8.3%) reveals that either non-albumin proteins effect equilibrium on a per weight basis more than albumin, or there is another factor that has not been investigated, such as the competitive binding of phosphate ions from PBS [38].

5. Conclusion

A series of small droplets of blood and model fluids were deposited onto paper and the stain area to drop volume was measured for droplets of increasing volume. The model fluids studied consist of a selection of simple fluids varying in surface tension and viscosity, as well as blood plasma and protein solutions of different concentrations. The stain area-droplet volume relationship was studied. This was performed under controlled conditions (23 °C and 50% RH) under which evaporation was negligible. To better distinguish the effect of wetting from radial wicking in a porous material, the contact angle of plasma and water were measured over smooth cellulose films.

The area of the stain achieved by the radial wicking of a droplet of controlled volume deposited onto paper is very reproducible. Stain area scales linearly with droplet volume. The slope of the stain area-droplet volume relationship (gradient) is indicative of the fluid composition and the paper structure. The gradient is however nearly independent of fluid viscosity and surface tension. Blood has the lowest gradient, followed by plasma, protein solutions and the model simple fluids each having nearly identical slopes. This different behaviour was attributed to the adsorption of protein onto paper, affecting the solid-liquid (γ_{sl}) interfacial energy. The protein content of BSA solutions and blood was found to strongly effect the gradient and therefore the equilibrium stain size. This is due to the increase in surface energy that occurs after protein adsorption onto the cellulose fluid interface. Previous studies have shown that the ratio of surface tension to viscosity is a critical parameter for situations under non-equilibrium wicking conditions [12–14]. However, our results were found to be almost independent of the ratio. The paper ratio factor (PRF) is proposed as a new measure of the relative stain sizes in different papers and is compared to the ratio of thicknesses to identify effects from paper structure.

The reproducibility of stain area-droplet volume on paper, its ease of measurement combined with the slope (gradient) being a function of fluid properties all make blood stain analysis very attractive for diagnostic applications. Blood stain analysis could become the basis for a new generation of high throughput and very fast blood diagnostic systems.

Acknowledgments

This research was funded by an ARC Linkage grant (LP160100544) and Haemokinesis.

References

[1] M. Al-Tamimi, W. Shen, R. Zeineddine, H. Tran, G. Garnier, Validation of paper-based assay for rapid blood typing, Anal. Chem. 84 (3) (2012) 1661–1668.
[2] W. Then, M. Li, H. McLiesh, W. Shen, G. Garnier, The detection of blood group phenotypes using paper diagnostics, Vox sanguinis 108 (2) (2015) 186–196.
[3] R. Chen, L. Zhang, D. Zang, W. Shen, Blood drop patterns: formation and applications, Adv. Colloid Interface Sci. 231 (2016) 1–14.
[4] D.J. Greenblatt, Reduced serum albumin concentration in the elderly: a report from the boston collaborative drug surveillance program, J. Am. Geriatr. Soc. 27 (1) (1979) 20–22.
[5] B.N. Azab, V.R. Bhatt, S. Vonfrolio, R. Bachir, V. Rubinshteyn, H. Alkaied, A. Habeshy, J. Patel, A.I. Picon, S.W. Bloom, Value of the pretreatment albumin to globulin ratio in predicting long-term mortality in breast cancer patients, Am. J. Surg. 206 (5) (2013) 764–770.
[6] M. Otagiri, V.T.G. Chuang, Albumin in Medicine: Pathological and Clinical Applications, Springer, 2016.
[7] H. Orelma, I. Filpponen, L.-S. Johansson, J. Laine, O.J. Rojas, Modification of cellulose films by adsorption of CMC and Chitosan for controlled attachment of biomolecules, Biomacromolecules 12 (12) (2011) 4311–4318.
[8] M. Thiriet, The Biology and Mechanics of Blood Flows, Springer, 2008.
[9] A. Copley, G. Stainsby, Flow Properties of Blood, Pergamon Press, 1960.
[10] M. Brust, C. Schaefer, R. Doerr, L. Pan, M. Garcia, P. Arratia, C. Wagner, Rheology of human blood plasma: viscoelastic versus newtonian behavior, Phys. Rev. Lett. 110 (7) (2013) 078305.
[11] A. Borhan, K. Rungta, On the radial spreading of liquids in thin porous substrates, J. Colloid Interface Sci. 154 (1) (1992) 295–297.
[12] D. Danino, A. Marmur, Radial capillary penetration into paper: limited and unlimited liquid reservoirs, J. Colloid Interface Sci. 166 (1) (1994) 245–250.
[13] T. Gillespie, The spreading of low vapor pressure liquids, J. Colloid Sci. 13 (1958) 32–50.
[14] E. Kissa, Capillary sorption in fibrous assemblies, J. Colloid Interface Sci. 83 (1) (1981) 265–272.
[15] A. Marmur, Penetration and displacement in capillary systems of limited size, Adv. Colloids Interface Sci. 39 (1992) 13–33.
[16] J. Kestin, M. Sokolov, W.A. Wakeham, Viscosity of liquid water in the range- 8 c to 150 c, J. Phys. Chem. Ref. Data 7 (3) (1978) 941–948.
[17] I.S. Khattab, F. Bandarkar, M.A.A. Fakhree, A. Jouyban, Density, viscosity, and surface tension of water+ ethanol mixtures from 293 to 323k, Korean J. Chem. Eng. 29 (6) (2012) 812–817.
[18] M.L. Sheely, Glycerol viscosity tables, Ind. Eng. Chem. 24 (9) (1932) 1060–1064.
[19] K. Takamura, H. Fischer, N.R. Morrow, Physical properties of aqueous glycerol solutions, J. Petrol. Sci. Eng. 98 (2012) 50–60.
[20] H. Tavana, C.-H. Kuo, Q.Y. Lee, B. Mosadegh, D. Huh, P.J. Christensen, J.B. Grotberg, S. Takayama, Dynamics of liquid plugs of buffer and surfactant solutions in a micro-engineered pulmonary airway model, Langmuir 26 (5) (2009) 3744–3752.
[21] J.D. Berry, M.J. Neeson, R.R. Dagastine, D.Y. Chan, R.F. Tabor, Measurement of surface and interfacial tension using pendant drop tensiometry, J. Colloid Interface Sci. 454 (2015) 226–237.
[22] S. Zaitsev, Dynamic surface tension measurements as general approach to the analysis of animal blood plasma and serum, Adv. Colloid Interface Sci. 235 (2016) 201–213.
[23] Huang Z, Raghuwanshi VS, Garnier G. Functionality of immunoglobulin g and immunoglobulin m antibody physisorbed on cellulosic films. Front Bioeng Biotechnol 5.
[24] J. Su, C.J. Garvey, S. Holt, R.F. Tabor, B. Winther-Jensen, W. Batchelor, G. Garnier, Adsorption of cationic polyacrylamide at the cellulose–liquid interface: a neutron reflectometry study, J. Colloid Interface Sci. 448 (2015) 88–99.
[25] J. Li, X. Li, S. Michielsen, Alternative method for determining the original drop volume of bloodstains on knit fabrics, Forensic Sci. Int. 263 (2016) 194–203.
[26] H.-C. Chang, Electrokinetic transport of red blood cells in microcapillaries, Electrophoresis 23 (2002) 2165–2173.
[27] C. Zhu, I. Dobryden, J. Ryden, S. Oberg, A. Holmgren, A.P. Mathew, Adsorption behavior of cellulose and its derivatives toward Ag(i) in aqueous medium: an AFM, spectroscopic, and DFT study, Langmuir 31 (45) (2015) 12390–12400.
[28] G. Vazquez, E. Alvarez, J.M. Navaza, Surface tension of alcohol water+ water from 20 to 50. degree. c, J. Chem. Eng. Data 40 (3) (1995) 611–614.

[29] D.R. Schuchard, J.C. Berg, Liquid transport in composite cellulose superabsorbent fiber networks, Wood Fiber Sci. 23 (3) (2007) 342–357.
[30] A. Nilghaz, L. Zhang, W. Shen, Coffee stains on paper, Chem. Eng. Sci. 129 (2015) 34–41.
[31] R.D. Deegan, O. Bakajin, T.F. Dupont, G. Huber, S.R. Nagel, T.A. Witten, Capillary flow as the cause of ring stains from dried liquid drops, Nature 389 (6653) (1997) 827–829.
[32] R. Chen, L. Zhang, D. Zang, W. Shen, Wetting and drying of colloidal droplets: Physics and pattern formation, in: Advances in Colloid Science, InTech, 2016.
[33] T. Young, An essay on the cohesion of fluids, Philos. Trans. R. Soc. Lond. 95 (1805) 65–87.
[34] D. Brutin, Droplet Wetting and Evaporation: from Pure to Complex Fluids, Academic Press, 2015.
[35] B.S. Westerlind, J.C. Berg, Surface energy of untreated and surface-modified cellulose fibers, J. Appl. Polym. Sci. 36 (3) (1988) 523–534.
[36] K. Niegelhell, M. Sußenbacher, J. Sattelkow, H. Plank, Y. Wang, K. Zhang, S. Spirk, How bound and free fatty acids in cellulose films impact nonspecific protein adsorption, Biomacromolecules 18 (12) (2017) 4224–4231.
[37] K.T. Hodgson, J.C. Berg, The effect of surfactants on wicking flow in fiber networks, J. Colloid Interface Sci. 121 (1) (1988) 22–31.
[38] Z. Yang, C. Zhang, Adsorption/desorption behavior of protein on nanosized hydroxyapatite coatings: a quartz crystal microbalance study, Appl. Surf. Sci. 255 (8) (2009) 4569–4574.

Journal of Colloid and Interface Science 541 (2019) 312–321

Contents lists available at ScienceDirect

Journal of Colloid and Interface Science

journal homepage: www.elsevier.com/locate/jcis

Regular Article

Dynamics of stain growth from sessile droplets on paper

Michael J. Hertaeg [a], Rico F. Tabor [b], Joseph D. Berry [c], Gil Garnier [a,*]

[a] BioPRIA and Department of Chemical Engineering, Monash University, Clayton, VIC 3800, Australia
[b] School of Chemistry, Monash University, Clayton, VIC 3800, Australia
[c] Department of Chemical and Biomolecular Engineering and the Particulate Fluids Processing Centre, University of Melbourne, Parkville, Victoria 3010, Australia

GRAPHICAL ABSTRACT

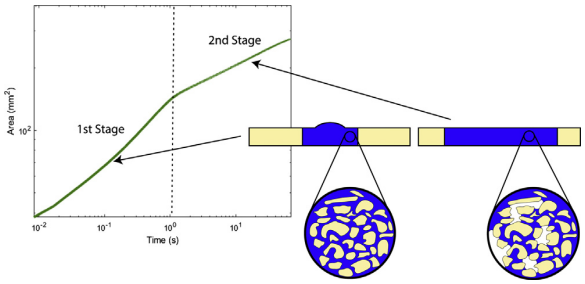

ARTICLE INFO

Article history:
Received 29 November 2018
Revised 8 January 2019
Accepted 9 January 2019
Available online 16 January 2019

Keywords:
Radial wicking
Stain area
Paper
Wetting
Kinetics
Modelling
Sessile droplets

ABSTRACT

Hypothesis: The rate of stain growth of a sessile droplet deposited on paper has been previously studied (Kissa, 1981; Danino and Marmur, 1994; Kawase et al., 1986; Borhan and Rungta, 1993) but is not fully understood. In particular, the mechanism by which the abrupt decrease in growth rate occurs is unknown. This process is expected to follow a model where the disappearance of the droplet is represented by a change to the boundary condition at the droplet-paper interface when the volume of the fluid inside the paper is equal to the volume of the simulated droplet.
Experiments: The stain size of sessile droplets on paper was monitored against time. A series of fluids varying in surface tension and viscosity was studied. The kinetics of stain growth was modelled and compared with experiments and existing models of stain growth.
Findings: The measured stain area formed by a sessile droplet deposited on paper follows a two regime mechanism (Danino and Marmur, 1994). In the initial regime, the dynamics are governed by the filling of pores. However, in the later stage, the process is influenced by the emptying/redistribution of fluid. Simulations show that experimental results are well described by a model that identifies the change in boundary conditions after the droplet is no longer present above the paper, coupled with the change to a redistribution dominated mechanism.

1. Introduction

Wicking has been described for many years by the Lucas-Washburn equation [5,6]. This model assumes the substrate material to be a collection of cylindrical capillaries and gives fairly good correlation with experimental results in a variety of porous materials [7,8]. However, there are several critical and restrictive simplifications required that prevent generalisation of the model to all wicking applications. The two most notable assumptions of the Lucas-Washburn equation are: (i) the unidirectional requirements and (ii) the definition of a sharp interface where the

* Corresponding author.
E-mail address: Gil.Garnier@monash.edu (G. Garnier).

https://doi.org/10.1016/j.jcis.2019.01.032
0021-9797/

material transitions from 100% saturated to 0% saturated at the wicking front. These two assumptions do not apply for many systems including droplets wicking on paper. To overcome these simplifications, previous researchers have derived relations based on Darcy's law for flow through porous media. These approaches allow for the description of wicking in complex geometries and semi-saturated media and are used in the design of many paper-based diagnostic devices [9].

The deposition of a droplet of liquid onto the surface of a thin porous material like paper is a special wicking case that has received particular attention. Droplets wicking on porous media and the kinetics of stain growth play a critical role in many industrial applications, including printing for communication and functional uses such as biodiagnostic manufacturing. Fundamentally, modelling the kinetics of droplet wicking, from sessile droplet to stain at equilibrium, has remained a complex and elusive task. This process is different from the case of a infinite reservoir system because at some finite time after deposition, the droplet will completely be absorbed by the paper, changing the nature of the process significantly. These two stages are usually referred to as stage one (droplet disappearing from the surface of the paper) and stage two (absorbed droplet redistributing/wicking in paper). As stage two is much longer than stage one, most of the models have been focused there. Many models based on Darcy's law have been proposed. However, all have relied on many empiricisms to fit results [1,2,10,11]. All of these relations can be broadly expressed in the functional form:

$$A \propto t^m, \tag{1}$$

where A is the wetted area, t the time after deposition and m is a constant. The evolution of the stain area produced by a wicking droplet is quite well represented by this power law. However, the value of m is higher in the first stage than in the second stage. The stated values of m for each stage vary but are in the range of 0.39–0.50 for the first stage and 0.10–0.33 for the second stage [1–4]. These discrepancies have been attributed to differences between fluids, droplet sizes, absorption by fibers, temperature and humidity; however, no model has been able to explain the large variation reported.

Marmur [12] presented an analytical model for radial wicking where the material is modelled as a gap between two plates with liquid being introduced from a hole in the center of the top plate. Marmur's equation expressed in terms of area [4] is given as:

$$\frac{A}{A_o}\left(\ln\frac{A}{A_o}-1\right) = -1 + \left(\frac{2\pi d\gamma\cos\theta}{3A_o\mu}\right)t. \tag{2}$$

Here A is wetted area, A_o is the area of the inlet, d is the separation of the two plates, γ is the liquid–vapour surface tension of the liquid, θ is the contact angle and μ is the viscosity. This approach is similar to that of Lucas and Washburn as it also assumes a sharp interface. Despite this, the equation predicts radial wicking behavior from infinite reservoirs quite well [2,4] and results from Danino and Marmur [2] imply that it also can be used to model stage one of droplet wicking. For the droplet wicking case, it is not clear what value to use for A_o; however, the fitted values are physically reasonable.

The effectiveness of Marmur's equation in predicting stage one behavior implies that the distribution of fluid creates an abrupt transition between fully saturated and dry paper. However, after the consumption of the reservoir (stage two), liquid motion is primarily driven by the redistribution effect [13] which is why Marmur's equation is no longer appropriate. The redistribution effect is the emptying of initially filled large pores into smaller pores due to the higher capillary pressures there. Our previous work has identified that this motion will continue until a position is reached that is determined by the system's solid–liquid interfacial energy [14].

Several numerical studies have predicted wicking behavior from infinite reservoirs using Richards' equation, developed to determine liquid distribution in soils [15–18]. Some of these studies simulate radial wicking and correlate well with both experimental results and Marmur's relation (Eq. (2)). The present work applies previously developed numerical schemes to model the radial wicking of fluid from a sessile droplet. This is done by applying the same Dirichlet (saturated) boundary conditions [19] used for infinite systems at the droplet interface until the simulated droplet is consumed. After this a Neumann (no flux) boundary condition [19] is used.

It is the objective of this study to measure and model the wicking dynamics of a sessile droplet deposited onto paper. We also aim to identify and quantify the mechanisms controlling the stain growth in paper. This knowledge is required to engineer accurate and predictive paper diagnostics for biomedical applications [20]. A secondary objective of the study is to develop a rigorous, accurate and physically meaningful alternative to the Lucas-Washburn equation.

2. Methods

2.1. Simulation

2.1.1. Model development

Richards' equation can be described as Darcy's law with allowances for mass conservation where the permeability of the porous material is proportional to the local volume fraction [21],

$$\frac{\partial\phi}{\partial t} = \nabla\cdot\left(\frac{K(\phi)}{\mu}\nabla P\right) \tag{3}$$

here ϕ is the relative volume fraction expressed relative to maximum saturation $\phi = \epsilon/\epsilon_s$, ϵ is the volume fraction expressed in volume of fluid per volume of paper and ϵ_s is the saturated volume fraction, $K(\phi)$ is the permeability as a function of volume fraction, μ is viscosity and P is pressure.

In a wicking situation where there is no externally applied pressure gradient and gravitational effects can be ignored, pressure variation is caused solely by Laplace pressure at liquid–vapour interfaces. This pressure will be a function of volume fraction as the liquid–vapour interfaces will be in small pores with higher Laplace pressures at low volume fractions, and will move to large pores with lower Laplace pressures at high volume fractions. With this, Eq. (3) becomes the diffusion equation where diffusivity is a simple function of pressure, permeability and viscosity:

$$\frac{\partial\phi}{\partial t} = \nabla\cdot\left(\frac{D(\phi)}{\mu}\nabla\phi\right), \tag{4}$$

$$D(\phi) = K(\phi)\frac{\partial P(\phi)}{\partial\phi}. \tag{5}$$

This approach was verified by several previous studies [15–18]. However, each of those used a different function for permeability and pressure distribution. One of the simplest systems of constitutive equations for permeability and pressure was implemented by Perez-Cruz [15] and is reproduced here. This model expresses the combined effects of varying pressure and permeability as an effective scaled diffusivity. Due to the factor of viscosity in Eq. (4), $D(\phi)$ is not a true diffusivity and therefore does not have the units m^2/s. This scaled diffusivity can be expressed as a power law relation with volume fraction [15]:

$$D(\phi) = D_0\phi^n \tag{6}$$

where D_0 is the viscosity scaled diffusivity at saturation and n is a constant calculated from a substrate's pore size distribution index [22]. Perez-Cruz fit n to results. However, pore size distribution index (λ), and therefore n, can be calculated by fitting Eq. (7) to experimental porosimetry data (Fig. 3):

$$\phi = \left(\frac{P(\phi)}{P_c}\right)^{-\lambda}, \tag{7}$$

$$n = 2 + \frac{1}{\lambda}, \tag{8}$$

where P_c is atmospheric pressure. These relations are based on the Brooks Corey model for water penetration in soils [22].

2.1.2. Model implementation

The solution of Eq. (4) was carried out in arb, an open source finite volume solver [23] on a two-dimensional axisymmetric domain (Fig. 1). Boundary conditions were initially no flux on all external edges, except the top region covered by the droplet at $0 > r > R_0$. Here, the value of phi was fixed at the saturation value of the material until the total volume of liquid in the domain reaches the volume of the simulated droplet at $t = t_{abs}$. For $t > t_{abs}$ the boundary condition at the droplet interface was changed to the zero flux condition. This procedure simulates the transition from stage one to stage two radial wicking where the droplet disappears from the surface of the paper. This process ignores the changes in droplet radius discussed in previous literature [24] as the effects on larger scale behavior are secondary. A structured mesh was used to better capture the sharp front that is created, with four divisions used in the vertical direction as the problem is essentially one-dimensional. This is because the small thickness of the paper relative to its length means that vertical equilibrium occurs so quickly that a one-dimensional simulation would have also been appropriate. A two-dimensional domain was however investigated to make the initial surface saturation boundary condition where the droplet resides more intuitive. The results of a mesh refinement study are shown in supplementary information for an n value of 8. This value was chosen as it is higher than any n value used in results and therefore represents a worst case, where the simulation would be most dependent on mesh quality. This is because higher n values cause a sharper interface to form. A mesh spacing of $\delta x = 0.02R_0$ was chosen as this kept simulations to a reasonable time and corresponded to less than a 5% variation from the finest mesh tested. To simulate the first stage a time step $\delta t = 0.01$ s was chosen to ensure that t_{abs} was calculated to sufficient accuracy. During the second stage the time step was increased incrementally to a maximum of 0.04 s to save computational time. Time step sensitivity analysis of the same test case as the mesh resolution study was carried out, showing that the choice of $\delta t =$ 0.01–0.04 s was sufficient for accuracy and stability of the numerical solution.

Stain boundary was calculated by identifying a radial position that corresponded to a relative volume fraction (ϕ) of 0.01. As volume fraction decreases extremely quickly near the edge of a stain, the criterion of stain front definition did not affect results. This model uses 7 input parameters: V_D droplet volume, μ viscosity, h paper thickness, D_0 diffusivity at maximum saturation, n linear function of pore distribution index, A_0 initial droplet area and ϵ_s saturation volume fraction. While some of these parameters can be directly measured and some must be fitted, all have a physical meaning in the first stage of the simulation. As n is only based on pore distribution index in the first stage it is an empirical fitting parameter in the second.

2.2. Experimental

2.2.1. Materials

Analytical grade glycerol, decane and ethanol were purchased from Merck, Sigma and Thermo Fisher Scientific, respectively. Densities of glycerol, decane and ethanol solutions were interpolated from data measured by Sheely [25], Liu et al. [26] and Khattab et al. [27] respectively. Tests were performed on Whatman 41 filter paper and Advantec GA-55 glass fiber filters. Deionized water for tests and dilutions was purified from tap water with a Direct-Q water purification system to a minimum resistivity of 18.2 MΩ·cm. Queens blue food dye was used to dye water soluble fluids.

2.2.2. Methods

Droplets were produced with an adjustable needle and a syringe pump in the same way as our previous study [14]. The syringe pump provided a constant flow rate to the needle which causes droplets of repeatable size to detach and periodically fall from the needle. Droplet size was quantified using a Mettler Toledo TLE balance before the needle was directed onto the paper surface. The average weight of 4 previous droplets divided by the density of the fluid was used to estimate the volume of the droplet that fell onto the paper. Droplet size was controlled by altering needle size. Stain size data were recorded by a Point Grey Flea3 camera mounted on a track that captured the reflected bottom view of the paper. The images were captured at 120 frames per second. A diagram of the experimental setup is shown in Fig. 2. All tests were performed in a 23 °C 50% relative humidity environment. To

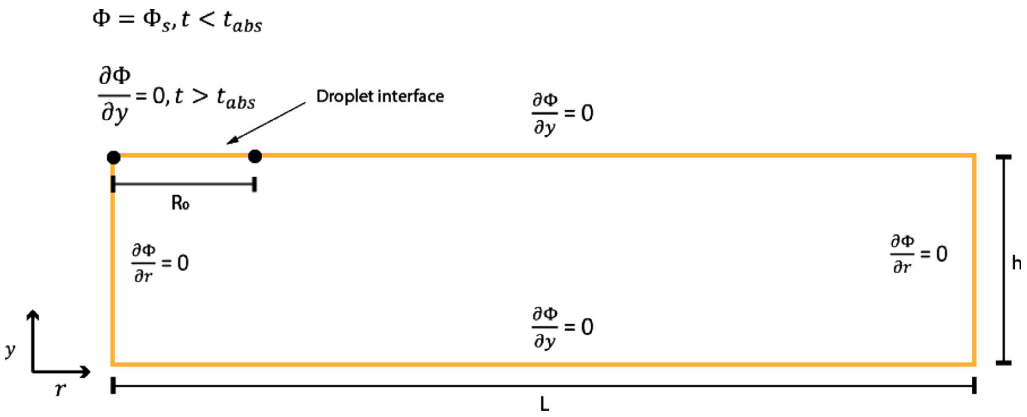

Fig. 1. Diagram of simulation domain with implemented boundary conditions.

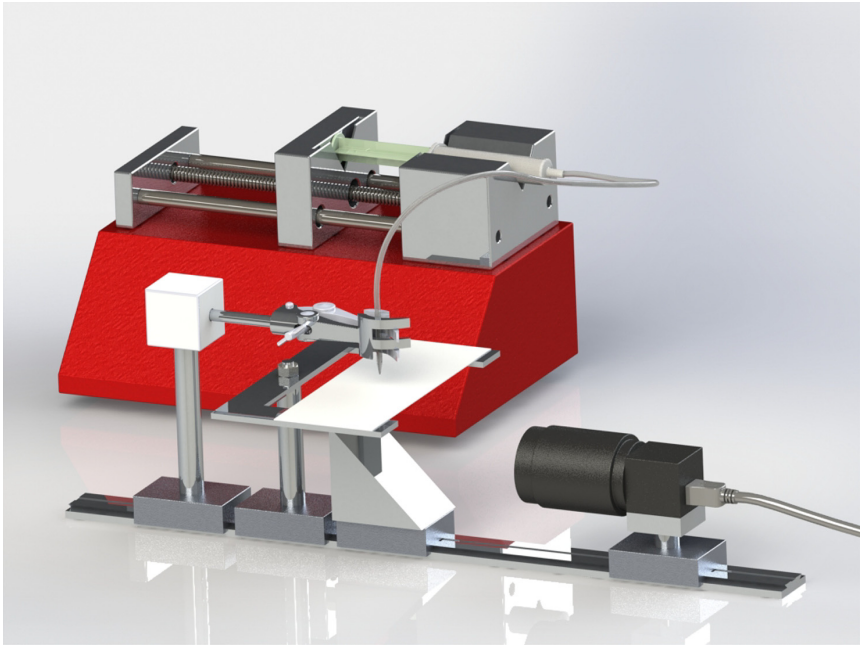

Fig. 2. Syringe pump and needle experimental setup. The side mounted camera and 45 degree mirror are shown.

improve contrast, 3 wt% of food dye solution was added to the aqueous solutions. Tests were performed to ensure the dye at the concentration studied did not affect results. Although the dynamic wicking measurements without dye were prone to noise, there was no significant differences between dyed and not dyed fluids. This dye was assumed to have the same properties as water and was included in solution concentration calculations. Droplet disappearance times were found using a side mounted Phantom VEO 410L high speed camera recording at 4000 fps. No adequate dye was found for decane as all dyes separated chromatographically due to their affinity for cellulose. Due to this, no contrast agent was used and as a result there is more noise in the decane recordings.

2.2.3. Porosimetry

Porosimetry measurements were performed with a mercury porosimeter (Micrometrics AutoPore IV 9500). This characterises the infiltration against pressure. To convert this into data that can be compared to Eq. (7), the infiltration values were divided by their maximum value; this gave infiltration data relative to maximum saturation. The pressures were converted to a radius and then back to a pressure using the Laplace equation applied on circular capillaries using the surface tension of mercury and then back with the surface tension of water. The values of surface tension and contact angle used are shown in Table 1.

3. Results

3.1. Porosimetry

To verify the use of Eq. (6), porosimetry measurements were carried out. This allowed the fitting of model pressure curves (Eq. (7)) to porosimetry data to determine the pore distribution index and therefore the value of n. Fig. 3 shows the comparison between porosimetry data calculated using the surface tension and contact angle of water. A pressure curve corresponding to an n value of 2.2 is fitted, with good correlation between model and experimental data.

3.2. Initial penetration

Simultaneously recording the side and bottom views of the paper substrate allowed the delay between droplet impact and stain appearance to be measured on all types of paper tested. A high-speed recording of this imaged at 8000 fps is given in supplementary information. This recording shows that the vertical

Table 1
Fluid properties used.

Fluid	Concentration wt%	Density (kg/m^3 × 10^3)	Surface Tension (mN/m)	Viscosity (mPa·s)	Advancing contact angle on cellulose (deg)
Mercury	100%		485 [28]		130 [28]
Water	100%	1.00 [29]	72.31 [30]	0.93 [29]	13.5 [14]
Glycerol	10%	1.02 [25]	71.97 [31]	1.21 [25]	
Glycerol	20%	1.05 [25]	71.4 [31]	1.63 [25]	
Glycerol	40%	1.10 [25]	69.6 [31]	3.40 [25]	
Glycerol	60%	1.15 [25]	68.1 [31]	9.63 [25]	
Ethanol	20%	0.93 [27]	32.27 [27]	2.52 [27]	
Ethanol	40%	0.89 [27]	27.65 [27]	2.49 [27]	
Ethanol	90%	0.80 [27]	23.09 [27]	1.38 [27]	
Decane	100%	0.73 [26]	24.47 [26]	0.85 [26]	

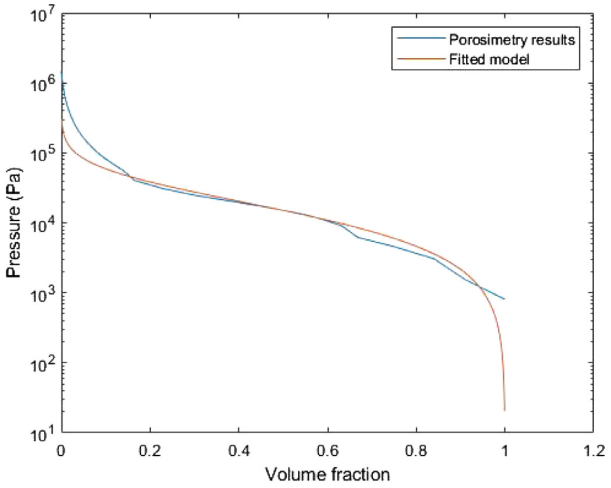

Fig. 3. Comparison of the theoretical model (Eq. (7)) with the mercury porosimetry measurement on Whatman 41 filter paper. Volume fraction is calculated as the volume of fluid in the paper divided by the volume at maximum saturation.

penetration of the droplet into paper occurs so quickly as to be considered instantaneous over the time scale of the stain growth. This finding was consistent for all types of paper tested. This very short time scale of vertical penetration also shows that the vertical variation of fluid will be insignificant in this study. This, combined with ignoring the variation between the paper machine (MD) and cross (CD) directions that is known to cause slightly elliptical stains [32] allows the process to be considered as one dimensional.

3.3. Stain growth

The stain sizes with time for a series of model fluids on Whatman 41 paper are shown in Fig. 4. The stain size data was recorded over different time intervals. The main focus was on the early to mid stages and longer recordings took up significant hard disk space and were minimised. Due to this, the relative length of the curves in Fig. 4 vary and are only indicative of the recording time. The wicking behaviour of droplets of water, ethanol and glycerol solutions on paper was studied. These liquids were selected to provide a variety of viscosity and surface tension conditions for a homologous series of fluids. Droplets of different diameter were deposited on paper and the stain area was recorded as a function of time. Results show that the larger droplets cause larger stain area; however, these area kinetics measurements are not scalable by any simple function of droplet volume. In some cases, droplets of slightly larger volumes created smaller stain sizes or vice versa (Fig. 4d); the droplet volume difference over which this occurs gives an indication of experimental error. Fluids of high surface tension wick faster than fluids of low surface tension. Fluids of high viscosity wick slower than fluids of low viscosity. These trends are consistent with Marmur's equation [12] (Eq. 2) as well as the Lucas-Washburn equation [6].

3.4. Transition point

A two-stage wicking behavior becomes clearly apparent on a log-log scale for all fluids tested. The linear counterparts to the data in Fig. 4 are shown in supplementary information. The transition point between the two stages was identified from the sudden change in the gradient in the log-log curves. The questions to address are therefore whether these two stages have a physical meaning, and what are the mechanisms driving the phenomena.

From the gradient of the log-log curves, the exponent m (Eq. (1)) can be calculated before and after transition. For all aqueous solutions tested on paper, the value of m for each system ranged between 0.26–0.44 for the first stage and between 0.12–0.20 for the second stage. These values are slightly lower than those reported in most previous studies on radial wicking [1,2,10].

Fig. 5 shows the results of the same test with decane. In this case there is no clearly defined transition point, and the stains are much larger than those from similar volumes of aqueous solutions at all times. This size difference is highlighted by the plot utilising the same axis dimensions as those in Fig. 4.

Before stain growth data for different fluids can be compared (Fig. 4), several droplets of similar size but from different fluids must be compared. Unfortunately, due to varying densities and surface tensions of fluids, any needle of a given diameter produced droplets of different size for different fluids. This meant it was not always possible to accurately predict the size of the droplet. Reproducing identically sized droplets proved challenging for the different fluids. To overcome this issue, the data was fitted to a function of volume at every frame to determine the area's dependence on droplet volume at that time. This function could then be interpolated to a desired droplet volume to estimate the stain area at any volume for each frame. By combining these interpolated area values, an estimate of the spreading dynamics could be calculated. The results from interpolation agree with experimental data extremely well and all areas were found to be strongly linear with droplet volume at any given time. This means that the dynamics of stain growth of a droplet of any size can be predicted accurately using the results of two droplet sizes. This linearity was also demonstrated in our previous study [14], where the area to droplet volume relationship at equilibrium was found to be linear.

Using the data in Fig. 4, the area of the stain at the transition can be plotted as a function of droplet volume. This is shown in Fig. 6a. This demonstrates that the stain transition area forms a linear relation with droplet volume and is independent of fluid properties. Aqueous solutions at high concentrations of ethanol and glycerol deviate from this trend slightly.

Fig. 6b illustrates the timing of the stain transition point relative to the timing of droplet disappearance above the surface of the paper for water, 40% ethanol and 60% glycerol solutions. The same figure with data from all water solutions is in supplementary information. Fig. 6b also shows that linear fits are reasonable for both stain size transition and droplet disappearance. Using these linear fits for all fluids, the timing of stain size transition and droplet disappearance of a 10 μL droplet is interpolated and compared in Fig. 6c. It shows that the timing of the two phenomena is related; as one gets longer, the timing of the other generally follows proportionally. The figure also shows that droplet disappearance always occurs before the stain growth transition.

4. Discussion

4.1. Stain growth

Fig. 7 shows the results of an interpolation for the wetting area produced by a 10 μL droplet of several model fluids on Whatman 41 filter paper for the beginning of the wicking period. There are minor differences in the transient behavior of the stain area kinetics among the various aqueous solution droplets. However, the late stages appear to converge. This late stage convergence was discussed in our previous study [14] where the equilibrium stain size was analysed for a series of fluids. Here, decane produces a much larger stain size than those from the other fluids tested, despite having a similar surface tension to the 90% ethanol solution. The viscosity of decane is slightly lower than that of any other fluids

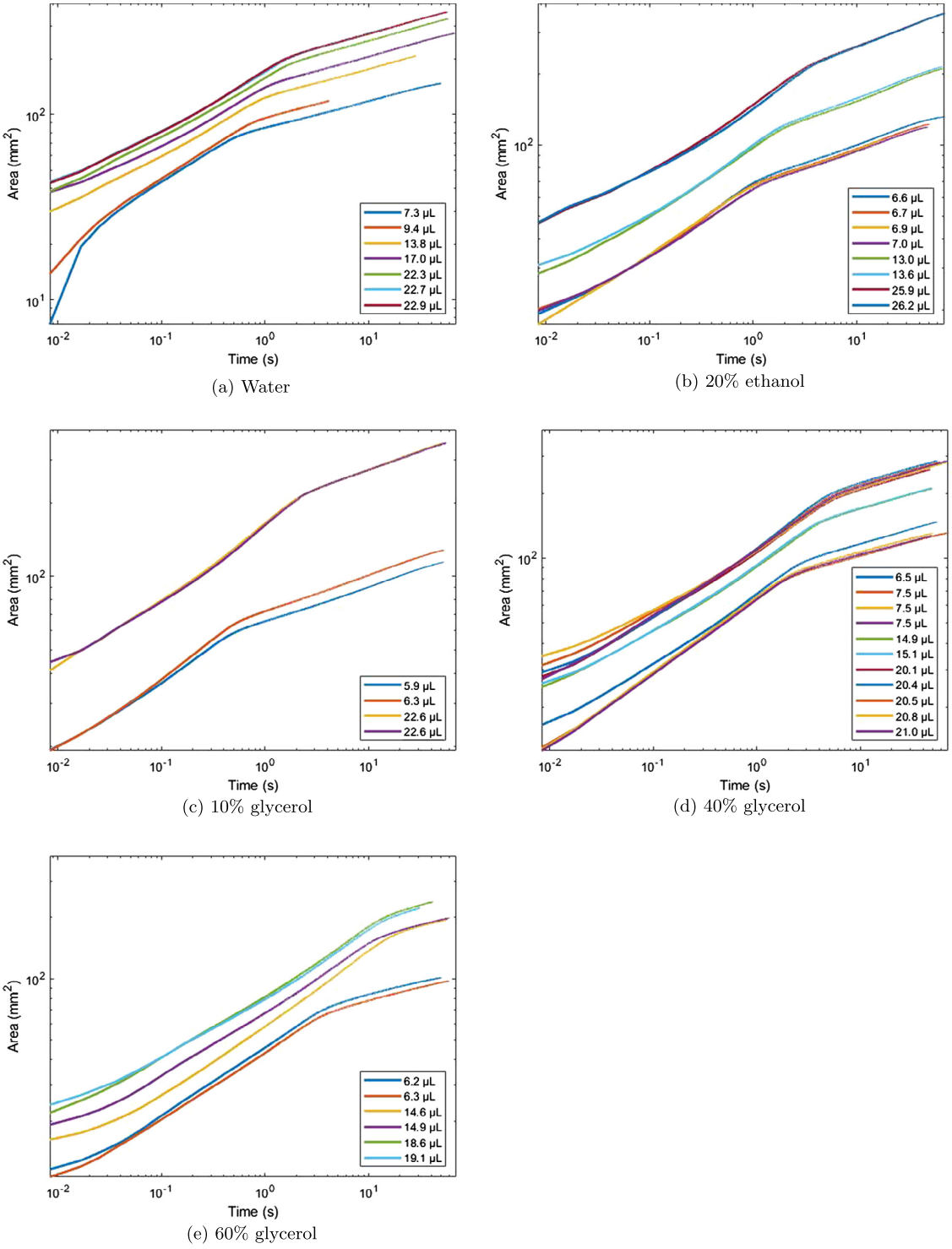

(a) Water (b) 20% ethanol

(c) 10% glycerol (d) 40% glycerol

(e) 60% glycerol

Fig. 4. Evolution of stain size with time for a variety of fluids and droplet sizes on Whatman 41 filter paper.

studied (Table 1). However, based on the relatively low sensitivity to viscosity found with the other measurements, it is unlikely that the slightly lower viscosity of decane is responsible for the huge discrepancy in stain behaviour observed. The high stain size of decane was previously attributed to the purely non-polar behaviour of the fluid, preventing any swelling of the cellulose fibers through relaxation of the intra and inter hydrogen bonding among fibers [3]. Swelling of fibers results in a smaller amount of fluid

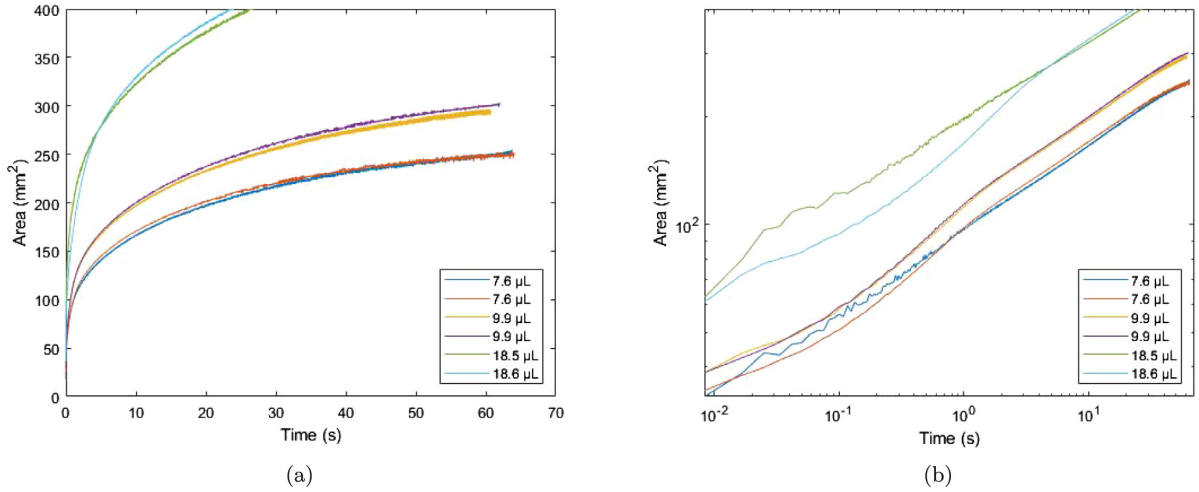

Fig. 5. Stain size with time for decane on filter paper.

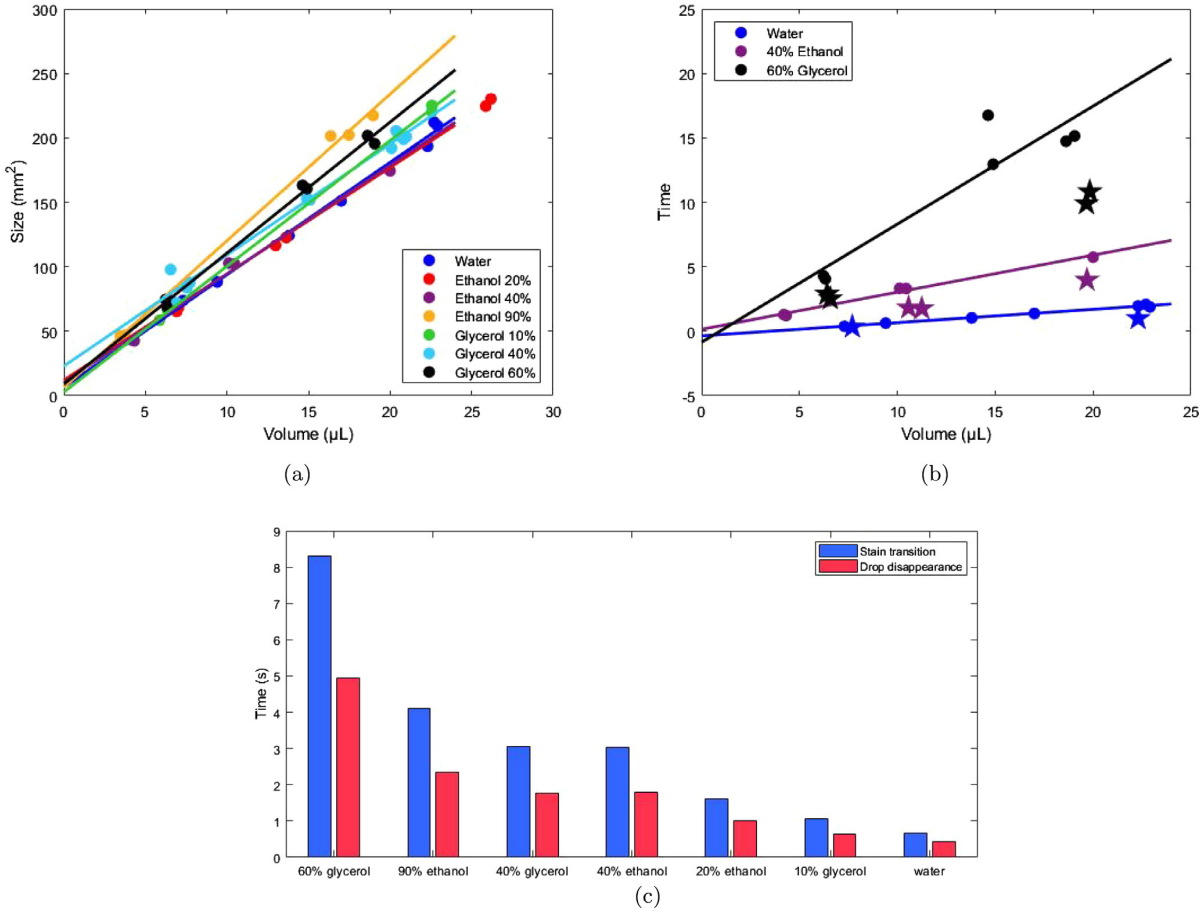

Fig. 6. (a) Area at which stain transition occurs with droplet volume for all model fluids. (b) Time at which the stain wicking transition occurs as a function of droplet volume for 3 representative fluids. Stars represent the time at which each droplet disappears from the surface of paper. (c) Interpolated stain size transition and drop disappearance time data at 10 µL.

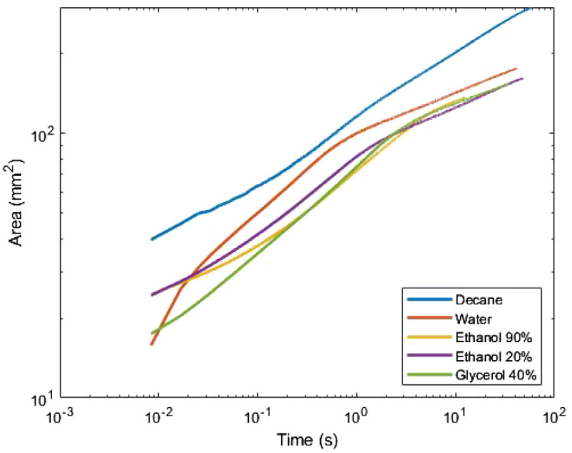

Fig. 7. Interpolated data showing the spreading of 10 μL droplets on a loglog scale.

available, therefore effectively decreasing the liquid volume available to wick out. The swelling fibers will also physically become larger, decreasing pore size [33]. Neither the effect of pore size change or liquid consumption has been thoroughly quantified. Schuchard and Berg [33] studied the effect of swelling fibers on vertical imbibition from an infinite reservoir. They reported the difference between a swelling and a non-swelling fluid could be accounted for by a reduction of the effective capillary radius in the Lucas-Washburn equation [5,6] for normal paper fibers.

4.2. Mechanism of the stage transition

A two-stage wicking regime is clearly seen on the log-log scale of stain size as a function of time (Fig. 4). These regimes are very reproducible and were systematically observed for all fluids except for decane on paper. Several explanations for this two-stage process were investigated. First, as decane is known not to swell cellulose fibers [33] the transition could indicate the time at which the fibers have swollen by an amount that would affect wicking. Tests on filter papers performed with glass fibers (non-swelling) are given in supplementary information and also revealed a two-stage process, very similar to that observed on cellulosic fibers. This observation reveals that swelling is unlikely to be responsible. A second possible explanation is the absorption of the droplet into the paper. This process is likely to affect results as its timing correlates with the stain transition (Fig. 6b). However, as this absorption also occurs with decane droplets, it is unlikely to be a dominant mechanism. Third, the transition could represent a transition from wicking through a fully saturated to a partially saturated substrate. This is likely to affect results; however, as there is little previous work on the subject, the dominance of this mechanism is unknown and needs to be further probed. This was achieved here by modelling.

The transition from a fully saturated to a semi saturated mechanism also explains the delay seen between stain transition and droplet disappearance shown in Fig. 6b. It is reasonable to assume that the propagation of the effect of the droplet disappearance (lowering of the local volume fraction), requires a finite period of time to reach the outside of the stain. Also, the decreased volatility of decane, compared to aqueous solutions, is unlikely to be responsible for the change in transition phenomena as it would result in a smaller amount of evaporation occurring. Our previous study demonstrated [14] that even with the more volatile fluids, no significant evaporation occurs over the time scale studied. Therefore, lowering the evaporation further is expected to have no effect.

4.3. Simulation results

The model developed predicts the wicking behavior of sessile droplets onto a porous surface. It requires 7 input parameters to calculate stain size as a function of time: droplet volume (V_D), viscosity (μ), paper thickness (h), scaled diffusivity at saturation (D_0), pore distribution index (λ), initial wet area (A_0) and saturation volume fraction (ϵ_s). Each of these variables has a clear physical meaning and most can be identified experimentally [16]. Although the choice for droplet volume, paper thickness and viscosity is trivial, the selection of the remaining variables is more difficult. For the given case, a value for n and therefore λ was extrapolated from porosimetry measurement in Fig. 3, and a value for A_0 was found by scaling the stage one data with Marmur's equation (Eq. (2)). The value of A_0 that results in a linear relation with time is chosen as the A_0 for that situation. An estimation for ϵ_s can be found by measuring the difference between the dry weight and the wet weight of a paper sample. This was reported for Whatman 41 filter paper previously [14] and the volume fraction of water in wet paper can be calculated to be 0.62. The testing standard used (TAPPI 441) for wet weight characterisation includes a rolling step between blotting papers that is designed to remove excess water. However, this rolling method might also remove some excess water that will otherwise remain in a droplet wicking case. For these reasons, the actual saturated value is likely to be slightly higher than measured. A value of $\epsilon_s = 0.7$ best fits our results. The results of a simulation with these calculated parameters and fitting just the D_0 value is shown in Fig. 8. Parameter used in this simulation are shown in Table 2. Viscosity of water is taken from literature [29].

Although modelling well represents experiments in the first stage, poor agreement is observed for the second stage. It is clear that the 7 parameters chosen do not fit the second stage. This is not surprising, as only infusion porosimetry data was used to calculate n. Hysteresis in porosimetry experiments is well documented [34] and its relevance to wicking reported [35]. As the liquid redistribution (second) phase is dominated by the emptying of pores, it is not surprising that a single value of n cannot capture both the first and second stages. Fig. 9 shows the results of a simulation with a value of n that changes for the second stage. This value was found by fitting the stain area data. This value could not be externally calculated because it is an effective n for the specific combination of infiltration and redistribution occurring in the second stage which is rather complex. Both experimental

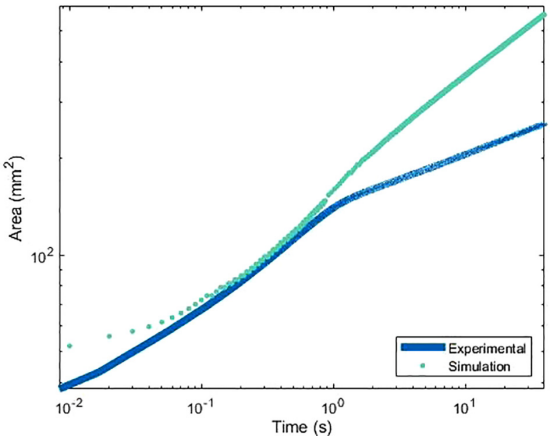

Fig. 8. Comparison of experimental versus calculated values of area as a function of time on a log-log scale.

Table 2
Parameters used for Fig. 8.

Parameter	Value
V_D	17 μL
μ	0.93 mPa·s
h	226 μm
D_0	12.09 nPa·m^2
A_0	43.01 mm^2
ϵ_s	0.7
n	2.2

Table 3
Parameters used for Fig. 9.

Parameter	Water Case	40% Glycerol Case
V_D	17 μl	17 μL
μ	0.93 mPa·s	3.40 mPa·s
h	226 μm	226 μm
D_0	12.09 nPa·m^2	12.09 nPa·m^2
A_0	43.01 mm^2	43.01 mm^2
ϵ_s	0.7	0.7
n stage 1	2.2	2.2
n stage 2	5	4

and simulation results are also shown for a 17 μL droplet of water and 40% glycerol solution in Fig. 9. The only difference between these two simulations is a change in the viscosity parameter and a refitted second stage n value. Parameters used are given in Table 3. The viscosity of a 40% glycerol solution was interpolated from results of Sheely [25]. The fitted value for second stage n was different between the two fluids, with each requiring a different fitted n value for the second stage. The fitted value for n during the second stage is 5 and 4 for water and glycerol respectively. The experimental results for glycerol are interpolated from data in Fig. 4d as a droplet of exactly 17 μL droplet was not tested. The water case is very well described by the model except for a slight deviation at later times. This is most likely because evaporation and swelling become more dominant in the later stages and are not included in this model. The glycerol simulation predicts behavior very well in the first stage; however, it deviates more than water in the second. This implies that higher viscosities slightly invalidate the assumption that the redistribution of fluid can be represented by a simple constant exponent n. Although the broad behavior is still represented. Simulations of different droplet sizes with appropriate changes to V_D and A_0 and keeping all else constant also fit experimental data. However, small droplets (<10 μL) are not well described by the model. This is likely because the small reservoir results in a larger fraction of the stain having never achieved full saturation. This would make redistribution more dominant through the whole process, and would mean that both the calculated n value for the first stage and the fitted value of n for larger droplets for the second stage may not be an appropriate choice. The constant size of the fully saturated boundary condition in the first stage would also be less appropriate for a small droplet [24].

The abrupt transition from stage one to stage two and the flat region immediately after is caused by the sudden shift in n at the stage transition of the simulation. In reality, both the transition from saturated to a no flux boundary condition and the change in n value happens gradually as the droplet is consumed and the dominant spreading mechanism changes from infiltration to redistribution. This is a simplification and a more complete model would account for this gradual shift. Not enough is known about porosimetry hysteresis and how it is affected by local volume fraction history to account for this effect. However, the broad effects are well described by the simplification introduced here. It is also relevant that the simulation results for the no hysteresis case (Fig. 8) look very similar to results with decane in that no significant transition is observable. The simulation can be made to fit decane results with a single value of n, however this requires new fitted values for A_0, D_0 and n. This may be because the wetting characteristics of decane on cellulose are such that the diffusivity experiences no significant hysteresis, and this affects the calculated parameters.

Although surface tension and contact angle of the fluid are used in calculating n from porosimetry data, these are also likely to effect A_0 and D_0; these were not included as input parameters in the model. Both of these quantities for water and glycerol are very similar [31], which explains why the model still fits experimental data between these two fluids.

The results of these simulations show that there are two dominant driving mechanisms behind the two-stage transition. First, the change from saturated to non-saturated boundary conditions at the center of the stain. Second, a change in how pressure and permeability vary as functions of volume fraction between systems that are dominated by pore filling and pore emptying.

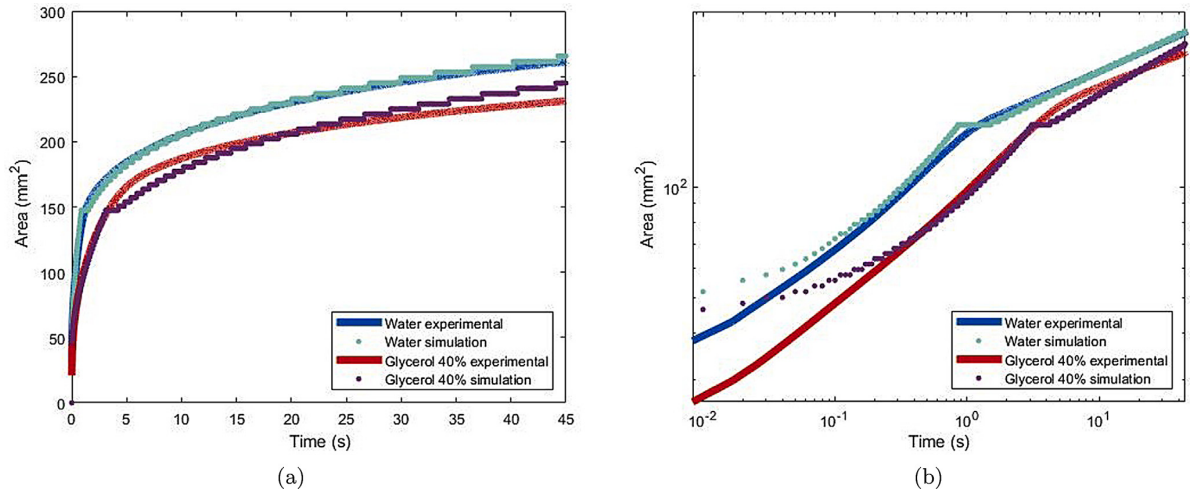

Fig. 9. Simulation and experimental results for water and 40% glycerol solution on a linear and log-log scale.

5. Conclusion

The evolution in time of the stain area produced by a sessile droplet deposited on paper was measured, modelled and analysed. A series of fluids varying in surface tension and viscosity was examined. A new model to describe the data has been developed based on Richards' equation [21] and is easily resolved numerically in one dimension using experimentally measured boundary conditions and input parameters. This expands on previous work [10–12,15,18] where imbibition into linear and radial systems from an infinite reservoir has been investigated and modeled.

Radial wicking kinetics with all tested liquids besides decane showed two-stages, with a fast initial growth regime followed by a slower regime. The first regime corresponds to the liquid absorbing into the paper by wicking, while the second represents liquid redistribution [2]. This work identifies the cause of the transition between the two regimes to be the disappearance of the droplet coupled with the shift in mechanism due to the redistribution occurring in the second phase. This modeling technique also describes well the experimental results for both regimes. Further, the 7 parameters of the model have all a physical meaning and can be either measured experimentally or calculated.

This research contributes to the fundamental understanding of the wicking mechanism. The proposed modeling technique allows the quantification and prediction of stain dynamics in a variety of industrially relevant situations that were previously deemed too complex. The wicking of a finite reservoir is a common process in the printing, textile, agriculture and medical industries, and the development of a method of prediction will assist in the design and optimisation of new technologies. This study also provides a rigorous and physically meaningful alternative to the semi-empirical Lucas-Washburn equation to describe the wicking kinetics of droplets in real porous media.

Acknowledgments

This research was funded by an ARC Linkage grant (LP160100544) and Haemokinesis.

Appendix A. Supplementary material

Supplementary data associated with this article can be found, in the online version, at https://doi.org/10.1016/j.jcis.2019.01.032.

References

[1] E. Kissa, Capillary sorption in fibrous assemblies, J. Colloid Interface Sci. 83 (1) (1981) 265–272.
[2] D. Danino, A. Marmur, Radial capillary penetration into paper: limited and unlimited liquid reservoirs, J. Colloid Interface Sci. 166 (1) (1994) 245–250.
[3] T. Kawase, S. Sekoguchi, T. Fujii, M. Minagawa, Capillary spreading of liquids, Text. Res. J. 56 (7) (1986) 409–414.
[4] K. Borhan, A. Rungta, An experimental study of the radial penetration of liquids in thin porous substrates, J. Colloid Interface Sci. (1993) 403–411.
[5] V.R. Lucas, Ueber das zitgesetz des kapillaren aufstiegs von flüssigkeiten, Kolloid-Zeitschrift 23 (1) (1918) 15–22.
[6] E.W. Washburn, The dynamics of capillary flow, Phys. Rev. 17 (3) (1921) 273–283.
[7] K. Li, D. Zhang, H. Bian, C. Meng, Y. Yang, Criteria for applying the lucas-washburn law, Sci. Rep. 5 (2015) 1–7.
[8] M.M. Gong, D. Sinton, Turning the page: Advancing paper-based microfluidics for broad diagnostic application, Chem. Rev. 117 (12) (2017) 8447–8480.
[9] E. Elizalde, R. Urteaga, C.L.A. Berli, Rational design of capillary-driven flows for paper-based microfluidics, Lab Chip 15 (10) (2015) 2173–2180.
[10] T. Gillespie, The spreading of low vapor pressure liquids in paper, J. Colloid Sci. 13 (1) (1958) 32–50.
[11] A. Borhan, K.K. Rungta, On the radial spreading of liquids in thin porous substrates, J. Colloid Interface Sci. 154 (1) (1992) 295–297.
[12] A. Marmur, The radial capillary, J. Colloid Interface Sci. 124 (1) (1988) 250–256.
[13] A. Marmur, Penetration and displacement in capillary systems of limited size, Adv. Colloid Interface Sci. 39 (C) (1992) 13–33.
[14] M.J. Hertaeg, R.F. Tabor, G. Garnier, Effect of protein adsorption on the radial wicking of blood droplets in paper, J. Colloid Interface Sci. 528 (2018) 116–123.
[15] A. Perez-Cruz, I. Stiharu, A. Dominguez-Gonzalez, Two-dimensional model of imbibition into paper-based networks using Richards' equation, Microfluid. Nanofluid. 21 (5) (2017) 1–12.
[16] D. Rath, N. Sathishkumar, B.J. Toley, Experimental measurement of parameters governing flow rates and partial saturation in paper-based microfluidic devices, Langmuir 34 (30) (2018) 8758–8766.
[17] S. Jaganathan, H.V. Tafreshi, B. Pourdeyhimi, A realistic modeling of fluid infiltration in thin fibrous sheets, J. Appl. Phys. 105 (11) (2009), https://doi.org/10.1063/1.3141737.
[18] A. Ashari, T.M. Bucher, H.V. Tafreshi, M.A. Tahir, M.S. Rahman, Modeling fluid spread in thin fibrous sheets: Effects of fiber orientation, Int. J. Heat Mass Transf. 53 (9-10) (2010) 1750–1758.
[19] S.C. Chapra, R.P. Canale, Numerical Methods For Engineers, Mcgraw-Hill, New York, 1998.
[20] W.L. Then, M. Li, H. McLiesh, W. Shen, G. Garnier, The detection of blood group phenotypes using paper diagnostics, Vox Sang. 108 (2) (2015) 186–196.
[21] L.A. Richards, Capillary conduction of liquids through porous mediums, J. Appl. Phys. 1 (5) (1931) 318–333.
[22] H. Huinink, Fluids in Porous Media, Morgan & Claypool Publishers, 2016.
[23] D.J.E. Harvie, An implicit finite volume method for arbitrary transport equations, ANZIAM J. 52 (0) (2012) 1126–1145.
[24] V.M. Starov, S.A. Zhdanov, S.R. Kosvintsev, V.D. Sobolev, M.G. Velardec, Spreading of liquid drops over porous substrates, Adv. Colloid Interface Sci. 104 (2003) 123–158.
[25] M.L. Sheely, Glycerol viscosity tables, Ind. Eng. Chem. 24 (9) (2013) 1060–1064.
[26] Y. Liu, R. Difoggio, K. Sanderlin, L. Perez, J. Zhao, SMeasurement of density and viscosity of dodecane and decane with a piezoelectric tuning fork over 298-448 K and 0.1-137.9 MPa, Sens. Actuators, A 167 (2) (2011) 347–353.
[27] I.S. Khattab, F. Bandarkar, M.A.A. Fakhree, A. Jouyban, Density, viscosity, and surface tension of water+ ethanol mixtures from 293 to 323 K, Korean J. Chem. Eng. 29 (6) (2012) 812–817.
[28] H. Giesche, Mercury porosimetry: A general (practical) overview, Part. Part. Syst. Char. 23 (1) (2006) 9–19.
[29] J. Kestin, M. Sokolov, W.A. Wakeham, Viscosity of liquid water in the range- 8 C to 150 C, J. Phys. Chem. Ref. Data 7 (3) (1978) 941–948.
[30] G. Vazquez, E. Alvarez, J.M. Navaza, Surface tension of alcohol water+ water from 20 to 50. degree. C, J. Chem. Eng. Data 40 (3) (1995) 611–614.
[31] K. Takamura, H. Fischer, N.R. Morrow, Physical properties of aqueous glycerol solutions, J. Petrol. Sci. Eng. 98 (2012) 50–60.
[32] N. Walji, B.D. MacDonald, Influence of geometry and surrounding conditions on fluid flow in paper based devices, Micromachines 7 (5) (2016) 73.
[33] D.R. Schuchard, J.C. Berg, Liquid transport in composite cellulose-superabsorbent fiber networks, Wood Fiber Sci. 23 (3) (2007) 342–357.
[34] J. Kloubek, Hysteresis in porosimetry, Powder Technol. 29 (1) (1981) 63–73.
[35] M. Landeryou, I. Eames, A. Cottenden, Infiltration into inclined fibrous sheets, J. Fluid Mech. 529 (2005) 173–193.

LANGMUIR

pubs.acs.org/Langmuir Article

Radial Wicking of Biological Fluids in Paper

Michael J. Hertaeg, Rico F. Tabor, Joseph D. Berry, and Gil Garnier*

Cite This: *Langmuir* 2020, 36, 8209–8217 Read Online

ACCESS | Metrics & More | Article Recommendations | Supporting Information

ABSTRACT: In this study, we analyze stain growth kinetics from droplets of biological fluids such as blood, plasma, and protein solutions on paper both experimentally and numerically. The primary difference of biological fluids from a simple fluid is a significant wetting/dewetting hysteresis in paper. This becomes important in later stages of droplet wicking, after the droplet has been completely absorbed into paper. This is shown by anomalous power dependence of area with time in the later stages of radial wicking. At early stages, current numerical wicking models can predict stain growth of biological fluids. However, at later stages, the introduction of hysteresis complicates modeling significantly. We show that the cause of the observed hysteresis is due to contact angle effects and that this is the dominant mechanism that leads to the anomalous stain growth kinetics measured uniquely in biological fluids. Results presented will streamline the design process of paper-based diagnostics, allowing a modeling approach instead of a trial and error method.

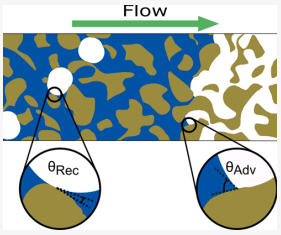

INTRODUCTION

Paper-based diagnostics are integral in an industry-wide shift toward low-cost, point-of-care medical devices. Paper is a flexible platform for these devices because of its low cost and capacity to easily induce passive flows through wicking phenomena caused by capillary forces. Current devices on the market are typically reliant on a trial and error design process because not enough is known about wicking phenomena in paper. While wicking of simple fluids has been well studied as it is integral to many industrial applications including, textiles, printing, agricultural, and medicine,[1−6] wicking of complex fluids has not been studied in depth. This is required for the design of paper-based diagnostics as it will allow the efficient optimization of parameters such as paper properties and geometry. Also, as paper-based devices often involve reactions inside a wicking fluid, a thorough understanding of wicking phenomena is required before any sophisticated reaction optimization can take place. There are critical and distinct differences in the behavior of simple fluids when compared to complex biological fluids and suspensions. Also, the mechanism behind stain growth transition in droplet wicking remains unknown as it has been poorly studied. This lack of understanding is particularly acute for human blood on paper. Much of the literature on the topic is in the field of forensics and is focused on applications rather than fundamental understanding.[7−9]

Biological fluids have many different components that cause complexities. The cell component of blood introduces rheological changes such as a shear-thinning viscosity and granularity caused by the presence of highly deformable red blood cells (RBCs).[10] Also, the significant protein content and lipid component of blood plasma will adsorb onto both solid−liquid and liquid−vapor interfaces, affecting the contact angle, surface tension, and viscosity of the system nonuniformly.[11,12] The most abundant protein in blood is albumin[13] and has been shown to significantly impact wicking in paper.[11]

Wicking is caused by a negative pressure produced by the curved meniscus at the air−liquid interface between pores. The pressure developed in a pore can be approximated with the Young−Laplace equation applied for a capillary with a circular cross section and setting the atmospheric pressure to zero (eq 1)

$$P = -\frac{2\gamma \cos\theta}{R} \tag{1}$$

where P is the pressure on the liquid side of the meniscus, γ is the liquid−vapor surface tension, R is the radius of the capillary, and θ is the contact angle. This negative pressure causes Poiseuille flow toward the meniscus, drawing further fluid into the capillary and moving the interface. In a complex porous material like paper, the pore radius changes depending on position. Therefore, the capillary pressure is not constant and depends on the pore radius. The contact angle at the meniscus is also a critical parameter affecting the driving force.

The radial wicking of a droplet on paper is an example of a complex wicking scenario, and several studies have analyzed stain growth as a function of time.[14−17] In this situation, stain growth continues well after the droplet has absorbed into the paper and disappeared from the surface. The absorption of the drop a finite time after deposition causes a decrease in the spreading rate, which can be clearly identified from the stain

Received: May 5, 2020
Revised: June 18, 2020
Published: June 23, 2020

https://dx.doi.org/10.1021/acs.langmuir.0c01318
Langmuir 2020, 36, 8209–8217

growth kinetics plotted on a log–log scale. The two stages observed are referred to as stage one, where the drop is still present above the paper, and stage two, where the drop has been completely consumed. Before the transition, spreading is driven only by the infiltration of pores near the edge of the stain. After the transition, the reservoir of fluid is consumed and any further stain growth is caused by the redistribution of fluid from the large pores in the center to the unfilled small pores at the edge of the stain. This causes voids to form in the central region, creating receding air interfaces and therefore negative capillary pressures to form within large pores at the center of the stain. This effect causes impedance to further stain growth. At first, the small radius of the filling pores near the edge of the stain dominates and stain growth continues.[18] This becomes less dominant at later times as the meniscus in the center region moves into incrementally smaller pores. Stain growth transition was shown to depend on a hysteresis effect presenting as a difference between infiltration and emptying porous networks.[19] Our previous numerical study showed that including hysteresis is essential to produce clear second-stage transitions and that an increase of hysteresis severity results in a more drastic stage transition.[20] This reveals that the stain growth transition is not caused directly by the consumption of the droplet reservoir. Instead, the stage transition occurs because of a pore hysteresis that only becomes relevant once the droplet is consumed; this is because until this point there are no emptying pores. The cause of this hysteresis is poorly understood and is likely to be material dependent. However, the most likely causes are entrapment due to decreased pore interconnectivity, contact angle hysteresis, and fiber swelling.

It is the objective of this study to elucidate the cause of wetting/dewetting hysteresis in paper and the effect that biological components have on the radial wicking process (Figure 1). This is achieved through experimental analysis of

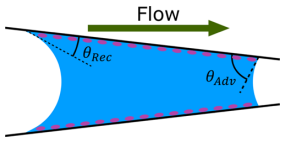

Figure 1. Advancing and receding contact angle in a model capillary with adsorbed biomolecules.

stain growth of biological fluids, contact angle experiments, full-morphology numerical analysis,[21] and continuum-scale modeling using the Richards equation.[22] This work enables the prediction of the wicking behavior of biological fluids for the efficient development of paper diagnostics.

EXPERIMENTAL SECTION

Materials. Cellulose films for contact angle experiments were prepared in the same way as several previous studies.[11,23,24] Here, a 0.5 wt % solution of cellulose acetate (Sigma-Aldrich) in acetone (analytical reagent, Thermo Fisher Scientific) was spin-coated onto glass and then soaked in a 0.5 wt % solution of sodium methoxide (Sigma-Aldrich) in methanol (Analytical reagent, Thermo Fisher Scientific). Whatman 41 filter paper was used for wicking tests, and the blood used was collected with consent by the Red Cross Blood Service Australia following strict ethics requirements. Blood was mixed with ethylenediaminetetraacetic acid (EDTA) as an anticoagulant at collection to prevent coagulation.

Methods. *Experimental Process.* Stain growth data were gathered by monitoring the stain size as a function of time after droplet deposition with the same setup as in our previous study.[20] The bottom view of the paper is captured using a Point Grey Flea3 camera directed onto a 45° mirror positioned underneath the paper. Examples of captured images are shown in Figure 2. Images were

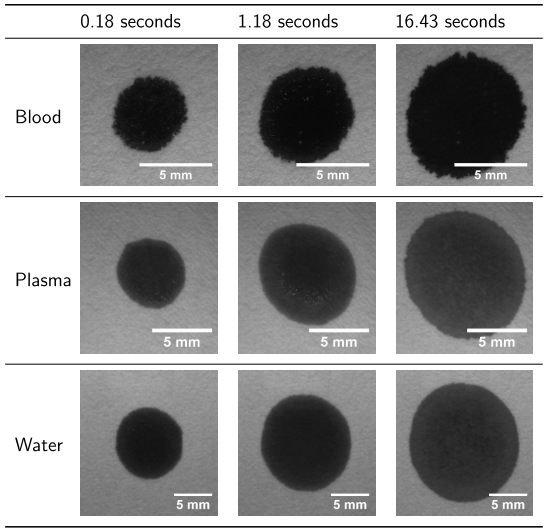

Figure 2. Progression of stains from similar volumes of blood, plasma, and water after droplet deposition on the same paper. Note the different sized scale bars for the different fluids. Droplet volumes: blood 12.9 μL, plasma 13.5 μL, and water 13.8 μL.

taken at a rate of 120 frames/s and analyzed in ImageJ to give area as a function of time. Droplets were created by pumping at a constant flow rate through a needle; this caused droplets of constant size to fall periodically. The size of the droplet was calculated from weight measured using a Mettler Toledo TLE balance before the needle was positioned above the paper. The average weight of the previous four droplets was divided by the fluid's density to estimate the volume of the droplet. The size of the droplet was altered using needles of varying outer diameters. Needles were made by hand by drawing out heated glass capillary tubes. Protein adsorption onto the needle resulted in varying drop volumes. To overcome this, the needles were submersed in the test fluid for 30 min prior to create a saturated layer of adsorbed biomolecules.

Contact angles were measured with an OCA35 Dataphysics contact angle instrument. For advancing and receding measurements, a pump rate of 20 μL/s was used. The presented values are the mean of at least six measurements, and the same batch of cellulose films was used to decrease variability. The static contact angles of blood, plasma, and water on silicon wafers were also measured. Advancing contact angles of water and plasma on cellulose have been previously reported.[11] These were measured and are presented again as a comparison with these new receding measurements with blood components. All wicking and contact angle tests were performed at 23 °C and 50% relative humidity.

The internal structure of the paper used was imaged with a Zeiss Xradia 520 Versa high-resolution X-ray computed tomography scanner. The size of the scan was 150 μm × 150 μm × 205 μm with a resolution of 0.46 μm (voxel volume = 0.46 μm × 0.46 μm × 0.46 μm). The images were binarized in ImageJ using ANKAphase plugin.[25] This plugin implements a phase-contrast algorithm,[26] which was required due to the low absorption of X-rays by cellulose. For analysis, the imaged section is required to be representative of the bulk. For this to be true, the size of the image must be larger than the length scale of heterogeneities in the material. This was confirmed by cropping the image to different sizes and calculating the average

https://dx.doi.org/10.1021/acs.langmuir.0c01318
Langmuir 2020, 36, 8209–8217

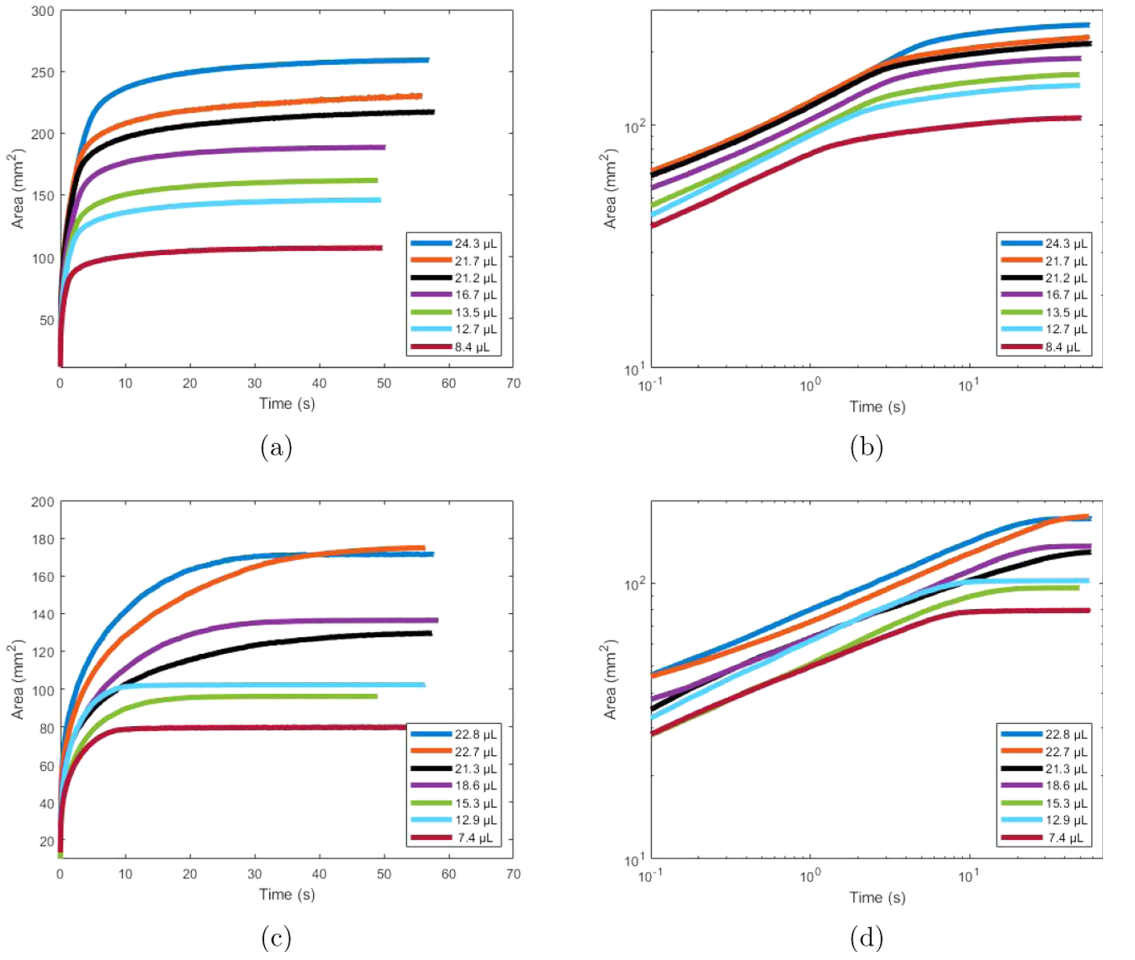

Figure 3. Evolution of stain growth with time for droplets of varying volumes. (a) Plasma linear scale, (b) plasma log scale, (c) blood linear scale, and (d) blood log scale.

volume fraction of the fibers in the new image. As the image size was increased, the average volume fraction plateaued to a constant, indicating that the taken image was large enough to be representative of the bulk properties of the paper.

Numerical Methods. The model selected adopts a similar approach to that of several previous studies.[20,27−29] The Richards equation eq 2 is used to relate volume fraction time and pressure.

$$\frac{\partial \phi}{\partial t} = \nabla \cdot \left(\frac{K(\phi)}{\mu} \nabla P \right) \tag{2}$$

where ϕ is the volume fraction divided by the maximum saturation in the material (ϵ_s), K is the permeability, μ is viscosity, P is pressure, and t is time. In most wicking systems, pressure is a function of only the volume fraction. Due to this, the simpler eq 3 can be used.

$$\frac{\partial \phi}{\partial t} = \nabla \cdot \left(\frac{D(\phi)}{\mu} \nabla \phi \right) \tag{3}$$

where $D(\phi)$ is given by

$$D(\phi) = K(\phi) \frac{\partial P(\phi)}{\partial \phi} \tag{4}$$

$$K(\phi) = K_0 \phi^{(3\lambda+2)/\lambda} \tag{5}$$

$$\frac{\partial P(\phi)}{\partial \phi} = \frac{\gamma \cos \theta P_m}{\lambda} \phi^{(-1-\lambda)/\lambda} \tag{6}$$

Expressions for $K(\phi)$ and $\frac{\partial P(\phi)}{\partial \phi}$ (eqs 5 and 6) can be derived using the Brooks−Coorey model.[30] Equation 6 has been altered to include a linear relationship with surface tension and the cosine of the contact angle. This relationship is predicted from eq 1. These expressions are substituted into eq 4 to give eqs 7 and 8.

λ is the pore distribution index derived from mercury porosimetry or full morphology. In the typical expression derived from the Brooks−Coorey analysis, the product $\frac{\gamma \cos \theta P_m}{\lambda}$ is represented as a single constant, usually defined as the capillary pressure at maximum saturation. This is sometimes set to atmospheric pressure and sometimes left as an empirical constant depending on best fit to data. Here, contributions from surface tension and contact angle on this constant are separated from the contribution from material choice P_m and λ. The effect of P_m is indistinguishable from K_0 in eq 8, so the estimation of this value is not possible. However, both of these constants should be properties of the paper and therefore constant between fluids. Therefore, the product $K_0 P_m$ can be calculated from

https://dx.doi.org/10.1021/acs.langmuir.0c01318
Langmuir 2020, 36, 8209−8217

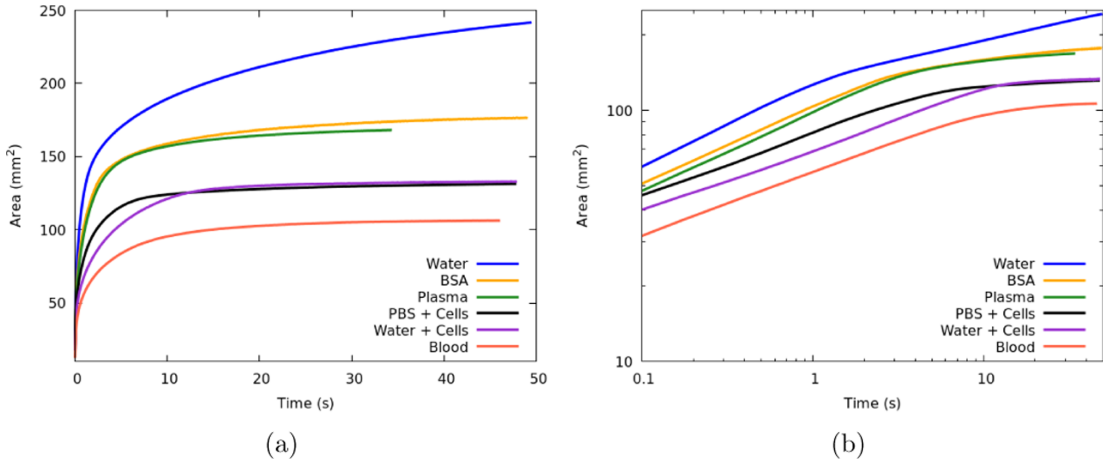

Figure 4. Stain growth of several biofluids interpolated to 15 μL.

experimental data using a single fluid and then used for all fluids on that same paper.

$$D(\phi) = D_0 \phi^{(2\lambda+1)/\lambda} \tag{7}$$

$$D_0 = \frac{K_0 P_m \gamma \cos\theta}{\lambda} \tag{8}$$

Once all substitutions have been made, eq 3 is solved using an implicit finite volume method using the open source PDE solver arb[31] over a two-dimensional axisymmetric domain. The same uniform structured mesh and temporal resolution were used as validated in our previous study.[20] $\delta r = 0.02 r_c$ and $\delta t = 0.01$ s, where r_c is the droplet radius. No flux boundary conditions are used on all external faces except for a small region where the droplet is in contact with the paper. Here, a saturated boundary condition is used. The simulation is stopped when the total volume of fluid inside the domain equals the specified volume of the initial droplet. This introduces three additional parameters: the thickness of the paper h, the volume of the droplet V, and the radius of the contact patch r_c. The radius of contact can be estimated using the following equation

$$r_c^3 \approx \frac{3V}{\pi}\left[\frac{\sin^3\theta}{2 - 3\cos\theta + \cos^3\theta}\right] \tag{9}$$

This equation is derived assuming spherical cap geometry on a solid surface. This is not rigorously exact on paper because some of the liquid is absorbed and the instantaneous contact angle over paper will be different from that calculated on other cellulose surfaces due to porosity and roughness. The simplifications introduced in the model mean that the real contact area differs slightly from the effective contact area used in simulations. This is likely caused by ignoring the effects of inertia and dynamic contact angle. Both of these effects have been shown to influence some wicking systems particularly at early times when velocities are high.[32−34] Despite this, eq 9 provides a robust approximation.

Fiber interconnectivity is analyzed with a full-morphology processing step. This is a quasi-static simulation technique to predict the pressure variation in a porous material at various levels of infiltration. It was first developed by Hazlett[21] and has since been used widely to analyze a variety of porous materials, including paper.[28,35] The method uses a three-dimensional (3D) geometry and relies on fitting spheres of constant diameter inside the void space in the geometry. These spheres are allowed to intersect each other but not with the fibers. As the Laplace equation (eq 1) can be used to relate the radius of these spheres to a pressure, the level of infiltration can be calculated as the original nonfiber volume in the paper minus the volume occupied by the overlapping spheres. This is achieved by labeling all voxels occupied by spheres and then adding the volume of all labeled voxels. In this way, the overlap between spheres can be overcome and the true volume of the nonwetting phase calculated accurately. Varying the size of the spheres allows the level of infiltration corresponding to each capillary pressure to be calculated.

Most previous studies have used a commercial implementation of the full-morphology algorithm called GeoDict by Math2Market. For this study, a custom full-morphology implementation was developed and written with Matlab. The code used can be found at https://github.com/MHertaeg/Full-Morphology.git.

RESULTS

Figure 2 demonstrates the stain progression at different times after droplet deposition on the same paper for similar volumes of blood, plasma, and water. Achieving identically sized droplets of different fluids was not possible because fluid surface tension and viscosity affect the volume of droplets generated with a needle. Even from the very early stages of stain growth, blood has a very small stain size followed by plasma and then water. Differences in stain size are highlighted by the change in scale bar length between fluids. There is also a difference between the roughness of the stain boundary of different fluids, clearly forming different fractal dimensions. The highest roughness is seen in blood followed by plasma and water. All stains are slightly elliptical, with the major axis aligned with the paper's machine direction, indicating the expected slight fiber alignment in that direction.

Figure 3 shows the growth of stain area with time from droplets of plasma and blood wicking on filter paper. The log-scale plots are presented, as the gradient of these indicates the power dependence of area with time. These log-scale plots clearly display two typically delineated linear regions.[20] These two regions identify the first and second stages of radial wicking. Although similar in form, blood wicks more slowly than plasma; this is shown by the different vertical scale used to plot the two fluids. It can also be seen that the stage transition occurs much later in blood than in plasma. Discrepancies in blood wicking show that variability is higher between donors with whole blood compared to plasma. This is due to differences in red blood cells between individuals.[36,37] Figure S1 in the Supporting Information shows the variability caused by different donors.

https://dx.doi.org/10.1021/acs.langmuir.0c01318
Langmuir 2020, 36, 8209−8217

Table I. Experimental Contact Angles and Stain Area Powers of Biofluids

fluid	advancing θ_{adv}	receding θ_{rec}	hysteresis $\cos(\theta_{rec}) - \cos(\theta_{adv})$	first-stage power	second-stage power
water	15	5	0.03	0.33 ± 0.11	0.15 ± 0.04
plasma	28	12	0.09	0.32 ± 0.02	0.06 ± 0.01
blood	46	3	0.30	0.24 ± 0.04	≈0

Stain growth tests were also performed with bovine serum albumin (BSA) solution, red cells suspended in phosphate-buffered saline (PBS), and water. This was undertaken to identify the effect cells and protein have on the wicking process. Cells combined with water were tested as this was anticipated to cause a significant number of cells to lyse (burst) driven by a high osmotic pressure difference between the cell and the bulk solution. Albumin is the most abundant protein in blood[13] and therefore serves as a simplified model of plasma. A BSA concentration of 83 g/L BSA in PBS was chosen as it is close to the protein concentration in plasma and has been shown to mimic the wicking behavior of plasma.[11] All red blood cell solutions were prepared at a concentration of 45% by volume to be similar to blood.[38] Stain growth kinetics from all of these fluids are compared to water[20] in Figure 4. As experimental limitations prevented measuring the stain growth from identically sized drops of different fluids, interpolated data must be used. This interpolation was achieved by finding the stain size at every time point and fitting to a linear function of drop volume. Then, using this function, the stain size at any drop volume could be estimated. By combining interpolated stain area data at each time point, the full stain growth plot of any sized droplet could be determined. Figures S1 and S2 in the Supporting Information show the fit of results to linear functions of drop volume for plasma and blood 30 s after droplet deposition. These can be used to demonstrate the small error introduced by this interpolation.

Figure 4 displays a significant difference between the stain growths of the different blood components and water. Pure water wicks very quickly followed by plasma, red blood cell solutions, and then whole blood. Stains from suspensions of blood cells in water and red blood cells in PBS achieve the same equilibrium size. However, red blood cells in water are slightly slower to reach equilibrium. As expected, the behavior of blood plasma is mimicked with the 83 g/L BSA solution. Comparing the gradient of a log–log plot reveals the power dependence of the relationship with time. This value has been quoted in previous studies[15,16] and is very reproducible between results of the same fluid and substrate. The calculated power values for different fluids are shown in Table I. All first-stage powers are similar, but second-stage powers vary significantly. The second-stage power for blood is effectively zero as the stains come to an abrupt halt after a short transition region.

Table I also shows advancing and receding contact angles of water, plasma, and blood on cellulose films. The biological fluids have significantly higher advancing contact angles when compared to water; however, receding angles do not show this trend. The receding angle for blood is lower than all other tested fluids although its difference from water is not significant, particularly considering the inaccuracies in measuring very low contact angles. Contact angle hysteresis is usually presented as a difference in angles. Here, the differences between cosines of the advancing and receding contact angles are displayed in Table I as this is how the contact angle is included in eq 1. This metric is presented to indicate the severity of contact angle hysteresis for these fluids. Plasma produces 3 times the contact angle hysteresis as that of water on cellulose; for blood, it is 10 times. These results demonstrate that there is a correlation between a severe contact angle hysteresis and a low second-stage power. Contact angle measurements for sessile droplets of water, plasma, and blood on silicon wafers were also performed. In this case, all fluids were found to have a similar contact angle of approximately 61°.

Numerical Results. Results of numerical simulations compared to experimental wicking in the first stage for water, plasma, and blood are shown in Figure 5. Good agreement is found apart from the very early stages and the region right before stage transition. The simulations also predict well the timing of the first to second stage transition as the end of simulation results correlates to the position of the change of gradient in the log–log experimental data. The parameters used for each result are shown in Table II. h is the thickness of the paper, ϵ_s is the saturation volume fraction, λ is the pore distribution index, μ is the dynamic viscosity of the fluids, θ is the contact angle, and r_c is the radius of the contact patch of the droplet.

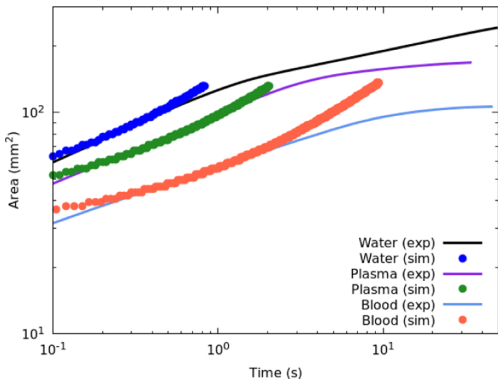

Figure 5. Simulation of the stain area as a function of time on log–log scale results for the first stage of wicking on paper. The parameters of Table II were used with eqs 3, 7, and 8.

Table II. Parameters Used in Figure 5

parameter	water	plasma	blood
V (μL)	15	15	15
μ (mPa·s)	0.93[39]	1.74[11]	4[10]
γ (mN/m)	72.31[40]	60	50
θ (deg)	15	28	46
h (μm)	226[11]	226[11]	226[11]
K_0P_m	8.61×10^{-7}	8.61×10^{-7}	8.61×10^{-7}
r_c (mm)	3.4	3.4	3.1
ϵ_s	0.7[20]	0.7[20]	0.7[20]
λ	5.0[20]	5.0[20]	5.0[20]

https://dx.doi.org/10.1021/acs.langmuir.0c01318
Langmuir 2020, 36, 8209–8217

h, ϵ_s, and λ are properties of the paper and have been calculated or measured in our previous study.[20] The value for K_0P_m was calculated with eq 8 using a previously reported value of D_0.[20] Viscosities are found from the literature. Both blood and plasma have been shown to be shear-thinning;[10] however, as the shear rate in wicking is likely to be very small, a constant viscosity is assumed. θ is the advancing contact angle from Table I.

A few studies have reported the surface tension of blood and plasma. However, the reported values vary significantly.[41−43] This variability could be caused by a number of factors: differences between individuals, use of different anticoagulants in blood collection, different storage conditions, or longer delays between donation and measurement. Variability is also caused by dynamic surface tension due to a transient adsorption of proteins that is rarely considered.[44] Pendant drop surface tensiometry[45] was performed on the samples of whole blood and plasma used in measurements. Due to the quickly changing surface tension right after droplet formation and its dependence on interface dynamics, results were variable. Representative measurements over a large time interval are presented in Figure S3 in the Supporting Information. These correlate with the range of values previously reported. The complex interfacial behavior of such systems means that the surface tension of these fluids will be a function of geometry and diffusion dynamics. Therefore, the effective surface tension in any particular system is difficult to estimate without precise measurements. For this reason, surface tension was fit to data, although the fitted values are within measured ranges for both plasma and blood. Values for r_c are also found by fitting to data. The fitted values are within 20% of the approximate values calculated from eq 9 using the volume of the droplet and the measured contact angle on cellulose.

Full-morphology analysis was performed to assess the effect of liquid entrapment due to insufficient pore interconnectivity and whether this is a primary cause of the observed hysteresis. This is achieved by changing the algorithm to only include a wetting phase infiltration if pores are connected to a wetting phase reservoir at the edge of the domain. This step is common in full-morphology algorithms to account for entrapment of both wetting and nonwetting phases.[46] With this condition included, the current analysis shows negligible change. This implies that the paper pores are sufficiently interconnected to prevent liquid entrapment.

■ DISCUSSION

Measurements of the stain area as a function of time from several biological fluids are shown in linear and log−log scales in Figure 4. A significant difference in the stain growth kinetics between biological fluids with substantial cell and protein content appears when compared to simple, pure fluids. The second-stage power is strongly system dependent for biological fluids (Table I). Previous numerical research[20] attributed a change in power in the second stage to porosimetry hysteresis. This hysteresis is caused by differences in wetting/dewetting phenomena, and a more severe hysteresis has been shown to cause a lower second-stage gradient. This is because dewetting only occurs when the pores begin to empty after the droplet has been consumed. This occurs at the end of the first stage as the droplet disappears from the surface of the paper. The low second-stage powers exhibited by biological fluids imply that hysteresis is more severe for these fluids. Therefore, to understand the wicking behavior of these complex fluids, the mechanism of porosimetry hysteresis is investigated.

When a droplet is deposited onto the surface of a wettable porous media made of interconnected pores, two phenomena happen concomitantly. The droplet absorbs within the surface and starts wicking along the pores or fibers of the media. Likewise, wicking is a two-step phenomenon dictated by two distinct mechanisms.[17] In the first stage, the pores are filled with fluid provided by the droplet that is slowly being consumed. After some time, the droplet disappears, which initiates the second stage of radial wicking. In this stage, the fluid required to fill pores on the outside of the stain is provided by emptying the larger pores, causing the larger pores to be refilled with air. After the transition, the mechanism responsible for stain growth changes from wetting for the first stage (fluid moving from the droplet into the pores) to a combined wetting/dewetting mechanism for the second[20] (fluid moving from large to small pores). The advancing and receding contact angles drive each process, respectively. Should the advancing and receding angles be similar, or close, such as for decane on paper, a single wicking stage is observed.[20] For most fluids and biological fluids in particular, this is not the case. Wetting and protein adsorption change the three interfacial tensions,[11] thus changing the wetting of an advancing or receding front of the liquid. This means that the advancing angle will be much higher than the receding angle. This affects the driving force behind stain growth and creates the second wicking stage discrepancy discovered in this study.

The developed model can predict the behavior in the first stage. Predictions in Figure 5 deviate from experimental results in the very early stages of stain growth because this region is dominated by effects that are not included in the model. These include inertial and surface impact/wetting effects. As biological fluids show more deviation from the model at early times, this is likely caused by biomolecule adsorption, which brings about dynamic changes in the contact angle, surface tension, and viscosity.[11,44] Results imply that this adsorption has a very short time scale in this system. This is why broad accuracy is achieved using constant parameters. The later stages, right before stage transition, are also not well predicted. This is because in reality, stage transition does not happen instantaneously when the drop is consumed. There is instead a finite time over which the transition occurs. During this transition, the assumptions of constant droplet contact radius and constant saturation are invalid. This is particularly true for blood as the low viscosity and surface tension combined with a high contact angle result in a very slow stage transition that is not captured by this model. Despite these discrepancies, simulation results demonstrate that differences in stain sizes between biological and simple fluids are explained solely by changes in surface tension, contact angle, and viscosity. Continuing the simulation with a shift in boundary conditions to model consumption of the droplet was previously investigated.[20] A good agreement was found for simple fluids; however, such an agreement could not be found for biological fluids. This is likely because hysteresis of contact angles of the wicking fluid is very severe in biological fluids and the simple power law model used previously to account for this in simple fluids is no longer sufficient.

Before a more complete model of second-stage wicking can be derived, the mechanism of porosimetry hysteresis in these systems must be determined and quantified. Three hysteresis

https://dx.doi.org/10.1021/acs.langmuir.0c01318
Langmuir 2020, 36, 8209−8217

mechanisms have been investigated: (1) entrapment in a porous network, (2) fiber swelling, and (3) contact angle hysteresis. The effect of these factors is analyzed below.

In a capillary system, infiltration of the wetting phase will occur only if the nonwetting phase has an evacuation route. Similarly, if a fully wet capillary system is emptied, full evacuation of the wetting phase will not happen unless all wet regions have a path to the applied suction. In paper, the entrapment of liquid could occur during the second stage if initial stages of emptying caused the isolation of small areas of the wetting fluid in isolated areas of smaller pores. This entrapment of fluid in the second stage would produce the observed hysteresis effect.

Full-morphology analysis was used to identify the effect of liquid entrapment. Analysis shows that pores in paper are sufficiently interconnected with a large range of pore sizes such that no entrapment occurs. Thus, limited pore connectivity cannot be the primary cause of the observed hysteresis. This is particularly evident when it is considered that the resolution used would not capture the very small connections caused by fiber overlaps and intrafiber crevices. These very small channels were shown to be partially responsible for fluid transport in paper[47] and would result in a higher than calculated pore connectivity. Figure S4 in the Supporting Information shows the results from full-morphology analysis in comparison to mercury porosimetry measurements fit to the Brooks–Coorey model of pore dynamics.[30] Mercury porosimetry data and model fit are reproduced from a previous study on the same paper.[20] Our full-morphology calculation is similar to model and experimental results. Discrepancies mostly at high and low volume fractions are caused by errors in both full-morphology and mercury porosimetry techniques. The true pressure against the volume fraction curve likely lies in between the two calculated values. Porosimetry results also demonstrate that the majority of the pores in paper are larger than the average size of red blood cells (6 μm).[10] This supports the use of the Richards equation in this system as it implies that blood can be modeled as a continuum.

Another possible cause of the observed hysteresis is paper swelling. This is because swelling fibers effectively consume fluid, removing it from the system and reducing the local pore radius and volume. This decreasing volume of fluid in the system could create a hysteresis effect. This is unlikely as this would not correspond with first-to-second stage transition unless swelling occurred suddenly a finite time after contact. Previous studies showed that the time scale of swelling in normal paper fibers is very short (less than 1 s), so this is unlikely to have an effect.[48] It was also found that a two-stage behavior is still observed in paper made with nonswelling glass fibers.[20] Therefore, swelling is also unlikely to be the cause of hysteresis.

Contact angles experience hysteresis because local physical and chemical heterogeneities produce pinning forces. This could affect the second-stage behavior significantly as the introduction of voids in the center of the stain in this stage creates receding interfaces. Any hysteresis in contact angles would alter the relative magnitude of the capillary pressures at the advancing and receding interfaces. As this is what determines the wicking rate in the second stage, results would likely be affected significantly. Results in Table I show that these systems do experience significant contact angle hysteresis and the trend in hysteresis matches that of the second-stage powers. Therefore, contact angle hysteresis is likely to be the cause of the two-stage behavior measured in radial wicking. This also explains the reported relationship between the contact angle and equilibrium size.[11] Contact angle hysteresis defines the additional resistance to stain growth in the second stage and the anomalous stain kinetics of biological fluids.

Increased advancing contact angle of biological fluids on cellulose has previously been shown to be caused by an increase in solid–liquid interfacial energy due to protein adsorption.[11] The new results presented here show that, in most cases, the receding angle remains low due to pinning forces resisting the triple line motion. These pinning forces could be produced by adsorbed protein and cells at the contact line. This pinning due to adsorbed constituents is commonly observed in many colloid suspensions and would be more severe in blood as compared to plasma. This behavior is matched by experimental results. This implies that the primary cause of the anomalous stain growth behavior of biological fluids is a severe contact angle hysteresis (Figure 1). This occurs because adsorbed biomolecules cause a high advancing contact angle but do not alter the receding angle significantly.

Attempts were made to alter the developed model to incorporate the effects of contact angle hysteresis. This was achieved by including contact angle as a function of the temporal gradient of volume fraction. To do this, eq 3 cannot be used as pressure is no longer solely a function of the volume fraction of fluid in pores. Equation 2 must be selected instead, which requires pressure to be calculated at each cell. A pressure equation can be derived by integrating eq 6; however, this introduces two numerical difficulties. First, the equation predicts a negative infinite pressure at $\phi = 0$; this can be overcome by assuming a linear function of pressure from a threshold minimum volume fraction. This had a negligible effect on results as it maintains the required high pressure gradient over areas with a small volume fraction that was not achieved by simply setting a lower pressure limit. Second, the new pressure field is discontinuous in regions where the temporal gradient of volume fraction changes signs or where the mechanism shifts from filling to emptying. This produces convergence difficulties that could not be resolved. A more detailed numerical study is required to properly resolve the effect of contact angle hysteresis in radial wicking.

The developed model is capable of predicting results in the first stage of wicking for all tested fluids by including values of surface tension, contact angle, and viscosity. This shows that the dynamics for complex fluids in this regime are driven by the same mechanisms as simple fluids.[20,27−29] Results highlight the role of hysteresis in these systems as it is the primary difference between the two stages. For biological fluids, wetting/dewetting hysteresis in the second stage is too severe to model with current techniques. Experimental and numerical investigations show that this hysteresis arises from contact angle effects due to the protein and cell component of the fluids. This identifies why the power relationship with time for these fluids is low.

■ CONCLUSIONS

In this study, the wicking of biological fluids including human blood, plasma, and protein solutions on paper was measured and modeled from first principles. This was to optimize the design of novel low-cost paper-based diagnostics. A combination of high-speed photography, image processing, and numerical modeling was used. The stain size of biological

https://dx.doi.org/10.1021/acs.langmuir.0c01318
Langmuir 2020, 36, 8209−8217

fluids on paper was recorded as a function of time. A unique second-stage behavior was discovered, differing from that of simple fluids. The two-phase wicking behavior of biological fluids on paper is best visualized by following the stain area as a function of time on a log–log plot. The cause of the second wicking stage of biological fluids is a severe wetting/dewetting hysteresis. Wetting experiments with model systems revealed contact angle hysteresis to be the most likely cause of hysteresis. Fiber swelling and liquid entrapment in porous media were also investigated and dismissed. The difference between first stages exhibited by the different fluids tested was solely driven by differences in viscosity, surface tension, and contact angle. This was demonstrated with a good fit to numerical modeling in the first stage. These results give significant insights into the wicking of biological fluids in paper, particularly in finite reservoir systems where the investigated hysteresis will be significant. This knowledge now enables the development and optimization of a new generation of low-cost diagnostic devices with powerful tools such as computational fluid dynamics and mathematical modeling.

■ ASSOCIATED CONTENT

Supporting Information

The Supporting Information is available free of charge at https://pubs.acs.org/doi/10.1021/acs.langmuir.0c01318.

Fit of linear interpolation to results for plasma (Figure S1); fit of linear interpolation to results for blood (Figure S2); pendant drop tensiometry results for water, plasma, and blood (Figure S3); comparison of full-morphology calculation to mercury porosimetry (Figure S4) (PDF)

■ AUTHOR INFORMATION

Corresponding Author

Gil Garnier − *BioPRIA and Department of Chemical Engineering, Monash University, Clayton, VIC 3800, Australia;* orcid.org/0000-0003-3512-0056; Email: gil.garnier@monash.edu

Authors

Michael J. Hertaeg − *BioPRIA and Department of Chemical Engineering, Monash University, Clayton, VIC 3800, Australia*

Rico F. Tabor − *School of Chemistry, Monash University, Clayton, VIC 3800, Australia;* orcid.org/0000-0003-2926-0095

Joseph D. Berry − *Department of Chemical and Biomolecular Engineering and the Particulate Fluids Processing Centre, University of Melbourne, Parkville, VIC 3052, Australia*

Complete contact information is available at: https://pubs.acs.org/10.1021/acs.langmuir.0c01318

Notes

The authors declare no competing financial interest.

■ ACKNOWLEDGMENTS

This research was funded by an ARC Linkage grant (LP160100544), Haemokinesis, and an Australian Government Research Training Program (RTP) Scholarship. The research was supported in part by Monash eResearch Centre and eSolutions-Research Support Services through the use of the MonARCH HPC Cluster. Thanks to David Paganin for advice on the analysis of X-ray images and the Red Cross Australia for supplying blood products.

■ REFERENCES

(1) Kawase, T.; Sekoguchi, S.; Fujii, T.; Minagawa, M. Spreading of liquids in textile assemblies: Part I: Capillary spreading of liquids. *Text. Res. J.* **1986**, *56*, 409−414.

(2) Khan, M. S.; Thouas, G.; Shen, W.; Whyte, G.; Garnier, G. Paper diagnostic for instantaneous blood typing. *Anal. Chem.* **2010**, *82*, 4158−4164.

(3) Wijaya, M.; Leong, E. C.; Rahardjo, H. Effect of shrinkage on air-entry value of soils. *Soils Found.* **2015**, *55*, 166−180.

(4) Reed, C. M.; Wilson, N. Fundamentals of absorbency of fibres, textile structures and polymers. I: the rate of rise of a liquid in glass capillaries. *J. Phys. D: Appl. Phys.* **1993**, *26*, 1378.

(5) Al-Tamimi, M.; Shen, W.; Zeineddine, R.; Tran, H.; Garnier, G. Validation of paper-based assay for rapid blood typing. *Anal. Chem.* **2012**, *84*, 1661−1668.

(6) Liu, Z.; He, X.; Han, J.; Zhang, X.; Li, F.; Li, A.; Qu, Z.; Xu, F. Liquid wicking behavior in paper-like materials: mathematical models and their emerging biomedical applications. *Microfluid. Nanofluid.* **2018**, *22*, No. 132.

(7) Li, J.; Li, X.; Michielsen, S. Alternative method for determining the original drop volume of bloodstains on knit fabrics. *Forensic Sci. Int.* **2016**, *263*, 194−203.

(8) de Castro, T. C.; Carr, D. J.; Taylor, M. C.; Kieser, J. A.; Duncan, W. Drip bloodstain appearance on inclined apparel fabrics: Effect of prior-laundering, fibre content and fabric structure. *Forensic Sci. Int.* **2016**, *266*, 488−501.

(9) Ramsthaler, F.; Schlote, J.; Wagner, C.; Fiscina, J.; Kettner, M. The ring phenomenon of diluted blood droplets. *Int. J. Leg. Med.* **2016**, *130*, 731−736.

(10) Thiriet, M. *The Biology and Mechanics of Blood Flows*; Springer, 2008.

(11) Hertaeg, M. J.; Tabor, R. F.; Garnier, G. Effect of protein adsorption on the radial wicking of blood droplets in paper. *J. Colloid Interface Sci.* **2018**, *528*, 116−123.

(12) Hagiwara, T.; Nattawut, P.; Shibata, M.; Sakiyama, T. Monitoring of adsorption behaviors of bovine serum albumin onto a stainless steel surface by the quartz crystal microbalance based on admittance analysis. *Biosci., Biotechnol., Biochem.* **2017**, *81*, 783−789.

(13) Greenblatt, D. J. Reduced serum albumin concentration in the elderly: a report from the Boston Collaborative Drug Surveillance Program. *J. Am. Geriatr. Soc.* **1979**, *27*, 20−22.

(14) Gillespie, T. The spreading of low vapor pressure liquids in paper. *Journal of Colloid Science* **1958**, *13*, 32−50.

(15) Kissa, E. Capillary sorption in fibrous assemblies. *J. Colloid Interface Sci.* **1981**, *83*, 265−272.

(16) Danino, D.; Marmur, A. Radial capillary penetration into paper: limited and unlimited liquid reservoirs. *J. Colloid Interface Sci.* **1994**, *166*, 245−250.

(17) Borhan, A.; Rungta, K. K. An experimental study of the radial penetration of liquids in thin porous substrates. *J. Colloid Interface Sci.* **1993**, 403−411.

(18) Marmur, A. Penetration and displacement in capillary systems of limited size. *Adv. Colloid Interface Sci.* **1992**, *39*, 13−33.

(19) Kloubek, J. Hysteresis in porosimetry. *Powder Technol.* **1981**, *29*, 63−73.

(20) Hertaeg, M. J.; Tabor, R. F.; Berry, J. D.; Garnier, G. Dynamics of stain growth from sessile droplets on paper. *J. Colloid Interface Sci.* **2019**, *541*, 312−321.

(21) Hazlett, R. D. Simulation of capillary-dominated displacements in microtomographic images of reservoir rocks. *Transp. Porous Media* **1995**, *20*, 21−35.

(22) Richards, L. A. Capillary conduction of liquids through porous mediums. *J. Appl. Phys.* **1931**, *1*, 318−333.

(23) Huang, Z.; Raghuwanshi, V. S.; Garnier, G. Functionality of immunoglobulin g and immunoglobulin M antibody Physisorbed on cellulosic Films. *Front. Bioeng. Biotechnol.* **2017**, *5*, No. 41.

(24) Su, J.; Garvey, C. J.; Holt, S.; Tabor, R. F.; Winther-Jensen, B.; Batchelor, W.; Garnier, G. Adsorption of cationic polyacrylamide at the cellulose-liquid interface: A neutron reflectometry study. *J. Colloid Interface Sci.* **2015**, *448*, 88−99.
(25) Weitkamp, T.; Haas, D.; Wegrzynek, D.; Rack, A. ANKAphase: software for single-distance phase retrieval from inline X-ray phase-contrast radiographs. Erratum. *J. Synchrotron Radiat.* **2013**, *20*, 205.
(26) Paganin, D.; Mayo, S. C.; Gureyev, T. E.; Miller, P. R.; Wilkins, S. W. Simultaneous phase and amplitude extraction from a single defocused image of a homogeneous object. *J. Microsc.* **2002**, *206*, 33−40.
(27) Perez-Cruz, A.; Stiharu, I.; Dominguez-Gonzalez, A. Two-dimensional model of imbibition into paper-based networks using Richards' equation. *Microfluid. Nanofluid.* **2017**, *21*, No. 98.
(28) Ashari, A.; Bucher, T. M.; Tafreshi, H. V.; Tahir, M. A.; Rahman, M. S. A. Modeling fluid spread in thin fibrous sheets: Effects of fiber orientation. *Int. J. Heat Mass Transfer* **2010**, *53*, 1750−1758.
(29) Jaganathan, S.; Tafreshi, H. V.; Pourdeyhimi, B. A realistic modeling of fluid infiltration in thin fibrous sheets. *J. Appl. Phys.* **2009**, *105*, No. 113522.
(30) Huinink, H. *Fluids in Porous Media*; Morgan & Claypool Publishers, 2016.
(31) Harvie, D. J. E. An implicit finite volume method for arbitrary transport equations. *ANZIAM J.* **2010**, *52*, 1126−1145.
(32) Lavi, B.; Marmur, A.; Bachmann, J. Porous media characterization by the two-liquid method: Effect of dynamic contact angle and inertia. *Langmuir* **2008**, *24*, 1918−1923.
(33) Bosanquet, C. L. V. On the flow of liquids into capillary tubes. *London, Edinburgh Dublin Philos. Mag. J. Sci.* **1923**, *45*, 525−531.
(34) Martic, G.; Gentner, F.; Seveno, D.; Coulon, D.; De Coninck, J.; Blake, T. D. A molecular dynamics simulation of capillary imbibition. *Langmuir* **2002**, *18*, 7971−7976.
(35) Masoodi, R.; Pillai, K. M. *Wicking in Porous Materials: Traditional and Modern Modeling Approaches*; CRC Press, 2012; pp 136−140.
(36) Sala, C.; Ciullo, M.; Lanzara, C.; Nutile, T.; Bione, S.; Massacane, R.; D'Adamo, P.; Gasparini, P.; Toniolo, D.; Camaschella, C. Variation of hemoglobin levels in normal Italian populations from genetic isolates. *Haematologica* **2008**, *93*, 1372−1375.
(37) Ravenhill, B. J.; Kanjee, U.; Ahouidi, A.; Nobre, L.; Williamson, J.; Goldberg, J. M.; Antrobus, R.; Dieye, T.; Duraisingh, M. T.; Weekes, M. P. Quantitative comparative analysis of human erythrocyte surface proteins between individuals from two genetically distinct populations. *Commun. Biol.* **2019**, *2*, No. 350.
(38) Billett, H. H. *Hemoglobin and Hematocrit*, 3rd ed.; Butterworths, 1990.
(39) Kestin, J.; Sokolov, M.; Wakeham, W. A. Viscosity of liquid water in the range- 8 C to 150 C. *J. Phys. Chem. Ref. Data* **1978**, *7*, 941−948.
(40) Vazquez, G.; Alvarez, E.; Navaza, J. M. Surface tension of alcohol water+ water from 20 to 50. degree. C. *J. Chem. Eng. Data* **1995**, *40*, 611−614.
(41) Rosina, J.; Kvasnak, E.; Suta, D.; Kolarova, H.; Malek, J.; Krajci, L. Temperature dependence of blood surface tension. *Physiol. Res.* **2007**, *56*, S93.
(42) Sobac, B.; Brutin, D. Desiccation of a sessile drop of blood: cracks, folds formation and delamination. *Colloids Surf., A* **2014**, *448*, 34−44.
(43) Tarasevich, Y. Y.; Vodolazskaya, I. V.; Bondarenko, O. P. Modeling of spatial-temporal distribution of the components in the drying sessile droplet of biological fluid. *Colloids Surf., A* **2013**, *432*, 99−103.
(44) Zaitsev, S. Dynamic surface tension measurements as general approach to the analysis of animal blood plasma and serum. *Adv. Colloid Interface Sci.* **2016**, *235*, 201−213.
(45) Berry, J. D.; Neeson, M. J.; Dagastine, R. R.; Chan, D. Y. C.; Tabor, R. F. Measurement of surface and interfacial tension using pendant drop tensiometry. *J. Colloid Interface Sci.* **2015**, *454*, 226−237.
(46) Becker, J.; Schulz, V.; Wiegmann, A. Numerical determination of two-phase material parameters of a gas diffusion layer using tomography images. *J. Fuel Cell Sci. Technol.* **2008**, *5*, No. 021006.
(47) Roberts, R.; Senden, T.; Knackstedt, M.; Lyne, M. B.; et al. Spreading of aqueous liquids in unsized papers is by film flow. *J. Pulp Pap. Sci.* **2003**, *29*, 123−131.
(48) Schuchard, D. R.; Berg, J. C. Liquid transport in composite cellulose-superabsorbent fiber networks. *Wood Fiber Sci.* **2007**, *23*, 342−357.

https://dx.doi.org/10.1021/acs.langmuir.0c01318
Langmuir 2020, 36, 8209−8217